UNIVERSITY
OF OSLO

Lin Xue

Communication and interaction among surface-adhered membranous protocells

Thesis submitted for the degree of *Philosophiae Doctor*

Department of Chemistry

Faculty of Mathematics and Natural Sciences

Centre for Molecular Medicine Norway

Faculty of Medicine

MDCCCXI

2023

Series of dissertations submitted to the
Faculty of Mathematics and Natural Sciences, University of Oslo
No. 2744

ISSN 1501-7710

Cover: UiO.
Print production: Graphic center, University of Oslo.

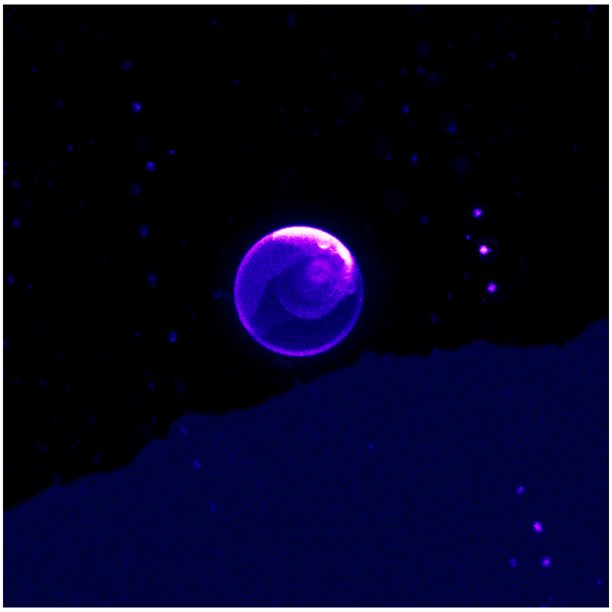

Kunst er menneskets trang til krystalisation.

Art is the human craving for crystallization.

Edvard Munch

Preface

This thesis is submitted in partial fulfillment of the requirements for the degree of *Philosophiae Doctor* at the Department of Chemistry, Faculty of Mathematics and Natural Sciences, University of Oslo. The research presented in this thesis, including three original papers as well as additional results, has been carried out under the supervision of Dr. Irep Gözen during the period 2019 to 2022 at the Laboratory of Bionanotechnology and Membrane Systems, Centre for Molecular Medicine Norway, Faculty of Medicine, University of Oslo. Over the years, the group of supervisors consisted of Dr. Irep Gözen, Prof. Michele Cascella and Prof. Reidar Lund. Financial support has been provided by UiO: Life Sciences Convergence Environment.

Acknowledgements

I would like to take this opportunity to express my deepest gratitude and appreciation to all the people who have supported me throughout my Ph.D. and contributed to the completion of this thesis.

First and foremost, I am immensely grateful to my main supervisor, Prof. Michele Cascella, and co-supervisor Prof. Reidar Lund, for their constant guidance, invaluable insights, and continuous encouragement. Their expertise and mentorship have been instrumental in shaping my research and pushing me to achieve my best. I would also like to thank Prof. Ute Krengel, whose mentorship and discussions have played a pivotal role in my growth as a researcher.

I would like to express my sincere appreciation to the people at the Department of Chemistry, especially the members of the Krengel's and Lund's groups, as well as Prof. Steven Ray Haakon Wilson and Prof. Stian Svelle, for their support and the enriching academic environment they have provided throughout my doctoral studies. Their commitment to excellence in research and education has been a constant inspiration to me.

I am grateful to my colleagues and fellow researchers at the Centre for Molecular Medicine Norway. Elif, Karolina, Aysu, Inga, Annie, Maivizhi, Jicheng and Ingrid, thank you for sharing the moments in the cold and dark confocal room and for putting up with all the jokes I made about vesicles. Your support and encouragement have made my research journey more enjoyable and rewarding. May the exhibition of NanoCosmos be remembered as a joyful experience.

My heartfelt thanks go to my friends in Oslo, Amiran, Miina, Erchen, Stephan, Yael, Edna, Zhuokun, Ru, Alexandre, Gabriella, Ying, Jia, Juan, Jia, Zhiyuan, and Yunxi, and in Sweden, Junjie, Yidong, Yibo, Ziyu, Guo, Qianqian, Xixi, and Axel. Their encouragement and support have made it possible for me to overcome challenges and maintain my motivation. I would also like to thank Tianyu, Etay, Ziyu, Songyao, Haipeng, and all my friends in China for being my pillars of support throughout this dissertation.

Finally, I would like to express my deep gratitude to my parents and my family for their unwavering support, patience, and love through all the ups and downs of my life. Your belief in me has been the driving force behind my accomplishments, and I am forever grateful.

Lin Xue

Oslo, December 2023

Table of Contents

Preface....v

Abbreviations....ix

List of Publications....xi

Summary....xiii

Sammendrag....xv

1 Introduction....1

- 1.1 Origin of life and protocells....1
  - 1.1.1 Definition of life....3
  - 1.1.2 Environmental conditions....3
  - 1.1.3 The earliest record of life on Earth....7
  - 1.1.4 Hypothesis about life....7
  - 1.1.5 Protocell compartmentalization....12
  - 1.1.6 Protocell population and intercellular communication....14
- 1.2 Surface energy and the possible implication of surfaces....21
  - 1.2.1 Surface free energy and wetting phenomena....21
  - 1.2.2 Surfaces used in this thesis and their natural analogues....23
- 1.3 Lipid membrane....23
  - 1.3.1 The chemistry of lipid molecules....24
  - 1.3.2 Self-assembly and hydrophobic effect....26
  - 1.3.3 Membrane surface energy....27
  - 1.3.4 Formation of vesicles....28
  - 1.3.5 Phospholipid vesicles....30
  - 1.3.6 Supported lipid membranes....31
  - 1.3.7 Double bilayer spreading....32
  - 1.3.8 Membrane rupturing and nanotube formation....33
  - 1.3.9 Formation of protocell-nanotube networks and the temperature effect....34
  - 1.3.10 Transport among protocells via tunneling nanotubes....35

1.3.11 Membrane permeability and transient pores 37
1.3.12 Membrane fusion 38
1.3.13 Motility of lipid vesicles 39
2 Aim of the projects 41
3 Heat-induced rapid growth of protocell from protocell-nanotube network 43
4 Cargo transport in protocell-nanotube network 45
5 Cationic liposome-assisted cargo delivery 47
6 Materials and methods 49
6.1 Preparation of lipid vesicles 49
6.2 Surface fabrication 50
6.3 Optical microscopy 52
6.4 Differential interference contrast microscopy 52
6.5 Fluorescence and confocal microscopy 53
6.6 Infrared laser heating system 56
6.7 The microfluidic pipette 58
7 Conclusion and outlook 61
References 63
Publications 87

Abbreviations

A. baylyi	*Acinetobacter baylyi*
AF	Amorphous fluoropolymer
B. subtilis	*Bacillus subtilis*
CC	Carbonaceous chondrite
CLSM	Confocal laser scanning microscopy
CPP	Critical packing parameter
DIC	Differential interference contrast
DOTAP	Dioleoyl-3-trimethylammonium propane
DPPC	Dipalmitoylphosphatidylcholine
E-beam	Electron-beam
E. coli	*Escherichia coli*
EC	Enstatite chondrite
FRAP	Fluorescence recovery after photobleaching
FRET	Förster resonance energy transfer
GUV	Giant unilamellar vesicle
IR	Infrared
LUCA	Last universal common ancestor
LUV	Large unilamellar vesicle
MLV	Multilamellar vesicle
NA	Numerical aperture
PC	Phosphatidylcholine
PDMS	Polydimethylsiloxane
PE	Phosphatidylethanolamine
PVD	Physical vapor deposition

QCM	Quartz crystal microbalance
SIM	Structured illumination microscopy
STED	Stimulated emission depletion
SUV	Small unilamellar vesicle
TNT	Tunneling nanotube
UV	Ultraviolet

List of Publications

Paper I. E. S. Köksal, S. Liese, **L. Xue**, R. Ryskulov, L. Viitala, A. Carlson, I. Gözen.

Rapid growth and fusion of protocells in surface-adhered membrane networks[1]

Small, 2020, 16, 2002529.

DOI: https://doi.org/10.1002/smll.202002529.

Paper II. I. J. Schanke†, **L. Xue**†, K. Spustova, I. Gözen.

Transport among protocells via tunneling nanotubes[2]

Nanoscale, 2022, 14 (29), 10418–10427.

DOI: https://doi.org/10.1039/D2NR02290G.

†These authors contributed equally to this work.

Paper III. **L. Xue**, A. B. Stephenson, I. Gözen.

Liposome-assisted in-situ cargo delivery to artificial cells and cellular subcompartments

Submitted manuscript

DOI: https://doi.org/10.1101/2022.04.27.489538

List of related peer-reviewed publications by the author that are not included in the thesis

Paper IV. K. Spustova, **L. Xue**, R. Ryskulov, A. Jesorka, I. Gözen

Manipulation of lipid membranes with thermal stimuli[3]

Membrane Lipids, 2022, 209-225.

DOI: https://doi.org/10.1007/978-1-0716-1843-1_17.

Paper V. I. Gözen, E.S. Köksal, I. Põldsalu, **L. Xue**, K. Spustova, E. Pedrueza-Villalmanzo, R. Ryskulov, F. Meng, A. Jesorka.

Protocells: milestones and recent advances[4]

Small, 2022, 18, 2106624.

DOI: https://doi.org/10.1002/smll.202106624

During my PhD studies, I also explored lipid vesicle fusion on solid surfaces. Part of this work was presented as poster contribution in International Conference on Engineering Synthetic Cells and Organelles (SynCell) 2022, as well as in Molecular Origins of Life, Munich 2022.

Summary

This thesis provides experimental evidence for rudimentary communication and interaction in protocells and protocell populations, highlighting their potential role in the transition from prebiotic soft matter compartments to the first living cells at the origin of life.

The research demonstrates that self-spreading of lipid reservoirs on solid surfaces can spontaneously form surface-supported double bilayer membranes that can further transform into protocell-nanotube networks. Elevated temperature (40 °C – 70 °C) can promote nucleation and growth of protocells within the network, and further elevation of local temperature (90 °C) induces fusion of neighboring protocells. Upon fusion, the RNA internalized in one of the protocells can be redistributed to the fused protocell. The lipid nanotubes within these networks allow the transport of molecular cargo, including water-soluble dye, RNA and DNA, between connecting protocells. The transport is diffusion driven and is found to be highly dependent on the geometric parameters of the networks, such as the size of the protocells and the length and diameter of the nanotubes, which are characterized by an analytical model.

This thesis also presents a protocol for the delivery of membrane-impermeable molecules, such as oligonucleotides and global proteins, into surface-adhered giant vesicles using small cationic vesicles as carriers. The positively charged cationic vesicle membranes can fuse with the negatively charged giant vesicle membranes. Cargo loaded in the small vesicles can be released into the giant vesicles upon membrane fusion. Furthermore, based on this protocol, it is shown that the giant vesicles can accommodate simple enzymatic reactions, providing a practical bottom-up approach for constructing synthetic cells with functional components.

Sammendrag

Denne avhandlingen gir eksperimentelle bevis for rudimentær kommunikasjon og interaksjon i protoceller og protocellepopulasjoner, og fremhever deres potensielle rolle i overgangen fra prebiotiske bløtstoffkompartimenter til de første levende cellene ved livets opprinnelse.

Forskningen viser at selvspredning av lipidreservoarer på faste overflater spontant kan danne overflatestøttede doble dobbeltlagsmembraner som videre kan omdannes til protocelle-nanorør-nettverk. Forhøyet temperatur (40 °C - 70 °C) kan fremme kjernedannelse og vekst av protokollceller i nettverket, og ytterligere forhøyelse av lokal temperatur (90 °C) induserer fusjon av naboprotokollceller. Ved fusjon kan RNA som er internalisert i en av protokollcellene omfordeles til den fusjonerte protokollcellen. Lipidnanorørene i disse nettverkene tillater transport av molekylær last, inkludert vannløselig fargestoff, RNA og DNA, mellom sammenhengende protoceller. Transporten er diffusjonsdrevet og viser seg å være svært avhengig av de geometriske parametrene til nettverkene, som størrelsen på protocellene og lengden og diameteren på nanorørene, som er karakterisert ved hjelp av en analytisk modell.

Til slutt presenterer denne avhandlingen en protokoll for levering av membran-impermeable molekyler, som oligonukleotider og globale proteiner, inn i overflateadhererte gigantiske vesikler ved hjelp av små kationiske vesikler som bærere. De positivt ladede kationiske vesikkelmembranene kan smelte sammen med de negativt ladede gigantiske vesikkelmembranene. Last lastet i de små vesiklene kan frigjøres i de gigantiske vesiklene ved membranfusjon. Videre, basert på denne protokollen, er det vist at de gigantiske vesiklene kan romme enkle enzymatiske reaksjoner, noe som gir en praktisk nedenfra-og-opp-tilnærming for å konstruere syntetiske celler med funksjonelle komponenter.

1 Introduction

The origin of life on early Earth remains a fundamental mystery and is widely regarded as one of the most pressing questions in scientific research[5]. The earliest known evidence of living cells is in the form of bacterial colonies[6], in which individual bacteria can exchange metabolic materials with their neighbors. To study the transition from prebiotic entities to the first living cells, soft matter structures called protocells have been synthesized in the laboratory as model compartments[4,7–12] with properties and behaviors similar to those of primitive cells. In this thesis, we present experimental studies of protocells and protocell populations, which seeks to elucidate the potential for communication and interaction among surface-adherent protocells.

In this first chapter, Section 1.1 discusses established and recent findings and hypotheses on protocells and related origin of life studies, while Section 1.2 introduces the intrinsic energy of solid surfaces and its implications for protocells. Subsequently, Section 1.3 describes the self-assembly of lipids and the mechanism of lipid membranes, which are essential for understanding the properties of membranous protocells.

Chapter 2 presents the scope and motivation of the studies presented in this thesis. Chapter 3 summarizes the main findings of Paper I, which focuses on the heat-assisted formation of surface-adhered protocell-nanotube networks. Chapter 4 presents the main findings of Paper II, which investigates nanotube-mediated cargo transport within protocell-nanotube networks. Chapter 6 summarizes the main results of Paper III, which demonstrates liposome-based methods for the delivery of membrane-impermeable cargo into protocellular compartments. Chapter 6 describes the experimental methods and techniques used in this thesis. Finally, Chapter 7 concludes the studies and provides an outlook for future investigations.

1.1 Origin of life and protocells

Evidence on the evolutionary timeline of Earth suggests that the age of our planet is approximately 4.5 billion years (Gy)[13,14], followed by the appearance of liquid water[15] and organic matter, and finally the emergence of the first living cells approximately 3.5 billion years ago (Gya)[6,16]. However, there is a lack of knowledge about the transition from inanimate to living matter. Figure 1.1 shows the candidates that might be present in the primordial soup, such as fragments of genetic polymers, organic or inorganic compartments, clay particles and amphiphilic molecules. Exactly how these building blocks would harmoniously assemble under prebiotic conditions into life-like precursor structures called protocells and the successive transformations they would undergo to eventually evolve into living cells is currently unknown.

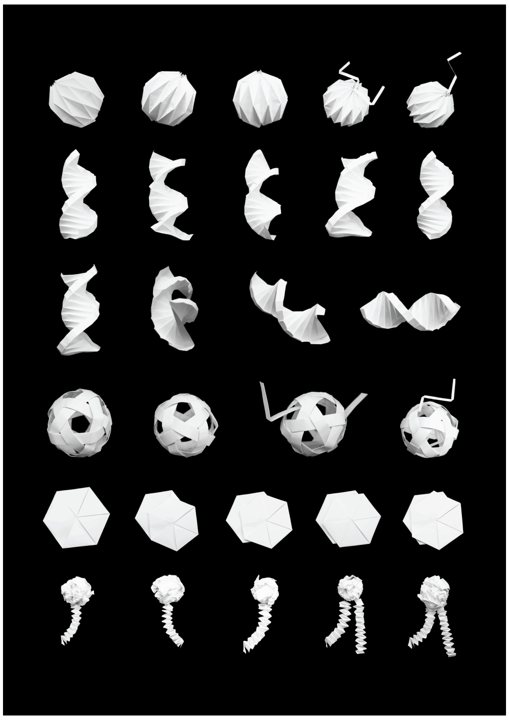

Figure 1.1. Illustration showing a simplified inventory of prebiotically relevant components that would have been available in the condition of the early Earth. First row: membranous compartments; second and third rows: genetic polymers; fourth row: rock microcavities; fifth row: clay particles; sixth row: fatty acids and phospholipids.

In Section 1.1, I will first present commonly accepted definitions of life, followed by an overview of the environmental conditions on the early Earth in which life could have emerged. I will then discuss the possible sources and origins of organic matter and the earliest fossil evidence, highlighting the knowledge gap between the two. Next, I will introduce the established hypotheses for the origin of life and explain the possible physicochemical mechanisms for the formation of protocells. I will then discuss the possibility of the emergence of protocell populations on the early Earth and point out their potential evolutionary advantages over individual protocells. At the end of the chapter, I will describe possible means of communication and interaction among protocells, and finally provide a comparison with modern cell populations.

1.1.1 Definition of life

How life could have arisen is closely related to the question of what life is. So far, there is no solid consensus on the definition of life[17], although many versions have been proposed. One of the best known definitions comes from the NASA's Exobiology Program: "*Life is a self-sustaining chemical system capable of Darwinian evolution*"[18]. This definition is quite broad and relatively impractical, especially from the point of view of experimental researchers. The theoretical biologist Tibor Ganti proposed the chemoton model as a minimal living system[19]. A chemoton, short for chemical automation, consists of three subsystems: the metabolic subsystem, the two-dimensional membrane, and the genetic information subsystem. The metabolic subsystem is a chemical reaction network that can absorb nutrients to reproduce itself and produce compounds needed by the other two subsystems. The membrane subsystem forms a boundary that encloses the other two subsystems, and it is capable of reproducing itself using the compounds produced by the metabolic subsystem. The genetic subsystem can perform template-based polymerization of the compounds synthesized by the metabolic system. The by-products of polymerization are essential for the membrane formation. In this way, all three subsystems are interconnected and function cooperatively. Later, Pohorille and Deamer proposed 7 criteria for building an ideal minimal cell[20]: a genetic polymer, a supply of monomers for the polymer, a source of chemical energy for biochemical reaction, a catalytic activity for replication, a self-reproducing membrane, a division mechanism, and the regulation of all the processes. These points overlap greatly with the chemoton model.

1.1.2 Environmental conditions

With the establishment of a habitable Earth with hydrosphere and the presence of organic matter, the origin of life would most likely have occurred in the Eoarchean period (4-3.5 Gya)[6,21]. The Earth's environment today may be very different from the early Earth. One way to understand what the favorable sites for the origin of life might be is to consider the environmental conditions of the early Earth. The concept of urability, which refers to the geophysical and geochemical conditions for the origin of life[22], was proposed by Deamer, Cary, and Damer in 2022. In total 28 urable conditions are identified, including 12 geophysical, 14 geochemical, and 2 combinatorial. Figure 1.2 shows some of these urable conditions. For example, the concentration of ions in the aqueous environment is one of the geochemical factors. Compared to marine habitats, freshwater environments are considered more conducive to urability[23–25]. These urable conditions overlap to create a urable center that is suitable for protocell assembly. The urable center is also expected to increase in size and diversity as protocells become sufficiently robust to survive the environmental stress and adapt to changing conditions. In this section, I will outline and explain some of the critical conditions that would have a significant impact on protocell formation and the later emergence of the first living cell, namely liquid water (hydrosphere), atmosphere, ultraviolet (UV) radiation, and minerals and rocks.

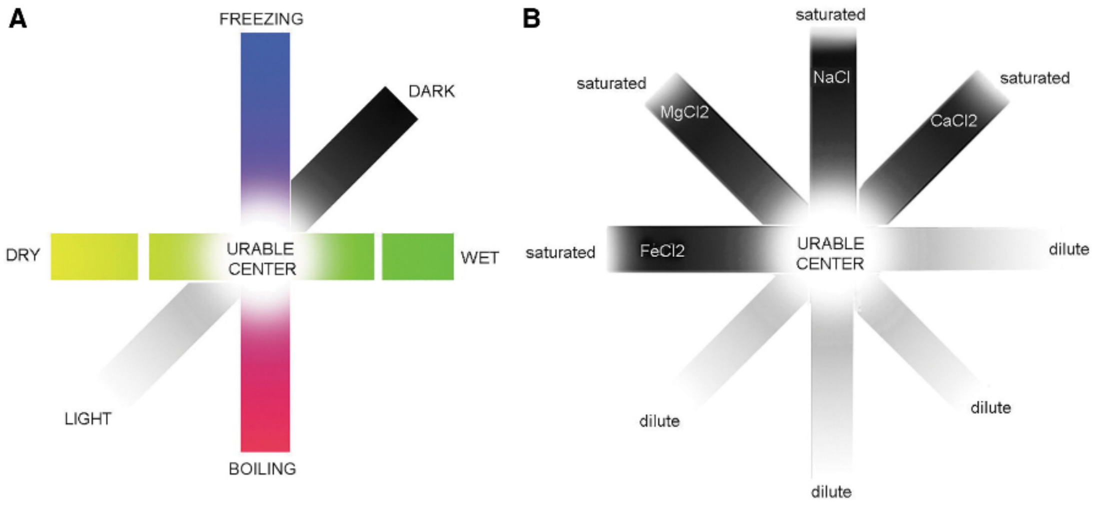

Figure 1.2. Examples of urable (biophysical and biochemical) conditions for the emergence of life on a planet. (a) Dry-wet: the amount of water as a solvent for the prebiotic reaction; freezing-boiling: the water temperature; light-dark: the intensity of light energy on the surface of the planet. (b) The concentrations of ionic solutes in aqueous environment. *Reprinted with permission from Reference 22. Copyright 2022, Mary Ann Liebert, Inc.*

Atmosphere

Although the origin of the early atmosphere is still debated, the atmosphere on the early Earth was significantly different in composition from the atmosphere we have today. We refer to the early atmosphere as the primary and secondary atmosphere. Any primary atmosphere captured during the accretion of the terrestrial planets would have been lost[26]. The secondary atmosphere would have been formed by the volcanic outgassing of the volatiles trapped in the Earth's interior[26]. The outgassing of volatiles in the impacting chondrites would also contribute to the formation of the secondary atmosphere[27]. The secondary atmosphere after the period of the late heavy bombardment (4.5-3.8 Gya)[26] is of particular interest for the origin of life. The post-heavy bombardment atmosphere was considered to be weakly reduced, probably dominated by CO_2 and N_2, with traces of CO and H_2[26,27]. The well-known Miller-Urey experiment[28] used an artificial atmosphere composed of CH_4, NH_3, H_2, and H_2O to produce a variety of biologically relevant organic molecules such as sugars and amino acids. However, CH_4 and NH_3 may not have been available at that stage of the atmosphere.

Water

Water is the medium for life as we know it on Earth[29] and is massively involved in biochemical reactions and metabolism. It is a polar molecule that can form hydrogen bonds, and the associated hydrophobic effect is fundamental to the self-assembly of amphiphiles that leads to protocell formation (see Section 1.3.2). Based on oxygen isotopes in Hadean zircons, the presence of liquid water could be dated to 4.3 Gya[30]. Although the origin of water on early Earth is still unclear, it has been suggested that water ice could have been delivered to Earth by carbonaceous chondrite (CC) meteorites[31–34]. This is supported by the Advent of Bio-elements model[35]. According to this two-step model, the dry Earth was formed, followed by the delivery of an atmosphere and ocean to the dry Earth by the icy asteroids from the outer part of the asteroid belt delivered at ~4.4 Gya. Enstatite chondrite (EC) meteorites were formed in the inner Solar System, which was too warm to retain water ice, whereas CC meteorites were formed in the outer Solar System, which was water-rich[36]. A new study proposed EC meteorites instead of EC meteorites as the primary source of water[37]. According to the calculation of Piani et al., EC meteorites could have contained a high amount of water, equivalent to the volume of three oceans on the early Earth[37]. In addition, EC meteorites have a similar isotropic composition to the materials that formed the terrestrial Earth.

UV light

UV radiation on the early Earth was considered to be the main energy source for probiotic reactions such as the synthesis of RNA and DNA building blocks[38]. During the Archean eon (4-2.5 Gya), it has been suggested that the Sun was ~25% less luminous and thus ~35% reduced luminosity in the biologically effective UV wavelength[39]. Cockell's computational model shows that high fluxes of UV-B (280 nm-315 nm) and UV-C (200-280 nm) penetrated the primary atmosphere and reached the planetary surface due to the absence of the ozone column[40]. Short-wavelength UV, especially UV-C (200-280 nm), has been shown to be more harmful to microorganisms than UV-A (315-400 nm)[41]. However, intense UV irradiation can destroy organic compounds by breaking chemical bonds as in photolysis[42]. It has also been shown experimentally that ocean water can effectively attenuate UV irradiation, protecting the prebiotically relevant molecules[42–44]. In addition, the optical properties of the micrometer-sized fatty acid vesicles were analyzed using a computational model[45], suggesting that they could have acted as Mie scattering particles for the incident UV-C light, specifically in the region of 180-210 nm, thus preventing the destruction of the DNA and other essential molecules encapsulated in the vesicles. These could have shed light on the hypothesis of the deep hydrothermal vent as the preferred site for origin of life, described in Section 1.1.4.

Minerals and rocks

Rocks are aggregates of minerals, inorganic compounds with fixed chemical compositions and specific crystal structures. There are about 4300 identified types of minerals on the modern Earth. While primary minerals are formed by cooling and crystallization of magma, secondary minerals are later transformed from primary minerals by weathering and alteration on the planet's surface[46]. The diversity of minerals comes from the ten stages of mineral evolution[47]. Planetary accretion occurred from stages 1 to 2 of mineral evolution. Later, stages 3 to 6, called the era of crust and mantle reworking (~4.55-2.5 Gya), are highly relevant for the emergence of life. Clay minerals, quartz, and mica are examples of minerals from these stages[47]. Mineral surfaces can provide sites for the adsorption and concentration of organic molecules in a dilute aqueous environment, and can facilitate catalysis of chemical reactions of biomolecules such as polymerization of nucleotides[48]. In addition, minerals can promote vesicle formation in mineral-lipid interactions[49]. Microcavities in rocks can act as compartments that promote molecular crowding and accommodate chemical reactions[50–53]. Therefore, microcavities are considered as one of the candidates for model protocells along with other membrane-encapsulating entities[4].

Clay minerals are of particular interest in terms of enabling the adsorption of organic molecules and promoting chemical reactions[54,55]. For example, both single- and double-stranded nucleic acids have been shown to adsorb onto clay minerals[56,57]. In addition, nucleotides can oligomerize on clay mineral surfaces[58]. A simulation study showed that hydrophobic collapse of peptide chains, an essential mechanism of protein folding, can occur within the clay layers[59]. In particular, montmorillonite, a natural clay mineral, is able to protect the catalytic RNA molecule from intense UV radiation[60] via the RNA-montmorillonite interaction, which is influenced by the pH and divalent cations[61].

The silica surface, usually found as quartz or sand in its mineral form, plays a role in the adsorption of biomolecules[48,62,63] and in the polymerization of amino acids[64]. Recently, an experimental study has shown that mica surfaces, a group of silicate minerals, are capable of promoting coacervation of quaternized dextran and single-stranded oligonucleotides[65]. The size and morphology, either single phase or biphasic, of the coacervates is determined by the functionalization[65], i.e., the surface charges. The interaction between solid surfaces and lipid membranes is the main focus of this dissertation. In all the experiments, a synthetic quartz-like SiO_2 surface was used to induce self-spreading of lipid reservoirs and as a solid support for lipid vesicles.

1.1.3 The earliest record of life on Earth

Given that the earliest biosignature remains controversial[6,66,67], the search for unambiguous evidence of the first living system is challenging. For example, the pseudofossil problem refers to the argument that life-like microstructures in ancient rocks do not convincingly indicate the presence of living organisms (microfossils), even though they fulfill numerous biogenicity criteria[67–69]. On the contrary, these pseudofossils could have been produced by abiotic chemistry. Despite the controversies, the 3.43 Gy-old stromatolites from the Pilbara Craton of Western Australia have been documented as the oldest fossil[6,16,66,70–72]. Stromatolites are sedimentary rocks formed by microbial precipitation. Recently, five types of abiotic spheroidal microstructures have been discovered in the Strelley Pool Formation of the Pilbara Craton[73]. One type of these spheroid structures, with a subspherical vesicle bounded by a quartz grain wall, could be interpretated by the authors as a possible microfossil. Together with the organic-walled microfossils from 3.2 Gya[74], they all resemble microbial colonies or eukaryotic microorganisms in which a single cell is in physical contact with its neighbors, facilitating material exchange. Stromatolites and microfossils provide us with a possible way in which the first living cell existed. If the first living cell exists in the form of a population of cells, it seems conceivable that the primitive cell could also have originated as a community of cells and then evolved into the first living population of cells. This is an alternative way of understanding the origin of life and evolution. I will introduce the concept of protocell populations and compare them to modern cell populations in Section 1.1.6.

1.1.4 Hypothesis about life

Based on the environmental conditions on the early Earth, as well as the oldest microfossil evidence of the first living entity, various theories of how life originated have been proposed. In this section, I will discuss the possible sources of organic matter and then give an overview of the established hypotheses that have had a major impact on the study of the origin of life.

Source of organic matter

Organic molecules are essential for the origin of life, especially for the formation of protocells. Among these organics, amphiphiles, such as fatty acids and phospholipids, are of particular interest for the formation of membrane boundary. Genetic fragments are another important player as they are responsible for carrying hereditary information in protocell replication. Amino acids are also within the scope, as they are the building blocks for proteins, which perform sophisticated molecular machinery in the later period of life evolution.

It is believed that there are two proposed sources of organic matter on the early Earth. According to the first conceivable circumstance, organic matter could have been delivered by meteorites during the late heavy bombardment at the end of the Hadean eon, probably earlier than 4.48 Gya[75]. Amphiphiles present in the Murchison meteorite[76] with short hydrocarbon chains such as monocarboxylic acids can self-assemble into membranous vesicles[77,78]. Recently, Oba and coworkers identified a variety of purine and pyrimidine nucleobases and their analogs in carbonaceous meteorite extracts[79]. This work demonstrates the diversity of nucleobases in meteorites that provide the building blocks for DNA and RNA synthesis under probiotic conditions. In addition to the delivery of organic matter, the panspermia hypothesis, which originated with the Greek philosopher Anaxagoras, suggests that a pre-existing living system could have been delivered to Earth from extraterrestrial space[80–82]. The associated lithopanspermia hypothesis proposes the transport of microorganisms within rocks[80]. Theoretical and experimental work has been carried out to investigate the survival of living matter in the space environment traveling from the initial planet to Earth[83].

The second plausible scenario is that organic molecules could have been synthesized under the geothermal conditions of the early Earth. The formation of organic molecules from inorganic precursors was first demonstrated by Miller and Uray in 1953[28]. In their experimental study, reducing gases such as methane, ammonia, and hydrogen, along with liquid water, were kept in a sterile and sealed chamber, resembling the early Earth's atmosphere. When continuous heating and electrical sparks were artificially introduced into the system, several amino acids such as glycine and alanine were detected. However, the atmospheric composition assumed in this study has been challenged as inconsistent with the current model of the early Earth. A re-evaluated experiment using neutral gas mixtures (carbon dioxide and nitrogen) was performed and resulted in the production of a significant number of amino acids[84]. Criticism on laboratory simulations remains, for example, the ingredients for prebiotic synthesis should closely represent the geochemical conditions and not be predetermined by the experimentalists[85]. Later, experiments showed that mixtures of monocarboxylic acids and alcohols were produced by Fischer-Tropsch synthesis under extremely high temperature conditions (up to 400 °C), mimicking hydrothermal vents[86,87]. In a recent study, long-chain hydrocarbons up to 24 carbons were synthesized under hydrothermal conditions (~300 °C, 30 MPa) using iron and cobalt metals as catalysts[88]. A range of gases and organic molecules including H_2S, CH_4, acetic acid and thiols have been detected in fluid inclusions in 3.5 billion-year-old barites from the Dresser Mine[89]. The barites are interbedded with stromatolites, suggesting that primordial ingredients are available in fluid inclusions and may have fueled microbial communities[89]. Ménez and coworkers recently demonstrated a new routine for abiotic synthesis that occurred in fluid inclusion in olivine microcavities in deep-sea hydrothermal vent environments, resulting in diverse polyaromatic materials[53].

As particular interest for the compartmentalization of the protocell, phospholipid synthesis has been demonstrated under prebiotic conditions[90,91]. In particular, phosphatidylcholine[92] (PC) and phosphatidylethanolamine[93] (PE) have been synthesized at temperatures ranging from 25 to 100 °C under prebiotically relevant conditions. Devaraj and coworkers reported the synthesis of natural diacylphospholipids from enzyme-free conditions in water[94]. Phosphate (PO_4^{3-}) is important for prebiotic chemistry, especially for phospholipid synthesis[95]. However, phosphate can react with Ca^{2+} in water to precipitate in the form of apatite minerals, which have low solubility. This makes it difficult to incorporate into the synthesis. A solution to this problem can be found in the carbonate-rich lakes, where Ca^{2+} is strongly precipitated by the alkalinity of the carbonate, leading to the accumulation of phosphate[96]. On the early Earth, carbonate-rich lakes could have formed from carbonic acid weathering of rocks in a CO_2-rich atmosphere. Alternatively, phosphate can be produced by the reaction of the phosphide mineral (schreibersite) in enstatite meteorites with HS^- in water, catalyzed by UV light[97]. A recent study argued that reduced phosphorus may have been produced by lightning strikes on the early Earth[98].

Synthesis of nucleotides[99,100] and ribonucleotides under prebiotic conditions[101,102] has also been achieved. Ju et al. demonstrated the abiotic synthesis of ribonucleotides from ribonucleosides in an aqueous droplet containing KH_2PO_4 at room temperature[103]. Sutherland and coworkers reported the coproduction of purine ribonucleosides and purine deoxynucleosides in the presence of UV light and sulfite[104]. Ribosylation of pyrimidine nucleobases has recently been achieved using metal cations and clay minerals[105]. Jerome et al. reported the conversion of ribonucleoside triphosphates to polyribonucleic acid containing 100-300 nucleotides catalyzed by mafic rock glasses[106]. Sahai and coworkers reported RNA polymerization in a prebiotic environment using amino acids and montmorillonite as catalysts[107]. Free-thaw cycles were found to promote nucleotide activation and RNA replication[108]. Aminoacyl-RNA synthesis was also demonstrated under prebiotic conditions[109].

Condensation reactions including peptide synthesis, phosphorylation, oligomerization[110], and DNA replication[111] can be promoted by the water-air interface. Rajamani and coworkers showed that phospholipids can promote the formation of peptides and amino acids under dry-wet cycles[112]. Prebiotic peptide synthesis within fatty acid vesicles has also been demonstrated[113].

Established hypotheses

Numerous hypotheses have been proposed and established to address the problem of the origin of life. The primordial soup[114,115], the RNA world[116], and the lipid world[117] are the best known. It was Oparin[114] and Haldane[115,118] who initiated the origin of life research in the 1920s and proposed the concept of the primordial soup, an aqueous suspension of inorganic molecules under the primitive oxygen-poor atmosphere. These molecules can undergo chemical evolution, leading to prebiotic reactions and eventually the emergence of the first forms of life. Oparin also introduced the term coacervate[114], a gel-like substance formed by the aggregation of macromolecules such as proteins. Coacervates, as membraneless compartments, can grow in size and potentially give rise to primitive cells.

The RNA world, proposed by Rich in 1962[119,120] and named by Gilbert in 1986[116], is a hypothetical stage in the evolution of life where the RNA molecule can carry the genetic information and catalyze the chemical reactions (ribozyme)[116]. In this hypothesis, self-replicating RNA is considered to be the earliest genetic polymer capable of storing hereditary information prior to DNA due to its single helix structure. Thus, it is a demonstration of the information subsystem in the chemoton model (see Section 1.1.1), which is autocatalytic[8]. RNA synthesis under prebiotic conditions was considered challenging for a long time until recent studies demonstrated its feasibility[101,102]. The RNA world hypothesis has been further developed by other related theories, such as the 'RNA-peptide world'[121], which suggests an intermediate period in the transition from the RNA-catalyst world to the protein-catalyst world. This model is supported by the recent finding that non-canonical RNA bases can directly establish peptide synthesis on RNA[122], implying the co-evolution of RNAs and peptides that are covalently linked.

As explained in Section 1.1.1, one of the three subsystems in the chemoton model is the membrane boundary. Amphiphilic molecules such as lipids can spontaneously form complex structures such as micelles and bilayer membrane-enveloped vesicles. This has been summarized in the lipid world hypothesis proposed by Segré, Ben-Eli, Deamer, and Lancet[117,123]. Within the lipid assemblies, the encapsulated chemical reactants are in close proximity and thus the reaction rate is enhanced[124]. According to the lipid world hypothesis, amphiphiles have the ability to catalyze the self-generation process as an analogous concept to ribozyme in the RNA world. Amphiphiles also have the ability to store genetic information in the form of lipid composition and transfer compositional information to the next generation of vesicle membrane[125]. A lipid membrane is considered autopoietic in the sense that it "*continuously produces the components that specify it, while at the same time realizing it as a* *concrete unity in space and time*"[126]. An example is the reverse micelle system composed of octanoic acid[127]. Lipid assemblies can also exhibit collective behaviors such as competition and selection[128]. Encapsulated RNA in fatty acid vesicles drives the growth of the vesicle membrane, resulting in competition among protocells[129]. The experimental evidence contained in this dissertation shows that lipid membranes can form nanotubular networks that allow the exchange of encapsulated genetic polymers in adjacent compartments, as in Paper II, or act as microcontainers to accommodate enzymatic reactions, as in Paper III. These works could be conceptualized in the lipid world hypothesis and provide a model system for future studies.

Considering the environmental conditions and the available hypotheses on the origin of life, we can ask the next question: what are the possible places that favor the formation of protocells and the evolution toward life? In today's deep-sea hydrothermal vents, various species of bacteria and archaea have been discovered despite the abnormal living conditions. Therefore, the deep-sea hydrothermal vent is considered to be one of the plausible aqueous environments for the origin of life[130]. There are two different types of submarine hydrothermal vents: Black Smoker and Lost City. In Black Smoker hydrothermal vents, such as the Brandon vent on the southern East Pacific Rise[131], temperatures can reach 405 °C. The chemistry is driven by the magma chamber and the seawater effluents from the vents are typically acidic (pH=2-3), containing high levels of CO_2, H_2S, and H_2. Such extremely high temperatures are considered unsuitable for living systems, except for some microbial communities such as hyperthermophilic archaea, which can survive at 121 °C (Reference 132). The second type of hydrothermal vent, the off-axis vents, called the Lost City, was first discovered in 2001[133], where the geochemical process known as serpentinization takes place. Serpentinization consumes the mineral olivine, sea water, and dissolved CO_2 to produce serpentine, magnetite, brucite, H_2, and CH_4. Because the hydrothermal fluids are not in close contact with the magma chamber, it offers a much milder temperature (50-90 °C) and alkaline pH (9-11). Hypotheses such as the iron-sulfur world[134] and the zinc world[135] address the synthesis of organic molecules in the hydrothermal vent. The local environment around the hydrothermal vent supports the growth of microbial communities, particularly methane-cycling archaea[136]. Microbial colonization of archaea and bacteria has been observed in the Old City, a Lost City type hydrothermal vent discovered in 2021[137]. These mineral-adhered cells adopt rod or coccoidal shapes, or are organized in filaments, providing a unique perspective on the interaction between solid surface and soft matter, which is the focus of this thesis (see Chapter 2).

Deep-sea hydrothermal vent has received much criticism, mainly due to its high salinity, which is less conducive to self-assembly and polymerization of simple organic compounds[22,138]. As an alternative to deep-sea hydrothermal vent, life could have originated in a freshwater hydrothermal field. For example, the warm little pond hypothesis was first proposed by Darwin[139] and was later elaborated by the hot spring water pond hypothesis proposed by Damer and Deamer[24,25]. The hydrothermal field can provide a dehydration-rehydration (dry-wet) cycle. In the context of protocell formation, the dehydration phase allows amphiphilic molecules adsorbed on surfaces to assemble into multilamellar structures[140]. Upon rehydration, the dry multilamellar matrix would transform into a vesicle, potentially encapsulating the polymers concentrated in the dehydration phase[24,141,142]. Several studies have argued that dry-wet cycling would benefit the polymerization of biopolymers[143,144]. In addition, dry-wet cycling alters the phase behavior and thus the compartmentalization of coacervates[145]. The hot spring pond hypothesis was supported by the field study in the Pilbara Craton of Western Australia[146]. A recent study by Rosas and Korenaga supported the origin of life on land rather than in an oceanic environment based on modelling of the Archaean seafloor[147].

1.1.5 Protocell compartmentalization

Compartmentalization is a common feature of all modern cells and is therefore considered an essential step in the origin of life. The formation of compartments has a significant impact on protocell capabilities[50], such as replication[148] and metabolism[149,150]. Various compartmentalized protocell models have been proposed and developed to study the emergence of primitive cells in the laboratory. Inorganic compartment model protocells include rock microcavities[52], clay particles[151], colloidosomes[152], aerosols[153], gas bubbles[154], and ice crystals[155]. Other model protocells include coacervates[156–158] formed by liquid-liquid phase separation of macromolecules resembling membraneless organelles in cells, such as aggresomes in bacteria[159] and Cajal bodies in eukaryotic cells[160]. Since biological cells are ubiquitously enveloped by lipid membrane and lipids may have been present on early Earth (see Source of organic matter in Section 1.1.4) and self-assembled into membranous compartments[161], lipid vesicles are considered particularly valuable for the membranous protocell model in many studies[162,163], and thus it is the focus of this dissertation. The aqueous environment is fundamental for the self-assembly of amphiphiles into organized membranous structures. Here, I will describe the formation of lipid-based membranous protocells in bulk solution and on solid substrates.

Protocell formation in bulk solution

Amphiphilic mixtures extracted from Murchison meteorites, such as monocarboxylic acids, are capable of assembling into bilayer membrane vesicles in neutral pH to alkaline solution and encapsulating hydrophilic molecules such as DNA and pyranine dye[77,164,165]. Formation of long-chain (C_{10}-C_{15}) fatty acid vesicles was also found to be favored in an alkaline hydrothermal environment, i.e., pH ~6.5 and >12 at modern seawater salinity[166], and the most favorable temperature for vesicle formation is ~70 °C. In addition, the stability of fatty acid vesicles can be enhanced by incorporating C_{10} isoprenoids into the fatty acid membrane[167]. It has been shown that the fatty acid giant vesicles are capable of encapsulating RNA during their self-assembly, and they can self-divide in the presence of excess micelles[168]. A dehydration-rehydration event could promote the formation of single-chain amphiphile vesicles at acidic pH and confer a selective advantage of thin-walled vesicles for RNA encapsulation[140]. Encapsulation and redistribution of genetic polymers within the protocell are the key steps in protocell replication and evolution. Freeze-thaw cycling allows mixing of RNA substrates and ribozyme encapsulated in separate phospholipid vesicles without vesicle fusion[169]. Similarly, thermal cycling induces disassembly and reassembly (membrane-oil transition) of fatty acid vesicles, resulting in mixing of membrane lipids as well as encapsulated RNAs[170]. A recent study showed that the presence of double-stranded RNA can induce aggregation of dipalmitoylphosphatidylcholine (DPPC) vesicles through sequence-dependent RNA-lipid interactions[171]. The division of assembled protocells has also been demonstrated using thermal convection that mimics fractures and compartments in porous rocks in a deep-sea hydrothermal vent. Such temperature fluctuations, above and below the phase transition temperature of the lipid membrane, drive the fission of phospholipid giant vesicles[172]. Stability of lipid compartments under high concentration of Mars-relevant salt conditions and high hydrostatic pressure has been studied, showing that giant vesicles composed of unsaturated chain lipids would tend to shrink but maintain their integrity[173]. However, vesicular bilayer membranes composed of long-chain saturated phospholipids may fold into a bicontinuous cubic structure (non-lamellar lipid phase) when the magnesium perchlorate concentration exceeds 0.25M.

Protocell formation on solid substrates

Clay montmorillonite, as available minerals under early Earth conditions(see Minerals and rocks in Section 1.1.2) can serve as solid substrates to accelerate the assembly of fatty acid micelles into vesicles[174]. Adding a small amount of montmorillonite (0.6 mg/ml) to the reaction mixture was found to increase the rate of myristoleate vesicle formation by a factor of 100, and the reaction rate increased linearly with increasing montmorillonite concentration as more mineral surfaces are available[174]. Self-assembly of phospholipids can also take place on glass microspheres with a diameter of ~5 μm, resulting in the formation of giant vesicles. Upon addition of oleic acid, these surface-supported giant vesicles can grow in size and divide to produce daughter vesicles[175]. When a phospholipid multilamellar vesicle (MLV) interacts with silicon oxide surfaces, a topological transformation occurs (Figure 2.1a), producing hundreds of surface-adhered vesicular protocells that are interconnected with lipid nanotubes[176]. Furthermore, the nucleation, growth, and fusion of the protocells can be enhanced by the elevated temperature (see Paper I and Chapter 3). Changing the fatty acid ratio in the phospholipid-fatty acid membrane gives the protocell network a different topology, for example, vesicles adopt an elongated shape[177]. In follow-up studies, Köksal and coworkers tested the interactions of MLVs with various natural surfaces, including olivine, granite, and Martian meteorite, and observed foam-like protocell colonies[178]. In combination with fusogenic agents such as calcium ions, aluminum oxide (Al_2O_3), aluminum (Al), or silicon oxide (SiO_2), surface-adhered giant vesicles can undergo morphological transformations such as invagination, subcompartmentalization, and pseudo-division[179].

1.1.6 Protocell population and intercellular communication

It is widely believed that a single cell evolved from a protocell during the transition from non-living to living systems. Given the earliest form of living cells, stromatolites (see Section 1.1.3), which indicate the coexistence of individual bacteria in a confined microbial colony, is it possible that populations of protocell were initially formed and evolved directly into the first populations of living cells?

Hypotheses of protocell population

In their hot spring hypothesis, Deamer and Damer[25] proposed that the progenote, a hydrogel-like entity, can be formed in the transition phase during the dry-wet cycle of the membranous protocell in a small pond. The progenote resembles the protocell population, and within the protocell population, each individual protocell is in physical contact with the neighboring protocells, allowing them to exchange metabolic materials and collectively adapt to environmental changes. A similar scenario has been proposed by Walton and Shorttle, called the scum hypothesis, where a multicompartmentalized microlayer consisting of aggregated amphiphile vesicles could have formed near the air-water interface in a dilute aqueous environment[180]. Compared to individual free-floating vesicles, this foam-like scum layer could provide better preservation and sharing of genetic material, as well as pronounced enrichment of prebiotically relevant reactants such as phosphorus[181].

Experimental approaches toward protocell population

Compared to a single protocell, a population of protocells allows individual members to communicate in terms of content exchange, establish physical contact and interaction with the neighboring entity, cooperate and exhibit collective behaviors, and minimize the destructive effect for each protocell from environmental changes. A simulation study showed that multicellular aggregates could perform chemotaxis more efficiently than single cells[182]. While most studies focus on the functionality or complexity of individual protocells[183–185], recent efforts have been made to develop model systems of protocell populations to address this aspect[186,187]. Protocell populations have been created from various types of materials, such as lipid vesicles, protein-polymer conjugates, and coacervates, and have achieved rudimentary functionality to some extent, such as morphological differentiation[188] and quorum sensing[189,190]. Prototissues, for example, in which protocells are in close contact, can be made using 3D-printing[191], microfluidic devices[192–194], optical tweezers[195], magnetic fields[196,197], sound waves[198], or chemical linkers[199–205]. In addition, surface-adhered vesicle-nanotube networks have been created to study the intercellular transport of small molecules[206]. All of these artificial systems require sophisticated fabrication and manipulation techniques, and are therefore less relevant to early Earth conditions. Nevertheless, there are few examples of protocell population that are foam-like vesicular structures formed spontaneously by either the phospholipid vesicles with designed membrane composition on solid substrates[178,207] (Figure 1.3) or the mixtures of amphiphiles extracted from Murchison meteorites[165].

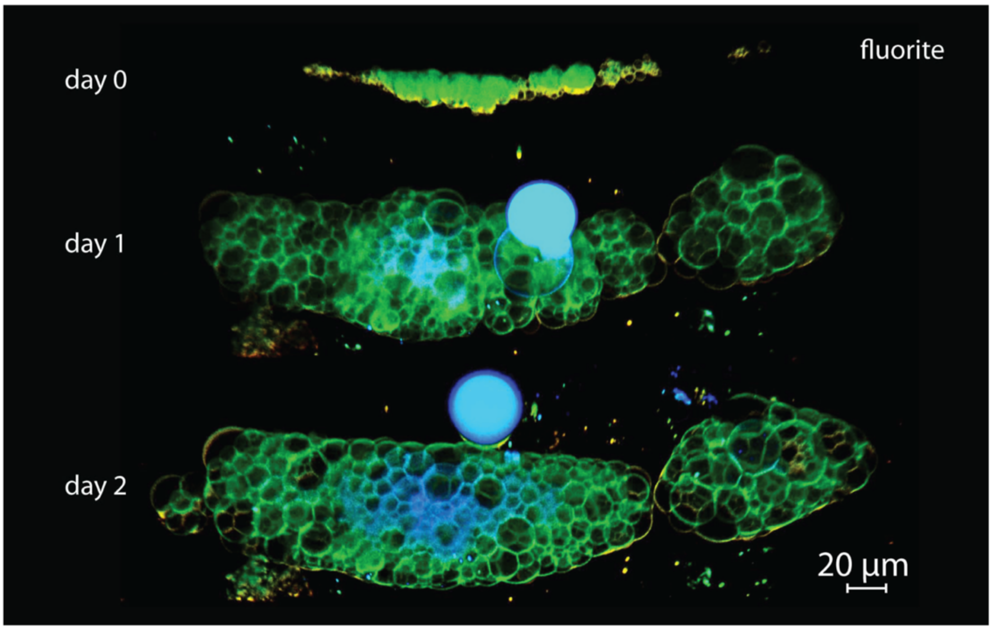

Figure 1.3. Confocal micrograph of foam-like protocell colonies formed spontaneously on a fluorite surface over the course of three days. *Reprinted with permission from Reference 178. Copyright 2022 Wiley-VCH GmbH.*

Cell-cell communication and tunneling nanotubes

Looking at single cells today, what are the possible ways for protocells to communicate? In eukaryotic multicellular organisms, intercellular connections are established by cell junctions, which allow the transport of electrical current and small molecules, and are represented by gap junctions in animals[208], plasmodesmata in plants[209], and septal pores in filamentous fungi[210]. In the scenario where animal cells are motile, cell-cell adhesion is strongly inhibited (contact inhibition of locomotion) when migrating cells collide with another cell[211–213]. The molecular mechanism of this process has been elucidated and is characterized by sequential steps including cell-cell contact, inhibition of protrusions, contraction of protrusions, and repolarization and migration away from the collision[213]. In collective cell migration scenarios, cadherin-based adhesion complexes at interface of cell-substrate as well as cell-cell junctions, are used to achieve coordinated movements, for example in tissue organization[214].

Intercellular communication in bacterial cells is of a special nature. Living in a biofilm environment, bacteria can perform quorum sensing by emitting low molecular weight signaling molecules that can diffuse and be captured by the other cell within the population to regulate gene expression and thus population density[215]. Similarly, quorum sensing has been discovered in yeast using aromatic alcohols and oxylipins as signaling mediators to induce morphological changes[216]. In addition, long-distance communication among yeast colonies can be mediated by the volatile gas ammonia, resulting in the regulation of colony density[216,217]. Electrical sensing has been recognized as a novel communication mechanism in the bacterial biofilm of *Bacillus subtilis* (*B. subtilis*), such that potassium ions released by the starved cell can regulate the transmembrane voltage and thus the nutrient consumption of the cells at the periphery of the biofilm[218,219]. In this way, nutrients can be retributed and made available to the starving cells in the interior of the biofilm. When bacteria encounter surfaces, they can perform tactile sensing using their flagellar motor as a sensor to promote the synthesis of polysaccharide adhesin and thus surface anchoring[220].

In addition to quorum sensing and electrical sensing, which are diffusive chemical communications, bacterial cells within communities exhibit contact-based physical interaction and spatial organization in colony structures[221]. Xiong et al. showed an example of physical interaction between two different bacterial species in a microbial colony[222]. They observed that when both species grew in the same colony, the non-motile *Escherichia coli* (*E. coli*) hitchhiked on the motile *Acinetobacter baylyi* (*A. baylyi*) cells, resulting in the formation of a floral pattern in the colony (Figure 1.4). In an additional experiment, colonies of these two species were initially separated, and as the colonies grew, the *A. baylyi* colony pushed the *E. coli* colony away, forming a floral pattern in certain directions[222].

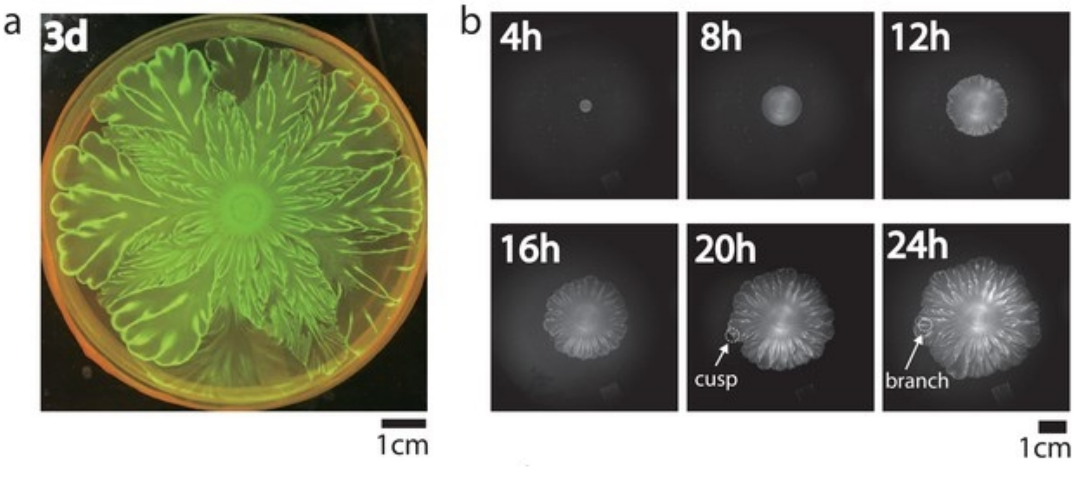

Figure 1.4. Floral pattern generated by the co-culture of *E. coli* and *A. baylyi* cells with *E. coli* cells hitchhiking on *A. baylyi* cells. *Reprinted with permission from Reference 222. Copyright 2020 under Creative Commons license (CC BY 4.0).*

Bacterial cells such as *B. subtilis* and *E. coli* can form intercellular nanotubular conduits, known as tunneling nanotubes (TNTs), between the same or different species. These F-actin-containing membrane nanotubes allow long-distance transport of cytoplasmic molecules, plasmids and organelles between neighboring cells[223] (Figure 1.5a). Pospíšil and coworkers[224] show the evidence that bacterial nanotube formation is associated with stress condition and cell death. The authors suggest that nanotubes are a post-mortem phenomenon involved in cell disintegration, but are unlikely to be involved in the exchange of cytoplasmic content between living cells. The mechanism of bacterial nanotube formation is controversial. A study by Baidya et al. suggests that bacteria may use cell wall remodeling enzymes for nanotube extrusion and penetration into target cells[225]. Recently, nanotube connections between marine bacterial cells have also been discovered[226]. In addition to the exchange of cytoplasmic contents, nanotubes could induce bacterium-bacterium and bacterium-organic matter interactions, leading to the formation of microaggregates on coastal marine surface[226]. Surprisingly, TNTs have also been observed in membrane-containing viruses. Bacteriophages can transform their lipid vesicles into proteo-lipid tubes to penetrate the bacterial cell envelop and allow their double-stranded DNA to be delivered into the host cell[227].

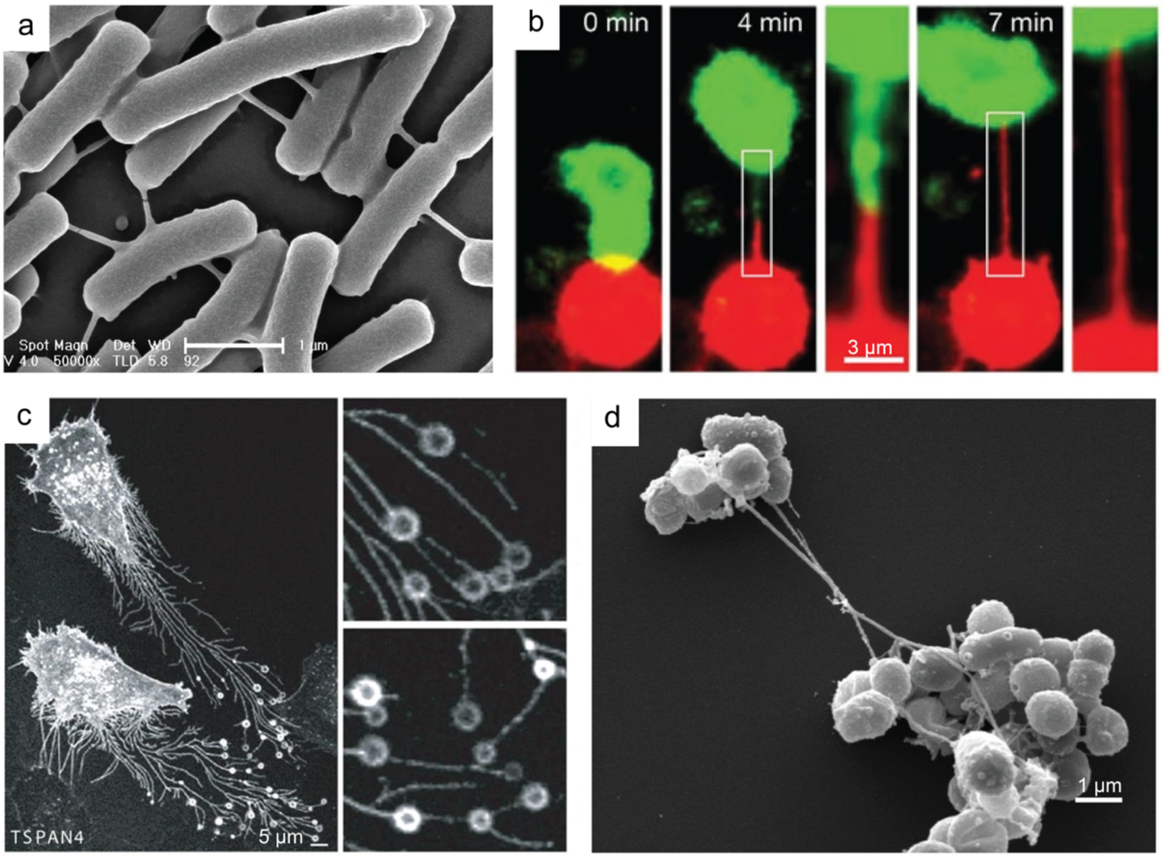

Figure 1.5. Tunneling nanotubes in bacterial, eukaryotic, and archaeal cells. (a) Scanning electron microscope image of membrane nanotubes in *E. coli* bacteria. *Reproduced with permission from Reference 223. Copyright 2011 Elsevier.* (b) Fluorescence micrograph showing the formation of nanotubes after contact between infected (red) and uninfected (green) T cells. The nanotubes allow HIV virus to spread between T cells. *Reproduced with permission from Reference 228. Copyright 2008 Springer Nature.* (c) Confocal micrographs of migrasomes in migrating NRK cells. *Reproduced with permission from Reference 229. Copyright 2014 Springer Nature.* (d) Scanning electron microscope image of nanotubes bridging a cluster of *Thermococcus* cells (archaea). *Reproduced with permission from Reference 230. Copyright 2021 Oxford University Press.*

In fact, TNTs were first discovered in mammalian cells in 2004[231], and they are ubiquitous in three domains of cellular life as an effective means of intercellular communication without crossing the membrane boundary[232–235] (Figure 1.5). With diameters of 20-700 nm and lengths of up to 100 μm (Reference 232), mammalian nanotubes hovered over the substrate allow the selective transfer of membrane vesicles and organelles and hinder the passive transfer of small molecules such as fluorescent dye calcein between connected cells[231]. TNTs can also facilitate the bidirectional propagation of electrical signals (ionic currents) between distant cells[236]. Two proposed mechanisms have been proposed for nanotube formation in animal cells[237]: a membrane protrusion originating from one cell extends to neighboring cells[231]; two cells make contact and then move apart[228] (Figure 1.5b). Recently, super-resolution imaging elucidated the developmental process of TNTs in the Hela cell, which is initiated by the contact of filopodia extending from each cell to form a double filopodial bridge[238]. The mechanically deformed double filopodial bridge is then transformed into a closed-ended TNT. A study showed that TNTs in migrating tumor cells can indeed interact with the fibrous microenvironment that mimics the extracellular matrix, and nanotube formation is dependent on cell migration[239]. In particularly, the velocity of nanotube-mediated intercellular transport of cargo was found to be lower in a longer nanotube.

The formation of TNTs can be triggered by a variety of viruses, and the formed nanotubes can be used to spread infection[240]. For example, nanotubes generated by T cell contact may have mediated HIV transmission from the infected to uninfected T cells[228,241] (Figure 1.5b). Similarly, severe acute respiratory syndrome coronavirus 2 (SARS-CoV-2) can hijack TNTs and spread between human neuronal cells[242]. Nanotubes also mediate inter- organelles communication. Mitochondrial nanotunnels, double-membrane protrusions that connect donating and receiving mitochondria, allow the transport of membrane proteins, ions, and RNA[243]. Migrasomes, the newly discovered extracellular vesicles, are generated at the intersection of retraction fibers, membrane protrusions left behind by migrating cells[229,244,245] (Figure 1.5c). Once the retraction fiber breaks, proteins and mRNA encapsulated within migrasomes can be released and taken up by the recipient cells, i.e., migracytosis[246].

Membranous nanotubes are also discovered in archaea[230]. Ca. P. syntrophicum, archaea from deep-sea sediments, has long and branched membrane protrusions[247]. Halophilic archaea can form cell-cell bridges similar to nanotubes (50-100 nm wide) between the mating cells and facilitate the exchange of ribosomes as well as long filamentous structures[248]. Thermococcus species of hyperthermophilic archaea can form more than one nanotube (up to three) with diameters of 60-80 nm connecting the neighboring cells, and these nanotubes have been suggested to be involved in cell-cell communication[249] (Figure 1.5d).

In this thesis, the spontaneous formation of protocell-nanotube networks between surface-adhered protocells has been observed (see Section 1.3.8 and 1.3.9), and the formation process can be sufficiently enhanced by increasing the local temperature (see Section 1.3.9), as presented in Paper I. The nanotubes within the networks allow the transport of molecules between the connecting protocells, driven by the concentration gradients (see Section 1.3.10), as presented in Paper II.

1.2 Surface energy and the possible implication of surfaces

Minerals and rocks as natural solid surfaces were abundant on Earth during the Hadean Eon (4.5-4 Gya) and the Early Archean Eon (4-2.5 Gya), covering the period of the transition from non-living to living. As it has been highlighted in *Minerals and rocks* in Section 1.1.2 as well as *Protocell formation on solid substrates* in Section 1.1.5, surfaces play an important role throughout protocell formation and evolution, particularly lipid adsorption, accelerated compartmentalization, and membrane topological transformation. In this section, I will introduce the concept of surface free energy to better illustrate how the interplay between soft matter and solid substrates could potentially impact chemical communication and physical interaction among membranous protocells.

1.2.1 Surface free energy and wetting phenomena

The surface free energy of solid materials results from the excess energy present in the molecules located at the interface compared to those in the bulk phase. Molecules in the bulk phase experience a balanced set of interactive forces from their neighboring molecules, whereas molecules at the interface lack cohesive interaction from their neighbors in all directions (Figure 1.6). This results in the presence of unsatisfied bonds in the molecules at the interface, ultimately leading to an increase in the surface free energy.

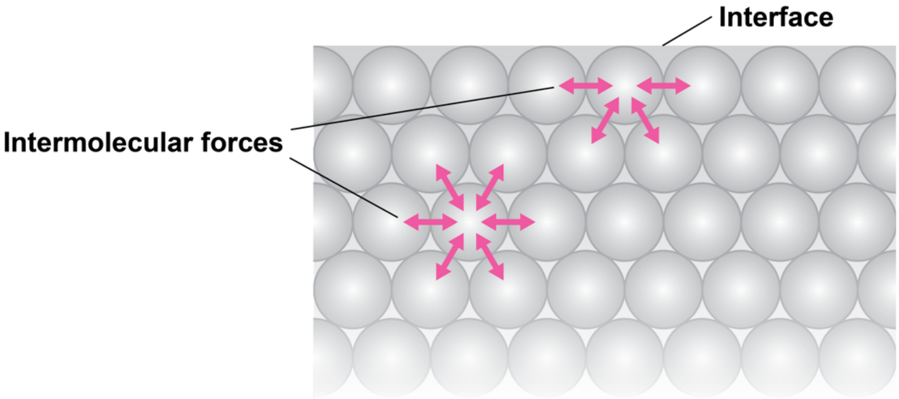

Figure 1.6. Intermolecular forces in the bulk phase and at the interface of a solid material.

When a block of solid material is split into two separate pieces, the intermolecular bonds within the material are disrupted and two new surfaces are created. In such a scenario, the surface energy (σ) can be related to the work (W) required to break the material and the area of the newly created surfaces (A):

$$\sigma = \frac{1}{A} W \tag{1.1}$$

Surface energy is expressed in units of energy per unit area (mJ/m^2) or tension per unit length (mN/m). To minimize its surface energy, a solid surface tends to establish physical contact, i.e., intermolecular interaction, with other matter such as air, water, and surfactants, a phenomenon known as wetting. For example, a spherical water droplet will adhere to and spread out on a solid surface. The degree of wetting, or wettability, can be characterized by the contact angle (θ), which is the angle between the liquid-vapor interface and the solid-liquid interface. The balance of surface tensions at the solid-vapor interface (γ_{SV}), the solid-liquid interface (γ_{SL}), and the liquid-vapor interface (γ_{LV}) determines the contact angle, which is expressed in Young's equation:

$$\gamma_{SV} = \gamma_{SL} + \gamma_{LV} \cos\theta \tag{1.2}$$

In high energy surfaces ($\sigma > 100$ mM/m)[250], the intermolecular interactions involve strong chemical bonds such as covalent, ionic, or metallic bonds that require a significant amount of energy to break. Metals, metal oxides, and glasses are some examples of high energy surfaces[250]. These hydrophilic surfaces have a contact angle that is less than 90°, indicating that the surface is easily wetted (Figure 1.7a). Total wetting occurs when the contact angle is zero. In contrast, low energy surfaces ($\sigma < 50$ mM/m) such as polymers SU-8 and Teflon AF, are bound together by relatively weak physical forces, such as van der Waals forces and hydrogen bonds[250]. As a result, less energy is required to break the molecular interaction. The contact angle for low energy surfaces exceeds 90° (Figure 1.7b), which inhibits surface wetting. Surfaces that achieve a contact angle greater than 150° are considered superhydrophobic (Figure 1.7c) and are able to repel water, resulting in a phenomenon known as the lotus effect, which allows for of self-cleaning properties[251]. In addition to hydrophobicity, other properties such as surface charge and surface topology (roughness) can affect the way a surface interacts with soft materials such as lipid membranes[252–255].

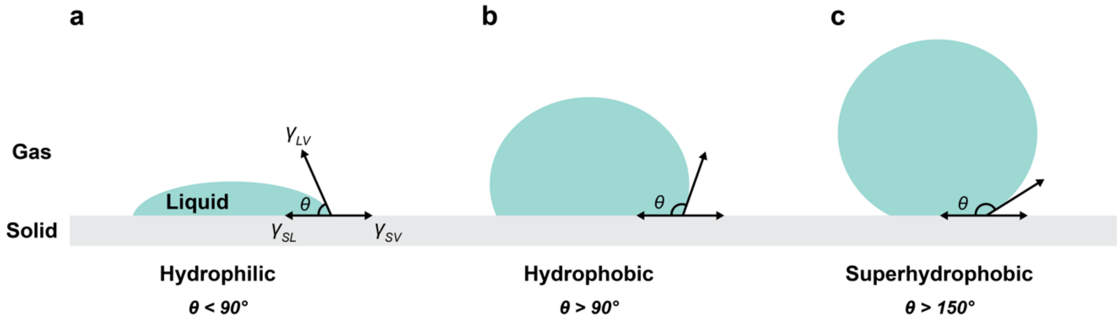

Figure 1.7. Wetting of liquid on different solid surfaces: (a) hydrophilic, (b) hydrophobic, (c) superhydrophobic.

1.2.2 Surfaces used in this thesis and their natural analogues

In the context of the origin of life, natural surfaces in the form of minerals and rocks, have intrinsic energy that could have been harvested by amphiphiles to develop membranous structures and even to undergo further shape transformations such as the division of vesicular protocells. In the early Earth environment, SiO_2 could be found in its crystalline mineral, quartz, which was abundant on the Hadean Earth. In the works presented in this thesis, engineered SiO_2 (see Section 6.2 for the preparation of surfaces) were used as a high energy surface for the interactions with lipid membranes. In Paper III, the SiO_2 surface provides adhesive support for giant vesicles during their fusion with cationic liposomes. In Paper I and II, SiO_2 surface enables the spreading of lipid reservoirs as a double bilayer membrane and induces the rupture of the upper membranes (with respect to the surface), leading to the formation of protocell-nanotube networks.

1.3 Lipid membrane

Cells in all domains of life are separated from their external environment by two-dimensional lipid membranes, which also serve to compartmentalize and facilitate essential functions in protocell formations (see Section 1.1.5). However, the origin and evolution of these membranes remains an open question. It has been suggested that after the last universal common ancestor (LUCA), the lipid divide occurred in the early evolution of lipid membranes[256,257], referring to the difference in membrane lipid chirality between bacteria and eukaryotes, and archaea. Specifically, phospholipid membranes in bacteria and eukaryotes are composed of ester-linked fatty acids, whereas archaeal membranes contain ether-linked isoprenoid-chains. Thus, it is theorized that the LUCA membrane lipids would have been heterochiral[256].

In this section, I will describe the self-assembly mechanism of lipid molecules and the energetic perspective of the formation of protocell-nanotube networks, which is a key model system in this dissertation. I will also highlight the nanotube-mediated cargo transport between protocells, and discuss membrane fusion and membranous compartment migration, which are crucial for protocell formation and evolution.

1.3.1 The chemistry of lipid molecules

Cell membranes are predominantly composed of lipids, which are amphiphilic molecules with hydrophilic headgroups and hydrophobic tails. Phospholipids (Figure 1.8a), which consist of fatty acid tails (Figure 1.8b) linked to a phosphate headgroup through a glycerol backbone, are a common type of lipid in cell membranes. The length of the hydrocarbon chains in the fatty acid tails ranges from 10 to 18 carbons, and unsaturated carbon-carbon bonds may be present. The phase transition temperature at which lipids change from the ordered gel phase to the disordered liquid crystalline phase typically increases as the chain length increases or the number of unsaturated bonds decreases[258]. The phosphate headgroup can be a simple phosphatidic acid or it can be decorated with different functional groups as in PC or PE. These modifications affect the charge of the headgroup and thus the overall charge of the lipid. Cardiolipin (Figure 1.8c), a lipid with two phosphate headgroups and four fatty acid chains, can be synthesized by combining two phosphatidic acids. This lipid is mainly found in the inner mitochondrial membranes and can stabilize the negative membrane curvature[259]. The focus of this dissertation is on the protocell membranes, which are mainly composed of bacterial (*E. coli*) and plant (soybean) phospholipids, which are specifically discussed in Paper I and II.

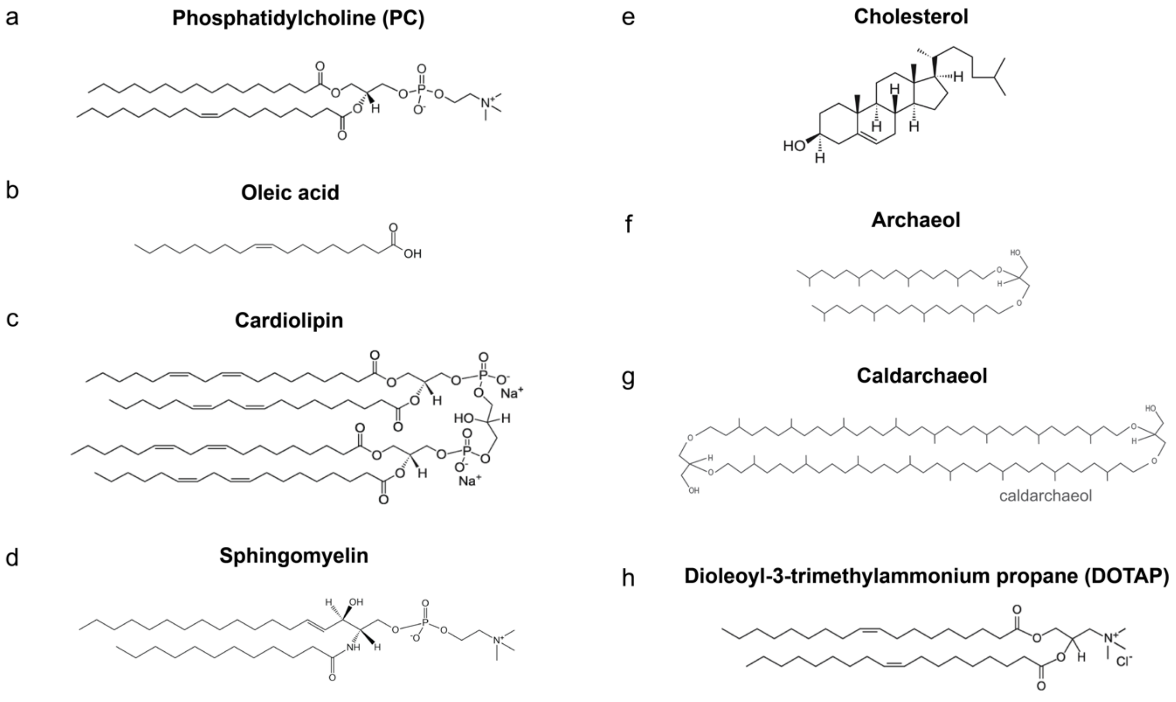

a Phosphatidylcholine (PC)

b Oleic acid

c Cardiolipin

d Sphingomyelin

e Cholesterol

f Archaeol

g Caldarchaeol

h Dioleoyl-3-trimethylammonium propane (DOTAP)

Figure 1.8. Examples of natural and synthetic lipid molecules. (a) Phospholipid, (b) fatty acid, (c) cardiolipin, (d) sphingolipid, (e) cholesterol, (f) archaeal ether lipid, (g) archaeal bolalipid, and (h) cationic lipid.

In addition to phospholipids, there are other types of lipids that contribute to the structure and function of the cell membrane, as shown in Figure 1.8. Sphingolipids (Figure 1.5d) are similar in size to glycerol-based phospholipids, but are synthesized from the precursor sphingosine, which has a long hydrocarbon chain (C=18). Sphingolipids play important roles in cell recognition and signaling[260]. Cholesterol (Figure 1.8e) has a unique structure consisting of four hydrocarbon rings and a hydrocarbon tail, as well as a hydroxyl group. Its presence in the membrane affects the fluidity and mechanical properties of the lipid bilayer[261,262]. Lipopolysaccharides are found exclusively in the outer membrane of Gram-negative bacteria, where they form a permeability barrier that protects the bacterial cell from certain chemical attacks, such as antibiotics[263]. In the presence of divalent cations such as Ca^{2+}, lipopolysaccharide can be cross-linked into two-dimensional elastic networks[264]. Unlike the conventional lipids mentioned above, which form bilayer membranes, bolalipids/bipolar lipids (Figure 1.8g) consist of two extended hydrocarbon tails capped by two polar headgroups and organize as a monolayer in archaeal membranes[265]. They can adopt two different configurations in the membrane: the "O-shapes", in which the polar headgroups are located on opposite sides of the membrane, or the "U-shapes", in which both polar headgroups are located on the same side of the membrane[266]. Archaeal membranes also contain distinct ether phospholipids (Figure 1.8f), in which isoprenoid chains are linked to glycerophosphate headgroups via ether bonds[267]. Ether lipids allow archaeal membranes to maintain a liquid-crystalline phase over a wide temperature range (0-100 °C)[268] and exhibit very low permeability to ions and small molecules[267], which is thought to contribute to the survival of archaea under extreme environmental conditions, such as high pressure and temperature (see Section 1.1.4).

From an evolutionary perspective, fatty acids have been proposed as the building blocks for protocell membranes before phospholipids due to their simpler structures. Compared to phospholipid membranes, fatty acid membranes are more permeable and have a significantly higher flip-flop rate (milliseconds versus days)[269–271], the time it takes for a lipid to translocate from one leaflet to the other in a bilayer. In addition, fatty acid membranes are more sensitive to the local pH and lipid concentration. It has been proposed that while fatty acid membranes were present in primitive protocells, they transitioned over time to phospholipid-dominated membranes, resulting in the hybrid membranes of the transitional phase[270]. This hybrid membrane provides an advantage in membrane growth.

In addition to natural lipids, synthetic lipids with unique surface charges and membrane organization have been used in many biotechnological applications, particularly in cell transfection[272]. Lipid vesicles (see Section 1.3.5) and lipid nanoparticles made of cationic lipids (Figure 1.8h) or ionized lipids serve as carriers for drug delivery[273,274]. In Paper III, we demonstrated the delivery of various biologically relevant molecules, including RNAs, DNAs, and proteins into cell-sized giant vesicles using the cationic lipid dioleoyl-3-trimethylammonium propane (DOTAP) (Figure 1.8h).

1.3.2 Self-assembly and hydrophobic effect

Water molecules have a tendency to form hydrogen bonds with neighboring water molecules[275]. When lipids are added to the solution, the nonpolar moiety of the lipids disrupts this network and reduces the number of available orientations of the water molecule. As a result, the entropy of the system decreases, leading to an increase in the Gibbs free energy G ($\Delta G = \Delta H - T\Delta S$, where H is the enthalpy and T is the absolute temperature). To minimize the free energy of the system, lipids self-assemble into organized structures with a hydrophobic core, which expels water molecules and allows them to regain their orientations, leading to an increase in the entropy of the system.

Lipid self-assembly leads to the formation of different energetically favorable structures. This process is highly dependent on the geometry of the lipid molecules, which can be evaluated by the critical packing parameter (CPP)[276], defined as $CPP = V/al$, where V is the volume of the hydrophobic tails, a is the cross-sectional area of the hydrophilic headgroup, and l is the length of the hydrophobic tails. Depending on the value of CPP, lipids can form different structures: spherical micelles (CPP < 1/3) for cone-shaped lipids, cylindrical micelles (1/3 < CPP < 1/2) for truncated cone-shaped lipids, and bilayers (1/2 < CPP < 1) for cylindrical lipids[277]. Inverted micelles or microemulsions are preferred when CPP > 1(Reference 277).

1.3.3 Membrane surface energy

Lipid membranes are only nanometers thick, much smaller than their lateral dimensions, which can be as large as micrometers. Therefore, when studying membranes on a scale significantly larger than the size of a single lipid molecule, it is appropriate to treat the three-dimensional lipid membranes as two-dimensional rigid sheets exhibiting elastic and fluidic properties. This can be accomplished using the continuum model. The elastic energy of a lipid membrane, denoted by F, can be described as:

$$F = \int dA \left[\frac{\kappa}{2}(c_1 + c_2 - c_0)^2 + \bar{\kappa} c_1 c_2 + \sigma\right] \tag{1.3}$$

The first and second terms in the integral represent the Helfrich membrane curvature energy[278]. The first term is the bending energy of the membrane, where dA is the surface area element and κ is the bending rigidity. The bending rigidity corresponds to the energy required to change the membrane curvature and is typically on the order of tens of k_bT[279]. The value of κ is significantly affected by the lipid composition and the ionic concentration in the solution[280]. c_1 and c_2 are the two principal curvatures of the membrane, while c_0 is the spontaneous curvature. The spontaneous curvature arises as a result of the asymmetry between the inner and outer leaflets of the bilayer membrane[281]. Positive or negative membrane curvature is essential for various dynamic cellular processes, such as migration, fusion, and division, which require deformation of the cell membrane. Membrane curvature can be induced, for example, by altering the lipid composition or by using membrane proteins[282]. In all model membrane systems studied in my dissertation, spontaneous curvature can be considered negligible since the lipid compositions are identical in both leaflets of the membrane.

The second term in the integral, $\bar{\kappa}c_1c_2$, corresponds to the Gaussian curvature. The Gaussian modulus $\bar{\kappa}$ is of the same order as κ, but has a negative value[283]. If there is no significant topological change in the structures of interest, the surface integral over the Gaussian curvature remains constant, making the value of $\bar{\kappa}$ irrelevant. When a nanotube transforms into a spherical vesicle, the Gaussian curvature term can be disregarded, and the bending energy term dominates the membrane curvature energy.

The third term in the integral represents the membrane tension, denoted by σ. Relaxed membranes have low membrane tension and may be subject to fluctuations. Mechanical stretching can increase membrane tension, leading to an increase in membrane area and a corresponding increase in the distance between individual lipid molecules. However, the lipid membrane can only stretch up to 5% of its initial area[279] before the membrane tension reaches the lysis tension (approximately 5-10 mN/m), causing the membrane to rupture[284].

1.3.4 Formation of vesicles

Due to the hydrophobic effect, lipids can self-assemble into a bilayer in an aqueous environment, adopting the shape of a free-standing bilayer disk, as shown in Figure 1.9a. To prevent the hydrophobic moiety of the lipids from being exposed to water molecules, the lipids at the periphery of the bilayer disk arrange themselves into micelle-like structures where the inter-lipid distance is greater compared to the lipids in the center of the disk. This spatial organization of the lipids imposes an edge energy cost[285]. The edge energy E_{edge} is proportional to the radius of the bilayer disk, r:

$$E_{edge} = 2\pi r\gamma \tag{1.4}$$

where γ is the edge tension (5-10 pN)[286–288]. In the context of a growing bilayer disk induced by increased lipid concentration, the cost of edge energy increases accordingly. To overcome this energy cost, the free-standing bilayer disk undergoes a spontaneous bending process that results in the formation of a spherical vesicle with a radius R ($R = r/2$), as shown in Figure 1.9b. The energy cost associated with this transformation can be quantified in terms of the bending energy of the resulting vesicle:

$$E_{bend} = 4\pi(2\kappa + \bar{\kappa}) \tag{1.5}$$

where κ is the bending modulus and $\bar{\kappa}$ is the Gaussian modulus. The bending modulus typically has a value of 10-20 $k_b T$ (Reference 279), while the Gaussian modulus is of the same order of magnitude but with a negative sign. The shape transformation is determined by the ratio of the bending energy of a vesicle, E_{bend}, to the edge energy cost of a bilayer disk, E_{edge}. If $E_{bend}/E_{edge} < 1$, vesicle formation is favored. The critical radius for the bilayer disk can be calculated, above which the bilayer disk will bend and form a spherical compartment.

$$\frac{4\pi(2\kappa + \bar{\kappa})}{2\pi r \gamma} < 1 \tag{1.6}$$

$$r > \frac{2(2\kappa + \bar{\kappa})}{\gamma} \tag{1.7}$$

Therefore, when the radius of the free-standing bilayer disk, *r*, exceeds $20\, k_b T / 10\, pN$ (approximately in the nanometer scale), the disk will undergo bending and transform into a vesicle with nanometer dimensions.

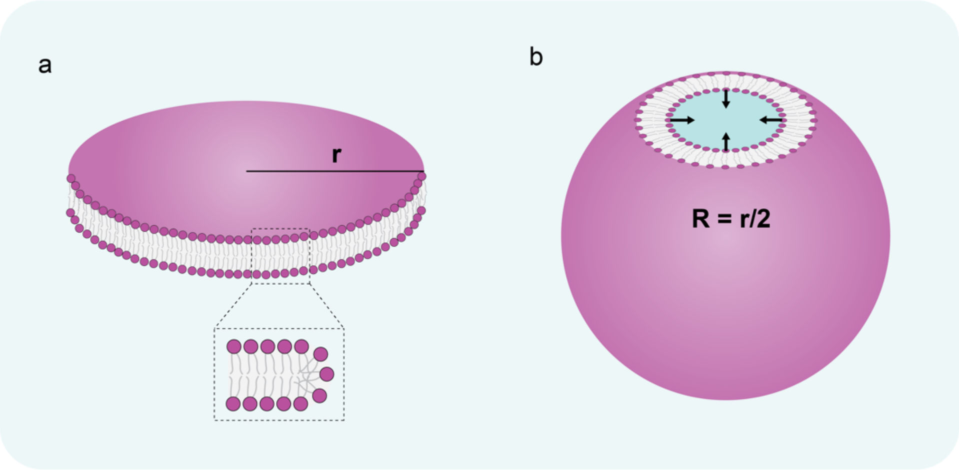

Figure 1.9. Transformation of a free-standing bilayer disk (a) into a spherical vesicle (b).

1.3.5 Phospholipid vesicles

Phospholipids have the ability to spontaneously assemble into vesicles in an aqueous environment. The resulting vesicles can be categorized by size, including small (<0.1 µm), large (0.1-1 µm) and giant vesicle (>1 µm). Vesicles can also be identified by their lamellarity, such as unilamellar or multilamellar vesicles (see Section 6.1 for vesicle preparation). Small and large unilamellar vesicles (SUVs and LUVs, Figure 1.10a) closely resemble extracellular vesicles found in biological systems[289], and are of great interest for drug and vaccine delivery[273,274]. Giant unilamellar vesicles (GUVs, Figure 1.10b) are cell-sized compartments that have been used as model protocells and synthetic/artificial cells[290]. In Paper III, positively charged SUVs were used as carriers to deliver molecular cargo into surface-adhered GUVs via membrane fusion. MLVs (Figure 1.10c) are "onion-shell" membrane structures containing multiple densely packed lipid bilayers. They are found in biological cells known as lamellar bodies[291], which are lipid-protein complexes that serve as lipid stores[292], in addition to the intracellular organelles called lipid droplets, which consist of a neutral lipid core surrounded by a phospholipid monolayer membrane[293]. In Paper I and II, MLVs were exploited as lipid reservoirs. Their self-spreading on solid surfaces (see Section 1.3.7) initiates the generation of surface-adhered protocell-nanotube networks as well as flat giant lipid compartments. Since the lipid reservoirs are connected to the subsequently formed structures, the lipids within the MLVs are continuously extracted from the reservoirs and eventually depleted.

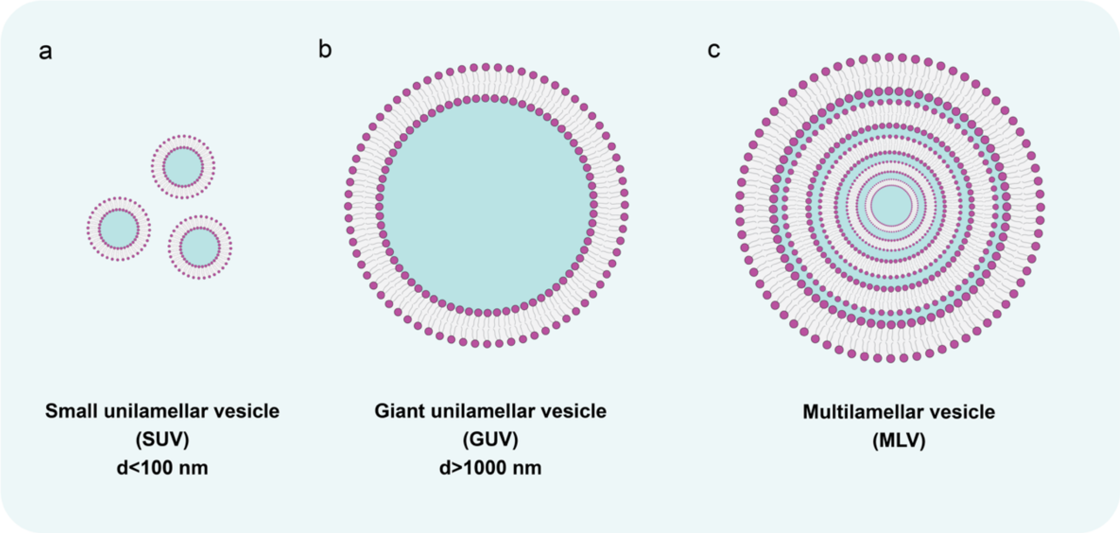

Figure 1.10. Lipid vesicles of different sizes and lamellarities. (a) Small unilamellar vesicle, (b) giant unilamellar vesicle, and (c) multilamellar vesicle.

1.3.6 Supported lipid membranes

Biological membranes are intricate and dynamic structures composed of lipid bilayers and membrane proteins that are either embedded in or attached to them. In order to study the underlying membrane-based cellular processes as well as their potential biotechnological applications, planar membranes on solid supports have been extensively reconstituted with bespoke components and widely used as model systems[294]. These model systems have been used to study, for example, membrane-membrane recognition in immune responses[295] and directional transport of molecular cargo on membranes[296].

One way to obtain a supported membrane is the Langmuir-Blodgett[297]/Langmuir-Schaefer technique[298,299]. In brief, a solid substrate is immersed in an aqueous solution where the water-air interface is covered by lipids. The substrate is then pulled out of the solution, resulting in the deposition of the lipids onto the substrate. Another approach to the formation of supported membranes is the rupture of surface-adsorbed SUVs[254,300]. SUVs are brought to the solid substrate, and upon adhesion, they rupture to form small bilayer membrane patches. When the substrate is fully covered by them, they eventually fuse to form a continuous supported membrane. The basal membranes of surface-adhered GUVs can be considered supported membranes[179,301]. In the presence of strong surface adhesion, GUVs will also rupture and form supported membrane patches[302–305].

An alternative method for the formation of supported membranes is the self-spreading of lipid reservoirs in the form of MLVs. Self-spreading occurs spontaneously due to the minimization of the free energy in the system and is a wetting phenomenon (see Section 1.2.1). Depending on the nature of the solid substrate, such as its hydrophobicity and surface charge, the adhered lipid reservoir can spread in the form of a monolayer[306,307], a single bilayer[308,309], or a double bilayer membrane[176,284,309] (see Section 1.3.7). Monolayer spreading is favored on hydrophobic substrates, such as SU-8 photoresist or Teflon amorphous fluoropolymer (AF) resin[306], while single bilayer spreading is observed on glass substrates[308,309] and double bilayer spreading on SiO_2[176,284,309]. In the case of supported single and double bilayer membranes, a thin layer of water (1-2 nm) is trapped between the bilayer and the substrate[310,311].

Fusogenic agents, such as multivalent ions, facilitate the adhesion of supported membranes to negatively charged hydrophilic substrates. Ca^{2+} and Mg^{2+} have been shown to create pinning sites by bridging the phosphate headgroups of lipids to the substrate[312,313], thereby promoting adhesion. The degree of pinning can be modulated by adjusting the ionic strength[314], for example by introducing chelators[179,315].

1.3.7 Double bilayer spreading

The self-spreading of a lipid reservoir on a solid substrate is a manifestation of the tension-driven mass transfer of lipids known as the Marangoni flow. During this process, lipids from the reservoir continuously flow towards the edge of the double bilayers membrane in a treadmill-like motion[309], as shown in Figure 1.11. The driving force for this spreading is the free energy gain in the system where the tension gradient must be satisfied. This means that the surface tension of the solid substrate wetted by the lipid (σ_l) must be lower than the surface tension of the solid substrate wetted by the aqueous solution (σ_a):

$$\sigma_s = \sigma_a - \sigma_l \tag{1.8}$$

Taking into account the internal tension of the lipid reservoir (σ_0), which opposes the spreading, the spreading power (S) is thus given by:

$$S = \sigma_s - \sigma_0 = \sigma_a - \sigma_l - \sigma_0 \tag{1.9}$$

Spontaneous spreading occurs when the spreading power has a positive sign, indicating that $\sigma_a > \sigma_l$ and $\sigma_s > \sigma_0$.

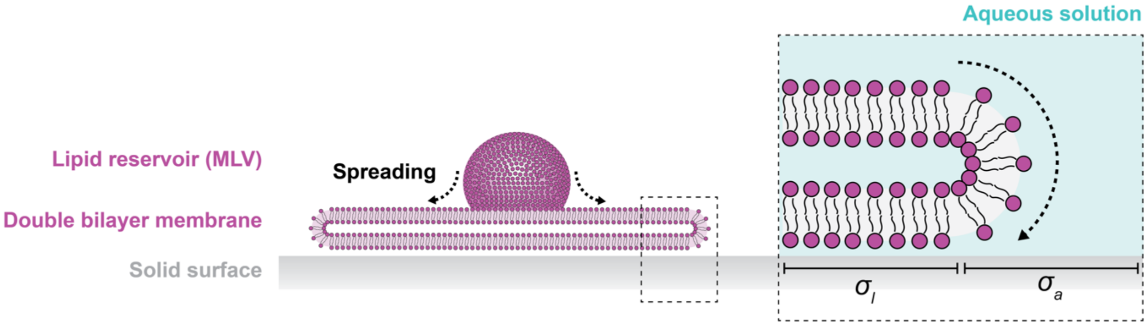

Figure 1.11. Self-spreading of double bilayers on a solid substrate.

Divalent cations, such as Ca^{2+}, can bridge the negatively charged surface and the phosphate headgroups of lipids[316], thereby enhancing the spreading of MLVs. The spreading of lipid reservoirs results in surface-adhered double bilayer membranes that are homogeneous in lipid composition, as presented in Paper I and II.

1.3.8 Membrane rupturing and nanotube formation

The spreading process is driven by the continuous adhesion of the membrane to the solid substrate. When the lipid reservoir is completely depleted, resulting in insufficient lipid supply for spreading, the distal membrane (upper bilayer with respect to the substrate) is stretched. Consequently, the membrane tension increases and when the membrane tension surpasses the lysis tension (5-10 mN/m), the distal membrane ruptures[284]. The propagation of the membrane rupture leads to the immobilization of the distal membrane patch, which is pinned to the proximal membrane by the Ca^{2+} in the ambient buffer solution. The edge of this pinned membrane patch is rapidly elongated by the continuous retraction of the distal membrane, resulting in an increase in the edge energy cost of the rectangular membrane patch, which is proportional to the patch length (l) and the edge tension (γ) (5-10 pN)[286–288]:

$$E_{edge} = l\gamma \tag{1.10}$$

To reduce the edge energy cost, the membrane patch tends to form a toroidal nanotube[176]. The bending energy of a lipid nanotube with a length l and a radius r can be calculated using the Helfrich bending energy equation[278]:

$$E_{bend} = \frac{\pi l \kappa}{r} \tag{1.11}$$

If the edge energy of the membrane patch is greater than the bending energy of the nanotube, nanotube formation becomes energetically favorable.

$$\frac{E_{bend}}{E_{edge}} < 1 \tag{1.12}$$

$$\frac{\pi \kappa}{r\gamma} < 1 \tag{1.13}$$

$$r > \frac{\pi\kappa}{\gamma}$$

(1.14)

This suggests that a rectangular bilayer patch of a few nanometers long would bend to form a nanotube.

The surface free energy of a lipid nanotube adopts the form of

$$F = \frac{\pi l\kappa}{r} + 2\pi r l\sigma$$

(1.15)

where the first term is the bending energy, and the second term is the lateral membrane tension.

The free energy of the nanotube per unit length is then given by:

$$f_{nanotube} = \frac{\pi\kappa}{r} + 2\pi r\sigma$$

(1.16)

An expression for the equilibrium radius of the nanotube can be derived as follows:

$$r_0 = \sqrt{\frac{\kappa}{2\sigma}}$$

(1.17)

The equilibrium radius of a lipid nanotube is determined based on a balance between the membrane bending modulus κ (10-20 k_bT)[279] and the membrane tension σ (0.01-0.05 mN/m)[317,318]. Therefore, the typical radius of a lipid nanotube is about 50 nm, which is consistent with observations in biological systems such as TNTs[232,319] (see Section 1.1.6) and migrasomes[244], as well as in artificial systems[320,321].

1.3.9 Formation of protocell-nanotube networks and the temperature effect

Lipid nanotubes resulting from membrane rupture have higher membrane curvature than spherical vesicles, which is unfavorable in terms of membrane surface free energy. The transformation of a nanotube into a vesicle reduces the membrane curvature and minimizes the free energy of the system. Semispherical protocells nucleate from the intersection in nanotube networks[176,315] and grow over time into spherical compartments with a continuous supply of lipid materials. These protocells are interconnected by lipid nanotubes in a protocell-nanotube network, which was investigated in Paper I and II.

The time scale for protocell vesiculation typically ranges from hours to days at room temperature, but it can be significantly shortened by physical stimuli such as elevated temperature. In Paper I, we demonstrated that local heating accelerates the nucleation and growth of protocells. An increase in temperature leads to an increase in membrane fluidity and membrane tension[322]. As a result, the Marangoni flow occurs in such a way that lipids migrate at a higher rate toward the heated, high-tension region, facilitating the maturation of protocells.

The mature protocells within the network that have established physical contact with neighbors can undergo fusion, which is facilitated by an increase in temperature. This process results in fewer compartments of larger diameter. In Paper I, we combined experimental observations and a mathematical model to show that fusion between adjacent protocells occurs either at the protocell equator or at the connecting nanotube (see Section 1.3.12). The former results in the formation of a stable pore between two compartments. In both scenarios, the bending energy of the system is minimized, although fusion mediated by the connecting nanotube is energetically the most favorable.

1.3.10 Transport among protocells via tunneling nanotubes

Membrane nanotubes are ubiquitous in biological systems spanning all domains of life, including archaea, bacteria, plants, and animals[232–235] (see Section 1.1.6). Communication between cells via TNTs allows the direct transport of signaling molecules, plasmids and organelles[223,231,323]. In open-ended TNTs, active transport of organelles and vesicles within the lumen of nanotubes is mediated by F-actin or other motor proteins[324]. Intrinsically, molecular cargo can be transported simply by diffusion (Brownian motion) along a concentration gradient in nanotubes[325,326]. Cargo transport can also be driven by membrane tension (Marangoni flow)[327–330] or by an applied electric field[331,332].

In Paper II, we investigated the molecular diffusion between interconnected protocells via nanotubes in protocell-nanotube networks. The size of the molecules transported is much smaller than the diameter of the nanotubes. Here we can consider two spherical protocells that are connected to each other by a single nanotube, where only one of the protocells is loaded with molecules (Figure 1.12). The molecules would continuously diffuse toward the unfilled protocell until the concentration in both protocells reaches equilibrium. The diffusive transport is governed by the concentration gradient, which decays exponentially with time $\left(e^{-\frac{t}{\tau_{relax}}}\right)$[333,334]. The relaxation time (τ_{relax}), which is the time for the system to reach chemical equilibrium in a condition of constant diffusion rate, can be calculated as:

$$\tau_{relax} = \frac{V_1 V_2}{V_1 + V_2}\left(\frac{L}{\pi r^2 D}\right) \tag{1.18}$$

where V_1 and V_2 are the volumes of the two protocells, while L and r are the length and the radius of the nanotube, respectively. D is the diffusion coefficient of the transported molecules. Assuming an equal diameter of 5 µm for both protocells, a nanotube length of 5 µm, a nanotube radius of 50 µm, and a diffusion coefficient of small fluorescent dye molecules such as fluorescein[335] or ATTO 488 (Reference 336) at room temperature ($D = 400\ \mu m^2/s$), the relaxation time is found to be on the order of minutes. This agrees with our experimental results presented in Paper II, where we further demonstrated the effect of each geometric parameter on the molecular transport.

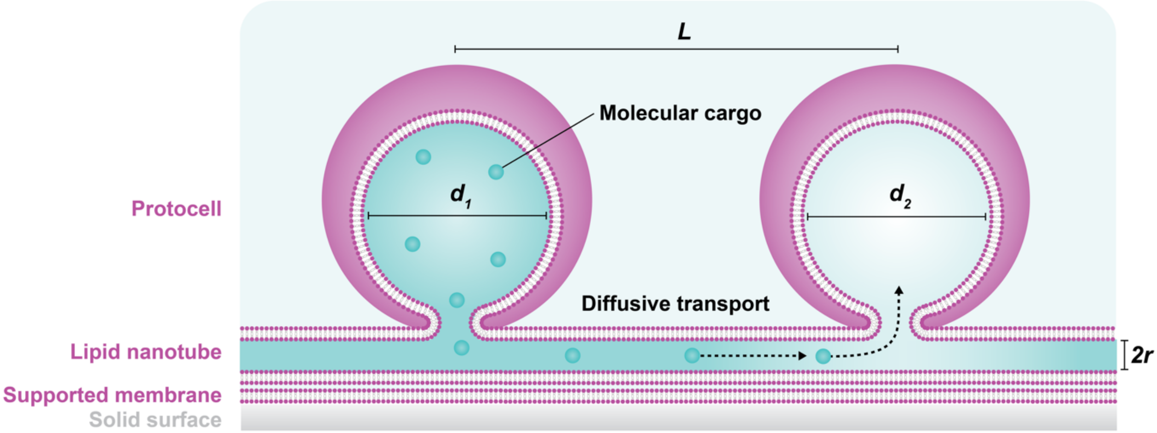

Figure 1.12. Cargo transport between two protocells through a lipid nanotube.

The diffusive motion of cargo molecules is characterized by another time scale, referred to as the traffic time $\tau_{traffic}$, which corresponds to the time required for molecules to be transported between two protocells[337]. It is determined by the expression:

$$\tau_{traffic} = \frac{R}{Dr}$$

(1.19)

where R is the radius of the protocell. In the system considered here, the estimated value of the traffic time is on the order of seconds, which is much smaller than the relaxation time.

In addition to diffusive transport, the Marangoni flow can be used for controlled transport of cargo towards regions of high membrane tension[328,329]. In this context, we can again consider a lipid nanotube interconnecting two spherical vesicles with a difference in membrane tension ($\Delta\sigma$). The time required to transfer a fraction f of the overall volume of the sending vesicle to the receiving vesicle can be approximated as:

$$t \approx \left(\frac{R}{r}\right)^3 \frac{L\eta}{\Delta\sigma} f$$

(1.20)

where η is the viscosity of water. For a system with $R = 2.5\,\mu m$, $r = 50\,nm$, $L = 5\,\mu m$, $\Delta\sigma = 10^{-5} N/m^2$, $\eta = 10^{-3}\frac{N}{m^2}s$, and $f = 0.1$, we obtain $t = 6.25\,s$. Hurtig and Orwar reported on tension-driven transport of bacteria either encapsulated inside the nanotube or adhered to the outer surface of the nanotube membrane[328]. In this study, the size of the bacteria ($2 \times 0.8\,\mu m$) exceeded the size of the nanotube ($r \approx 100\,nm$). The velocity of the intra- and extra-tubular transport was measured to be 21.8 and 38.5 µm/s, respectively.

1.3.11 Membrane permeability and transient pores

Biomembranes are well-defined boundaries that separate the internal cellular space from the external medium. These membranous boundaries exhibit selective permeability to organic and inorganic molecules[338]. Small molecules, such as water and gases, can easily diffuse across the bilayers[201,339], while the penetration of large and charged molecules is severely hindered[340]. The lipid composition of the membrane also affects permeability, with different types of lipids exhibiting different levels of permeability. Biological cells use membrane proteins to facilitate active transmembrane transport of functional macromolecules along or against the concentration gradients[340]. Nevertheless, in the context of the origin of life, primitive cells would have lacked a well-developed molecular machinery on their membrane for the uptake of biological constituents, particularly genetic polymers. Instead, one possibility is that the amphiphiles self-assembled into primitive cellular compartments in an aqueous environment rich in solutes, leading to spontaneous entrapment of solutes[168]. Alternatively, solutes can have been internalized through the transient pores in the membrane. Lipid membranes can open nanometer-sized transient pores[341] under high membrane tension induced by mechanical stress[342], osmotic pressure[343], or intense optical illumination[286]. Opening the pores reduces the membrane area and releases the excess internalized volume, resulting in a decrease in membrane tension[344]. Eventually, the pores close, driven by the edge tension of the curved bilayer interface at the edge of the pores[287]. Based on the experimental observations and simulations reported by Spustova and colleagues, a surface-adhered lipid container of micrometer dimensions appears to simultaneously accommodate 3 to 5 transient nanopores.

In the studies presented in Paper I and II, a mild hydrodynamic flow generated by the microfluidic pipette (see Section 6.7) was applied to lipid compartments. This flow induced an increase in membrane tension that facilitated the formation of transient nanopores, allowing the encapsulation of small fluorescent molecules, RNA and DNA within the compartments.

1.3.12 Membrane fusion

Membrane fusion is a fundamental process in several cellular trafficking and communication pathways, including endocytosis and exocytosis in eukaryotic cells[345]. In addition, muscle growth and repair in mammalian cells depends on the fusion of muscle precursor cells, known as myoblasts, to form multinucleated myotubes that can then fuse with other myotubes[346,347]. Membrane fusion requires the coordination of fusion proteins on the membrane, which generate a force that brings two bilayers into close proximity[348]. Alternatively, fusion can occur in protein-free biomembranes by various mechanisms, such as local heating[195,349], electrostatic interactions[350], nanoparticles[351,352] and osmotic pressure[353].

In Paper I, we showed that the fusion of protocellular compartments can be facilitated by the temperature increase resulting from laser heating. Upon fusion, the RNA molecules trapped in one of the compartments can be redistributed to the fused compartments. The phenomenon of membrane fusion has been proposed as a plausible mechanism to provide additional membranes and genetic materials, which could have acted as a source of nutrition for the growth of protocells during the origin of life[169,353,354].

In Paper III, we reported the fusion of small cationic liposomes with giant vesicle membranes, driven by the electrostatic interactions between countercharged lipid headgroups. The fusion process is controlled by the proportions of charged lipids in the fusing membranes. A low percentage of cationic lipids in liposomes leads to partial fusion states such as docking or hemifusion[355,356], whereas a high amount of cationic lipids leads to full fusion, allowing the mixing of contents between the liposomes and giant vesicles[350,357].

1.3.13 Motility of lipid vesicles

Migratory phenomena are commonly observed in all cell types during embryonic development and tissue regeneration[358]. Cell migration is a cyclic process that is spatially and temporally regulated by cytoskeletal redistribution[359]. To initiate cell migration, cells extend protrusions such as lamellipodia or filopodia in the direction of migration via actin polymerization, which establish adhesion to the extracellular matrices and serve as traction sites for migration. These protrusions are then disassembled at the rear of the cell as it moves over the adhesion sites. It is noteworthy that migrating cells exhibit a calcium gradient from the rear to the front, with calcium-rich microdomains known as calcium flickers appearing at the front of the migrating cell where the calcium concentration is the lowest[360]. These calcium flickers play a critical role in guiding the directional movement of cells. Mimicking this cytoskeleton-based cell migration, lipid vesicles can acquire motility in response to external stimuli such as adhesion gradients[361,362], divalent cations[363,364], local heating[365,366], and magnetic fields[367]. As mentioned in Section 1.3.6, the presence of Ca^{2+} generates the pinning sites between lipid membranes and between membranes and substrates, thereby controlling the wetting and det-wetting of membrane structures[363,365]. Our system is closely related to the haptotactic motion of negatively charged vesicles adhering to a positively charged supported bilayer[361], as reported by Solon and colleagues. Such surfing-like motion is driven by lipid transfer between the vesicle and the supported bilayer, which creates a charge (adhesion) gradient between the front and the back of the vesicle, promoting motion in the direction of the adhesion gradient. Alternatively, an adhesion gradient can be established by the asymmetric distribution of membrane-binding Min proteins at the contact edges of the GUV and the supported bilayer[362] where both membranes are negatively charged and pinned by the presence of cations in the buffer solution. The adhesion gradient together with the deformation of the GUV membranes forms a mechanochemical feedback mechanism, promoting persistent motile movement of the GUV (Figure 1.13).

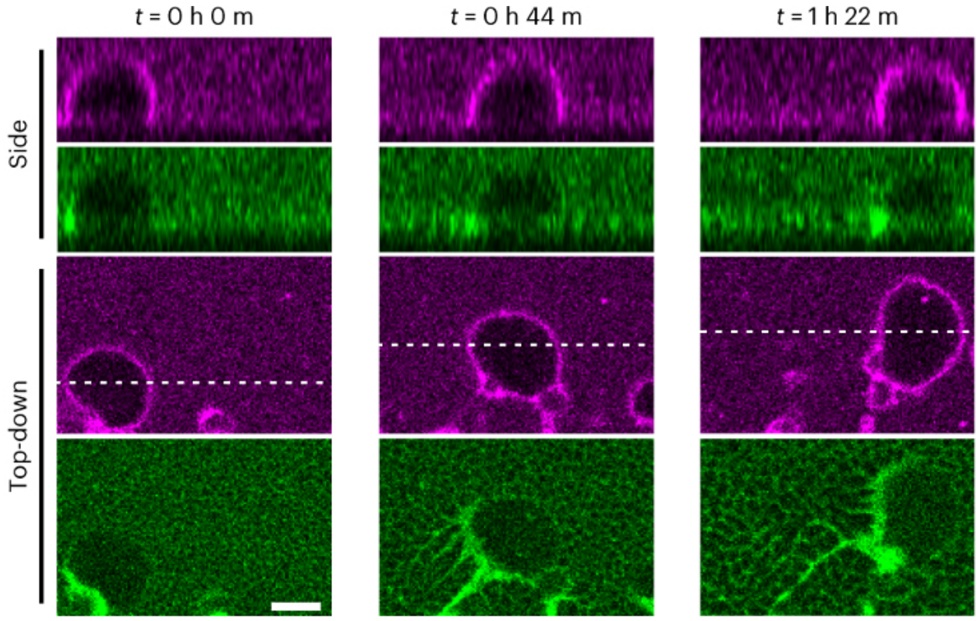

Figure 1.13. Confocal micrographs showing GUV sliding on a supported bilayer membrane induced by asymmetric accumulation of membrane-binding MinE proteins. MinD is color-coded in magenta and MinE is in green. Scale bar 5 µm. *Reproduced with permission from Reference 362. Copyright 2023 under Creative Commons license (CC BY 4.0).*

2 Aim of the projects

The ability to communicate and interact between the same or different cell species is ubiquitous in three domains of life along the biological evolution. Protocells, as hypothetical precursors to the first living cells, are highly simplified in structure and function, and thus could have lacked an evolved molecular machinery for contact-dependent interaction as well as chemical signaling. Ongoing research is revealing a great diversity in the materials that make up the protocell, accentuating the versatile characteristics of the individual protocell. However, the establishment of protocell communities and study of their potential collective behavior under prebiotic conditions are underexplored, especially for the lipid membrane-enveloped protocells. How could protocells have evolved into LUCA? Could protocells have developed colony-like superstructures along the transition to the living entity? What interactive behaviors could have occurred within protocell populations? Could different types of protocells have competed or cooperated for self-replication? Was it possible to share internalized content among protocells in a protective manner? How could protocells have adapted to environmental changes? Could protocells have functioned as chemical reactors as well as carriers of genetic fragments? All these open questions in the context of the origin of life are within the scope of my dissertation.

This thesis is entirely dedicated to the demonstration of rudimentary inter-protocellular interactions, either spontaneous or triggered by external stimuli. The membranous protocell system is capable of transforming between different membrane morphologies, energetically supported by the membrane-solid surface interactions. Adhesion of lipid reservoirs on solid surfaces triggers the formation of flat giant vesicles (Figure 2.1a) and ultimately the development of protocell-nanotube networks (Figure 2.1b,c) that provide an experimental platform to study communication and interaction in protocells. Specifically, this thesis is conducted to achieve four objectives:

(1) **To study the heat-enhanced emergence, growth, and fusion of lipid vesicles within protocell-nanotube networks.** Environmental temperature is thought to play an essential role in the origin of life. Based on the previous discovery and characterization of spontaneously formed protocell-nanotube networks, how local heating would affect the formation of the networks and induce redistribution of encapsulated cargo (Figure 2.1b) is of interest for the emergence of the first living cells. The results are presented in Paper I and summarized in Chapter 3, and the associated protocol for applying optical heating is presented in Paper IV and Section 6.6.

(2) **To Investigate the diffusive transport of cargo molecules between lipid vesicles through interconnected nanotubes.** The nanotubes connecting the protocells have been suggested to allow the transfer of various cargoes within the network (Figure 2.1c), yet no experimental evidence has been provided to support such a hypothesis. Due to the difficulty of visualizing the internalized cargo within the thin nanotubes, we instead elucidate the transport event by monitoring the replenishment of cargo in the protocells that are out of equilibrium in cargo distribution. This is presented in Paper II and Chapter 4.

(3) **To demonstrate proof-of-concept for controlled delivery of membrane-impermeable cargo into giant vesicles using fusogenic liposomes as cargo carriers.** Macromolecules with biological function are impermeable to lipid bilayers. Efficient transmembrane transport of cargo is required to perform prebiotically relevant chemical reactions inside the protocells. By combining cationic liposomes and an open-volume microfluidic device, we aim to establish a protocol for local delivery of a collection of cargoes, ranging from genetic polymers to global proteins, into a surface-adhered GUV (Figure 2.1d). In addition, we intend to incorporate an enzymatic reaction within the GUV and its subcompartments. Proof of concept is presented in Paper III and Chapter 5.

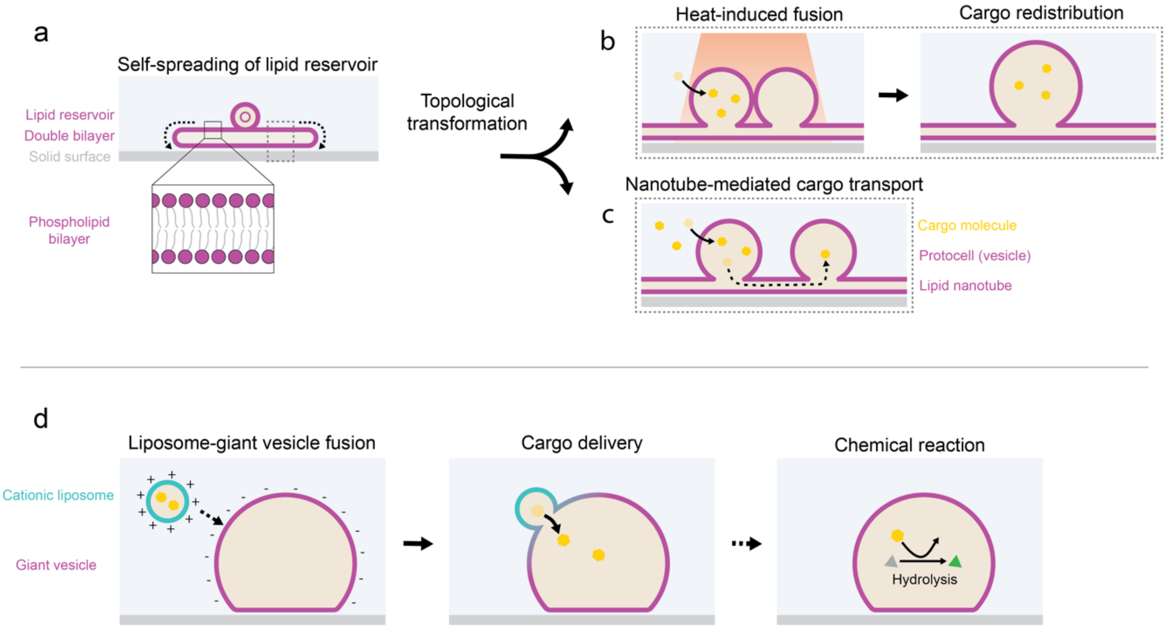

Figure 2.1. Graphical summery of communication and interaction among model protocells in different manners. Lipid vesicles are considered as membranous model protocell in the context of origin of life in this thesis. Cyan and magenta colors represent different membrane compositions.

3 Heat-induced rapid growth of protocell from protocell-nanotube network

This chapter summarizes the main findings presented in Paper I and describe my contributions to the study.

Paper I. *Rapid growth and fusion of protocells in surface-adhered membrane networks*

In Paper I, we showed that elevating temperature promoted vesicle nucleation, growth, and fusion in surface-adhered vesicle-nanotube networks. The local temperature gradient created by IR-B laser heating was applied to the selected membrane region. Immediate nucleation of vesicles from nanotube networks was observed within a few minutes when the temperature was increased from 20 to ~40 °C, while at room temperature the spontaneous formation of vesicles takes a few hours. Further increase in temperature (~70 °C) facilitated the rapid growth of newly nucleated vesicles. Our analysis reveals that vesicle formation occurred preferentially at the intersections in the nanotube networks. Rapid fusion between adherent vesicles in close proximity was induced by increasing the temperature to ~90 °C. Finite element simulation showed that fusion between two vesicles connected by the same nanotube is energetically more favorable than fusion between two vesicles located on different nanotubes, where a stable pore remains in the fused compartment after fusion. Finally, we observed RNA encapsulation inside the vesicles. Moreover, upon vesicle fusion induced by heating, the RNA encapsulated in one of the two compartments was redistributed to the fused compartments.

Contribution: Performed the local temperature measurements for the IR-laser heating experiment. Analyzed the data and determined the local temperature gradient. Contributed to the writing of the manuscript.

4 Cargo transport in protocell-nanotube network

In this chapter, the main findings reported in Paper II and my contribution to the study are described.

Paper II. *Transport among protocells via tunneling nanotubes*

In Paper II, we demonstrated a feasible way for protocells to communicate at the early Earth conditions. The transport of genetic fragments was mediated by lipid nanotubes connecting protocells in the protocell-nanotube networks described in Paper II. The fluorescently labeled cargo molecules, such as water-soluble dye ATTO 488, RNA and DNA oligomers, were encapsulated inside the protocells that are free of membrane fluorophores. Fluorescence recovery after photobleaching (FRAP) was then used to study the conductivity of the nanotubular connection. After photobleaching the fluorophores in one of the protocells in the networks, we observed recovery of fluorescence intensity in the bleached region, indicating replenishment of active fluorophores in the adjacent compartments to the bleached compartment through the connecting nanotubes. Lastly, we investigated the influence of geometrical parameters, such as the size of the compartments and the length and diameter of the nanotubes, on the recovery, i.e., the transport of the cargo, using an analytical model. We concluded that tunneling nanotubes could have allowed the transport of prebiotic constituents between primitive cells without crossing the membrane boundary.

Contribution: Suggested suitable cargo molecules for the study of molecular transport within protocell-nanotube networks. Proposed the application of the FRAP experiment to the selected vesicles. Performed the confocal microscopy experiments and evaluated the data. Contributed to the writing of the manuscript.

5 Cationic liposome-assisted cargo delivery

This chapter presents the main findings of Paper III and the author's contribution to it.

Paper III. *Liposome-assisted in-situ cargo delivery to artificial cells and cellular subcompartments*

In Paper III, we reported a highly controlled method for the delivery of membrane-impermeable cargo into a surface-adhered giant lipid compartment resembling an artificial cell by using cationic liposomes as cargo carriers. Upon electrostatically driven membrane fusion between the giant vesicles and the liposomes, a variety of biologically relevant components, including water-soluble dyes ATTO 488, fluorescently labeled RNA and DNA oligomers, polysaccharides, and globular proteins, can be delivered into the giant vesicles. We monitored the fusion process by FRET between donor and acceptor fluorophores initially embedded in the membrane of the giant vesicles and the liposomes. We observed highly efficient membrane fusion within a few minutes. Finally, we performed enzymatic reactions inside the giant vesicle and additionally observed the spontaneous subcompartmentalization and generation of reaction products in one of the subcompartments. As a complement to the other available techniques, liposome-assisted delivery in this work demonstrates an alternative way to internalize compounds of interest into lipid-based artificial cells with designed functions, which could also be used as model protocells to study protocell communication at the origin of life.

Contribution: Proposed the cargo molecules and established the protocol for the liposome-assisted delivery method. Suggested the membrane-conjugated fluorophores as FRET pair to monitor the membrane fusion, and the enzyme and substrate molecules for the enzymatic reaction occurring inside the giant vesicle. Performed all confocal microscopy experiments and analyzed the data. Calculated the membrane areas and volumes of the giant vesicle before and after fusion with cationic liposomes. Contributed to the drafting of the manuscript.

6 Materials and methods

This chapter describes the experimental methods that are essential for the research presented in this thesis. These methods include vesicle preparation, surface fabrication, imaging techniques and micromanipulation techniques involving local laser heating and microfluidic devices.

6.1 Preparation of lipid vesicles

The work presented in this dissertation involves the preparation of SUVs, GUVs and MLVs using various natural lipids extracted from plant or bacterial cells, as well as synthetic cationic lipids. Fluorophore-conjugated lipids were incorporated into the bilayer membranes to enable fluorescence imaging (see Section 6.5).

The vesicles were prepared by using the dehydration-rehydration method[368], as shown in Figure 6.1. Initially, the lipids were dissolved in chloroform and mixed in an appropriate molar ratio in a pear-shaped flask. The chloroform was then removed under vacuum (20 kPa) for 6 hours using a rotary evaporator, resulting in a dry lipid film on the flask wall. The lipid film was rehydrated overnight with an aqueous buffer containing 1% glycerol, resulting in swelling of the lipid film. The presence of glycerol prevented the complete dehydration of the lipid film, allowing the separation of the lipid bilayers[369]. The hydrated suspension was subjected to sonication for less than 20 seconds to reduce the size and lamellarity of the lipid reservoirs, leading to the formation of MLVs and GUVs. The resulting vesicle stock suspension can be stored at -20 °C for future use. To prepare the MLV and GUV samples for microscopic observation, a 4 μl volume of the stock suspension was deposited on a glass coverslip and then dehydrated in a vacuum desiccator for 20 minutes. The dried film was then rehydrated with the desired buffer for the experiment.

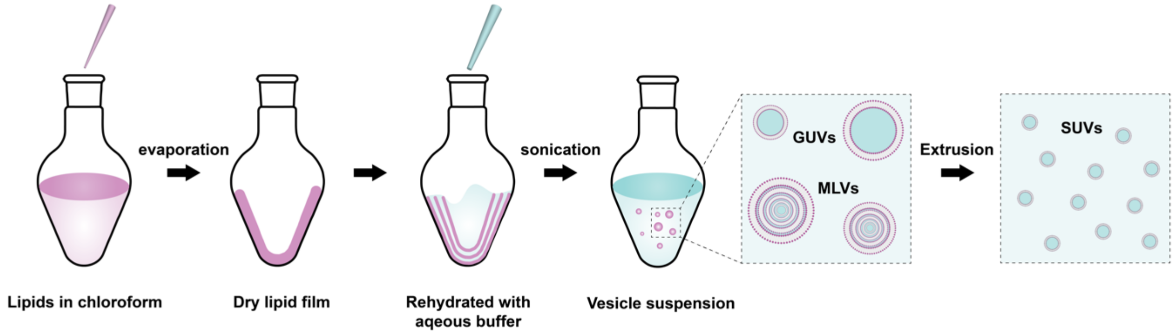

Figure 6.1. Schematic drawing of the preparation of lipid vesicles by the dehydration-rehydration method. After rehydration and subsequent sonication of the dry lipid film, a vesicle suspension containing multi- or unilamellar vesicles of different size can be obtained. Extrusion of the vesicle suspension produces SUVs with the desired size distribution.

In Paper III, SUVs were prepared using the extrusion technique[254,370]. Extrusion is a widely used method for the formation of SUVs, in which the size of the vesicles is reduced by mechanical force[370]. To prepare SUVs, the vesicle stock suspension was diluted with the desired buffer and subjected to continuous sonication for several minutes. The sonicated suspension was then extruded through a polycarbonate membrane with a defined pore size, such as 100 nm[371]. During extrusion, the vesicles were deformed by shear stress at the pore walls and adopted an elongated shape. The final diameter of the vesicles was slightly different from the pore size, and the size distribution of the extruded vesicles depended on other factors such as lipid composition, the number of extrusion cycles, and the extrusion temperature[370,371].

6.2 Surface fabrication

The solid surfaces used in this thesis were fabricated in the Micro- and Nanofabrication Cleanroom Laboratory, commonly referred to as MiNaLab, at the University of Oslo. The cleanroom provides a controlled environment with minimal contamination, achieved through ventilation control and air filtering. It significantly reduces the concentration of airborne particles, especially those with nano- and micrometer diameters. The average concentration of airborne particles in urban environments is approximately 300-400 million particles/m^3 (Reference [372]). In contrast, ISO Class 1 cleanrooms limit the maximum number of 100 nm particles to 10/m^3 (Reference [373]), which is critical for the fabrication of microelectronic devices and pharmaceutical production.

The sub-micrometer-thick SiO_2 surfaces used in in this thesis work were fabricated using the electron-beam (e-beam) physical vapor deposition (PVD) technique[374]. Prior to deposition, glass cover slides were loaded into the deposition chamber, which was evacuated to a pressure of at least 10^{-4} Torr. Briefly, a heated tungsten filament emitted electrons that were accelerated and focused onto the crucible containing the material source, as shown in Figure 6.2. The materials bombarded by the electron beam were transformed into a gaseous phase and then precipitated as a thin film on the glass substrates. The focused beam heated only the material source, while the crucible is water-cooled, enabling high purity deposition[375]. During deposition, a quartz crystal microbalance (QCM) was used to monitor the deposited film thickness in real-time[376]. The thickness was determined by measuring the decrease in frequency of a quartz crystal resonator resulting from the increasing mass of the deposited film. The deposited SiO_2 film has a final thickness of 84 nm, making it optically transparent and well-suited for microscopy. The final thickness of the deposited film was measured using an ellipsometer, which uses non-contact analysis of the change in polarization of light reflected from the sample surface. By comparing the experimental data with an established model for the given deposited film and substrate[377], the thickness parameters of the sample can be determined. With sub-nanometer resolution, ellipsometry is a highly accurate method for measuring film thickness.

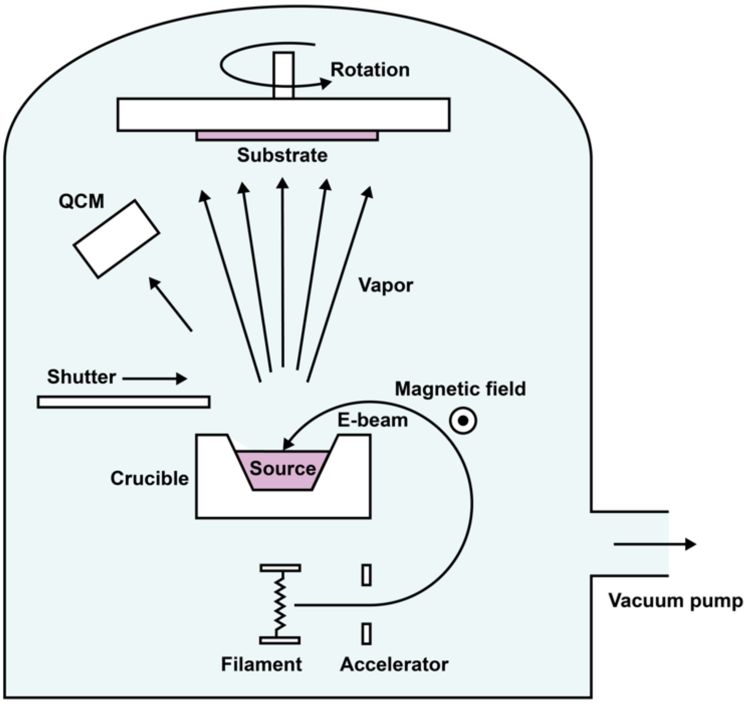

Figure 6.2. Illustration showing the deposition of thin SiO_2 films on glass substrates by using e-beam PVD. The SiO_2 source placed inside the crucible is bombarded by the electron beam to evaporate and deposit as a thin film on the substrate.

6.3 Optical microscopy

In this thesis, optical microscopy techniques, namely differential interference contrast microscopy and confocal laser scanning microscopy, were used to image biomembranes and other relevant biological components in the specimen. The resolution of an optical microscope, defined as the minimum distance (*d*) between two distinct points that can be resolved, is closely related to the numerical aperture (NA) of the objective and other optics in the light path. The NA is given by:

$$NA = nsin\theta \tag{6.1}$$

where *n* is the refractive index of the imaging medium and *θ* is the angular aperture. An oil immersion objective has a higher refractive index (*n* = 1.52) than a non-immersion objective (*n* ≈ 1 for air), resulting in a larger NA. The resolution limit also depends on the wavelength of the light in the vacuum (λ) used for imaging (Rayleigh criterion), as given by:

$$d = 0.61\frac{\lambda}{NA} \tag{6.2}$$

For example, an oil immersion objective ($NA = 1.4$) coupled with green light ($\lambda = 500\,nm$) yields a theoretical lateral resolution limit of 217 nm. To exceed the diffraction limit, several super-resolution microscopy techniques have been developed, including structured illumination microscopy (SIM) and stimulated emission depletion (STED) microscopy, which can achieve lateral resolutions below 50 nm (Reference [378]).

6.4 Differential interference contrast microscopy

In Paper II, differential interference contrast microscopy (DIC) microscopy was used to image the protocell-nanotube networks in the absence of fluorophore-conjugated lipids. DIC microscopy is a label-free imaging technique for biological specimens that are generally transparent and lack optical contrast under bright field illumination[379]. This technique uses transmitted light and is based on interferometry, providing a pseudo 3D relief shading image. Figure 6.3a illustrates the light path and optics used in DIC microscopy. Initially, unpolarized light from the light source is polarized by a polarizer and enters the first Nomarski prism, which separates the incoming light into two orthogonally polarized parts: the sampling and reference beams. These two beams have different optical path lengths and thus undergo a phase change as they pass through adjacent regions of the specimen that differ in refractive index or thickness. The objective then collects the transmitted light from the specimen, and the beams travels through the second Nomarski prism, where they are recombined into the same polarization. The second polarizer allows the recombined beam to interfere with each other, creating a brightening or darkening effect in the images that provides a pseudo 3D appearance of the specific area in the specimen. The use of polarizers in the light path reduces the amount of light reaching the detector, requiring a powerful light source for DIC.

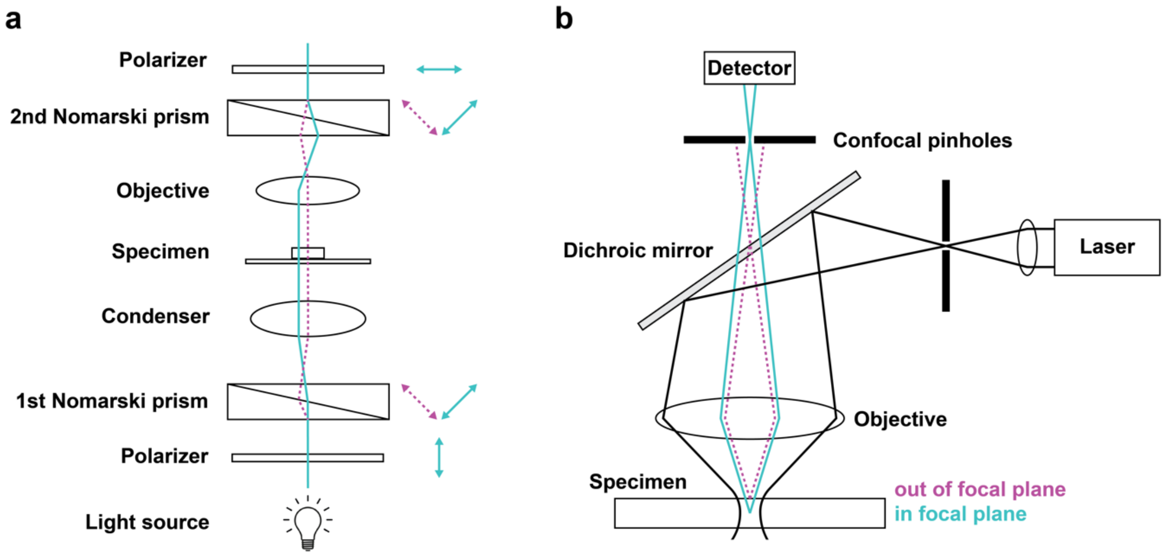

Figure 6.3. Schematics of optical paths in DIC microscopy (a) and CLSM (b). In DIC microscopy, the sampling and reference beams experience the difference in refractive index or thickness in the adjacent areas of the specimen, and therefore the combined beams can interfere and give a pseudo 3D contrast of the specimen. (b) In CLSM, the confocal pinholes select only the light emitted by the fluorophores that are in the focal plane, increasing the signal-to-noise ratio of the 2D images and allowing the reconstruction of 3D images by changing the scanning height.

6.5 Fluorescence and confocal microscopy

The lipid bilayer is optically transparent and has a thickness of approximately 4-5 nm, which is below the diffraction limit of light microscopy. As a result, most of the experiments in my dissertation involved the use of fluorophore-conjugated lipid molecules as probes to visualize the lipid membranes by fluorescence microscopy. Fluorophore molecules typically contain several aromatic groups and can selectively absorb light of a certain wavelength and subsequently emit light of a longer wavelength (Stokes shift). Upon excitation, the fluorophore molecule absorbs a photon and is promoted from the singlet ground state (S_0) to the excited singlet state (S_1). The timescale for absorption is on the order of 10^{-15} s. Each electronic state comprises multiple vibrational levels. Subsequently, the excited molecule will dissipate energy through vibrational relaxation (10^{-12} – 10^{-10} s) to reach the lowest vibrational level of the excited state. Finally, the molecule returns to the ground state by emitting a photon, which is the fluorescence process. Fluorescence occurs on a timescale of 10^{-10} to 10^{-7} s. The simplified Jablonski diagram in Figure 6.4a illustrates the above processes, with other non-radiative processes neglected in this scheme.

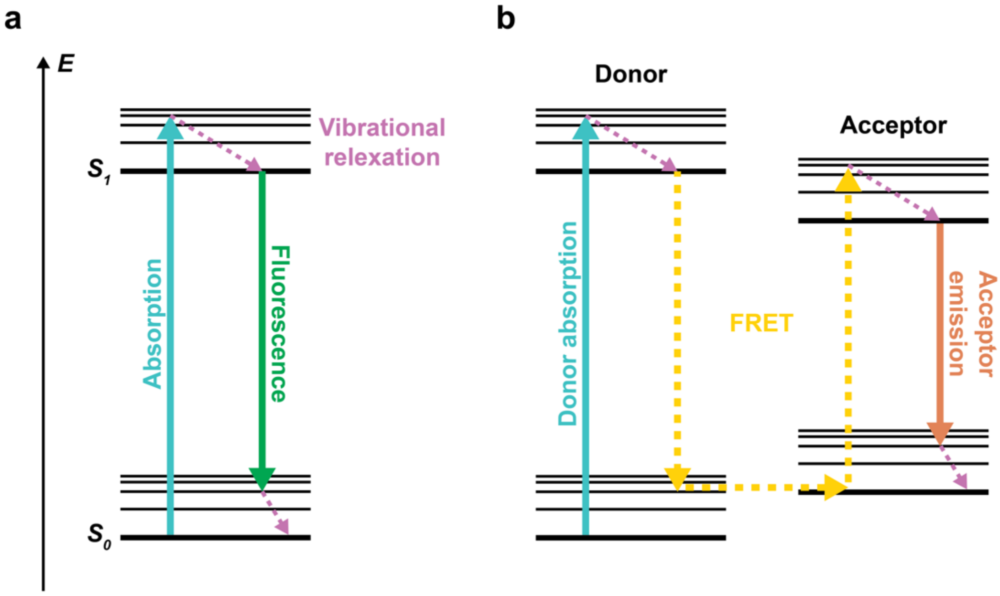

Figure 6.4. Simplified Jablonski diagram of fluorophore molecules undergoing fluorescence (a) and FRET (b).

The use of multiple fluorophores with distinct absorption and emission spectra allows the simultaneous visualization of different molecules and structures in a sample. In Paper I and III, we labeled lipid membranes and encapsulated cargo molecules, such as RNAs and proteins, with different fluorophores. However, overlapping excitation and emission wavelengths of different fluorophores can result in fluorescence crosstalk, which can obscure and produce a false fluorescence signal, thereby interfering with intensity-based measurement. When the excitation spectrum of one fluorophore (donor) overlaps with the emission spectrum of the other fluorophore (acceptor), which is in close proximity (1-10 nm), FRET occurs between the donor and acceptor. Figure 6.4b shows the Jablonski diagram of FRET. The excited donor transfers energy directly to the acceptor, initially in its ground state, in a non-radiative manner, resulting in the excitation of the acceptor to the excited state and ultimately acceptor emission. Since the FRET efficiency is inversely proportional to the sixth power of the distance between the donor and acceptor[380], FRET can be used to measure small changes in the distance between two molecules, typically on the order of nanometers, in biophysical studies such as lipid diffusion in membranes[381,382] and DNA double-strand hybridization[11,307]. In Paper III, we labeled the membranes of liposomes and giant vesicles with a pair of FRET fluorophores to monitor lipid mixing induced by membrane fusion.

The quality of imaging and signal-based measurements in microscopy experiments can be adversely affected by photobleaching. Prolonged or intense exposure to light can lead to the degradation or nonspecific reaction of the fluorophore molecule with surrounding molecules, rendering it unable to fluoresce permanently[383]. However, photobleaching can also be intentionally used in microscopy-based techniques such as FRAP to study the mobility of fluorescent molecules in biological samples, especially the fluidity of lipid bilayers[254,384]. Briefly, high intensity illumination is used to photobleach fluorescent molecules within a defined region of the sample. Driven by Brownian motion, non-photobleached molecules diffuse throughout the sample and replace the photobleached molecules in the initial photobleached region, where the fluorescence intensity gradually increases, or recovers, over time. In Paper II, we used FRAP to investigate the diffusive transport of the water-soluble dye, as well as fluorescently labeled RNA and DNA, between surface-adhered protocells through interconnected lipid nanotubes.

CLSM is a widely used imaging technique in life science research. Compared to widefield fluorescence microscopy, which detects fluorescence from the entire specimen, CLSM can significantly improve the signal-to-noise ratio by using pinholes to eliminate background fluorescence[385]. As illustrated in Figure 6.3b, two pinholes are located at confocal positions. The laser beam passes through the first pinhole, and after being directed by the dichroic mirror, the beam is focused onto a small portion of the specimen, leading to fluorescence. The light emitted by the excited fluorophores is filtered by the dichroic mirror and enters the second pinhole, which is positioned at the focal plane and allows only the light coming from the targeted point of the specimen to be detected. The focused beam can scan a defined area in the specimen, providing a 2D image at a given height. By moving the stage vertically, images can be scanned at different heights to obtain a reconstructed 3D image. CLSM is a powerful imaging tool for reconstructing 3D images of micrometer-scale membrane structures, such as protocell-nanotube networks and surface-adhered GUVs.

6.6 Infrared laser heating system

Biomembranes can undergo changes in permeability[386,387] and mechanics[388] in response to thermal stimuli. In Paper I, we performed local heating using an infrared (IR) laser fiber to rapidly nucleate, grow, and fuse lipid vesicles within a protocell-nanotube network. Water and lipid molecules have relatively high absorption coefficients above 1450 nm, corresponding to the IR-B regime (1400–3000 nm)[389,390]. In contrast, their absorptions are negligible in the IR-A regime (780–1400 nm), which is the IR window in biological tissues. Therefore, we used an IR-B laser (1470 nm) coupled to an optical fiber to generate local heating. The tip of the optical fiber was positioned 20-50 µm above the surface-adhered sample using a 3-axis micromanipulator. By turning on the laser, IR radiation from the flat fiber tip affected only a conical volume of water in close proximity to the surface-adhered membranes[3]. By adjusting the laser power, distinct temperature gradients could be achieved. The elevated temperature was characterized using a calibrated microthermocouple, as depicted in Figure 6.5. The thermocouple was initially placed in the center of the heated region, slightly above the surface, and by moving it along the z-direction, we recorded the local temperatures (Figure 6.5b,c). Measurements were made for different laser powers. The local temperatures were estimated to be 40 °C, 70 °C, and 90 °C when the laser current was set to 0.73 A, 0.97 A, and 1.22 A, respectively (Figure 6.5d).

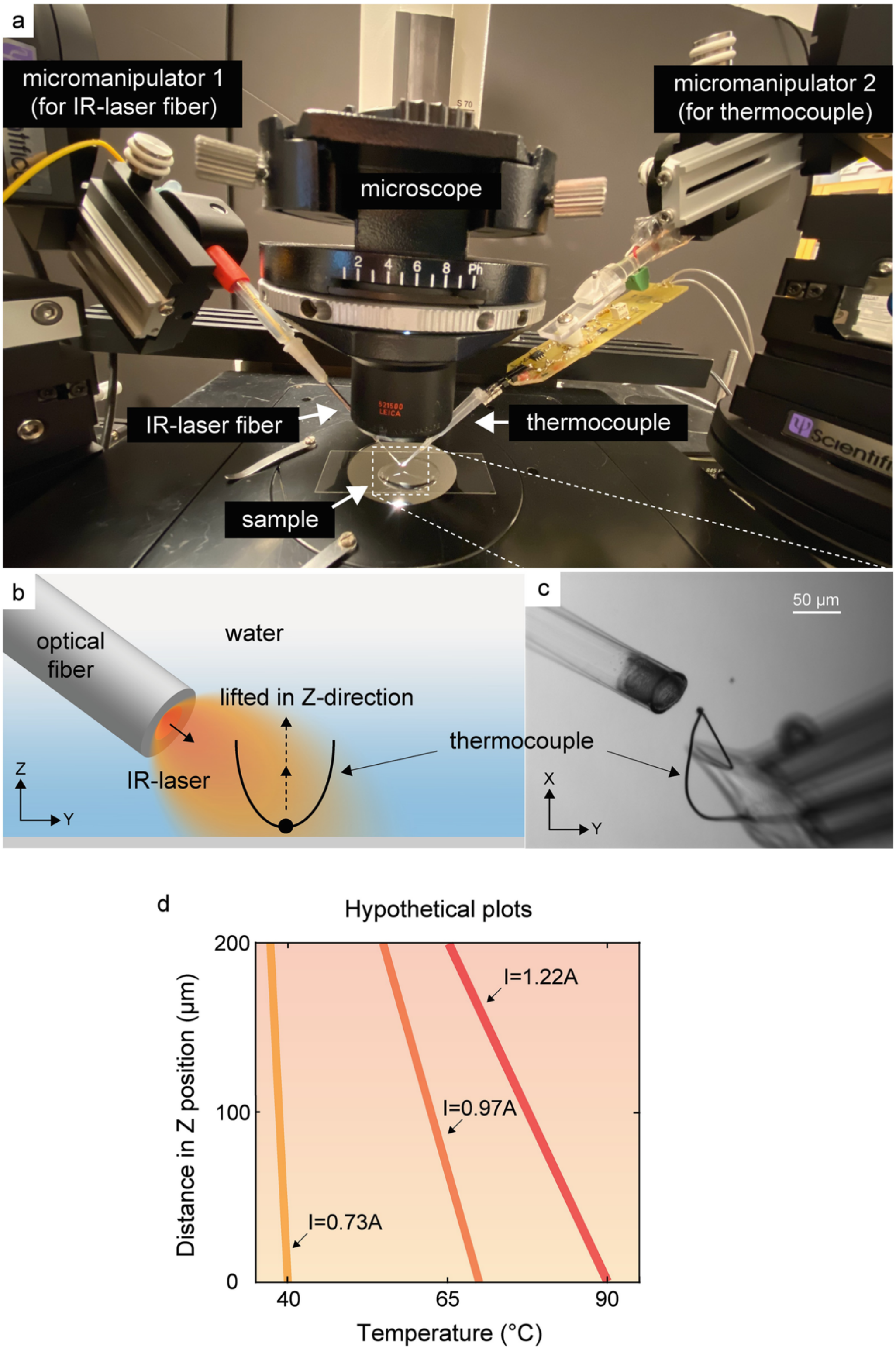

Figure 6.5. Optical fiber-based IR laser heating and temperature measurement. (a) Photo showing the experimental setup of IR laser heating. (b) Side view Illustration showing an optical fiber immersed in water and a microthermocouple that can be moved in z-direction. (c) Bright field micrograph of the same setup as in (b) from the top view. (d) Plots show that the hypothetical temperature increases with decreasing distance from the surface. *Reprinted with permission from Reference 3. Copyright 2022 Springer Nature.*

6.7 The microfluidic pipette

Microfluidics is a powerful technology used to manipulate and process sub-microliter fluids in channels with micrometer dimensions[391]. This technology enables precise control of flow rates and low samples and reagents consumption. Microfluidic devices typically operate under laminar flow conditions characterized by low Reynolds numbers. This helps to prevent the mixing of fluids flowing together, which facilitates the exchange of molecules by diffusion, thereby providing high resolution and sensitivity for separation and detection.

In this thesis, we used an open-volume microfluidic device, known as the microfluidic pipette[392,393], made of the optically transparent elastomer polydimethylsiloxane (PDMS). The pipette tip was immersed in buffer solution, and positioned in close proximity to the sample, and operated in a non-contact manner using a 3-axis micromanipulator. The pipette tip created a hydrodynamically confined flow volume, or recirculation zone, within the observation chamber by applying positive pressure to the center channel to inject fluid and negative pressure to the adjacent channels to aspirate solution, as shown in Figure 6.6. Typically, an outflow rate of ~10 nL s^{-1} can be achieved[393], and the ratio of outflow to inflow determines the size of the recirculation zone. The fluid within this recirculation zone has a high convection-to-diffusion ratio, or Péclet number, which hinders dispersion across the zone boundary. As a result, the recirculating fluid does not mix with the ambient buffer. The pipette contains four reservoir wells that can hold different solutions of interest. During the experiments, it is possible to quickly switch between the available solutions.

In Paper III, a variety of membrane-impermeable cargoes, such as water-soluble dyes, fluorescently labeled genetic polymers, sugars, and proteins, were encapsulated in fusogenic liposomes and delivered to the surface-adhered GUVs using the microfluidic pipette. Similarly, in Paper I and II, a microfluidic pipette was employed in a manner analogous to the superfusion technique used in cell culture[394] to deliver fluorescent dyes such as fluorescein or ATTO 488, or fluorescently labeled RNA or DNA oligomers to surface-adhered nanotube-connected lipid compartments.

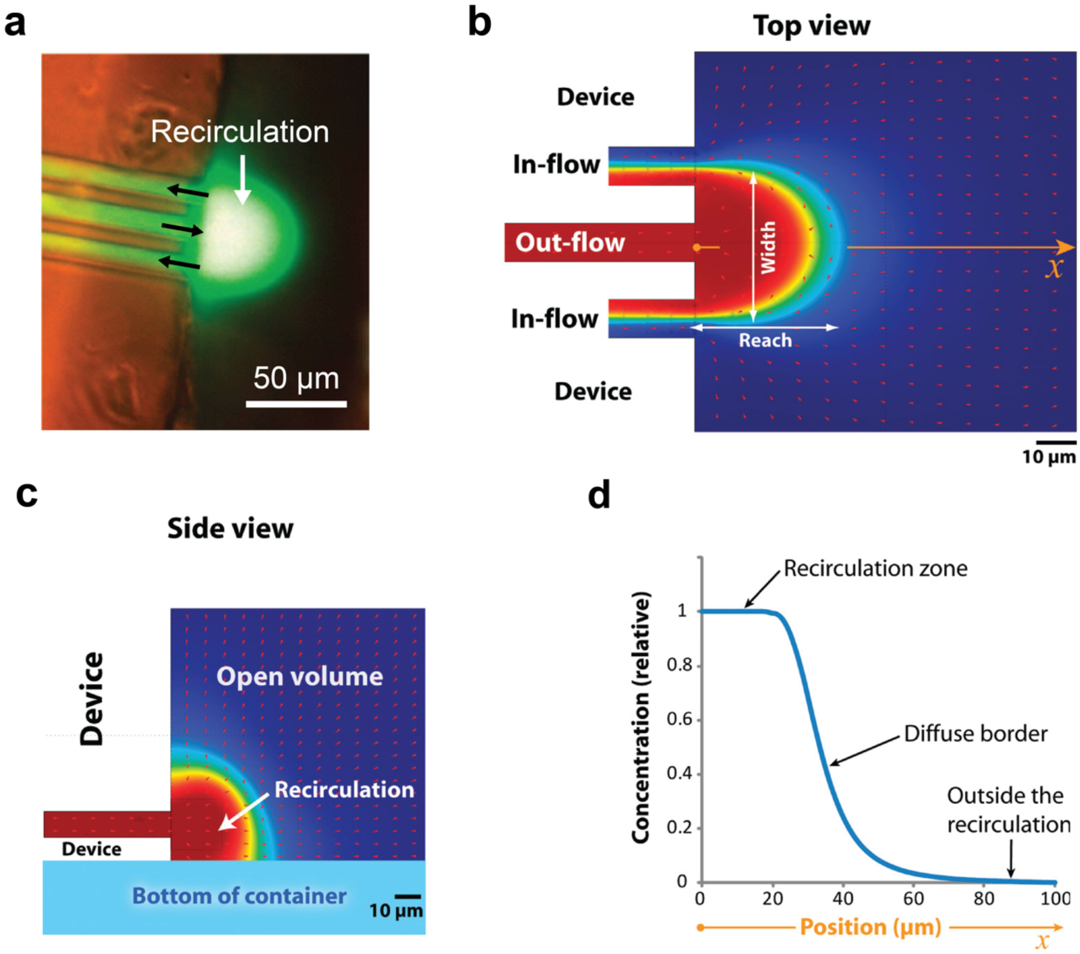

Figure 6.6. Flow recirculation in the microfluidic pipette. (a) Micrograph showing the recirculation zone of fluorescein solution (in green) in front of the pipette tip, created by the injecting flow (outflow) in the middle channel and the aspirating flow (inflow) in the two adjacent channels. The outflow/inflow ratio is 0.52. Top view (b) and side view (c) of the finite element simulation showing the flow field (red arrows) and the concentration of fluorescein (blue for 0% and red for 100%) when the outflow/inflow ratio is 0.5. (d) Plot showing the concentration distribution of fluorescein as a function of distance from the channel outlet along the channel axis x shown in (b). *Reprinted with permission from Reference 392. Copyright 2010 American Chemical Society.*

7 Conclusion and outlook

This thesis provides the experimental evidence for the origin of life hypothesis that protocells may have emerged under prebiotic conditions and formed colony-like protocell populations in the transition to the first living cell populations. Within these populations of protocell, each individual protocell is capable of exchanging contents with its neighbors, mediated by the interconnected membrane nanotubes that spontaneously formed.

The interactions between protocells and their adhering solid surfaces are the main findings presented in this thesis. Specifically, the intrinsic energies of solid surfaces, such as minerals and rocks on early Earth, can be harvested by organic matter adhering to them. By adhering to engineered silica surfaces, lipid assemblies have been found to undergo topological transformations on their membranes, including tubulation, vesiculation, and fusion. These observations have led to the suggestion that populations of protocell may develop on solid surfaces.

Tunneling nanotubes are a ubiquitous communication tool in all domains of life. Similarly, lipid nanotubes within protocell-nanotube networks facilitate the transport of diffusive cargo between protocells without the need to cross the membrane boundaries. However, the transport of high molecular weight cargoes or over long distances within a network may be hindered by diffusion limits. Therefore, investigating transport driven by other mechanisms, such as membrane tension and electric fields, holds great potential for future studies and can improve communication within synthetic cell populations with increased control and precision. In addition, protocell-nanotube networks may have provided a confined microenvironment for prebiotic chemical reactions, i.e., reagents can be stored in separate compartments and recruited to react through nanotube connections. This can be used as an effective bottom-up approach to achieve higher complexity in synthetic cells.

This thesis also explores the intricate interactions between protocells and RNA. Protocells are capable of entrapping RNA present in the environment during self-assembly into compartments. Moreover, self-assembled protocellular compartments can uptake external RNA through transient membrane pores. Encapsulated RNA can then be redistributed upon fusion of adjacent protocells or transported to distant protocells through connecting nanotubes.

The spontaneous formation of protocells and even protocell populations under primitive Earth conditions is a critical step toward the origin of life. The development of intrinsic mechanisms for intercellular interaction within protocell populations, and for adaptation to the environmental changes, would have greatly benefited their eventual transformation into the first living cell populations. This has not yet been supported by systematic experimental evidence. Future studies could investigate the physical interactions between different protocell species, as well as the topological transformation of protocell membranes in response to physicochemical stimulation in the microenvironment.

The results presented in this thesis provide valuable insights into the mechanisms and processes that may have contributed to the emergence and evolution of the primitive forms of life, thus advancing our understanding of the origin of life and having potential implications for the fields of astrobiology and synthetic biology. To further our understanding of the driving force of membrane fusion and the mechanism of mechanical interaction, future investigations could focus on quantitatively determining the influence of membrane lipid composition on local membrane tension at the edge of spreading membranous protocells. In addition, the role of surfaces with bespoke patterns or functionalization[395–397] in protocell interactions can be explored. Such investigations will enhance our understanding of the complex interactions between protocells and their environment, and aid in the design and construction of synthetic systems.

References

(1) Köksal, E. S.; Liese, S.; Xue, L.; Ryskulov, R.; Viitala, L.; Carlson, A.; Gözen, I. Rapid Growth and Fusion of Protocells in Surface-Adhered Membrane Networks. *Small Weinh. Bergstr. Ger.* **2020**, *16* (38), 2002529-n/a. https://doi.org/10.1002/smll.202002529.

(2) Schanke, I. J.; Xue, L.; Spustova, K.; Gözen, I. Transport among Protocells *via* Tunneling Nanotubes. *Nanoscale* **2022**, *14* (29), 10418–10427. https://doi.org/10.1039/D2NR02290G.

(3) Spustova, K.; Xue, L.; Ryskulov, R.; Jesorka, A.; Gözen, I. Manipulation of Lipid Membranes with Thermal Stimuli. *Membr. Lipids Methods Protoc.* **2022**, 209–225. https://doi.org/10.1007/978-1-0716-1843-1_17.

(4) Gözen, I.; Köksal, E. S.; Põldsalu, I.; Xue, L.; Spustova, K.; Pedrueza-Villalmanzo, E.; Ryskulov, R.; Meng, F.; Jesorka, A. Protocells: Milestones and Recent Advances. *Small* **2022**, *18* (18), 2106624. https://doi.org/10.1002/smll.202106624.

(5) Szostak, J. How Did Life Begin? *Nature* **2018**, *557* (7706), S13–S13. https://doi.org/10.1038/d41586-018-05098-w.

(6) Javaux, E. J. Challenges in Evidencing the Earliest Traces of Life. *Nature* **2019**, *572* (7770), 451–460. https://doi.org/10.1038/s41586-019-1436-4.

(7) Monnard, P.-A.; Deamer, D. W. Nutrient Uptake by Protocells: A Liposome Model System. *Orig Life Evol Biosph* **2001**, *31* (1–2), 147–155. https://doi.org/10.1023/A:1006769503968.

(8) Szostak, J. W.; Bartel, D. P.; Luisi, P. L. Synthesizing Life. *Nature* **2001**, *409* (6818), 387–390. https://doi.org/10.1038/35053176.

(9) Mansy, S. S.; Schrum, J. P.; Krishnamurthy, M.; Tobé, S.; Treco, D. A.; Szostak, J. W. Template-Directed Synthesis of a Genetic Polymer in a Model Protocell. *Nature* **2008**, *454* (7200), 122–125. https://doi.org/10.1038/nature07018.

(10) Dzieciol, A. J.; Mann, S. Designs for Life: Protocell Models in the Laboratory. *Chem Soc Rev* **2012**, *41* (1), 79–85. https://doi.org/10.1039/c1cs15211d.

(11) Qiao, Y.; Li, M.; Booth, R.; Mann, S. Predatory Behaviour in Synthetic Protocell Communities. *Nat. Chem.* **2017**, *9* (2), 110–119. https://doi.org/10.1038/nchem.2617.

(12) Donau, C.; Späth, F.; Sosson, M.; Kriebisch, B. A. K.; Schnitter, F.; Tena-Solsona, M.; Kang, H.-S.; Salibi, E.; Sattler, M.; Mutschler, H.; Boekhoven, J. Active Coacervate Droplets as a Model for Membraneless Organelles and Protocells. *Nat. Commun.* **2020**, *11* (1). https://doi.org/10.1038/s41467-020-18815-9.

(13) Patterson, C. Age of Meteorites and the Earth. *Geochim. Cosmochim. Acta* **1956**, *10* (4), 230–237. https://doi.org/10.1016/0016-7037(56)90036-9.

(14) Allègre, C. J.; Manhès, G.; Göpel, C. The Age of the Earth. *Geochim. Cosmochim. Acta* **1995**, *59* (8), 1445–1456. https://doi.org/10.1016/0016-7037(95)00054-4.

(15) Cogley, J. G.; Henderson-Sellers, A. The Origin and Earliest State of the Earth's Hydrosphere. *Rev. Geophys.* **1984**, *22* (2), 131. https://doi.org/10.1029/rg022i002p00131.

(16) Djokic, T.; Van Kranendonk, M. J.; Campbell, K. A.; Walter, M. R.; Ward, C. R. Earliest Signs of Life on Land Preserved in ca. 3.5 Ga Hot Spring Deposits. *Nat. Commun.* **2017**, *8* (1), 15263. https://doi.org/10.1038/ncomms15263.

(17) Tirard, S.; Morange, M.; Lazcano, A. The Definition of Life: A Brief History of an Elusive Scientific Endeavor. *Astrobiology* **2010**, *10* (10), 1003–1009. https://doi.org/10.1089/ast.2010.0535.

(18) Luisi, P. L. About Various Definitions of Life. *Orig. Life Evol. Biosph.* **1998**, *28* (4), 613–622. https://doi.org/10.1023/A:1006517315105.

(19) Ganti, T. *The Principles of Life*; Szathmary, E., Griesemer, J., Eds.; Oxford University Press: Oxford, 2003.

(20) Pohorille, A.; Deamer, D. Artificial Cells: Prospects for Biotechnology. *Trends Biotechnol.* **2002**, *20* (3), 123–128. https://doi.org/10.1016/S0167-7799(02)01909-1.

(21) Knoll, A. H.; Nowak, M. A. The Timetable of Evolution. *Sci. Adv.* **2017**, *3* (5), e1603076. https://doi.org/10.1126/sciadv.1603076.

(22) Deamer, D.; Cary, F.; Damer, B. Urability: A Property of Planetary Bodies That Can Support an Origin of Life. *Astrobiology* **2022**. https://doi.org/10.1089/ast.2021.0173.

(23) Mulkidjanian Armen, Y.; Bychkov Andrew, Y.; Dibrova Daria, V.; Galperin Michael, Y.; Koonin Eugene, V. Origin of First Cells at Terrestrial, Anoxic Geothermal Fields. *Proc. Natl. Acad. Sci.* **2012**, *109* (14), E821–E830. https://doi.org/10.1073/pnas.1117774109.

(24) Damer, B.; Deamer, D. Coupled Phases and Combinatorial Selection in Fluctuating Hydrothermal Pools: A Scenario to Guide Experimental Approaches to the Origin of Cellular Life. *Life* **2015**, *5* (1), 872–887. https://doi.org/10.3390/life5010872.

(25) Damer, B.; Deamer, D. The Hot Spring Hypothesis for an Origin of Life. *Astrobiology* **2020**, *20* (4), 429–452. https://doi.org/10.1089/ast.2019.2045.

(26) James F. Kasting. Earth's Early Atmosphere. *Science* **1993**, *259* (5097), 920–926. https://doi.org/doi:10.1126/science.11536547.

(27) Zahnle, K.; Schaefer, L.; Fegley, B. Earth's Earliest Atmospheres. *Cold Spring Harb. Perspect. Biol.* **2010**, *2* (10), a004895–a004895. https://doi.org/10.1101/cshperspect.a004895.

(28) Stanley L. Miller; Harold C. Urey. Organic Compound Synthesis on the Primitive Earth. *Science* **1959**, *130* (3370), 245–251. https://doi.org/doi:10.1126/science.130.3370.245.

(29) Frenkel-Pinter, M.; Rajaei, V.; Glass, J. B.; Hud, N. V.; Williams, L. D. Water and Life: The Medium Is the Message. *J. Mol. Evol.* **2021**, *89* (1–2), 2–11. https://doi.org/10.1007/s00239-020-09978-6.

(30) Mojzsis, S. J.; Harrison, T. M.; Pidgeon, R. T. Oxygen-Isotope Evidence from Ancient Zircons for Liquid Water at the Earth's Surface 4,300 Myr Ago. *Nature* **2001**, *409* (6817), 178–181. https://doi.org/10.1038/35051557.

(31) Francois Robert. The Origin of Water on Earth. *Science* **2001**, *293* (5532), 1056–1058. https://doi.org/doi:10.1126/science.1064051.

(32) Sarafian Adam, R.; Nielsen Sune, G.; Marschall Horst, R.; McCubbin Francis, M.; Monteleone Brian, D. Early Accretion of Water in the Inner Solar System from a Carbonaceous Chondrite–like Source. *Science* **2014**, *346* (6209), 623–626. https://doi.org/10.1126/science.1256717.

(33) Peslier, A. H.; Schönbächler, M.; Busemann, H.; Karato, S.-I. Water in the Earth's Interior: Distribution and Origin. *Space Sci. Rev.* **2017**, *212* (1–2), 743–810. https://doi.org/10.1007/s11214-017-0387-z.

(34) R. Terik Daly; Peter H. Schultz. The Delivery of Water by Impacts from Planetary Accretion to Present. *Sci. Adv.* **2018**, *4* (4), eaar2632. https://doi.org/doi:10.1126/sciadv.aar2632.

(35) Maruyama, S.; Ebisuzaki, T. Origin of the Earth: A Proposal of New Model Called ABEL. *Geosci. Front.* **2017**, *8* (2), 253–274. https://doi.org/10.1016/j.gsf.2016.10.005.

(36) Morbidelli, A.; Chambers, J.; Lunine, J. I.; Petit, J. M.; Robert, F.; Valsecchi, G. B.; Cyr, K. E. Source Regions and Timescales for the Delivery of Water to the Earth. *Meteorit. Planet. Sci.* **2000**, *35* (6), 1309–1320. https://doi.org/10.1111/j.1945-5100.2000.tb01518.x.

(37) Piani, L.; Marrocchi, Y.; Rigaudier, T.; Vacher Lionel, G.; Thomassin, D.; Marty, B. Earth's Water May Have Been Inherited from Material Similar to Enstatite Chondrite Meteorites. *Science* **2020**, *369* (6507), 1110–1113. https://doi.org/10.1126/science.aba1948.

(38) Xu, J.; Chmela, V.; Nicholas; David; Mikołaj; Robert; Szabla, R.; Andrew; John. Selective Prebiotic Formation of RNA Pyrimidine and DNA Purine Nucleosides. *Nature* **2020**, *582* (7810), 60–66. https://doi.org/10.1038/s41586-020-2330-9.

(39) Zahnle, K. J.; Walker, J. C. G. The Evolution of Solar Ultraviolet Luminosity. *Rev. Geophys.* **1982**, *20* (2), 280–292. https://doi.org/10.1029/RG020i002p00280.

(40) Cockell, C. S. The Ultraviolet History of the Terrestrial Planets — Implications for Biological Evolution. *Planet. Space Sci.* **2000**, *48* (2), 203–214. https://doi.org/10.1016/S0032-0633(99)00087-2.

(41) Horneck, G. Responses ofBacillus Subtilis Spores to Space Environment: Results from Experiments in Space. *Orig. Life Evol. Biosph.* **1993**, *23* (1), 37–52. https://doi.org/10.1007/BF01581989.

(42) Ranjan, S.; Sasselov, D. D. Influence of the UV Environment on the Synthesis of Prebiotic Molecules. *Astrobiology* **2016**, *16* (1), 68–88. https://doi.org/10.1089/ast.2015.1359.

(43) H. James Cleaves; Stanley L. Miller. Oceanic Protection of Prebiotic Organic Compounds from UV Radiation. *Proc. Natl. Acad. Sci.* **1998**, *95* (13), 7260–7263. https://doi.org/doi:10.1073/pnas.95.13.7260.

(44) Ranjan, S.; Kufner, C. L.; Lozano, G. G.; Todd, Z. R.; Haseki, A.; Sasselov, D. D. UV Transmission in Natural Waters on Prebiotic Earth. *Astrobiology* **2022**, *22* (3), 242–262. https://doi.org/10.1089/ast.2020.2422.

(45) Lechuga, I.; Michaelian, K. Fatty Acid Vesicles as Hard UV-C Shields for Early Life. *Foundations* **2023**, *3* (1), 99–114. https://doi.org/10.3390/foundations3010010.

(46) James Cleaves Ii, H.; Michalkova Scott, A.; Hill, F. C.; Leszczynski, J.; Sahai, N.; Hazen, R. Mineral–Organic Interfacial Processes: Potential Roles in the Origins of Life. *Chem. Soc. Rev.* **2012**, *41* (16), 5502. https://doi.org/10.1039/c2cs35112a.

(47) Hazen, R. M.; Papineau, D.; Bleeker, W.; Downs, R. T.; Ferry, J. M.; McCoy, T. J.; Sverjensky, D. A.; Yang, H. Review Paper. Mineral Evolution. **2008**, *93* (11–12), 1693–1720. https://doi.org/10.2138/am.2008.2955.

(48) Hazen, R. M.; Sverjensky, D. A. Mineral Surfaces, Geochemical Complexities, and the Origins of Life. *Cold Spring Harb. Perspect. Biol.* **2010**, *2* (5), a002162. https://doi.org/https:doi.org/10.1101/cshperspect.a002162.

(49) Dalai, P.; Sahai, N. Mineral–Lipid Interactions in the Origins of Life. *Trends Biochem. Sci.* **2019**, *44* (4), 331–341. https://doi.org/10.1016/j.tibs.2018.11.009.

(50) Monnard, P.-A.; Walde, P. Current Ideas about Prebiological Compartmentalization. *Life* **2015**, *5* (2), 1239–1263. https://doi.org/10.3390/life5021239.

(51) Viennet, J.-C.; Bernard, S.; Le Guillou, C.; Sautter, V.; Grégoire, B.; Jambon, A.; Pont, S.; Beyssac, O.; Zanda, B.; Hewins, R.; Remusat, L. Martian Magmatic Clay Minerals Forming Vesicles: Perfect Niches for Emerging Life? *Astrobiology* **2021**, *21* (5), 605–612. https://doi.org/10.1089/ast.2020.2345.

(52) Morasch, M.; Liu, J.; Dirscherl, C. F.; Ianeselli, A.; Kühnlein, A.; Le Vay, K.; Schwintek, P.; Islam, S.; Corpinot, M. K.; Scheu, B.; Dingwell, D. B.; Schwille, P.; Mutschler, H.; Powner, M. W.; Mast, C. B.; Braun, D. Heated Gas Bubbles Enrich, Crystallize, Dry, Phosphorylate and Encapsulate Prebiotic Molecules. *Nat. Chem.* **2019**, *11* (9), 779–788. https://doi.org/10.1038/s41557-019-0299-5.

(53) Andreani, M.; Montagnac, G.; Fellah, C.; Hao, J.; Vandier, F.; Daniel, I.; Pisapia, C.; Galipaud, J.; Lilley, M. D.; Früh Green, G. L.; Borensztajn, S.; Ménez, B. The Rocky Road to Organics Needs Drying. *Nat. Commun.* **2023**, *14* (1), 347. https://doi.org/10.1038/s41467-023-36038-6.

(54) Gillams, R.; Jia, T. Mineral Surface-Templated Self-Assembling Systems: Case Studies from Nanoscience and Surface Science towards Origins of Life Research. *Life* **2018**, *8* (2), 10. https://doi.org/10.3390/life8020010.

(55) Kloprogge, J. T.; Hartman, H. Clays and the Origin of Life: The Experiments. *Life* **2022**, *12* (2), 259. https://doi.org/10.3390/life12020259.

(56) Cai, P.; Huang, Q.-Y.; Zhang, X.-W. Interactions of DNA with Clay Minerals and Soil Colloidal Particles and Protection against Degradation by DNase. *Environ. Sci. Amp Technol.* **2006**, *40* (9), 2971–2976. https://doi.org/10.1021/es0522985.

(57) Pedreira-Segade, U.; Hao, J.; Razafitianamaharavo, A.; Pelletier, M.; Marry, V.; Le Crom, S.; Michot, L.; Daniel, I. How Do Nucleotides Adsorb Onto Clays? *Life* **2018**, *8* (4), 59. https://doi.org/10.3390/life8040059.

(58) Ferris, J. P. Montmorillonite-Catalysed Formation of RNA Oligomers: The Possible Role of Catalysis in the Origins of Life. *Philos. Trans. R. Soc. B Biol. Sci.* **2006**, *361* (1474), 1777–1786. https://doi.org/10.1098/rstb.2006.1903.

(59) Erastova, V.; Degiacomi, M. T.; G. Fraser, D.; Greenwell, H. C. Mineral Surface Chemistry Control for Origin of Prebiotic Peptides. *Nat. Commun.* **2017**, *8* (1). https://doi.org/10.1038/s41467-017-02248-y.

(60) Biondi, E.; Branciamore, S.; Maurel, M.-C.; Gallori, E. Montmorillonite Protection of an UV-Irradiated Hairpin Ribozyme: Evolution of the RNA World in a Mineral Environment. *BMC Evol. Biol.* **2007**, *7* (S2), S2. https://doi.org/10.1186/1471-2148-7-s2-s2.

(61) de Oliveira, L. H.; Trigueiro, P.; Rigaud, B.; da Silva-Filho, E. C.; Osajima, J. A.; Fonseca, M. G.; Lambert, J.-F.; Georgelin, T.; Jaber, M. When RNA Meets Montmorillonite: Influence of the pH and Divalent Cations. *Appl. Clay Sci.* **2021**, *214*, 106234. https://doi.org/10.1016/j.clay.2021.106234.

(62) Rimola, A.; Costa, D.; Sodupe, M.; Lambert, J.-F.; Ugliengo, P. Silica Surface Features and Their Role in the Adsorption of Biomolecules: Computational Modeling and Experiments. *Chem. Rev.* **2013**, *113* (6), 4216–4313. https://doi.org/10.1021/cr3003054.

(63) Robert M. Hazen; Dominic Papineau; Wouter Bleeker; Robert T. Downs; John M. Ferry; Timothy J. McCoy; Dimitri A. Sverjensky; Hexiong Yang. Review Paper. Mineral Evolution. *Am. Mineral.* **2008**, *93* (11–12), 1693–1720. https://doi.org/doi:10.2138/am.2008.2955.

(64) Bedoin, L.; Alves, S.; Lambert, J.-F. Origins of Life and Molecular Information: Selectivity in Mineral Surface-Induced Prebiotic Amino Acid Polymerization. *ACS Earth Space Chem.* **2020**, *4* (10), 1802–1812. https://doi.org/10.1021/acsearthspacechem.0c00183.

(65) Chen, J.; Bai, Q.; Li, Y.; Liu, Z.; Li, Y.; Liang, D. Coacervates Forming Coexisting Phases on a Mineral Surface. *Langmuir* **2023**, *39* (16), 5814–5824. https://doi.org/10.1021/acs.langmuir.3c00101.

(66) Lepot, K. Signatures of Early Microbial Life from the Archean (4 to 2.5 Ga) Eon. *Earth-Sci. Rev.* **2020**, *209*, 103296. https://doi.org/10.1016/j.earscirev.2020.103296.

(67) McMahon, S.; Jordan, S. F. A Fundamental Limit to the Search for the Oldest Fossils. *Nat. Ecol. Evol.* **2022**, *6* (7), 832–834. https://doi.org/10.1038/s41559-022-01777-0.

(68) McMahon, S.; Cosmidis, J. False Biosignatures on Mars: Anticipating Ambiguity. *J. Geol. Soc.* **2021**, *179* (2), jgs2021-050. https://doi.org/10.1144/jgs2021-050.

(69) Rouillard, J.; van Zuilen, M.; Pisapia, C.; Garcia-Ruiz, J.-M. An Alternative Approach for Assessing Biogenicity. *Astrobiology* **2021**, *21* (2), 151–164. https://doi.org/10.1089/ast.2020.2282.

(70) Nutman, A. P.; Bennett, V. C.; Friend, C. R. L.; Van Kranendonk, M. J.; Chivas, A. R. Rapid Emergence of Life Shown by Discovery of 3,700-Million-Year-Old Microbial Structures. *Nature* **2016**, *537* (7621), 535–538. https://doi.org/10.1038/nature19355.

(71) Nutman, A. P.; Bennett, V. C.; Friend, C. R. L.; Van Kranendonk, M. J. In Support of Rare Relict ~3700 Ma Stromatolites from Isua (Greenland). *Earth Planet. Sci. Lett.* **2021**, *562*, 116850. https://doi.org/10.1016/j.epsl.2021.116850.

(72) Wacey, D.; Kilburn, M. R.; Saunders, M.; Cliff, J.; Brasier, M. D. Microfossils of Sulphur-Metabolizing Cells in 3.4-Billion-Year-Old Rocks of Western Australia. *Nat. Geosci.* **2011**, *4* (10), 698–702. https://doi.org/10.1038/ngeo1238.

(73) Coutant, M.; Lepot, K.; Fadel, A.; Addad, A.; Richard, E.; Troadec, D.; Ventalon, S.; Sugitani, K.; Javaux, E. J. Distinguishing Cellular from Abiotic Spheroidal Microstructures in the ca. 3.4 Ga Strelley Pool Formation. *Geobiology* **2022**. https://doi.org/10.1111/gbi.12506.

(74) Javaux, E. J.; Marshall, C. P.; Bekker, A. Organic-Walled Microfossils in 3.2-Billion-Year-Old Shallow-Marine Siliciclastic Deposits. *Nature* **2010**, *463* (7283), 934–938. https://doi.org/10.1038/nature08793.

(75) Mojzsis, S. J.; Brasser, R.; Kelly, N. M.; Abramov, O.; Werner, S. C. Onset of Giant Planet Migration before 4480 Million Years Ago. *Astrophys. J.* **2019**, *881* (1), 44. https://doi.org/10.3847/1538-4357/ab2c03.

(76) Huang, Y.; Wang, Y.; Alexandre, M. R.; Lee, T.; Rose-Petruck, C.; Fuller, M.; Pizzarello, S. Molecular and Compound-Specific Isotopic Characterization of Monocarboxylic Acids in Carbonaceous Meteorites. *Geochim. Cosmochim. Acta* **2005**, *69* (4), 1073–1084. https://doi.org/10.1016/j.gca.2004.07.030.

(77) Monnard, P.-A.; Deamer, D. W. Membrane Self-Assembly Processes: Steps toward the First Cellular Life. *Anat. Rec.* **2002**, *268* (3), 196–207. https://doi.org/10.1002/ar.10154.

(78) Deamer, D. W.; Pashley, R. M. Amphiphilic Components of the Murchison Carbonaceous Chondrite: Surface Properties and Membrane Formation. *Orig. Life Evol. Biosph.* **1989**, *19* (1), 21–38. https://doi.org/10.1007/bf01808285.

(79) Oba, Y.; Takano, Y.; Furukawa, Y.; Koga, T.; Glavin, D. P.; Dworkin, J. P.; Naraoka, H. Identifying the Wide Diversity of Extraterrestrial Purine and Pyrimidine Nucleobases in Carbonaceous Meteorites. *Nat. Commun.* **2022**, *13* (1). https://doi.org/10.1038/s41467-022-29612-x.

(80) Nicholson, W. L. Ancient Micronauts: Interplanetary Transport of Microbes by Cosmic Impacts. *Trends Microbiol.* **2009**, *17* (6), 243–250. https://doi.org/10.1016/j.tim.2009.03.004.

(81) Mitton, S. A Short History of Panspermia from Antiquity Through the Mid-1970s. *Astrobiology* **2022**, *22* (12), 1379–1391. https://doi.org/10.1089/ast.2022.0032.

(82) Adams, F. C.; Napier, K. J. Transfer of Rocks Between Planetary Systems: Panspermia Revisited. *Astrobiology* **2022**, *22* (12), 1429–1442. https://doi.org/10.1089/ast.2021.0187.

(83) Horneck, G.; Bücker, H.; Reitz, G. Long-Term Survival of Bacterial Spores in Space. *Adv. Space Res.* **1994**, *14* (10), 41–45. https://doi.org/10.1016/0273-1177(94)90448-0.

(84) Cleaves, H. J.; Chalmers, J. H.; Lazcano, A.; Miller, S. L.; Bada, J. L. A Reassessment of Prebiotic Organic Synthesis in Neutral Planetary Atmospheres. *Orig. Life Evol. Biospheres* **2008**, *38* (2), 105–115. https://doi.org/10.1007/s11084-007-9120-3.

(85) McCollom, T. M. Miller-Urey and Beyond: What Have We Learned About Prebiotic Organic Synthesis Reactions in the Past 60 Years? *Annu. Rev. Earth Planet. Sci.* **2013**, *41* (1), 207–229. https://doi.org/10.1146/annurev-earth-040610-133457.

(86) Nooner, D. W.; Gibert, J. M.; Gelpi, E.; Oró, J. Closed System Fischer-Tropsch Synthesis over Meteoritic Iron, Iron Ore and Nickel-Iron Alloy. *Geochim. Cosmochim. Acta* **1976**, *40* (8), 915–924. https://doi.org/10.1016/0016-7037(76)90140-X.

(87) Simoneit, B. R. T. Prebiotic Organic Synthesis under Hydrothermal Conditions: An Overview. *Adv. Space Res.* **2004**, *33* (1), 88–94. https://doi.org/10.1016/j.asr.2003.05.006.

(88) Daoping He; Xiaoguang Wang; Yang Yang; Runtian He; Heng Zhong; Ye Wang; Buxing Han; Fangming Jin. Hydrothermal Synthesis of Long-Chain Hydrocarbons up to C_{24} with $NaHCO_3$-Assisted Stabilizing Cobalt. *Proc. Natl. Acad. Sci.* **2021**, *118* (51), e2115059118. https://doi.org/doi:10.1073/pnas.2115059118.

(89) Mißbach, H.; Duda, J.-P.; Van Den Kerkhof, A. M.; Lüders, V.; Pack, A.; Reitner, J.; Thiel, V. Ingredients for Microbial Life Preserved in 3.5 Billion-Year-Old Fluid Inclusions. *Nat. Commun.* **2021**, *12* (1). https://doi.org/10.1038/s41467-021-21323-z.

(90) Hargreaves, W. R.; Mulvihill, S. J.; Deamer, D. W. Synthesis of Phospholipids and Membranes in Prebiotic Conditions. *Nature* **1977**, *266* (5597), 78–80. https://doi.org/10.1038/266078a0.

(91) Fiore, M.; Chieffo, C.; Lopez, A.; Fayolle, D.; Ruiz, J.; Soulère, L.; Oger, P.; Altamura, E.; Popowycz, F.; Buchet, R. Synthesis of Phospholipids Under Plausible Prebiotic Conditions and Analogies with Phospholipid Biochemistry for Origin of Life Studies. *Astrobiology* **2022**, *22* (5), 598–627. https://doi.org/10.1089/ast.2021.0059.

(92) Rao, M.; Eichberg, J.; Oró, J. Synthesis of Phosphatidylcholine under Possible Primitive Earth Conditions. *J. Mol. Evol.* **1982**, *18* (3), 196–202. https://doi.org/10.1007/bf01733046.

(93) Rao, M.; Eichberg, J.; Oró, J. Synthesis of Phosphatidylethanolamine under Possible Primitive Earth Conditions. *J. Mol. Evol.* **1987**, *25* (1), 1–6. https://doi.org/10.1007/bf02100033.

(94) Liu, L.; Zou, Y.; Bhattacharya, A.; Zhang, D.; Lang, S. Q.; Houk, K. N.; Devaraj, N. K. Enzyme-Free Synthesis of Natural Phospholipids in Water. *Nat. Chem.* **2020**, *12* (11), 1029–1034. https://doi.org/10.1038/s41557-020-00559-0.

(95) Gaylor, M. O.; Miro, P.; Vlaisavljevich, B.; Kondage, A. A. S.; Barge, L. M.; Omran, A.; Videau, P.; Swenson, V. A.; Leinen, L. J.; Fitch, N. W.; Cole, K. L.; Stone, C.; Drummond, S. M.; Rageth, K.; Dewitt, L. R.; Sarah; Karanauskus, V. Plausible Emergence and Self Assembly of a Primitive Phospholipid from Reduced Phosphorus on the Primordial Earth. *Orig. Life Evol. Biospheres* **2021**, *51* (3), 185–213. https://doi.org/10.1007/s11084-021-09613-4.

(96) Toner Jonathan, D.; Catling David, C. A Carbonate-Rich Lake Solution to the Phosphate Problem of the Origin of Life. *Proc. Natl. Acad. Sci.* **2020**, *117* (2), 883–888. https://doi.org/10.1073/pnas.1916109117.

(97) Ritson, D. J.; Mojzsis, S. J.; Sutherland, J. D. Supply of Phosphate to Early Earth by Photogeochemistry after Meteoritic Weathering. *Nat. Geosci.* **2020**, *13* (5), 344–348. https://doi.org/10.1038/s41561-020-0556-7.

(98) Hess, B. L.; Piazolo, S.; Harvey, J. Lightning Strikes as a Major Facilitator of Prebiotic Phosphorus Reduction on Early Earth. *Nat. Commun.* **2021**, *12* (1). https://doi.org/10.1038/s41467-021-21849-2.

(99) Hyo-Joong Kim; Steven A. Benner. Prebiotic Stereoselective Synthesis of Purine and Noncanonical Pyrimidine Nucleotide from Nucleobases and Phosphorylated Carbohydrates. *Proc. Natl. Acad. Sci.* **2017**, *114* (43), 11315–11320. https://doi.org/doi:10.1073/pnas.1710778114.

(100) Cafferty, B. J.; Fialho, D. M.; Khanam, J.; Krishnamurthy, R.; Hud, N. V. Spontaneous Formation and Base Pairing of Plausible Prebiotic Nucleotides in Water. *Nat. Commun.* **2016**, *7* (1), 11328. https://doi.org/10.1038/ncomms11328.

(101) Powner, M. W.; Gerland, B.; Sutherland, J. D. Synthesis of Activated Pyrimidine Ribonucleotides in Prebiotically Plausible Conditions. *Nature* **2009**, *459* (7244), 239–242. https://doi.org/10.1038/nature08013.

(102) Sidney Becker; Jonas Feldmann; Stefan Wiedemann; Hidenori Okamura; Christina Schneider; Katharina Iwan; Antony Crisp; Martin Rossa; Tynchtyk Amatov; Thomas Carell. Unified Prebiotically Plausible Synthesis of Pyrimidine and Purine RNA Ribonucleotides. *Science* **2019**, *366* (6461), 76–82. https://doi.org/doi:10.1126/science.aax2747.

(103) Ju, Y.; Zhang, H.; Wang, W.; Liu, Q.; Yu, K.; Kan, G.; Liu, L.; Jiang, J. Aqueous-Microdroplet-Driven Abiotic Synthesis of Ribonucleotides. *J. Phys. Chem. Lett.* **2022**, *13* (2), 567–573. https://doi.org/10.1021/acs.jpclett.1c03486.

(104) Xu, J.; Green, N. J.; Russell, D. A.; Liu, Z.; Sutherland, J. D. Prebiotic Photochemical Coproduction of Purine Ribo- and Deoxyribonucleosides. *J. Am. Chem. Soc.* **2021**, *143* (36), 14482–14486. https://doi.org/10.1021/jacs.1c07403.

(105) Chen, Q.-Q.; Zhao, Z.-R.; Wang, X. A Prebiotic Ribosylation of Pyrimidine Nucleobases Enabled by Metal Cations and Clay Minerals. *Life* **2021**, *11* (12), 1381. https://doi.org/10.3390/life11121381.

(106) Jerome, C. A.; Kim, H.-J.; Mojzsis, S. J.; Benner, S. A.; Biondi, E. Catalytic Synthesis of Polyribonucleic Acid on Prebiotic Rock Glasses. *Astrobiology* **2022**, *22* (6), 629–636. https://doi.org/10.1089/ast.2022.0027.

(107) Namani, T.; Snyder, S.; Eagan, J. M.; Bevilacqua, P. C.; Wesdemiotis, C.; Sahai, N. Amino Acid Specific Nonenzymatic Montmorillonite-Promoted RNA Polymerization. *ChemSystemsChem* **2021**, *3* (3). https://doi.org/10.1002/syst.202000060.

(108) Stephanie J. Zhang; Daniel Duzdevich; Dian Ding; Jack W. Szostak. Freeze-Thaw Cycles Enable a Prebiotically Plausible and Continuous Pathway from Nucleotide Activation to

Nonenzymatic RNA Copying. *Proc. Natl. Acad. Sci.* **2022**, *119* (17), e2116429119. https://doi.org/doi:10.1073/pnas.2116429119.

(109) Roberts, S. J.; Liu, Z.; Sutherland, J. D. Potentially Prebiotic Synthesis of Aminoacyl-RNA via a Bridging Phosphoramidate-Ester Intermediate. *J. Am. Chem. Soc.* **2022**, *144* (9), 4254–4259. https://doi.org/10.1021/jacs.2c00772.

(110) Deal, A. M.; Rapf, R. J.; Vaida, V. Water–Air Interfaces as Environments to Address the Water Paradox in Prebiotic Chemistry: A Physical Chemistry Perspective. *J. Phys. Chem. A* **2021**, *125* (23), 4929–4942. https://doi.org/10.1021/acs.jpca.1c02864.

(111) Ianeselli, A.; Atienza, M.; Kudella, P. W.; Gerland, U.; Mast, C. B.; Braun, D. Water Cycles in a Hadean CO2 Atmosphere Drive the Evolution of Long DNA. *Nat. Phys.* **2022**, *18* (5), 579–585. https://doi.org/10.1038/s41567-022-01516-z.

(112) Joshi, M. P.; Sawant, A. A.; Rajamani, S. Spontaneous Emergence of Membrane-Forming Protoamphiphiles from a Lipid–Amino Acid Mixture under Wet–Dry Cycles. *Chem. Sci.* **2021**, *12* (8), 2970–2978. https://doi.org/10.1039/d0sc05650b.

(113) Kwiatkowski, W.; Bomba, R.; Afanasyev, P.; Boehringer, D.; Riek, R.; Greenwald, J. Prebiotic Peptide Synthesis and Spontaneous Amyloid Formation Inside a Proto-Cellular Compartment. *Angew. Chem. Int. Ed.* **2021**, *60* (10), 5561–5568. https://doi.org/10.1002/anie.202015352.

(114) Oparin, A. I. *The Origin of Life*; Macmillan Comp.: N.Y, 1938.

(115) Haldane, J. B. S. The Origin of Life. *Ration. Annu.* **1929**, *148*, 3–10.

(116) Gilbert, W. Origin of Life: The RNA World. *Nature* **1986**, *319* (6055), 618–618. https://doi.org/10.1038/319618a0.

(117) Segré, D.; Ben-Eli, D.; Deamer, D. W.; Lancet, D. The Lipid World. *Orig. Life Evol. Biosph.* **2001**, *31* (1), 119–145. https://doi.org/10.1023/A:1006746807104.

(118) Tirard, S. J. B. S. Haldane and the Origin of Life. *J. Genet.* **2017**, *96* (5), 735–739. https://doi.org/10.1007/s12041-017-0831-6.

(119) Rich, A. On the Problems of Evolution and Biochemical Information Transfer. *Horiz. Biochem.* **1962**, 103–126.

(120) Neveu, M.; Kim, H.-J.; Benner, S. A. The "Strong" RNA World Hypothesis: Fifty Years Old. *Astrobiology* **2013**, *13* (4), 391–403. https://doi.org/10.1089/ast.2012.0868.

(121) Di Giulio, M. On the RNA World: Evidence in Favor of an Early Ribonucleopeptide World. *J. Mol. Evol.* **1997**, *45* (6), 571–578. https://doi.org/10.1007/PL00006261.

(122) Müller, F.; Escobar, L.; Xu, F.; Węgrzyn, E.; Nainytė, M.; Amatov, T.; Chan, C.-Y.; Pichler, A.; Carell, T. A Prebiotically Plausible Scenario of an RNA–Peptide World. *Nature* **2022**, *605* (7909), 279–284. https://doi.org/10.1038/s41586-022-04676-3.

(123) Lancet; Segrè; Kahana. Twenty Years of "Lipid World": A Fertile Partnership with David Deamer. *Life* **2019**, *9* (4), 77. https://doi.org/10.3390/life9040077.

(124) Saha, R.; Pohorille, A.; Chen, I. A. Molecular Crowding and Early Evolution. *Orig. Life Evol. Biospheres* **2014**, *44* (4), 319–324. https://doi.org/10.1007/s11084-014-9392-3.

(125) Daniel Segré; Dafna Ben-Eli; Doron Lancet. Compositional Genomes: Prebiotic Information Transfer in Mutually Catalytic Noncovalent Assemblies. *Proc. Natl. Acad. Sci.* **2000**, *97* (8), 4112–4117. https://doi.org/doi:10.1073/pnas.97.8.4112.

(126) Luisi, P. L.; Varela, F. J. Self-Replicating Micelles — A Chemical Version of a Minimal Autopoietic System. *Orig. Life Evol. Biosph.* **1989**, *19* (6), 633–643. https://doi.org/10.1007/bf01808123.

(127) Bachmann, P. A.; Walde, P.; Luisi, P. L.; Lang, J. Self-Replicating Reverse Micelles and Chemical Autopoiesis. *J. Am. Chem. Soc.* **1990**, *112* (22), 8200–8201. https://doi.org/10.1021/ja00178a073.

(128) Adamala, K.; Szostak, J. W. Competition between Model Protocells Driven by an Encapsulated Catalyst. *Nat. Chem.* **2013**, *5* (6), 495–501. https://doi.org/10.1038/nchem.1650.

(129) Chen, I. A.; Salehi-Ashtiani, K.; Szostak, J. W. RNA Catalysis in Model Protocell Vesicles. *J. Am. Chem. Soc.* **2005**, *127* (38), 13213–13219. https://doi.org/10.1021/ja051784p.

(130) Martin, W.; Baross, J.; Kelley, D.; Russell, M. J. Hydrothermal Vents and the Origin of Life. *Nat. Rev. Microbiol.* **2008**, *6* (11), 805–814. https://doi.org/10.1038/nrmicro1991.

(131) Von Damm, K. L.; Lilley, M. D.; Shanks, W. C.; Brockington, M.; Bray, A. M.; O'Grady, K. M.; Olson, E.; Graham, A.; Proskurowski, G. Extraordinary Phase Separation and Segregation in Vent Fluids from the Southern East Pacific Rise. *Earth Planet. Sci. Lett.* **2003**, *206* (3), 365–378. https://doi.org/10.1016/S0012-821X(02)01081-6.

(132) Kazem Kashefi; Derek R. Lovley. Extending the Upper Temperature Limit for Life. *Science* **2003**, *301* (5635), 934–934. https://doi.org/doi:10.1126/science.1086823.

(133) Kelley, D. S.; Karson, J. A.; Blackman, D. K.; Früh-Green, G. L.; Butterfield, D. A.; Lilley, M. D.; Olson, E. J.; Schrenk, M. O.; Roe, K. K.; Lebon, G. T.; Rivizzigno, P. An Off-Axis Hydrothermal Vent Field near the Mid-Atlantic Ridge at 30° N. *Nature* **2001**, *412* (6843), 145–149. https://doi.org/10.1038/35084000.

(134) Wächtershäuser, G. Groundworks for an Evolutionary Biochemistry: The Iron-Sulphur World. *Prog. Biophys. Mol. Biol.* **1992**, *58* (2), 85–201. https://doi.org/10.1016/0079-6107(92)90022-X.

(135) Mulkidjanian, A. Y.; Galperin, M. Y. On the Origin of Life in the Zinc World. 2. Validation of the Hypothesis on the Photosynthesizing Zinc Sulfide Edifices as Cradles of Life on Earth. *Biol. Direct* **2009**, *4* (1), 27. https://doi.org/10.1186/1745-6150-4-27.

(136) Deborah S. Kelley; Jeffrey A. Karson; Gretchen L. Früh-Green; Dana R. Yoerger; Timothy M. Shank; David A. Butterfield; John M. Hayes; Matthew O. Schrenk; Eric J. Olson; Giora Proskurowski; Mike Jakuba; Al Bradley; Ben Larson; Kristin Ludwig; Deborah Glickson; Kate Buckman; Alexander S. Bradley; William J. Brazelton; Kevin Roe; Mitch J. Elend; Adélie Delacour; Stefano M. Bernasconi; Marvin D. Lilley; John A. Baross; Roger E. Summons; Sean P. Sylva. A Serpentinite-Hosted Ecosystem: The Lost City Hydrothermal Field. *Science* **2005**, *307* (5714), 1428–1434. https://doi.org/doi:10.1126/science.1102556.

(137) Lecoeuvre, A.; Ménez, B.; Cannat, M.; Chavagnac, V.; Gérard, E. Microbial Ecology of the Newly Discovered Serpentinite-Hosted Old City Hydrothermal Field (Southwest Indian Ridge). *ISME J.* **2021**, *15* (3), 818–832. https://doi.org/10.1038/s41396-020-00816-7.

(138) Deamer, D.; Damer, B.; Kompanichenko, V. Hydrothermal Chemistry and the Origin of Cellular Life. *Astrobiology* **2019**, *19* (12), 1523–1537. https://doi.org/10.1089/ast.2018.1979.

(139) Follmann, H.; Brownson, C. Darwin's Warm Little Pond Revisited: From Molecules to the Origin of Life. *Naturwissenschaften* **2009**, *96* (11), 1265–1292. https://doi.org/10.1007/s00114-009-0602-1.

(140) Steller, L. H.; Van Kranendonk, M. J.; Wang, A. Dehydration Enhances Prebiotic Lipid Remodeling and Vesicle Formation in Acidic Environments. *ACS Cent. Sci.* **2022**, *8* (1), 132–139. https://doi.org/10.1021/acscentsci.1c01365.

(141) Damer, B. A Field Trip to the Archaean in Search of Darwin's Warm Little Pond. *Life* **2016**, *6* (2), 21. https://doi.org/10.3390/life6020021.

(142) Toppozini, L.; Dies, H.; Deamer, D. W.; Rheinstädter, M. C. Adenosine Monophosphate Forms Ordered Arrays in Multilamellar Lipid Matrices: Insights into Assembly of Nucleic Acid for Primitive Life. *PLoS ONE* **2013**, *8* (5), e62810. https://doi.org/10.1371/journal.pone.0062810.

(143) Hassenkam, T.; Damer, B.; Mednick, G.; Deamer, D. AFM Images of Viroid-Sized Rings That Self-Assemble from Mononucleotides through Wet–Dry Cycling: Implications for the Origin of Life. *Life* **2020**, *10* (12), 321. https://doi.org/10.3390/life10120321.

(144) Higgs, P. The Effect of Limited Diffusion and Wet–Dry Cycling on Reversible Polymerization Reactions: Implications for Prebiotic Synthesis of Nucleic Acids. *Life* **2016**, *6* (2), 24. https://doi.org/10.3390/life6020024.

(145) Fares, H. M.; Marras, A. E.; Ting, J. M.; Tirrell, M. V.; Keating, C. D. Impact of Wet-Dry Cycling on the Phase Behavior and Compartmentalization Properties of Complex Coacervates. *Nat. Commun.* **2020**, *11* (1), 5423. https://doi.org/10.1038/s41467-020-19184-z.

(146) Van Kranendonk, M. J.; Baumgartner, R.; Djokic, T.; Ota, T.; Steller, L.; Garbe, U.; Nakamura, E. Elements for the Origin of Life on Land: A Deep-Time Perspective from the Pilbara Craton of Western Australia. *Astrobiology* **2021**, *21* (1), 39–59. https://doi.org/10.1089/ast.2019.2107.

(147) Rosas, J. C.; Korenaga, J. Archaean Seafloors Shallowed with Age Due to Radiogenic Heating in the Mantle. *Nat. Geosci.* **2021**, *14* (1), 51–56. https://doi.org/10.1038/s41561-020-00673-1.

(148) Mizuuchi, R.; Ichihashi, N. Primitive Compartmentalization for the Sustainable Replication of Genetic Molecules. *Life* **2021**, *11* (3), 191. https://doi.org/10.3390/life11030191.

(149) Nader, S.; Sebastianelli, L.; Mansy, S. S. Protometabolism as Out-of-Equilibrium Chemistry. *Philos. Trans. R. Soc. Math. Phys. Eng. Sci.* **2022**, *380* (2227). https://doi.org/10.1098/rsta.2020.0423.

(150) Lane, N.; Martin, W. F. The Origin of Membrane Bioenergetics. *Cell* **2012**, *151* (7), 1406–1416. https://doi.org/10.1016/j.cell.2012.11.050.

(151) Fossum, J. O. Clay Nanolayer Encapsulation, Evolving from Origins of Life to Future Technologies. *Eur. Phys. J. Spec. Top.* **2020**, *229* (17–18), 2863–2879. https://doi.org/10.1140/epjst/e2020-000131-1.

(152) Sun, S.; Li, M.; Dong, F.; Wang, S.; Tian, L.; Mann, S. Chemical Signaling and Functional Activation in Colloidosome-Based Protocells. *Small* **2016**, *12* (14), 1920–1927. https://doi.org/10.1002/smll.201600243.

(153) Dobson, C. M.; Ellison, G. B.; Tuck, A. F.; Vaida, V. Atmospheric Aerosols as Prebiotic Chemical Reactors. *Proc. Natl. Acad. Sci.* **2000**, *97* (22), 11864–11868. https://doi.org/10.1073/pnas.200366897.

(154) Tekin, E.; Salditt, A.; Schwintek, P.; Wunnava, S.; Langlais, J.; Saenz, J.; Tang, D.; Schwille, P.; Mast, C.; Braun, D. Prebiotic Foam Environments to Oligomerize and Accumulate RNA. *ChemBioChem* **2022**, *23* (24). https://doi.org/10.1002/cbic.202200423.

(155) Attwater, J.; Wochner, A.; Pinheiro, V. B.; Coulson, A.; Holliger, P. Ice as a Protocellular Medium for RNA Replication. *Nat. Commun.* **2010**, *1* (1), 76. https://doi.org/10.1038/ncomms1076.

(156) Ghosh, B.; Bose, R.; Tang, T. Y. D. Can Coacervation Unify Disparate Hypotheses in the Origin of Cellular Life? *Curr. Opin. Colloid Interface Sci.* **2021**, *52*, 101415. https://doi.org/10.1016/j.cocis.2020.101415.

(157) Ianeselli, A.; Tetiker, D.; Stein, J.; Kühnlein, A.; Mast, C. B.; Braun, D.; Dora Tang, T. Y. Non-Equilibrium Conditions inside Rock Pores Drive Fission, Maintenance and Selection of Coacervate Protocells. *Nat. Chem.* **2022**, *14* (1), 32–39. https://doi.org/10.1038/s41557-021-00830-y.

(158) Nakashima, K. K.; Van Haren, M. H. I.; André, A. A. M.; Robu, I.; Spruijt, E. Active Coacervate Droplets Are Protocells That Grow and Resist Ostwald Ripening. *Nat. Commun.* **2021**, *12* (1). https://doi.org/10.1038/s41467-021-24111-x.

(159) Jin, X.; Lee, J.-E.; Schaefer, C.; Luo, X.; Wollman, A. J. M.; Payne-Dwyer, A. L.; Tian, T.; Zhang, X.; Chen, X.; Li, Y.; McLeish, T. C. B.; Leake, M. C.; Bai, F. Membraneless Organelles Formed by Liquid-Liquid Phase Separation Increase Bacterial Fitness. *Sci. Adv.* **2021**, *7* (43), eabh2929. https://doi.org/10.1126/sciadv.abh2929.

(160) Hirose, T.; Ninomiya, K.; Nakagawa, S.; Yamazaki, T. A Guide to Membraneless Organelles and Their Various Roles in Gene Regulation. *Nat. Rev. Mol. Cell Biol.* **2022**. https://doi.org/10.1038/s41580-022-00558-8.

(161) Podolsky, K. A.; Devaraj, N. K. Synthesis of Lipid Membranes for Artificial Cells. *Nat. Rev. Chem.* **2021**, *5* (10), 676–694. https://doi.org/10.1038/s41570-021-00303-3.

(162) Kurihara, K.; Okura, Y.; Matsuo, M.; Toyota, T.; Suzuki, K.; Sugawara, T. A Recursive Vesicle-Based Model Protocell with a Primitive Model Cell Cycle. *Nat. Commun.* **2015**, *6* (1), 8352. https://doi.org/10.1038/ncomms9352.

(163) Sarkar, S.; Das, S.; Dagar, S.; Joshi, M. P.; Mungi, C. V.; Sawant, A. A.; Patki, G. M.; Rajamani, S. Prebiological Membranes and Their Role in the Emergence of Early Cellular Life. *J. Membr. Biol.* **2020**, *253* (6), 589–608. https://doi.org/10.1007/s00232-020-00155-w.

(164) Deamer, D. W. The First Living Systems: A Bioenergetic Perspective. *Microbiol. Mol. Biol. Rev.* **1997**, *61* (2), 239–261. https://doi.org/10.1128/mmbr.61.2.239-261.1997.

(165) Dworkin, J. P.; Deamer, D. W.; Sandford, S. A.; Allamandola, L. J. Self-Assembling Amphiphilic Molecules: Synthesis in Simulated Interstellar/Precometary Ices. *Proc. Natl. Acad. Sci.* **2001**, *98* (3), 815–819. https://doi.org/10.1073/pnas.98.3.815.

(166) Jordan, S. F.; Nee, E.; Lane, N. Isoprenoids Enhance the Stability of Fatty Acid Membranes at the Emergence of Life Potentially Leading to an Early Lipid Divide. *Interface Focus* **2019**, *9* (6), 20190067. https://doi.org/10.1098/rsfs.2019.0067.

(167) Jordan, S. F.; Rammu, H.; Zheludev, I. N.; Hartley, A. M.; Maréchal, A.; Lane, N. Promotion of Protocell Self-Assembly from Mixed Amphiphiles at the Origin of Life. *Nat. Ecol. Evol.* **2019**, *3* (12), 1705–1714. https://doi.org/10.1038/s41559-019-1015-y.

(168) Kindt, J. T.; Szostak, J. W.; Wang, A. Bulk Self-Assembly of Giant, Unilamellar Vesicles. *ACS Nano* **2020**, *14* (11), 14627–14634. https://doi.org/10.1021/acsnano.0c03125.

(169) Salibi, E.; Peter, B.; Schwille, P.; Mutschler, H. Periodic Temperature Changes Drive the Proliferation of Self-Replicating RNAs in Vesicle Populations. *Nat. Commun.* **2023**, *14* (1), 1222. https://doi.org/10.1038/s41467-023-36940-z.

(170) Rubio-Sánchez, R.; O'Flaherty, D. K.; Wang, A.; Coscia, F.; Petris, G.; Di Michele, L.; Cicuta, P.; Bonfio, C. Thermally Driven Membrane Phase Transitions Enable Content Reshuffling in Primitive Cells. *J. Am. Chem. Soc.* **2021**, *143* (40), 16589–16598. https://doi.org/10.1021/jacs.1c06595.

(171) Czerniak, T.; Saenz James, P. Lipid Membranes Modulate the Activity of RNA through Sequence-Dependent Interactions. *Proc. Natl. Acad. Sci.* **2022**, *119* (4), e2119235119. https://doi.org/10.1073/pnas.2119235119.

(172) Kudella, P. W.; Preißinger, K.; Morasch, M.; Dirscherl, C. F.; Braun, D.; Wixforth, A.; Westerhausen, C. Fission of Lipid-Vesicles by Membrane Phase Transitions in Thermal Convection. *Sci. Rep.* **2019**, *9* (1). https://doi.org/10.1038/s41598-019-55110-0.

(173) Kriegler, S.; Herzog, M.; Oliva, R.; Gault, S.; Cockell, C. S.; Winter, R. Structural Responses of Model Biomembranes to Mars-Relevant Salts. *Phys. Chem. Chem. Phys.* **2021**, *23* (26), 14212–14223. https://doi.org/10.1039/D1CP02092G.

(174) Hanczyc, M. M.; Fujikawa, S. M.; Szostak, J. W. Experimental Models of Primitive Cellular Compartments: Encapsulation, Growth, and Division. *Science* **2003**, *302* (5645), 618–622. https://doi.org/10.1126/science.1089904.

(175) Fiore, M.; Maniti, O.; Girard-Egrot, A.; Monnard, P.-A.; Strazewski, P. Glass Microsphere-Supported Giant Vesicles for the Observation of Self-Reproduction of Lipid Boundaries. *Angew. Chem.* **2018**, *130* (1), 288–292. https://doi.org/10.1002/ange.201710708.

(176) Köksal, E. S.; Liese, S.; Kantarci, I.; Olsson, R.; Carlson, A.; Gözen, I. Nanotube-Mediated Path to Protocell Formation. *ACS Nano* **2019**, *13* (6), 6867–6878. https://doi.org/10.1021/acsnano.9b01646.

(177) Põldsalu, I.; Köksal, E. S.; Gözen, I. Mixed Fatty Acid-Phospholipid Protocell Networks. *Phys. Chem. Chem. Phys.* **2021**, *23* (47), 26948–26954. https://doi.org/10.1039/D1CP03832J.

(178) Köksal, E. S.; Põldsalu, I.; Friis, H.; Mojzsis, S. J.; Bizzarro, M.; Gözen, I. Spontaneous Formation of Prebiotic Compartment Colonies on Hadean Earth and Pre-Noachian Mars**. *ChemSystemsChem* **2022**, *4* (3). https://doi.org/10.1002/syst.202100040.

(179) Spustova, K.; Köksal, E. S.; Ainla, A.; Gözen, I. Subcompartmentalization and Pseudo-Division of Model Protocells. *Small* **2021**, *17* (2), 2005320. https://doi.org/10.1002/smll.202005320.

(180) Walton, C. R.; Shorttle, O. Scum of the Earth: A Hypothesis for Prebiotic Multi-Compartmentalised Environments. *Life* **2021**, *11* (9), 976. https://doi.org/10.3390/life11090976.

(181) Södergren, A. Role of Aquatic Surface Microlayer in the Dynamics of Nutrients and Organic Compounds in Lakes, with Implications for Their Ecotones. *Hydrobiologia* **1993**, *251* (1), 217–225. https://doi.org/10.1007/BF00007181.

(182) Colizzi, E. S.; Vroomans, R. M.; Merks, R. M. Evolution of Multicellularity by Collective Integration of Spatial Information. *eLife* **2020**, *9*, e56349. https://doi.org/10.7554/eLife.56349.

(183) Zepik, H. H.; Walde, P. Achievements and Challenges in Generating Protocell Models. *ChemBioChem* **2008**, *9* (17), 2771–2772. https://doi.org/10.1002/cbic.200800557.

(184) Toparlak, O. D.; Mansy, S. S. Progress in Synthesizing Protocells. *Exp. Biol. Med.* **2019**, *244* (4), 304–313. https://doi.org/10.1177/1535370218816657.

(185) Gao, N.; Mann, S. Membranized Coacervate Microdroplets: From Versatile Protocell Models to Cytomimetic Materials. *Acc. Chem. Res.* **2023**, *56* (3), 297–307. https://doi.org/10.1021/acs.accounts.2c00696.

(186) Green, D. W.; Watson, J. A.; Ben-Nissan, B.; Watson, G. S.; Stamboulis, A. Synthetic Tissue Engineering with Smart, Cytomimetic Protocells. *Biomaterials* **2021**, *276*, 120941. https://doi.org/10.1016/j.biomaterials.2021.120941.

(187) Toparlak, Ö. D.; Wang, A.; Mansy, S. S. Population-Level Membrane Diversity Triggers Growth and Division of Protocells. *JACS Au* **2021**, *1* (5), 560–568. https://doi.org/10.1021/jacsau.0c00079.

(188) Tian, L.; Li, M.; Patil, A. J.; Drinkwater, B. W.; Mann, S. Artificial Morphogen-Mediated Differentiation in Synthetic Protocells. *Nat. Commun.* **2019**, *10* (1), 3321. https://doi.org/10.1038/s41467-019-11316-4.

(189) Llopis-Lorente, A.; Buddingh', B. C.; Martínez-Máñez, R.; van Hest, J. C. M.; Abdelmohsen, L. K. E. Quorum Sensing Communication between Lipid-Based Artificial Cells. *Chem. Commun.* **2023**, *59* (5), 579–582. https://doi.org/10.1039/D2CC05367E.

(190) Niederholtmeyer, H.; Chaggan, C.; Devaraj, N. K. Communication and Quorum Sensing in Non-Living Mimics of Eukaryotic Cells. *Nat. Commun.* **2018**, *9* (1), 5027. https://doi.org/10.1038/s41467-018-07473-7.

(191) Alcinesio, A.; Meacock, O. J.; Allan, R. G.; Monico, C.; Restrepo Schild, V.; Cazimoglu, I.; Cornall, M. T.; Krishna Kumar, R.; Bayley, H. Controlled Packing and Single-Droplet Resolution of 3D-Printed Functional Synthetic Tissues. *Nat. Commun.* **2020**, *11* (1), 2105. https://doi.org/10.1038/s41467-020-15953-y.

(192) Ramsay, K.; Levy, J.; Gobbo, P.; Elvira, K. S. Programmed Assembly of Bespoke Prototissues on a Microfluidic Platform. *Lab. Chip* **2021**, *21* (23), 4574–4585. https://doi.org/10.1039/D1LC00602A.

(193) Ugrinic, M.; deMello, A.; Tang, T.-Y. D. Microfluidic Tools for Bottom-Up Synthetic Cellularity. *Chem* **2019**, *5* (7), 1727–1742. https://doi.org/10.1016/j.chempr.2019.03.012.

(194) Deng, N.-N.; Yelleswarapu, M.; Huck, W. T. S. Monodisperse Uni- and Multicompartment Liposomes. *J. Am. Chem. Soc.* **2016**, *138* (24), 7584–7591. https://doi.org/10.1021/jacs.6b02107.

(195) Bolognesi, G.; Friddin, M. S.; Salehi-Reyhani, A.; Barlow, N. E.; Brooks, N. J.; Ces, O.; Elani, Y. Sculpting and Fusing Biomimetic Vesicle Networks Using Optical Tweezers. *Nat. Commun.* **2018**, *9* (1), 1882. https://doi.org/10.1038/s41467-018-04282-w.

(196) Li, Q.; Li, S.; Zhang, X.; Xu, W.; Han, X. Programmed Magnetic Manipulation of Vesicles into Spatially Coded Prototissue Architectures Arrays. *Nat. Commun.* **2020**, *11* (1), 232. https://doi.org/10.1038/s41467-019-14141-x.

(197) Zhang, X.; Li, C.; Liu, F.; Mu, W.; Ren, Y.; Yang, B.; Han, X. High-Throughput Production of Functional Prototissues Capable of Producing NO for Vasodilation. *Nat. Commun.* **2022**, *13* (1), 2148. https://doi.org/10.1038/s41467-022-29571-3.

(198) Wang, X.; Tian, L.; Du, H.; Li, M.; Mu, W.; Drinkwater, B. W.; Han, X.; Mann, S. Chemical Communication in Spatially Organized Protocell Colonies and Protocell/Living Cell Micro-Arrays. *Chem. Sci.* **2019**, *10* (41), 9446–9453. https://doi.org/10.1039/c9sc04522h.

(199) Arulkumaran, N.; Singer, M.; Howorka, S.; Burns, J. R. Creating Complex Protocells and Prototissues Using Simple DNA Building Blocks. *Nat. Commun.* **2023**, *14* (1), 1314. https://doi.org/10.1038/s41467-023-36875-5.

(200) Heidari, A.; Sentürk, O. I.; Yang, S.; Joesaar, A.; Gobbo, P.; Mann, S.; de Greef, T. F. A.; Wegner, S. V. Orthogonal Light-Dependent Membrane Adhesion Induces Social Self-Sorting and Member-Specific DNA Communication in Synthetic Cell Communities. *Small* **2023**, 2206474. https://doi.org/10.1002/smll.202206474.

(201) Carrara, P.; Stano, P.; Luisi, P. L. Giant Vesicles “Colonies”: A Model for Primitive Cell Communities. *ChemBioChem* **2012**, *13* (10), 1497–1502. https://doi.org/10.1002/cbic.201200133.

(202) Casas-Ferrer, L.; Brisson, A.; Massiera, G.; Casanellas, L. Design of Vesicle Prototissues as a Model for Cellular Tissues. *Soft Matter* **2021**, *17* (19), 5061–5072. https://doi.org/10.1039/D1SM00336D.

(203) Omidvar, R.; Römer, W. Glycan-Decorated Protocells: Novel Features for Rebuilding Cellular Processes. *Interface Focus* **2019**, *9* (2), 20180084. https://doi.org/10.1098/rsfs.2018.0084.

(204) Šuštar, V.; Zelko, J.; Lopalco, P.; Lobasso, S.; Ota, A.; Ulrih, N. P.; Corcelli, A.; Kralj-Iglič, V. Morphology, Biophysical Properties and Protein-Mediated Fusion of Archaeosomes. *PLoS ONE* **2012**, *7* (7), e39401. https://doi.org/10.1371/journal.pone.0039401.

(205) Villringer, S.; Madl, J.; Sych, T.; Manner, C.; Imberty, A.; Römer, W. Lectin-Mediated Protocell Crosslinking to Mimic Cell-Cell Junctions and Adhesion. *Sci. Rep.* **2018**, *8* (1), 1932. https://doi.org/10.1038/s41598-018-20230-6.

(206) Sott, K.; Lobovkina, T.; Lizana, L.; Tokarz, M.; Bauer, B.; Konkoli, Z.; Orwar, O. Controlling Enzymatic Reactions by Geometry in a Biomimetic Nanoscale Network. *Nano Lett.* **2006**, *6* (2), 209–214. https://doi.org/10.1021/nl052078p.

(207) Spustova, K.; Katke, C.; Pedrueza Villalmanzo, E.; Ryskulov, R.; Kaplan, C. N.; Gözen, I. Colony-like Protocell Superstructures. *bioRxiv* **2021**, 2021.09.16.460583. https://doi.org/10.1101/2021.09.16.460583.

(208) Nielsen, M. S.; Nygaard Axelsen, L.; Sorgen, P. L.; Verma, V.; Delmar, M.; Holstein-Rathlou, N. Gap Junctions. In *Comprehensive Physiology*; Terjung, R., Ed.; Wiley, 2012; pp 1981–2035. https://doi.org/10.1002/cphy.c110051.

(209) McLean, B. G.; Hempel, F. D.; Zambryski, P. C. Plant Intercellular Communication via Plasmodesmata. *Plant Cell* **1997**, *9* (7), 1043–1054. https://doi.org/10.1105/tpc.9.7.1043.

(210) Bloemendal, S.; Kück, U. Cell-to-Cell Communication in Plants, Animals, and Fungi: A Comparative Review. *Naturwissenschaften* **2013**, *100* (1), 3–19. https://doi.org/10.1007/s00114-012-0988-z.

(211) Mayor, R.; Carmona-Fontaine, C. Keeping in Touch with Contact Inhibition of Locomotion. *Trends Cell Biol.* **2010**, *20* (6), 319–328. https://doi.org/10.1016/j.tcb.2010.03.005.

(212) Roycroft, A.; Mayor, R. Molecular Basis of Contact Inhibition of Locomotion. *Cell. Mol. Life Sci.* **2016**, *73* (6), 1119–1130. https://doi.org/10.1007/s00018-015-2090-0.

(213) Stramer, B.; Mayor, R. Mechanisms and in Vivo Functions of Contact Inhibition of Locomotion. *Nat. Rev. Mol. Cell Biol.* **2017**, *18* (1), 43–55. https://doi.org/10.1038/nrm.2016.118.

(214) Ladoux, B.; Mège, R.-M. Mechanobiology of Collective Cell Behaviours. *Nat. Rev. Mol. Cell Biol.* **2017**, *18* (12), 743–757. https://doi.org/10.1038/nrm.2017.98.

(215) Van Gestel, J.; Bareia, T.; Tenennbaum, B.; Dal Co, A.; Guler, P.; Aframian, N.; Puyesky, S.; Grinberg, I.; D’Souza, G. G.; Erez, Z.; Ackermann, M.; Eldar, A. Short-Range Quorum Sensing Controls Horizontal Gene Transfer at Micron Scale in Bacterial Communities. *Nat. Commun.* **2021**, *12* (1). https://doi.org/10.1038/s41467-021-22649-4.

(216) Yashiroda, Y.; Yoshida, M. Intraspecies Cell–Cell Communication in Yeast. *FEMS Yeast Res.* **2019**, *19* (7), foz071. https://doi.org/10.1093/femsyr/foz071.

(217) Palková, Z.; Janderová, B.; Gabriel, J.; Zikánová, B.; Pospíŝek, M.; Forstová, J. Ammonia Mediates Communication between Yeast Colonies. *Nature* **1997**, *390* (6659), 532–536. https://doi.org/10.1038/37398.

(218) Prindle, A.; Liu, J.; Asally, M.; Ly, S.; Garcia-Ojalvo, J.; Süel, G. M. Ion Channels Enable Electrical Communication in Bacterial Communities. *Nature* **2015**, *527* (7576), 59–63. https://doi.org/10.1038/nature15709.

(219) Bavaharan, A.; Skilbeck, C. Electrical Signalling in Prokaryotes and Its Convergence with Quorum Sensing in *Bacillus*. *BioEssays* **2022**, *44* (4), 2100193. https://doi.org/10.1002/bies.202100193.

(220) Hug, I.; Deshpande, S.; Sprecher, K. S.; Pfohl, T.; Jenal, U. Second Messenger–Mediated Tactile Response by a Bacterial Rotary Motor. *Science* **2017**, *358* (6362), 531–534. https://doi.org/10.1126/science.aan5353.

(221) Liu, W.; Tokuyasu, T. A.; Fu, X.; Liu, C. The Spatial Organization of Microbial Communities during Range Expansion. *Curr. Opin. Microbiol.* **2021**, *63*, 109–116. https://doi.org/10.1016/j.mib.2021.07.005.

(222) Xiong, L.; Cao, Y.; Cooper, R.; Rappel, W.-J.; Hasty, J.; Tsimring, L. Flower-like Patterns in Multi-Species Bacterial Colonies. *eLife* **2020**, *9*. https://doi.org/10.7554/elife.48885.

(223) Dubey, G. P.; Ben-Yehuda, S. Intercellular Nanotubes Mediate Bacterial Communication. *Cell* **2011**, *144* (4), 590–600. https://doi.org/10.1016/j.cell.2011.01.015.

(224) Pospíšil, J.; Vítovská, D.; Kofroňová, O.; Muchová, K.; Šanderová, H.; Hubálek, M.; Šiková, M.; Modrák, M.; Benada, O.; Barák, I.; Krásný, L. Bacterial Nanotubes as a Manifestation of Cell Death. *Nat. Commun.* **2020**, *11* (1). https://doi.org/10.1038/s41467-020-18800-2.

(225) Baidya, A. K.; Rosenshine, I.; Ben-Yehuda, S. Donor-Delivered Cell Wall Hydrolases Facilitate Nanotube Penetration into Recipient Bacteria. *Nat. Commun.* **2020**, *11* (1). https://doi.org/10.1038/s41467-020-15605-1.

(226) Patel, N.; Yamada, Y.; Azam, F. Bacterial Nanotubes as Intercellular Linkages in Marine Assemblages. *Front. Mar. Sci.* **2021**, *8*, 1817. https://doi.org/10.3389/fmars.2021.768814.

(227) Peralta, B.; Gil-Carton, D.; Castaño-Díez, D.; Bertin, A.; Boulogne, C.; Oksanen, H. M.; Bamford, D. H.; Abrescia, N. G. A. Mechanism of Membranous Tunnelling Nanotube Formation in Viral Genome Delivery. *PLoS Biol.* **2013**, *11* (9), e1001667. https://doi.org/10.1371/journal.pbio.1001667.

(228) Sowinski, S.; Jolly, C.; Berninghausen, O.; Purbhoo, M. A.; Chauveau, A.; Köhler, K.; Oddos, S.; Eissmann, P.; Brodsky, F. M.; Hopkins, C.; Önfelt, B.; Sattentau, Q.; Davis, D. M. Membrane Nanotubes Physically Connect T Cells over Long Distances Presenting a Novel Route for HIV-1 Transmission. *Nat. Cell Biol.* **2008**, *10* (2), 211–219. https://doi.org/10.1038/ncb1682.

(229) Ma, L.; Li, Y.; Peng, J.; Wu, D.; Zhao, X.; Cui, Y.; Chen, L.; Yan, X.; Du, Y.; Yu, L. Discovery of the Migrasome, an Organelle Mediating Release of Cytoplasmic Contents during Cell Migration. *Cell Res.* **2015**, *25* (1), 24–38. https://doi.org/10.1038/cr.2014.135.

(230) Liu, J.; Soler, N.; Gorlas, A.; Cvirkaite-Krupovic, V.; Krupovic, M.; Forterre, P. Extracellular Membrane Vesicles and Nanotubes in Archaea. *microLife* **2021**, *2*. https://doi.org/10.1093/femsml/uqab007.

(231) Rustom, A.; Saffrich, R.; Markovic, I.; Walther, P.; Gerdes, H.-H. Nanotubular Highways for Intercellular Organelle Transport. *Science* **2004**, *303* (5660), 1007–1010. https://doi.org/10.1126/science.1093133.

(232) Cordero Cervantes, D.; Zurzolo, C. Peering into Tunneling Nanotubes—The Path Forward. *EMBO J.* **2021**, *40* (8), e105789. https://doi.org/10.15252/embj.2020105789.

(233) Matko, J.; Toth, E. A. Membrane Nanotubes Are Ancient Machinery for Cell-to-Cell Communication and Transport. Their Interference with the Immune System. *Biol. Futura* **2021**, *72* (1), 25–36. https://doi.org/10.1007/s42977-020-00062-0.

(234) Driscoll, J.; Gondaliya, P.; Patel, T. Tunneling Nanotube-Mediated Communication: A Mechanism of Intercellular Nucleic Acid Transfer. *Int. J. Mol. Sci.* **2022**, *23* (10), 5487. https://doi.org/10.3390/ijms23105487.

(235) Gözen, I.; Dommersnes, P. Biological Lipid Nanotubes and Their Potential Role in Evolution. *Eur. Phys. J. Spec. Top.* **2020**, *229* (17–18), 2843–2862. https://doi.org/10.1140/epjst/e2020-000130-7.

(236) Wang, X.; Gerdes, H.-H. Long-Distance Electrical Coupling via Tunneling Nanotubes. *Biochim. Biophys. Acta BBA - Biomembr.* **2012**, *1818* (8), 2082–2086. https://doi.org/10.1016/j.bbamem.2011.09.002.

(237) Davis, D. M.; Sowinski, S. Membrane Nanotubes: Dynamic Long-Distance Connections between Animal Cells. *Nat. Rev. Mol. Cell Biol.* **2008**, *9* (6), 431–436. https://doi.org/10.1038/nrm2399.

(238) Chang, M.; Lee, O.; Bu, G.; Oh, J.; Yunn, N.-O.; Ryu, S. H.; Kwon, H.-B.; Kolomeisky, A. B.; Shim, S.-H.; Doh, J.; Jeon, J.-H.; Lee, J.-B. Formation of Cellular Close-Ended Tunneling Nanotubes through Mechanical Deformation. *Sci. Adv.* **2022**, *8* (13), eabj3995. https://doi.org/10.1126/sciadv.abj3995.

(239) Jana, A.; Ladner, K.; Lou, E.; Nain, A. S. Tunneling Nanotubes between Cells Migrating in ECM Mimicking Fibrous Environments. *Cancers* **2022**, *14* (8), 1989. https://doi.org/10.3390/cancers14081989.

(240) Jansens, R. J. J.; Tishchenko, A.; Favoreel, H. W. Bridging the Gap: Virus Long-Distance Spread via Tunneling Nanotubes. *J. Virol.* **2020**, *94* (8), e02120-19. https://doi.org/10.1128/JVI.02120-19.

(241) Eugenin, E. A.; Gaskill, P. J.; Berman, J. W. Tunneling Nanotubes (TNT) Are Induced by HIV-Infection of Macrophages: A Potential Mechanism for Intercellular HIV Trafficking. *Cell. Immunol.* **2009**, *254* (2), 142–148. https://doi.org/10.1016/j.cellimm.2008.08.005.

(242) Pepe, A.; Pietropaoli, S.; Vos, M.; Barba-Spaeth, G.; Zurzolo, C. Tunneling Nanotubes Provide a Route for SARS-CoV-2 Spreading. *Sci. Adv.* **2022**, *8* (29), eabo0171. https://doi.org/10.1126/sciadv.abo0171.

(243) Vincent, A. E.; Turnbull, D. M.; Eisner, V.; Hajnóczky, G.; Picard, M. Mitochondrial Nanotunnels. *Trends Cell Biol.* **2017**, *27* (11), 787–799. https://doi.org/10.1016/j.tcb.2017.08.009.

(244) Huang, Y.; Zucker, B.; Zhang, S.; Elias, S.; Zhu, Y.; Chen, H.; Ding, T.; Li, Y.; Sun, Y.; Lou, J.; Kozlov, M. M.; Yu, L. Migrasome Formation Is Mediated by Assembly of Micron-Scale Tetraspanin Macrodomains. *Nat Cell Biol* **2019**, *21* (8), 991–1002. https://doi.org/10.1038/s41556-019-0367-5.

(245) Fan, C.; Shi, X.; Zhao, K.; Wang, L.; Shi, K.; Liu, Y.-J.; Li, H.; Ji, B.; Jiu, Y. Cell Migration Orchestrates Migrasome Formation by Shaping Retraction Fibers. *J. Cell Biol.* **2022**, *221* (4). https://doi.org/10.1083/jcb.202109168.

(246) Zhu, M.; Zou, Q.; Huang, R.; Li, Y.; Xing, X.; Fang, J.; Ma, L.; Li, L.; Yang, X.; Yu, L. Lateral Transfer of mRNA and Protein by Migrasomes Modifies the Recipient Cells. *Cell Res.* **2021**, *31* (2), 237–240. https://doi.org/10.1038/s41422-020-00415-3.

(247) Imachi, H.; Nobu, M. K.; Nakahara, N.; Morono, Y.; Ogawara, M.; Takaki, Y.; Takano, Y.; Uematsu, K.; Ikuta, T.; Ito, M.; Matsui, Y.; Miyazaki, M.; Murata, K.; Saito, Y.; Sakai, S.; Song, C.; Tasumi, E.; Yamanaka, Y.; Yamaguchi, T.; Kamagata, Y.; Tamaki, H.; Takai, K. Isolation of an Archaeon at the Prokaryote–Eukaryote Interface. *Nature* **2020**, *577* (7791), 519–525. https://doi.org/10.1038/s41586-019-1916-6.

(248) Sivabalasarma, S.; Wetzel, H.; Nußbaum, P.; van der Does, C.; Beeby, M.; Albers, S.-V. Analysis of Cell–Cell Bridges in Haloferax Volcanii Using Electron Cryo-Tomography Reveal a

Continuous Cytoplasm and S-Layer. *Front. Microbiol.* **2021**, *11*, 612239. https://doi.org/10.3389/fmicb.2020.612239.

(249) Marguet, E.; Gaudin, M.; Gauliard, E.; Fourquaux, I.; le Blond du Plouy, S.; Matsui, I.; Forterre, P. Membrane Vesicles, Nanopods and/or Nanotubes Produced by Hyperthermophilic Archaea of the Genus *Thermococcus*. *Biochem. Soc. Trans.* **2013**, *41* (1), 436–442. https://doi.org/10.1042/BST20120293.

(250) Czolkos, I.; Jesorka, A.; Orwar, O. Molecular Phospholipid Films on Solid Supports. *Soft Matter* **2011**, *7* (10), 4562. https://doi.org/10.1039/c0sm01212b.

(251) Blossey, R. Self-Cleaning Surfaces — Virtual Realities. *Nat. Mater.* **2003**, *2* (5), 301–306. https://doi.org/10.1038/nmat856.

(252) Roiter, Y.; Ornatska, M.; Rammohan, A. R.; Balakrishnan, J.; Heine, D. R.; Minko, S. Interaction of Lipid Membrane with Nanostructured Surfaces. *Langmuir* **2009**, *25* (11), 6287–6299. https://doi.org/10.1021/la900119a.

(253) Goodchild, J. A.; Walsh, D. L.; Connell, S. D. Nanoscale Substrate Roughness Hinders Domain Formation in Supported Lipid Bilayers. *Langmuir* **2019**, *35* (47), 15352–15363. https://doi.org/10.1021/acs.langmuir.9b01990.

(254) Jõemetsa, S.; Spustova, K.; Kustanovich, K.; Ainla, A.; Schindler, S.; Eigler, S.; Lobovkina, T.; Lara-Avila, S.; Jesorka, A.; Gözen, I. Molecular Lipid Films on Microengineering Materials. *Langmuir* **2019**, *35* (32), 10286–10298. https://doi.org/10.1021/acs.langmuir.9b01120.

(255) Pfeiffer, I.; Seantier, B.; Petronis, S.; Sutherland, D.; Kasemo, B.; Zäch, M. Influence of Nanotopography on Phospholipid Bilayer Formation on Silicon Dioxide. *J. Phys. Chem. B* **2008**, *112* (16), 5175–5181. https://doi.org/10.1021/jp710614m.

(256) Lombard, J.; López-García, P.; Moreira, D. The Early Evolution of Lipid Membranes and the Three Domains of Life. *Nat. Rev. Microbiol.* **2012**, *10* (7), 507–515. https://doi.org/10.1038/nrmicro2815.

(257) Martin, H. S.; Podolsky, K. A.; Devaraj, N. K. Probing the Role of Chirality in Phospholipid Membranes. *ChemBioChem* **2021**, *22* (22), 3148–3157. https://doi.org/10.1002/cbic.202100232.

(258) Cevc, G. How Membrane Chain-Melting Phase-Transition Temperature Is Affected by the Lipid Chain Asymmetry and Degree of Unsaturation: An Effective Chain-Length Model. *Biochemistry* **1991**, *30* (29), 7186–7193. https://doi.org/10.1021/bi00243a021.

(259) Paradies, G.; Paradies, V.; Ruggiero, F. M.; Petrosillo, G. Role of Cardiolipin in Mitochondrial Function and Dynamics in Health and Disease: Molecular and Pharmacological Aspects. *Cells* **2019**, *8* (7). https://doi.org/10.3390/cells8070728.

(260) van Meer, G.; Hoetzl, S. Sphingolipid Topology and the Dynamic Organization and Function of Membrane Proteins. *FEBS Lett.* **2010**, *584* (9), 1800–1805. https://doi.org/10.1016/j.febslet.2009.10.020.

(261) Zhang, Y.; Li, Q.; Dong, M.; Han, X. Effect of Cholesterol on the Fluidity of Supported Lipid Bilayers. *Colloids Surf. B Biointerfaces* **2020**, *196*, 111353. https://doi.org/10.1016/j.colsurfb.2020.111353.

(262) Chakraborty, S.; Doktorova, M.; Molugu, T. R.; Heberle, F. A.; Scott, H. L.; Dzikovski, B.; Nagao, M.; Stingaciu, L.-R.; Standaert, R. F.; Barrera, F. N.; Katsaras, J.; Khelashvili, G.; Brown, M. F.; Ashkar, R. How Cholesterol Stiffens Unsaturated Lipid Membranes. *Proc. Natl. Acad. Sci.* **2020**, *117* (36), 21896–21905. https://doi.org/10.1073/pnas.2004807117.

(263) Bertani, B.; Ruiz, N. Function and Biogenesis of Lipopolysaccharides. *EcoSal Plus* **2018**, *8* (1), ecosalplus.ESP-0001-2018. https://doi.org/10.1128/ecosalplus.ESP-0001-2018.

(264) Herrmann, M.; Schneck, E.; Gutsmann, T.; Brandenburg, K.; Tanaka, M. Bacterial Lipopolysaccharides Form Physically Cross-Linked, Two-Dimensional Gels in the Presence of Divalent Cations. *Soft Matter* **2015**, *11* (30), 6037–6044. https://doi.org/10.1039/C5SM01002K.

(265) Jacquemet, A.; Barbeau, J.; Lemiègre, L.; Benvegnu, T. Archaeal Tetraether Bipolar Lipids: Structures, Functions and Applications. *Biochimie* **2009**, *91* (6), 711–717. https://doi.org/10.1016/j.biochi.2009.01.006.

(266) Galimzyanov, T. R.; Kuzmin, P. I.; Pohl, P.; Akimov, S. A. Elastic Deformations of Bolalipid Membranes. *Soft Matter* **2016**, *12* (8), 2357–2364. https://doi.org/10.1039/C5SM02635K.

(267) Caforio, A.; Driessen, A. J. M. Archaeal Phospholipids: Structural Properties and Biosynthesis. *Biochim. Biophys. Acta BBA - Mol. Cell Biol. Lipids* **2017**, *1862* (11), 1325–1339. https://doi.org/10.1016/j.bbalip.2016.12.006.

(268) Koga, Y. Thermal Adaptation of the Archaeal and Bacterial Lipid Membranes. *Archaea* **2012**, *2012*, 1–6. https://doi.org/10.1155/2012/789652.

(269) Simard, J. R.; Pillai, B. K.; Hamilton, J. A. Fatty Acid Flip-Flop in a Model Membrane Is Faster Than Desorption into the Aqueous Phase. *Biochemistry* **2008**, *47* (35), 9081–9089. https://doi.org/10.1021/bi800697q.

(270) Budin, I.; Szostak, J. W. Physical Effects Underlying the Transition from Primitive to Modern Cell Membranes. *Proc. Natl. Acad. Sci.* **2011**, *108* (13), 5249–5254. https://doi.org/10.1073/pnas.1100498108.

(271) Mansy, S. Model Protocells from Single-Chain Lipids. *Int. J. Mol. Sci.* **2009**, *10* (3), 835–843. https://doi.org/10.3390/ijms10030835.

(272) Hoekstra, S. A. D. Cationic Lipid-Mediated Transfectionin Vitroandin Vivo. *Mol. Membr. Biol.* **2001**, *18* (2), 129–143. https://doi.org/10.1080/09687680110057237.

(273) Tenchov, R.; Bird, R.; Curtze, A. E.; Zhou, Q. Lipid Nanoparticles—From Liposomes to mRNA Vaccine Delivery, a Landscape of Research Diversity and Advancement. *ACS Nano* **2021**, *15* (11), 16982–17015. https://doi.org/10.1021/acsnano.1c04996.

(274) Han, X.; Zhang, H.; Butowska, K.; Swingle, K. L.; Alameh, M.-G.; Weissman, D.; Mitchell, M. J. An Ionizable Lipid Toolbox for RNA Delivery. *Nat. Commun.* **2021**, *12* (1), 7233. https://doi.org/10.1038/s41467-021-27493-0.

(275) Vogler, E. A. Structure and Reactivity of Water at Biomaterial Surfaces. *Adv. Colloid Interface Sci.* **1998**, *74* (1–3), 69–117. https://doi.org/10.1016/S0001-8686(97)00040-7.

(276) Kumar, V. V. Complementary Molecular Shapes and Additivity of the Packing Parameter of Lipids. *Proc. Natl. Acad. Sci.* **1991**, *88* (2), 444–448. https://doi.org/10.1073/pnas.88.2.444.

(277) Kobierski, J.; Wnętrzak, A.; Chachaj-Brekiesz, A.; Dynarowicz-Latka, P. Predicting the Packing Parameter for Lipids in Monolayers with the Use of Molecular Dynamics. *Colloids Surf. B Biointerfaces* **2022**, *211*, 112298. https://doi.org/10.1016/j.colsurfb.2021.112298.

(278) Helfrich, W. Effect of Thermal Undulations on the Rigidity of Fluid Membranes and Interfaces. *J. Phys.* **1985**, *46* (7), 1263–1268. https://doi.org/10.1051/jphys:019850046070126300.

(279) Rawicz, W.; Olbrich, K. C.; McIntosh, T.; Needham, D.; Evans, E. Effect of Chain Length and Unsaturation on Elasticity of Lipid Bilayers. *Biophys. J.* **2000**, *79* (1), 328–339. https://doi.org/10.1016/S0006-3495(00)76295-3.

(280) Faizi, H. A.; Frey, S. L.; Steinkühler, J.; Dimova, R.; Vlahovska, P. M. Bending Rigidity of Charged Lipid Bilayer Membranes. *Soft Matter* **2019**, *15* (29), 6006–6013. https://doi.org/10.1039/C9SM00772E.

(281) Różycki, B.; Lipowsky, R. Spontaneous Curvature of Bilayer Membranes from Molecular Simulations: Asymmetric Lipid Densities and Asymmetric Adsorption. *J. Chem. Phys.* **2015**, *142* (5), 054101. https://doi.org/10.1063/1.4906149.

(282) McMahon, H. T.; Gallop, J. L. Membrane Curvature and Mechanisms of Dynamic Cell Membrane Remodelling. *Nature* **2005**, *438* (7068), 590–596. https://doi.org/10.1038/nature04396.

(283) Hu, M.; Briguglio, J. J.; Deserno, M. Determining the Gaussian Curvature Modulus of Lipid Membranes in Simulations. *Biophys. J.* **2012**, *102* (6), 1403–1410. https://doi.org/10.1016/j.bpj.2012.02.013.

(284) Gözen, I.; Dommersnes, P.; Czolkos, I.; Jesorka, A.; Lobovkina, T.; Orwar, O. Fractal Avalanche Ruptures in Biological Membranes. *Nat. Mater.* **2010**, *9* (11), 908–912. https://doi.org/10.1038/nmat2854.

(285) Antonietti, M.; Förster, S. Vesicles and Liposomes: A Self-Assembly Principle Beyond Lipids. *Adv. Mater.* **2003**, *15* (16), 1323–1333. https://doi.org/10.1002/adma.200300010.

(286) Karatekin, E.; Sandre, O.; Brochard-Wyart, F. Transient Pores in Vesicles. *Polym Int* **2003**, *52* (4), 486–493. https://doi.org/10.1002/pi.1007.

(287) Karatekin, E.; Sandre, O.; Guitouni, H.; Borghi, N.; Puech, P.-H.; Brochard-Wyart, F. Cascades of Transient Pores in Giant Vesicles: Line Tension and Transport. *Biophys. J.* **2003**, *84* (3), 1734–1749. https://doi.org/10.1016/S0006-3495(03)74981-9.

(288) Zhelev, D. V.; Needham, D. Tension-Stabilized Pores in Giant Vesicles: Determination of Pore Size and Pore Line Tension. *Biochim. Biophys. Acta BBA - Biomembr.* **1993**, *1147* (1), 89–104. https://doi.org/10.1016/0005-2736(93)90319-U.

(289) Jeppesen, D. K.; Zhang, Q.; Franklin, J. L.; Coffey, R. J. Extracellular Vesicles and Nanoparticles: Emerging Complexities. *Trends Cell Biol.* **2023**, S0962892423000053. https://doi.org/10.1016/j.tcb.2023.01.002.

(290) Dimova, R.; Marques, C. *The Giant Vesicle Book*; CRC Press, 2019.

(291) Klein, S.; Wimmer, B. H.; Winter, S. L.; Kolovou, A.; Laketa, V.; Chlanda, P. Post-Correlation on-Lamella Cryo-CLEM Reveals the Membrane Architecture of Lamellar Bodies. *Commun. Biol.* **2021**, *4* (1), 137. https://doi.org/10.1038/s42003-020-01567-z.

(292) Schmitz, G.; Müller, G. Structure and Function of Lamellar Bodies, Lipid-Protein Complexes Involved in Storage and Secretion of Cellular Lipids. *J. Lipid Res.* **1991**, *32* (10), 1539–1570. https://doi.org/10.1016/S0022-2275(20)41642-6.

(293) Thiam, A. R.; Farese Jr, R. V.; Walther, T. C. The Biophysics and Cell Biology of Lipid Droplets. *Nat. Rev. Mol. Cell Biol.* **2013**, *14* (12), 775–786. https://doi.org/10.1038/nrm3699.

(294) Richter, R. P.; Him, J. L. K.; Brisson, A. Supported Lipid Membranes. *Mater. Today* **2003**, *6* (11), 32–37. https://doi.org/10.1016/S1369-7021(03)01129-5.

(295) McConnell, H. M.; Watts, T. H.; Weis, R. M.; Brian, A. A. Supported Planar Membranes in Studies of Cell-Cell Recognition in the Immune System. *Biochim. Biophys. Acta BBA - Rev. Biomembr.* **1986**, *864* (1), 95–106. https://doi.org/10.1016/0304-4157(86)90016-X.

(296) Ramm, B.; Goychuk, A.; Khmelinskaia, A.; Blumhardt, P.; Eto, H.; Ganzinger, K. A.; Frey, E.; Schwille, P. A Diffusiophoretic Mechanism for ATP-Driven Transport without Motor Proteins. *Nat. Phys.* **2021**, *17* (7), 850–858. https://doi.org/10.1038/s41567-021-01213-3.

(297) Blodgett, K. B. Films Built by Depositing Successive Monomolecular Layers on a Solid Surface. *J. Am. Chem. Soc.* **1935**, *57* (6), 1007–1022. https://doi.org/10.1021/ja01309a011.

(298) Langmuir, I.; Schaefer, V. J. Activities of Urease and Pepsin Monolayers. *J. Am. Chem. Soc.* **1938**, *60* (6), 1351–1360. https://doi.org/10.1021/ja01273a023.

(299) Kurniawan, J.; Ventrici de Souza, J. F.; Dang, A. T.; Liu, G.; Kuhl, T. L. Preparation and Characterization of Solid-Supported Lipid Bilayers Formed by Langmuir–Blodgett Deposition: A Tutorial. *Langmuir* **2018**, *34* (51), 15622–15639. https://doi.org/10.1021/acs.langmuir.8b03504.

(300) Mapar, M.; Jõemetsa, S.; Pace, H.; Zhdanov, V. P.; Agnarsson, B.; Höök, F. Spatiotemporal Kinetics of Supported Lipid Bilayer Formation on Glass via Vesicle Adsorption and Rupture. *J. Phys. Chem. Lett.* **2018**, *9* (17), 5143–5149. https://doi.org/10.1021/acs.jpclett.8b02092.

(301) Seifert, U.; Lipowsky, R. Adhesion of Vesicles. *Phys. Rev. A* **1990**, *42* (8), 4768–4771. https://doi.org/10.1103/PhysRevA.42.4768.

(302) Hamai, C.; Cremer, P. S.; Musser, S. M. Single Giant Vesicle Rupture Events Reveal Multiple Mechanisms of Glass-Supported Bilayer Formation. *Biophys. J.* **2007**, *92* (6), 1988–1999. https://doi.org/10.1529/biophysj.106.093831.

(303) Wu, H.-L.; Chen, P.-Y.; Chi, C.-L.; Tsao, H.-K.; Sheng, Y.-J. Vesicle Deposition on Hydrophilic Solid Surfaces. *Soft Matter* **2013**, *9* (6), 1908–1919. https://doi.org/10.1039/C2SM27450G.

(304) Friddin, M. S.; Bolognesi, G.; Salehi-Reyhani, A.; Ces, O.; Elani, Y. Direct Manipulation of Liquid Ordered Lipid Membrane Domains Using Optical Traps. *Commun. Chem.* **2019**, *2* (1), 6. https://doi.org/10.1038/s42004-018-0101-4.

(305) Ngassam, V. N.; Su, W.-C.; Gettel, D. L.; Deng, Y.; Yang, Z.; Wang-Tomic, N.; Sharma, V. P.; Purushothaman, S.; Parikh, A. N. Recurrent Dynamics of Rupture Transitions of Giant Lipid Vesicles at Solid Surfaces. *Biophys. J.* **2021**, *120* (4), 586–597. https://doi.org/10.1016/j.bpj.2021.01.006.

(306) Czolkos, I.; Erkan, Y.; Dommersnes, P.; Jesorka, A.; Orwar, O. Controlled Formation and Mixing of Two-Dimensional Fluids. *Nano Lett.* **2007**, *7* (7), 1980–1984. https://doi.org/10.1021/nl070726u.

(307) Czolkos, I.; Hannestad, J. K.; Jesorka, A.; Kumar, R.; Brown, T.; Albinsson, B.; Orwar, O. Platform for Controlled Supramolecular Nanoassembly. *Nano Lett.* **2009**, *9* (6), 2482–2486. https://doi.org/10.1021/nl901254f.

(308) Tamura, F.; Tanimoto, Y.; Nagai, R.; Hayashi, F.; Morigaki, K. Self-Spreading of Phospholipid Bilayer in a Patterned Framework of Polymeric Bilayer. *Langmuir* **2019**, *35* (45), 14696–14703. https://doi.org/10.1021/acs.langmuir.9b02685.

(309) Raedler, J.; Strey, H.; Sackmann, E. Phenomenology and Kinetics of Lipid Bilayer Spreading on Hydrophilic Surfaces. *Langmuir* **1995**, *11* (11), 4539–4548. https://doi.org/10.1021/la00011a058.

(310) Tamm, L. K.; McConnell, H. M. Supported Phospholipid Bilayers. *Biophys. J.* **1985**, *47* (1), 105–113. https://doi.org/10.1016/S0006-3495(85)83882-0.

(311) Johnson, S. J.; Bayerl, T. M.; McDermott, D. C.; Adam, G. W.; Rennie, A. R.; Thomas, R. K.; Sackmann, E. Structure of an Adsorbed Dimyristoylphosphatidylcholine Bilayer Measured with Specular Reflection of Neutrons. *Biophys. J.* **1991**, *59* (2), 289–294. https://doi.org/10.1016/S0006-3495(91)82222-6.

(312) Akashi, K.-I.; Miyata, H.; Itoh, H.; Kinosita, K. Formation of Giant Liposomes Promoted by Divalent Cations: Critical Role of Electrostatic Repulsion. *Biophys. J.* **1998**, *74* (6), 2973–2982. https://doi.org/10.1016/s0006-3495(98)78004-x.

(313) Melcrová, A.; Pokorna, S.; Pullanchery, S.; Kohagen, M.; Jurkiewicz, P.; Hof, M.; Jungwirth, P.; Cremer, P. S.; Cwiklik, L. The Complex Nature of Calcium Cation Interactions with Phospholipid Bilayers. *Sci. Rep.* **2016**, *6* (1), 38035. https://doi.org/10.1038/srep38035.

(314) Kakimoto, Y.; Tero, R. Supported Lipid Bilayers of Escherichia Coli Extracted Lipids and Their Calcium Dependence. *Front. Mater.* **2018**, *5*, 48. https://doi.org/10.3389/fmats.2018.00048.

(315) Bilal, T.; Gzen, I. Formation and Dynamics of Endoplasmic Reticulum-like Lipid Nanotube Networks. *Biomater Sci* **2017**, *5* (7), 1256–1264. https://doi.org/10.1039/c7bm00227k.

(316) Richter, R.; Mukhopadhyay, A.; Brisson, A. Pathways of Lipid Vesicle Deposition on Solid Surfaces: A Combined QCM-D and AFM Study. *Biophys. J.* **2003**, *85* (5), 3035–3047. https://doi.org/10.1016/S0006-3495(03)74722-5.

(317) Gauthier, N. C.; Masters, T. A.; Sheetz, M. P. Mechanical Feedback between Membrane Tension and Dynamics. *Trends Cell Biol.* **2012**, *22* (10), 527–535. https://doi.org/10.1016/j.tcb.2012.07.005.

(318) Kozlov, M. M.; Chernomordik, L. V. Membrane Tension and Membrane Fusion. *Curr. Opin. Struct. Biol.* **2015**, *33*, 61–67. https://doi.org/10.1016/j.sbi.2015.07.010.

(319) Huang, L.; Zhang, J.; Wu, Z.; Zhou, L.; Yu, B.; Jing, Y.; Lin, D.; Qu, J. Revealing the Structure and Organization of Intercellular Tunneling Nanotubes (TNTs) by STORM Imaging. *Nanoscale Adv.* **2022**, *4* (20), 4258–4262. https://doi.org/10.1039/D2NA00415A.

(320) Lobovkina, T.; Dommersnes, P.; Joanny, J.-F.; Hurtig, J.; Orwar, O. Zipper Dynamics of Surfactant Nanotube Y Junctions. *Phys Rev Lett* **2006**, *97* (18), 188105–188105. https://doi.org/10.1103/PhysRevLett.97.188105.

(321) Roy, D.; Steinkühler, J.; Zhao, Z.; Lipowsky, R.; Dimova, R. Mechanical Tension of Biomembranes Can Be Measured by Super Resolution (STED) Microscopy of Force-Induced Nanotubes. *Nano Lett.* **2020**, *20* (5), 3185–3191. https://doi.org/10.1021/acs.nanolett.9b05232.

(322) Chaudhury, M. K.; Ohki, S. Correlation between Membrane Expansion and Temperature-Induced Membrane Fusion. *Biochim. Biophys. Acta BBA - Biomembr.* **1981**, *642* (2), 365–374. https://doi.org/10.1016/0005-2736(81)90452-1.

(323) Wang, X.; Gerdes, H. H. Transfer of Mitochondria via Tunneling Nanotubes Rescues Apoptotic PC12 Cells. *Cell Death Differ* **2015**, *22* (7), 1181–1191. https://doi.org/10.1038/cdd.2014.211.

(324) Gurke, S.; Barroso, J. F. V.; Gerdes, H.-H. The Art of Cellular Communication: Tunneling Nanotubes Bridge the Divide. *Histochem. Cell Biol.* **2008**, *129* (5), 539–550. https://doi.org/10.1007/s00418-008-0412-0.

(325) Jesorka, A.; Stepanyants, N.; Zhang, H.; Ortmen, B.; Hakonen, B.; Orwar, O. Generation of Phospholipid Vesicle-Nanotube Networks and Transport of Molecules Therein. *Nat. Protoc.* **2011**, *6* (6), 791–805. https://doi.org/10.1038/nprot.2011.321.

(326) Zhang, H.; Xu, S.; Jeffries, G. D. M.; Orwar, O.; Jesorka, A. Artificial Nanotube Connections and Transport of Molecular Cargo between Mammalian Cells. *Nano Commun. Netw.* **2013**, *4* (4), 197–204. https://doi.org/10.1016/j.nancom.2013.08.006.

(327) Dommersnes, P. G.; Orwar, O.; Brochard-Wyart, F.; Joanny, J. F. Marangoni Transport in Lipid Nanotubes. *Europhys. Lett. EPL* **2005**, *70* (2), 271–277. https://doi.org/10.1209/epl/i2004-10477-9.

(328) Hurtig, J.; Orwar, O. Injection and Transport of Bacteria in Nanotube-Vesicle Networks. *Soft Matter* **2008**, *4* (7), 1515–1520. https://doi.org/10.1039/b800333e.

(329) Karlsson, R.; Karlsson, A.; Orwar, O. Formation and Transport of Nanotube-Integrated Vesicles in a Lipid Bilayer Network. *J. Phys. Chem. B* **2003**, *107* (40), 11201–11207. https://doi.org/10.1021/jp034502l.

(330) Önfelt, B.; Nedvetzki, S.; Benninger, R. K. P.; Purbhoo, M. A.; Sowinski, S.; Hume, A. N.; Seabra, M. C.; Neil, M. A. A.; French, P. M. W.; Davis, D. M. Structurally Distinct Membrane Nanotubes between Human Macrophages Support Long-Distance Vesicular Traffic or Surfing of Bacteria. *J. Immunol.* **2006**, *177* (12), 8476–8483. https://doi.org/10.4049/jimmunol.177.12.8476.

(331) Tokarz, M.; Åkerman, B.; Olofsson, J.; Joanny, J.-F.; Dommersnes, P.; Orwar, O. Single-File Electrophoretic Transport and Counting of Individual DNA Molecules in Surfactant Nanotubes. *Proc. Natl. Acad. Sci.* **2005**, *102* (26), 9127–9132. https://doi.org/10.1073/pnas.0500081102.

(332) Tokarz, M.; Hakonen, B.; Dommersnes, P.; Orwar, O.; Åkerman, B. Electrophoretic Transport of Latex Particles in Lipid Nanotubes. *Langmuir* **2007**, *23* (14), 7652–7658. https://doi.org/10.1021/la700336u.

(333) Dagdug, L.; Berezhkovskii, A. M.; Shvartsman, S. Y.; Weiss, G. H. Equilibration in Two Chambers Connected by a Capillary. *J. Chem. Phys.* **2003**, *119* (23), 12473–12478. https://doi.org/10.1063/1.1626639.

(334) Lizana, L.; Konkoli, Z. Diffusive Transport in Networks Built of Containers and Tubes. *Phys Rev E Stat Nonlin Soft Matter Phys* **2005**, *72* (2 Pt 2), 026305–026305. https://doi.org/10.1103/PhysRevE.72.026305.

(335) Casalini, T.; Salvalaglio, M.; Perale, G.; Masi, M.; Cavallotti, C. Diffusion and Aggregation of Sodium Fluorescein in Aqueous Solutions. *J. Phys. Chem. B* **2011**, *115* (44), 12896–12904. https://doi.org/10.1021/jp207459k.

(336) Zhang, X.; Poniewierski, A.; Jelińska, A.; Zagożdżon, A.; Wisniewska, A.; Hou, S.; Hołyst, R. Determination of Equilibrium and Rate Constants for Complex Formation by Fluorescence Correlation Spectroscopy Supplemented by Dynamic Light Scattering and Taylor Dispersion Analysis. *Soft Matter* **2016**, *12* (39), 8186–8194. https://doi.org/10.1039/C6SM01791F.

(337) Stange, P.; Zanette, D.; Mikhailov, A.; Hess, B. Self-Organizing Molecular Networks. *Biophys. Chem.* **1998**, *72* (1–2), 73–85. https://doi.org/10.1016/S0301-4622(98)00124-0.

(338) Yandrapalli, N.; Robinson, T. Ultra-High Capacity Microfluidic Trapping of Giant Vesicles for High-Throughput Membrane Studies. *Lab. Chip* **2019**, *19* (4), 626–633. https://doi.org/10.1039/C8LC01275J.

(339) Bhatia, T.; Robinson, T.; Dimova, R. Membrane Permeability to Water Measured by Microfluidic Trapping of Giant Vesicles. *Soft Matter* **2020**, *16* (31), 7359–7369. https://doi.org/10.1039/D0SM00155D.

(340) Skinkle, A. D.; Levental, K. R.; Levental, I. Cell-Derived Plasma Membrane Vesicles Are Permeable to Hydrophilic Macromolecules. *Biophys. J.* **2020**, *118* (6), 1292–1300. https://doi.org/10.1016/j.bpj.2019.12.040.

(341) Levadny, V.; Tsuboi, T.; Belaya, M.; Yamazaki, M. Rate Constant of Tension-Induced Pore Formation in Lipid Membranes. *Langmuir* **2013**, *29* (12), 3848–3852. https://doi.org/10.1021/la304662p.

(342) Sandre, O.; Moreaux, L.; Brochard-Wyart, F. Dynamics of Transient Pores in Stretched Vesicles. *Proc. Natl. Acad. Sci.* **1999**, *96* (19), 10591–10596. https://doi.org/10.1073/pnas.96.19.10591.

(343) Levin, Y.; Idiart, M. A. Pore Dynamics of Osmotically Stressed Vesicles. *Phys. A* **2004**, *331* (3), 571–578. https://doi.org/10.1016/j.physa.2003.05.001.

(344) Gözen, I.; Dommersnes, P. Pore Dynamics in Lipid Membranes. *Eur. Phys. J. Spec. Top.* **2014**, *223* (9), 1813–1829. https://doi.org/10.1140/epjst/e2014-02228-5.

(345) Martens, S.; McMahon, H. T. Mechanisms of Membrane Fusion: Disparate Players and Common Principles. *Nat. Rev. Mol. Cell Biol.* **2008**, *9* (7), 543–556. https://doi.org/10.1038/nrm2417.

(346) Demonbreun, A. R.; Biersmith, B. H.; McNally, E. M. Membrane Fusion in Muscle Development and Repair. *Semin. Cell Dev. Biol.* **2015**, *45*, 48–56. https://doi.org/10.1016/j.semcdb.2015.10.026.

(347) Segal, D.; Dhanyasi, N.; Schejter, E. D.; Shilo, B.-Z. Adhesion and Fusion of Muscle Cells Are Promoted by Filopodia. *Dev. Cell* **2016**, *38* (3), 291–304. https://doi.org/10.1016/j.devcel.2016.07.010.

(348) Südhof, T. C.; Rothman, J. E. Membrane Fusion: Grappling with SNARE and SM Proteins. *Science* **2009**, *323* (5913), 474–477. https://doi.org/10.1126/science.1161748.

(349) Rørvig-Lund, A.; Bahadori, A.; Semsey, S.; Bendix, P. M.; Oddershede, L. B. Vesicle Fusion Triggered by Optically Heated Gold Nanoparticles. *Nano Lett.* **2015**, *15* (6), 4183–4188. https://doi.org/10.1021/acs.nanolett.5b01366.

(350) Lira, R. B.; Robinson, T.; Dimova, R.; Riske, K. A. Highly Efficient Protein-Free Membrane Fusion: A Giant Vesicle Study. *Biophys J* **2019**, *116* (1), 79–91. https://doi.org/10.1016/j.bpj.2018.11.3128.

(351) Arribas Perez, M.; Beales, P. A. Biomimetic Curvature and Tension-Driven Membrane Fusion Induced by Silica Nanoparticles. *Langmuir* **2021**, *37* (47), 13917–13931. https://doi.org/10.1021/acs.langmuir.1c02492.

(352) Tahir, M. A.; Guven, Z. P.; Arriaga, L. R.; Tinao, B.; Yang, Y.-S. S.; Bekdemir, A.; Martin, J. T.; Bhanji, A. N.; Irvine, D.; Stellacci, F.; Alexander-Katz, A. Calcium-Triggered Fusion of Lipid Membranes Is Enabled by Amphiphilic Nanoparticles. *Proc. Natl. Acad. Sci.* **2020**, *117* (31), 18470–18476. https://doi.org/10.1073/pnas.1902597117.

(353) Deshpande, S.; Wunnava, S.; Hueting, D.; Dekker, C. Membrane Tension–Mediated Growth of Liposomes. *Small* **2019**, *15* (38), 1902898. https://doi.org/10.1002/smll.201902898.

(354) Saha, R.; Chen, I. A. Origin of Life: Protocells Red in Tooth and Claw. *Curr. Biol.* **2015**, *25* (24), R1175–R1177. https://doi.org/10.1016/j.cub.2015.11.007.

(355) Witkowska, A.; Heinz, L. P.; Grubmüller, H.; Jahn, R. Tight Docking of Membranes before Fusion Represents a Metastable State with Unique Properties. *Nat. Commun.* **2021**, *12* (1), 3606. https://doi.org/10.1038/s41467-021-23722-8.

(356) Zubaite, G.; Hindley, J. W.; Ces, O.; Elani, Y. Dynamic Reconfiguration of Subcompartment Architectures in Artificial Cells. *ACS Nano* **2022**, *16* (6), 9389–9400. https://doi.org/10.1021/acsnano.2c02195.

(357) Zhao, J.; Zhang, Y.; Zhang, X.; Li, C.; Du, H.; Sønderskov, S. M.; Mu, W.; Dong, M.; Han, X. Mimicking Cellular Metabolism in Artificial Cells: Universal Molecule Transport across the Membrane through Vesicle Fusion. *Anal. Chem.* **2022**, *94* (9), 3811–3818. https://doi.org/10.1021/acs.analchem.1c04696.

(358) Ridley, A. J.; Schwartz, M. A.; Burridge, K.; Firtel, R. A.; Ginsberg, M. H.; Borisy, G.; Parsons, J. T.; Horwitz, A. R. Cell Migration: Integrating Signals from Front to Back. *Science* **2003**, *302* (5651), 1704–1709. https://doi.org/10.1126/science.1092053.

(359) Lauffenburger, D. A.; Horwitz, A. F. Cell Migration: A Physically Integrated Molecular Process. *Cell* **1996**, *84* (3), 359–369. https://doi.org/10.1016/S0092-8674(00)81280-5.

(360) Wei, C.; Wang, X.; Chen, M.; Ouyang, K.; Song, L.-S.; Cheng, H. Calcium Flickers Steer Cell Migration. *Nature* **2009**, *457* (7231), 901–905. https://doi.org/10.1038/nature07577.

(361) Solon, J.; Streicher, P.; Richter, R.; Brochard-Wyart, F.; Bassereau, P. Vesicles Surfing on a Lipid Bilayer: Self-Induced Haptotactic Motion. *Proc. Natl. Acad. Sci.* **2006**, *103* (33), 12382–12387. https://doi.org/10.1073/pnas.0601400103.

(362) Fu, M.; Burkart, T.; Maryshev, I.; Franquelim, H. G.; Merino-Salomón, A.; Reverte-López, M.; Frey, E.; Schwille, P. Mechanochemical Feedback Loop Drives Persistent Motion of Liposomes. *Nat. Phys.* **2023**. https://doi.org/10.1038/s41567-023-02058-8.

(363) Lobovkina, T.; Gözen, I.; Erkan, Y.; Olofsson, J.; Weber, S. G.; Orwar, O. Protrusive Growth and Periodic Contractile Motion in Surface-Adhered Vesicles Induced by Ca2+-Gradients. *Soft Matter* **2010**, *6* (2), 268–272. https://doi.org/10.1039/b916805m.

(364) Kodama, A.; Morandi, M.; Ebihara, R.; Jimbo, T.; Toyoda, M.; Sakuma, Y.; Imai, M.; Puff, N.; Angelova, M. I. Migration of Deformable Vesicles Induced by Ionic Stimuli. *Langmuir* **2018**, *34* (38), 11484–11494. https://doi.org/10.1021/acs.langmuir.8b02105.

(365) Gözen, I.; Shaali, M.; Ainla, A.; Örtmen, B.; Põldsalu, I.; Kustanovich, K.; Jeffries, G. D. M.; Konkoli, Z.; Dommersnes, P.; Jesorka, A. Thermal Migration of Molecular Lipid Films as a Contactless Fabrication Strategy for Lipid Nanotube Networks. *Lab. Chip* **2013**, *13* (19), 3822. https://doi.org/10.1039/c3lc50391g.

(366) Hill, E. H.; Li, J.; Lin, L.; Liu, Y.; Zheng, Y. Opto-Thermophoretic Attraction, Trapping, and Dynamic Manipulation of Lipid Vesicles. *Langmuir* **2018**, *34* (44), 13252–13262. https://doi.org/10.1021/acs.langmuir.8b01979.

(367) Li, Q.; Li, S.; Zhang, X.; Xu, W.; Han, X. Programmed Magnetic Manipulation of Vesicles into Spatially Coded Prototissue Architectures Arrays. *Nat. Commun.* **2020**, *11* (1), 232. https://doi.org/10.1038/s41467-019-14141-x.

(368) Karlsson, M.; Nolkrantz, K.; Davidson, M. J.; Strömberg, A.; Ryttsén, F.; Åkerman, B.; Orwar, O. Electroinjection of Colloid Particles and Biopolymers into Single Unilamellar Liposomes and Cells for Bioanalytical Applications. *Anal. Chem.* **2000**, *72* (23), 5857–5862. https://doi.org/10.1021/ac0003246.

(369) Nowacka, A.; Douezan, S.; Wadsö, L.; Topgaard, D.; Sparr, E. Small Polar Molecules like Glycerol and Urea Can Preserve the Fluidity of Lipid Bilayers under Dry Conditions. *Soft Matter* **2012**, *8* (5), 1482–1491. https://doi.org/10.1039/C1SM06273E.

(370) Hope, M. J.; Bally, M. B.; Webb, G.; Cullis, P. R. Production of Large Unilamellar Vesicles by a Rapid Extrusion Procedure. Characterization of Size Distribution, Trapped Volume and Ability to Maintain a Membrane Potential. *Biochim. Biophys. Acta BBA - Biomembr.* **1985**, *812* (1), 55–65. https://doi.org/10.1016/0005-2736(85)90521-8.

(371) Mayer, L. D.; Hope, M. J.; Cullis, P. R. Vesicles of Variable Sizes Produced by a Rapid Extrusion Procedure. *Biochim. Biophys. Acta BBA - Biomembr.* **1986**, *858* (1), 161–168. https://doi.org/10.1016/0005-2736(86)90302-0.

(372) Grobéty, B.; Gieré, R.; Dietze, V.; Stille, P. Airborne Particles in the Urban Environment. *Elements* **2010**, *6* (4), 229–234. https://doi.org/10.2113/gselements.6.4.229.

(373) Cobo, F.; Grela, D.; Conchal, A. Airborne Particle Monitoring in Clean Room Environments for Stem Cell Cultures. *Biotechnol. J.* **2008**, *3* (1), 43–52. https://doi.org/10.1002/biot.200700122.

(374) Singh, J.; Wolfe, D. E. Review Nano and Macro-Structured Component Fabrication by Electron Beam-Physical Vapor Deposition (EB-PVD). *J. Mater. Sci.* **2005**, *40* (1), 1–26. https://doi.org/10.1007/s10853-005-5682-5.

(375) Jamil, S.; Gupta, S. K.; Anbalagan, K.; Akhtar, J. Electron-Beam Assisted Physical Vapor Deposition of Polycrystalline Silicon Films. *Mater. Sci. Semicond. Process.* **2011**, *14* (3–4), 287–293. https://doi.org/10.1016/j.mssp.2011.05.011.

(376) Mattox, D. M. Handbook of Physical Vapor Deposition (PVD) Processing; William Andrew, 2010.

(377) Theeten, J.; Aspnes, D. Ellipsometry in Thin Film Analysis. *Annu. Rev. Mater. Sci.* **1981**, *11* (1), 97–122. https://doi.org/10.1146/annurev.ms.11.080181.000525.

(378) Schermelleh, L.; Ferrand, A.; Huser, T.; Eggeling, C.; Sauer, M.; Biehlmaier, O.; Drummen, G. P. C. Super-Resolution Microscopy Demystified. *Nat. Cell Biol.* **2019**, *21* (1), 72–84. https://doi.org/10.1038/s41556-018-0251-8.

(379) Tsunoda, M.; Isailovic, D.; Yeung, E. S. Real-Time Three-Dimensional Imaging of Cell Division by Differential Interference Contrast Microscopy: REAL-TIME 3-D IMAGING OF CELL DIVISION BY DIC MICROSCOPY. *J. Microsc.* **2008**, *232* (2), 207–211. https://doi.org/10.1111/j.1365-2818.2008.02091.x.

(380) Clegg, R. M. Fluorescence Resonance Energy Transfer. *Curr. Opin. Biotechnol.* **1995**, *6* (1), 103–110. https://doi.org/10.1016/0958-1669(95)80016-6.

(381) Furukawa, K.; Nakashima, H.; Kashimura, Y.; Torimitsu, K. Novel “Lipid-Flow Chip” Configuration to Determine Donor-to-Acceptor Ratio-Dependent Fluorescence Resonance Energy Transfer Efficiency. *Langmuir* **2008**, *24* (3), 921–926. https://doi.org/10.1021/la702695f.

(382) Boyd, M. A.; Kamat, N. P. Visualizing Tension and Growth in Model Membranes Using Optical Dyes. *Biophys. J.* **2018**, *115* (7), 1307–1315. https://doi.org/10.1016/j.bpj.2018.08.021.

(383) Demchenko, A. P. Photobleaching of Organic Fluorophores: Quantitative Characterization, Mechanisms, Protection. *Methods Appl. Fluoresc.* **2020**, *8* (2), 022001. https://doi.org/10.1088/2050-6120/ab7365.

(384) Oshima, A.; Nakashima, H.; Sumitomo, K. Evaluation of Lateral Diffusion of Lipids in Continuous Membranes between Freestanding and Supported Areas by Fluorescence Recovery after Photobleaching. *Langmuir* **2019**, *35* (36), 11725–11734. https://doi.org/10.1021/acs.langmuir.9b01595.

(385) Wilson, T. Resolution and Optical Sectioning in the Confocal Microscope: PROPERTIES OF THE FLUORESCENT CONFOCAL MICROSCOPE. *J. Microsc.* **2011**, *244* (2), 113–121. https://doi.org/10.1111/j.1365-2818.2011.03549.x.

(386) Andersen, T.; Kyrsting, A.; Bendix, P. M. Local and Transient Permeation Events Are Associated with Local Melting of Giant Liposomes. *Soft Matter* **2014**, *10* (24), 4268–4274. https://doi.org/10.1039/C4SM00410H.

(387) Urban, P.; Kirchner, S. R.; Mühlbauer, C.; Lohmüller, T.; Feldmann, J. Reversible Control of Current across Lipid Membranes by Local Heating. *Sci. Rep.* **2016**, *6* (1), 22686. https://doi.org/10.1038/srep22686.

(388) Bhojoo, U.; Chen, M.; Zou, S. Temperature Induced Lipid Membrane Restructuring and Changes in Nanomechanics. *Biochim. Biophys. Acta BBA - Biomembr.* **2018**, *1860* (3), 700–709. https://doi.org/10.1016/j.bbamem.2017.12.008.

(389) Hale, G. M.; Querry, M. R. Optical Constants of Water in the 200-Nm to 200-Mm Wavelength Region. *Appl. Opt.* **1973**, *12* (3), 555–563. https://doi.org/10.1364/AO.12.000555.

(390) Anderson, R. R.; Farinelli, W.; Laubach, H.; Manstein, D.; Yaroslavsky, A. N.; Gubeli III, J.; Jordan, K.; Neil, G. R.; Shinn, M.; Chandler, W.; Williams, G. P.; Benson, S. V.; Douglas, D. R.;

Dylla, H. F. Selective Photothermolysis of Lipid-Rich Tissues: A Free Electron Laser Study. *Lasers Surg. Med.* **2006**, *38* (10), 913–919. https://doi.org/10.1002/lsm.20393.

(391) Whitesides, G. M. The Origins and the Future of Microfluidics. *Nature* **2006**, *442* (7101), 368–373. https://doi.org/10.1038/nature05058.

(392) Ainla, A.; Jansson, E. T.; Stepanyants, N.; Orwar, O.; Jesorka, A. A Microfluidic Pipette for Single-Cell Pharmacology. *Anal. Chem.* **2010**, *82* (11), 4529–4536. https://doi.org/10.1021/ac100480f.

(393) Ainla, A.; Jeffries, G. D. M.; Brune, R.; Orwar, O.; Jesorka, A. A Multifunctional Pipette. *Lab. Chip* **2012**, *12* (7), 1255. https://doi.org/10.1039/c2lc20906c.

(394) Veselovsky, N. S.; Engert, F.; Lux, H. D. Fast Local Superfusion Technique. *Pflüg. Arch.* **1996**, *432* (2), 351–354. https://doi.org/10.1007/s004240050143.

(395) Nabika, H.; Sasaki, A.; Takimoto, B.; Sawai, Y.; He, S.; Murakoshi, K. Controlling Molecular Diffusion in Self-Spreading Lipid Bilayer Using Periodic Array of Ultra-Small Metallic Architecture on Solid Surface. *J. Am. Chem. Soc.* **2005**, *127* (48), 16786–16787. https://doi.org/10.1021/ja0559597.

(396) Furukawa, K.; Sumitomo, K.; Nakashima, H.; Kashimura, Y.; Torimitsu, K. Supported Lipid Bilayer Self-Spreading on a Nanostructured Silicon Surface. *Langmuir* **2007**, *23* (2), 367–371. https://doi.org/10.1021/la062911d.

(397) Miyazako, H.; Mabuchi, K.; Hoshino, T. Multi-Scale Lipid Membrane Flow by Electron Beam-Induced Electrowetting. *Adv. Mater. Interfaces* **2021**, *8* (18), 2100257. https://doi.org/10.1002/admi.202100257.

Publications

NANO · MICRO
small
www.small-journal.com

Rapid Growth and Fusion of Protocells in Surface-Adhered Membrane Networks

*Elif S. Köksal, Susanne Liese, Lin Xue, Ruslan Ryskulov, Lauri Viitala, Andreas Carlson, and Irep Gözen**

Elevated temperatures might have promoted the nucleation, growth, and replication of protocells on the early Earth. Recent reports have shown evidence that moderately high temperatures not only permit protocell assembly at the origin of life, but can have actively supported it. Here, the fast nucleation and growth of vesicular compartments from autonomously formed lipid networks on solid surfaces, induced by a moderate increase in temperature, are shown. Branches of the networks, initially consisting of self-assembled interconnected nanotubes, rapidly swell into microcompartments which can spontaneously encapsulate RNA fragments. The increase in temperature further causes fusion of adjacent network-connected compartments, resulting in the redistribution of the RNA. The experimental observations and the mathematical model indicate that the presence of nanotubular interconnections between protocells facilitates the fusion process.

1. Introduction

The important role of solid surface support for the autonomous formation of primitive protocells has been suggested earlier in the context of the origin of life.[1,2] Hanczyc et al. showed that vesicle formation from fatty acids was significantly enhanced in the presence of solid particle surfaces consisting of natural minerals or synthetic materials.[1,2] Particularly the silicate-based minerals accelerated the vesicle generation.

In a recent report, we showed the autonomous formation and growth of surface adhered protocell populations as a result of a sequence of topological transformations on a solid substrate.[3] Briefly, upon contact with a mineral-like solid substrate, a lipid reservoir spreads as a double bilayer membrane. The distal membrane (upper bilayer with respect to the surface) ruptures and forms a carpet of lipid nanotubes. Over the course of a few hours, fragments of these nanotubes swell into giant, strictly unilamellar vesicular compartments. This relatively slow process is entirely self-driven and only requires a lipid reservoir as source, a solid surface, and surrounding aqueous media. The resulting structure consists of thousands of lipid compartments, which are physically connected to each other via a network of nanotubes. This formation process and the ability of these compartments to encapsulate ambient molecules, and to separate and migrate to remote locations, lead to the formulation of a new protocell hypothesis.[4] This addresses open questions about how primitive protocells might have formed and replicated on the early Earth, what exact physicochemical mechanisms governed the growth and division of the membranes, and how cargo, e.g., RNA or other contents, was encapsulated and distributed. Prevailing hypotheses involving the self-assembly of amphiphiles in bulk aqueous medium explain the formation of protocells, but not the necessary subsequent steps, e.g., growth, replication, division, in a satisfactory manner.

In the former study, which was conducted at constant room temperature, the protocell nucleation and growth are slow processes occurring over the course of hours to days.[3] Under natural conditions, fluctuations in temperature are expected, the impact of which on the reported system has not been considered. Since the growth process is slow, the compartments often do not reach sizes large enough to establish physical contact in a reasonable time frame, and remain too far apart for fusion. Fusion has been considered a feasible means of protocell growth, a step required for self-proliferation.[5] In addition, the mechanical or osmotic stress on bilayer compartments can over time lead to the collapse of vesicular structures.[6]

In our current study we show that a temperature increase significantly accelerates the formation of membrane compartments and further initiates their fusion, which supports the recent findings of Jordan et al.[7] The accelerated nucleation and growth lead to maturation of compartments, which eventually

---

E. S. Köksal, L. Xue, Dr. I. Gözen
Centre for Molecular Medicine Norway
Faculty of Medicine
University of Oslo
Oslo 0318, Norway
E-mail: irep@uio.no
Dr. S. Liese, Dr. A. Carlson
Department of Mathematics
Faculty of Mathematics and Natural Sciences
University of Oslo
Oslo 0315, Norway
R. Ryskulov, Dr. L. Viitala, Dr. I. Gözen
Department of Chemistry and Chemical Engineering
Chalmers University of Technology
Göteborg SE-412 96, Sweden
Dr. I. Gözen
Department of Chemistry
Faculty of Mathematics and Natural Sciences
University of Oslo
Oslo 0315, Norway

The ORCID identification number(s) for the author(s) of this article can be found under https://doi.org/10.1002/smll.202002529.

DOI: 10.1002/smll.202002529

establish physical contact. The adjacent vesicular membranes fuse, resulting in redistribution of cargo, e.g., oligoribonucleotides. Nucleation and transformations strictly occur on the lipid nanotube networks and creates consistently and exclusively unilamellar membranous compartments. In addition to the experiments, we provide a finite element model which emphasizes that the presence of nanotubular connections between protocells facilitates the fusion. The findings can explain how protocells on the early Earth might have undergone rapid growth and replication, and provide new insight into our recently developed nanotube–protocell network hypothesis.[4]

2. Results

2.1. Enhanced Protocell Formation and Growth

We deposited a multilamellar reservoir on a SiO_2 surface. Note that the choice of substrate material has a profound influence on the nature of the surfactant film formed on the surface. On silicon dioxide the formation of a lipid double bilayer occurs consistently by spreading.[8] The reservoir spontaneously spreads on the surface in form of a circular double bilayer membrane.[9] The distal of the two stacked bilayers (upper bilayer with respect to the surface), ruptures due to continuous tensile stress,[9] resulting in formation of a network of nanotubes on the proximal bilayer.[3] Fragments of the nanotubes swell over time, and form unilamellar vesicular compartments. The autonomous transformation of lipid reservoirs into networks of surface-adhered protocells interconnected by lipid nanotubes, has been described by Köksal et al.[3]

This precursor structure is a lipid nanotube network residing on a bilayer patch (**Figure 1**a). Each liquid-filled nanotube has a cylindrical cross-section and consists of a single bilayer (inset to Figure 1a).[3] Next, we engage an IR-B (λ = 1470 nm) laser to achieve a mild temperature increase in the vicinity of the membrane (Figure 1b).[10] The IR radiation is applied through an optical fiber positioned by means of a mechanical micromanipulator on an inverted microscope (Section S1, Supporting Information). The position of the IR-laser fiber tip with respect to the lipid nanotube-covered membrane region is indicated by the yellow dashed lines in Figure 1c. Due to the flat fiber tip, the laser radiation is not focused, but affects a cone-shaped water volume that extends to the solid surface. Details of the experimental setup are shown in Figure S1 of the Supporting Information. The formation of giant unilamellar vesicles from disordered membrane layers induced by localized heating (>25 °C) has been reported before.[11,12] In our experiments, the thermal gradient leads to the instant formation and growth of vesicular compartments exclusively from the lipid nanotubes (Figure 1b). The formed compartments are strictly unilamellar[3] which is in contrast to the vesicles reported by Billerit et al.[11,12] where a lamellarity distribution typical for swelling of stacked bilayers was observed. The majority of techniques for artificial vesicle generation feature this distribution.[13,14] Figure 1c–e (Movie S1, Supporting Information) show the laser scanning confocal microscopy time series of the process schematically described in Figure 1a,b. Over the course of a few minutes of IR exposure, the unilamellar compartments form from the lipid nanotubes and rapidly grow (Figure 1d,e). The fiber is positioned above the sample at a tilted angle, therefore the beam projects onto an ellipse-shaped area, clearly visible from the distribution of the protocells in Figure 1d,e. The image series in Figure 1f–k (Movie S1, Supporting Information) demonstrate that the formed compartments are colocated with the nanotubes. During growth the compartments maintain their positions. In Figure 1l,m the transformation from tube to spherical compartment, is schematically shown. Due to the temperature increase, the membrane viscosity is reduced and tension increases, leading to rapid inflow of lipids from low tension areas. Combined with a reduction of the high membrane curvature, this results in minimization of the surface free energy of the system,[3] which is the driving force for the transformation.

Figure 2a (Movie S1, Supporting Information) is a snapshot from a confocal time series of a heated membrane region, showing protocell growth. We created 31 elliptical rings (a quarter of each shown as a yellow dashed line) on the membrane and calculated the protocell densities, i.e., the number of protocells per area between two consecutive rings (ΔAr_x). An exception is the smallest ellipse at the center which is considered as a whole. Figure 2b is a plot of the protocell density in each ring versus the minor ellipse radius (r_x) in Figure 2a. The graph indicates that the protocell density increases with the temperature, which, due to the acceptance-cone of the fiber is gradually decreasing with distance from the center. The image series in Figure 2c–f shows a membrane section decorated with lipid nanotubes, progressing to vesicular compartments. The confocal scans were recorded close to the proximal membrane (panel e), and across the equator of the vesicular compartments (panel d). Panel (f) is a 3D reconstruction of the nanotube-adhered protocells in panels (d and e). For comparison, five selected compartments in the different panels of Figure 2e,f are marked with numbers.

We used a microthermocouple to determine the temperature of the affected region in the experiments. The details of the measurement have been presented in Section S2 of the Supporting Information. The estimated temperatures are 40–90 °C. ≈40 °C leads to rapid nucleation, and ≈70 °C to rapid growth. ≈90 °C results in fusion of the compartments, which will be described in detail below.

For the membrane section depicted in Figure 2c–f (Movie S3, Supporting Information), the total count of the protocells versus time is shown in Figure 2g, and the average protocell diameter versus time in Figure 2h. The compartments nucleate instantly with activation of the IR-laser. Their number remains constant (Figure 2g), while their diameter is increasing (Figure 2h). The size distribution of the protocells at five different time points throughout the experiment is shown in Figure 2i. Small protocells (d < 1 µm) dominating at the early stages (orange histogram), later evolve into larger protocells (d > 3 µm, blue and purple histograms). The development of the membrane area and the internal volume of the protocells during the experiment (Figure 2c–f) is shown in Figure 2j. The total membrane area was ≈1250 µm² at the end of the experiment. This corresponds to a nanotube of 4 mm length (Ø = 100 nm). We do not observe such a high tubular density in Figure 2c. The membrane material forming the protocells therefore likely originates from a remote membrane reservoir and migrates through the nanotubes.[15,16] A comparison between panel (c) and (e) reveals that

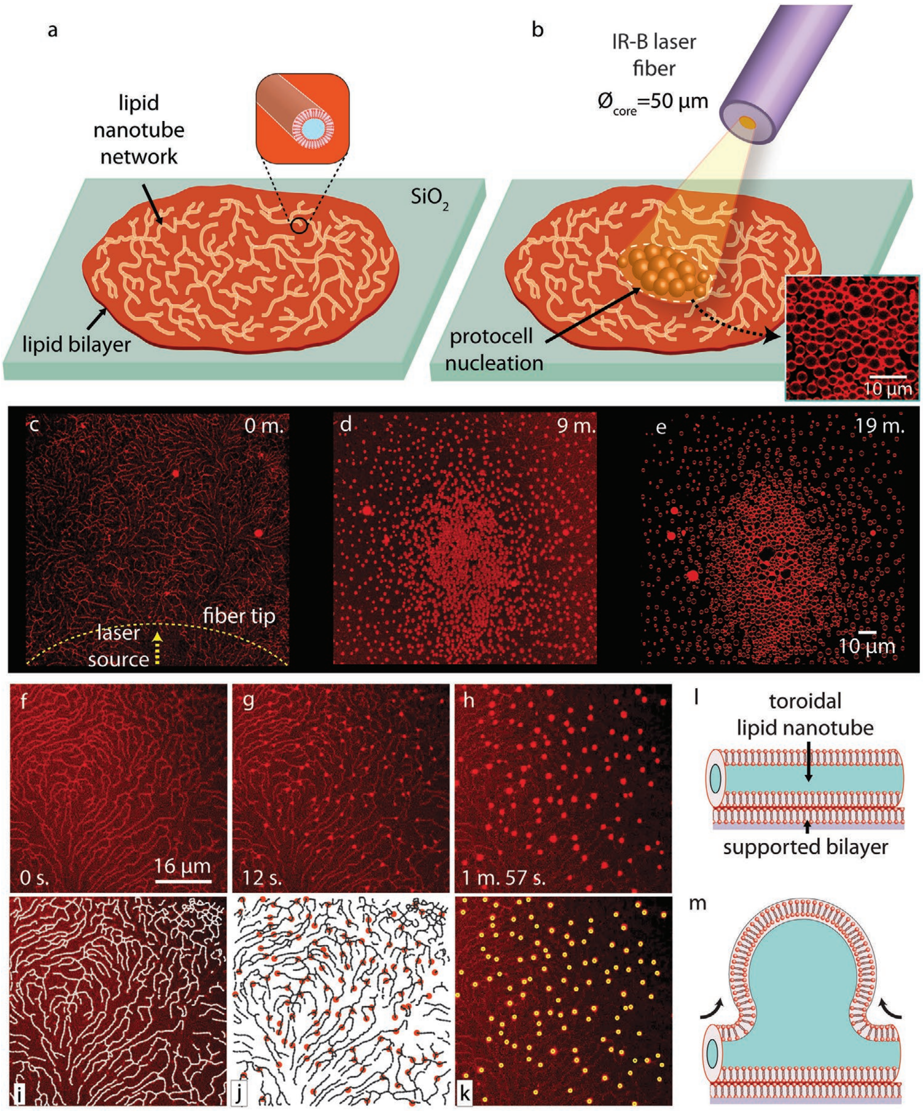

Figure 1. Heat-induced protocell formation from surface-adhered lipid nanotubes. a,b) Schematic drawing summarizing the experiment. (a) Network of hollow lipid nanotubes (inset) is residing on a SiO$_2$-adhered bilayer. (b) Rapid formation of protocells from the nanotubes as a result of mild heating. Inset on the lower right corner shows the confocal image of protocells formed as a result of this process. All experiments have been performed in biological buffers. c–e) Laser scanning confocal microscopy time series of the process schematically described in (a) and (b). f–k) Confocal images showing that the formed compartments and the nanotubes have colocalized. During growth, the compartments maintain their positions. (i) The outline of the nanotubes in panel (f). (j) The positions of the nucleation sites in (g), indicated with the red circles, are superimposed on the network outlined in (i). (k) The positions of the nucleation sites in (g and j) are superimposed on the image in (h). l–m) Schematic drawing depicting the transformation from a nanotube to a vesicular compartment.

the majority of the nanotubes remain intact. This means that they are not the major source of protocells formed in the process. Provision of the membrane material through the proximal bilayer is in principle also possible, but we have earlier presented the argument that this is rather unlikely.[3]

2.2. Protocell Fusion

We observe that the temperature increase further induces fusion of adjacent compartments. **Figure 3**a,b shows a membrane region in which rapid merging was observed. In Figure 3a the protocells are shown before fusion, and in Figure 3b after fusion. The areas in which fusion of two or more compartments occurs, are encircled in white dashed lines and numbered (panel a). The merged compartments are represented in Figure 3b by the same numbers. Figure 3c shows the number (orange graph) and average diameter (blue graph) of the protocells shown in Figure 3a,b over time (cf., Section S3 for details of the image analyses). The total number of compartments decreases, and the average diameter increases accordingly (panel c). The images in Figure 3 (Movies S4 and S5, Supporting Information) show

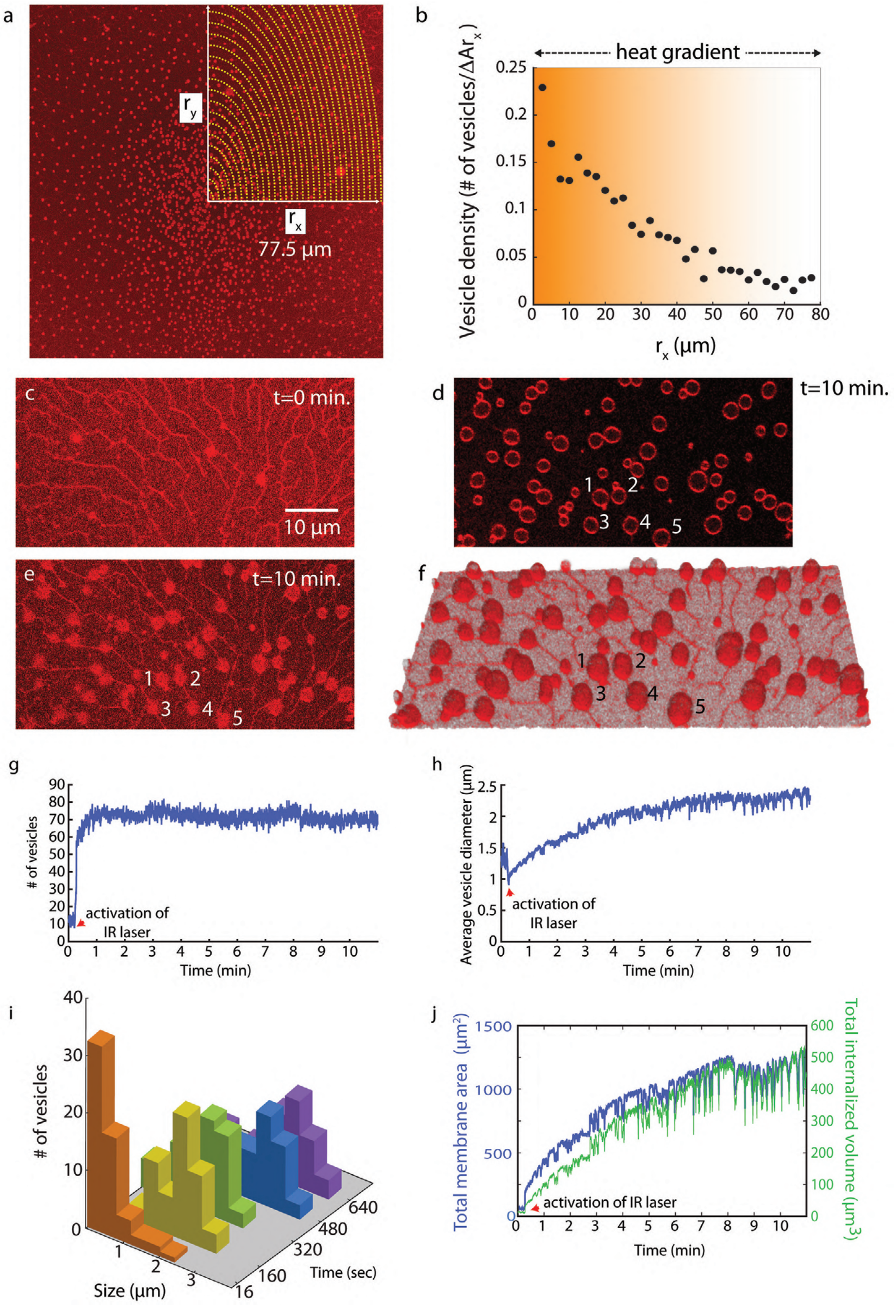

Figure 2. Characterization of protocell formation and growth induced by a mild heat gradient. a) laser scanning confocal image of a large membrane region with nucleating protocells. The area exposed to the IR laser is split to 31 hypothetical elliptical rings, the minor radius of which is expressed as r_x and the major radius, r_y. A quarter of the outline of each ring is shown in yellow dashed lines. r_x of the outmost ring is 77.5 µm. b) Plot showing the protocell density over distance r_x. The protocell density is calculated as the number of protocells in each individual elliptical ring. c–f) Confocal images of a nanotube network leading to nucleation and growth of protocells exposed to heat gradients for 10 min. c) Nanotube network before local heat exposure (d) cross-section of protocell sample from the equator after heat exposure (top view). (e) Cross-section of sample close to the surface after heat exposure (top view). (f) 3D reconstruction of the formed protocells. Plot showing g) the number and h) the average diameter of the protocells formed in (c–f) over 10 min. i) The histograms depicting the size distribution of protocells over time. Each color represents the size distribution at a given time point. j) Plots showing total membrane area and total membrane volume of the protocells in (c–f) during their formation and growth.

different surface regions of the same confocal microscopy recording. The black arrows in panel (c), labeled with panel names, indicate the time points at which the corresponding images were recorded.

We explored whether fusion events only occur among the compartments residing on the same nanotube, or if the fusion between compartments on different nanotubes is possible. We therefore investigated membrane regions of known network topology. Figure 3d–g,h–k shows the fusion of two different sets of compartments, each set residing on the same nanotube (black dashed lines). Three compartments marked with green asterisks in Figure 3d merge into a single protocell within a few seconds (panels e–g). In Figure 3h–k, five protocells (yellow asterisks) merge. In both cases, the fusing protocells reside on the same nanotube. If protocells located on different nanotubes grow and eventually establish physical contact, we also observe fusion events. Figure 3l–p (red asterisks) and Figure 3q–u (blue asterisks) depict two examples. The original positions of the nanotubes in each recording are indicated by black dashed lines (Figure 3l,q).

2.3. Mechanism of Fusion

Increase in temperature results in an increase in fluidity of the membrane, leading to the rapid fusion of the initially distinct, adjacent membranes.[17,18] Upon fusion, the membranes relax to a form that minimizes the membrane energy. The transformation from two small containers to a single large one reduces the curvature, while the membrane area is maintained. In our experiments, fusion of nanotube-connected lipid compartments can occur in two different ways: it either begins near their equator, i.e., where their lateral extension is the largest and the compartments touch first (**Figure 4**a), or they fuse at the base, mediated by the connecting membrane nanotube (Figure 4b). In order to determine which of these two scenarios is energetically the most favorable, we performed a set of numerical finite element simulations (cf., Section S4, Supporting Information, for details).[19,20] Since the thickness of the lipid bilayer (≈ 5 nm) is much smaller than the typical size of the membrane tube (>100 nm) and the attached compartment (>1 µm), we treated the membrane as a thin elastic surface. For the simulation, we considered two adjacent vesicular compartments of the same size, where the compartments share a surface-adhered membrane tube. The edges of the numerical domains were defined by open nanotubes which were restricted to form a cylinder of radius r_t. The tube length was set to 15 r_t and the total membrane area to 450 r_t^2. In dimensional units this corresponds to two spherical compartments, each with a diameter of ≈0.4 µm, connected through a tube with a diameter of ≈100 nm.

We keep the membrane area in the simulations constant such that the membrane shape and energy are solely determined by the minimization of the bending energy. In the initial configuration, the two compartments either form a fusion pore (neck) near their equator (Figure 4a), or they fuse by consuming the nanotube (Figure 4b). In both cases the bending energy of two well separated compartments, i.e., narrow neck with small Δl_n, is similar to the energy of two independent spherical compartments. In the latter case, we consider the portion of the tube that connects the two compartments, the neck region. In each simulation the circumference of the neck is kept constant, while the position of the neck is free and hence determined by the energy minimization. Figure 4c shows the development of the bending energies for fusion initiated at the equator (squares) and at the tube (circles), as we systematically increase the neck circumference Δl_n. We obtain the bending energy, according to the Helfrich theory[21] by integrating the square of the mean curvature H over the membrane surface area A: $E = \int dA \frac{\kappa}{2} H^2$, where κ is the bending rigidity. The energy is normalized by the bending energy of a spherical vesicle, $E_{\mathrm{sph}} = 8\pi\kappa$. If the vesicle fusion starts at the tube, we observe an increase in neck circumference Δl_n. Note that in this case the initial circumference $2\pi r_t$ is subtracted. As the neck expands, the vesicles fuse and the surface free energy decreases. For vesicle fusion at the base, the energy approaches that of a single spherical vesicle. By contrast, for vesicles fusing at the equator, the energy reaches a plateau that is about 75% larger than the energy of a spherical vesicle. If the vesicles start to fuse at their equator, a circular pore forms between the fusion site and the membrane tube. Our simulations show that the pore stabilizes with a diameter (IV in Figure 4a) similar to the diameter of the membrane tube (Figure 4d). The fusion process should predominantly start at the tube, since this scenario is energetically more favorable and allows for complete fusion of the two vesicles (cf., Section S4, Supporting Information, for model, and Section S5, Supporting Information, for corresponding experimental observations).

2.4. Encapsulation and Redistribution of RNA upon Fusion

In order to investigate the merging of the contents of fusing compartments, we employed an open-space microfluidic pipette[22] and loaded several compartments with fluorescently labeled RNA oligomers (**Figure 5**a). Open-space microfluidic delivery is an effective means to create a local chemical environment. Subsequently applied mild heating led to the fusion of the RNA-loaded protocells with adjacent, initially unloaded compartments, and the RNA oligomers were redistributed (Figure 5b). Figure 5c (Movie S7, Supporting Information) shows the loading process: a population of surface-adhered protocells in the recirculation zone of the microfluidic device, dispensing a solution containing fluorescent RNA fragments (top view). The border of the recirculation zone is marked with white dashed lines (Figure 5c). Initially, the protocells appear as black dots within the recirculation zone, since they only contain buffer (Figure 5c). Over time, some of the protocells encapsulate the RNA fragments (Figure 5d). Encapsulation of water-soluble fluorescein inside the surface-adhered protocells was shown earlier in a similar experiment at ambient temperature,[3] and explained by the involvement of transient pores of sufficient size and stability. We observe that the encapsulation efficiency of RNA oligomers is significantly smaller than of fluorescein (cf., Section S6, Supporting Information, for comparative experiments). We attribute this to both the size and the charge differences between the molecules. Figure 5e–m is a sequence depicting how the RNA fragments are redistributed

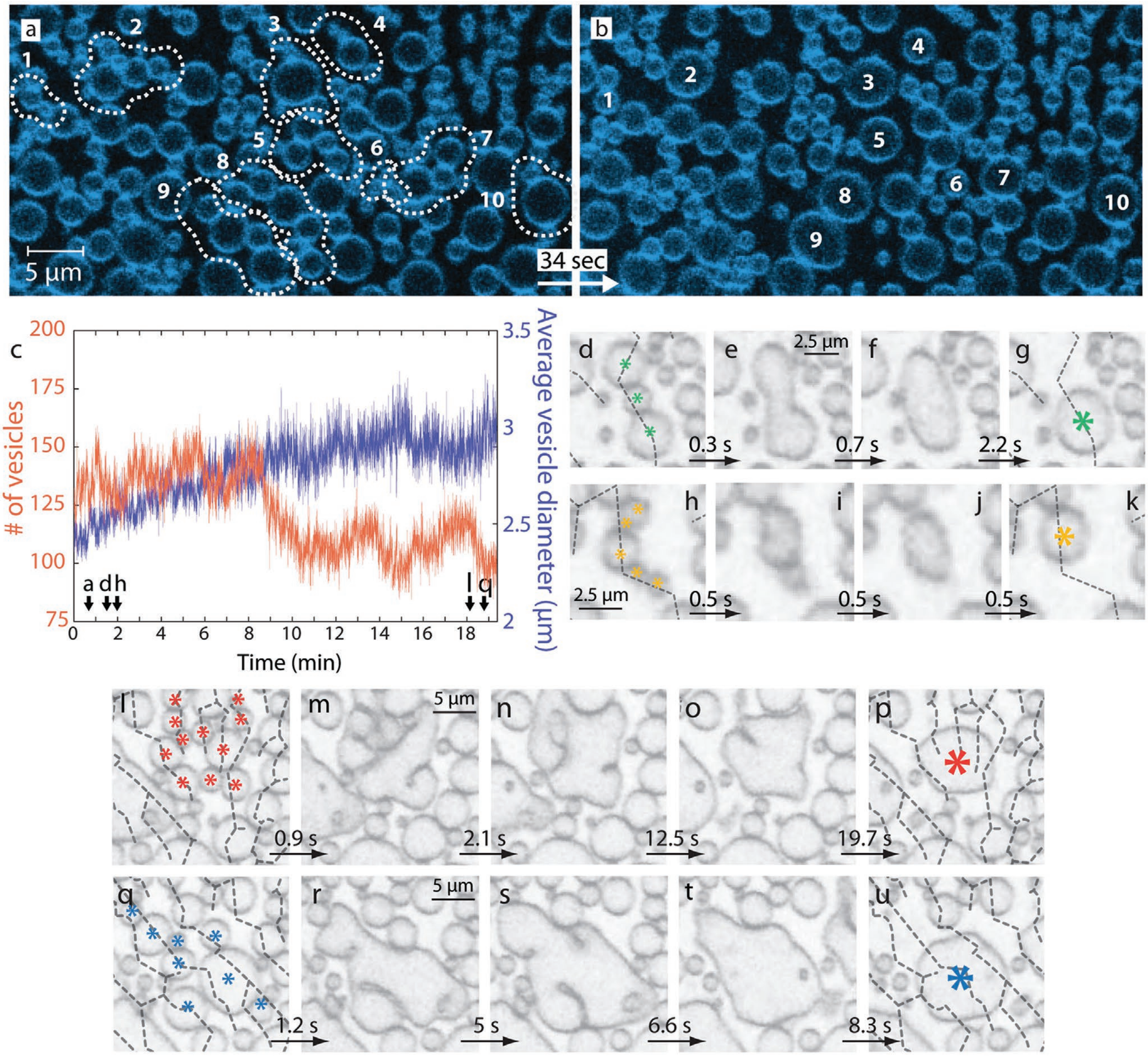

Figure 3. Heat induced protocell fusion. a,b) Confocal images showing the fusion of several protocells formed out of a lipid nanotube network upon exposure to the IR laser. The blue color assigned to the labeled lipid membranes is resulting from the false coloring of the gray scale images of the fluorescence signals, and is assigned arbitrarily. (a) The group of protocells which later merge after exposure to heat gradient, are encircled with dashed lines. Each encircled region is numbered. (b) The merged protocells. Each protocell has been formed or grown as a result of the fusion of the multiple, originally separated protocells shown in (a). The group of protocells and their fused version are numbered identically in (a) and (b). c) Plots showing the number of protocells (orange graph) and average protocell diameter (blue graph) over the complete course of the experiment partly shown in (a and b). d–k) Protocell fusion on same nanotube. (d–g) and (h–k) Two different fusion events in which the protocells on the same nanotube rapidly merge. l–u) Fusion of protocells which are originally located on separate nanotubes. (l–p) and (q–u) Two different events during which vesicular compartments, originally located on different nanotubes, later fuse.

during fusion. Figure 5c–g shows both the membrane and the RNA fluorescence emission channels, Figure 5h–j the membrane, and Figure 5k–m the RNA. Figure 5n–p shows the fluorescence intensity along the lines indicated with white dashed arrows in Figure 5k–m, respectively. The initially separate signals in Figure 5n merge into a signal of lower intensity (Figure 5o,p). The decrease may be due to two reasons. Upon activation of the IR laser the fluorescence intensity is reduced.[23] It is also possible that some of the internal contents is lost by leakage. The closure of the pores and retaining of the bulk of the encapsulated material is consistent with our earlier experiments of ≈3 orders of magnitude longer duration (seconds vs hours). Figure 5r–t (Movie S7, Supporting Information) shows snapshots of the fusion process of three compartments. In Figure 5s depicts the diffusion of fluorescent fragments during shape optimization of merging containers.

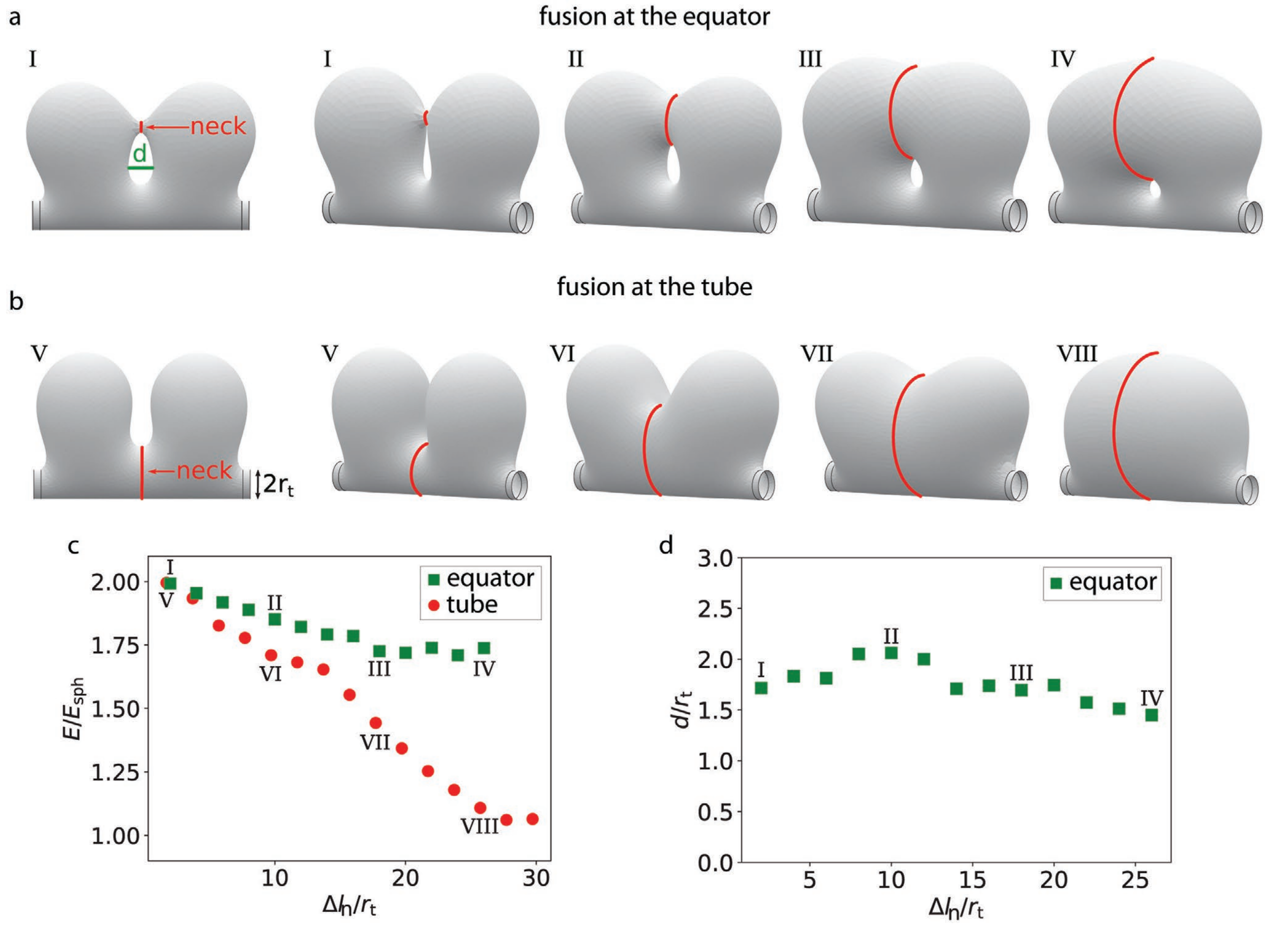

Figure 4. Mathematical model for fusion. Two compartments of equal size are connected to a membrane tube with diameter $2r_t$. Simulation snapshots are shown as the compartments fuse either a) at the compartments' equator region or b) at the connecting tube. The outer left snapshots on (a) and (b) show a side view parallel to the membrane tube, while the other snapshots are tilted to better illustrate the expansion of the fusion neck. c) The bending energy E, rescaled by the bending energy of the spherical compartment E_{sph}, decreases as the length of the contact line Δl_n increases. d) If the compartments fuse initially at their equator, a cavity forms between the fusion site and the membrane tube, with a stable diameter d that is similar to the diameter of the membrane tube.

3. Discussion

3.1. Protocell Nucleation Sites

Figure 2g reveals that, once the protocells nucleate, their total number remains constant during growth. This indicates that the sites of the nucleation are predetermined and nucleation is enhanced by the increased temperature. In Figure 1j the locations of the nucleation appear to coincide with Y- and V-junctions[24] on the nanotubes. Such membrane topologies are caused by pinning, i.e., simultaneous binding of Ca^{2+} to multiple lipid headgroups, which is facilitating the cohesion between two stacked bilayers[9,25,26] or between a bilayer and a solid interface.[9,27,28] In a previous study, the transformation of a Y-junction to a small vesicle, due to chemical chelator-induced depinning of Ca^{2+}, has been already shown.[24] In the current study, the Ca^{2+} depinning and reversal of membrane adhesion is not caused by chelators, but is due to the temperature increase.[10] The compartments are also observed exclusively at junction points (Figure 1j).

3.2. Mechanism of Rapid Growth and Fusion

The main driving force for the transformation of the nanotubes to protocellular compartments is the minimization of membrane curvature. The natural growth process in the previously reported system was slow (≈h).[3] The membrane replacement rate for the spontaneous inflation of a tube to a 5 µm vesicle, was estimated the to be $\approx 2 \times 10^{-3}$ µm^2 s^{-1}.[3] By contrast, in the current study the transformation occurs within minutes. We estimate the replacement rate to be 2 µm^2 s^{-1}, about three orders of magnitude higher than observed at room temperature. We attribute the facilitated protocell growth to the enhanced ability of lipid material to flow to the area of nucleation, due to the temperature increase in that area. The locally elevated temperature causes an increase in the membrane fluidity and in the membrane tension in the affected area. The tension increase causes Marangoni flow of lipids in the surrounding membrane region with relatively low membrane tension, toward the heated membrane region with high tension.

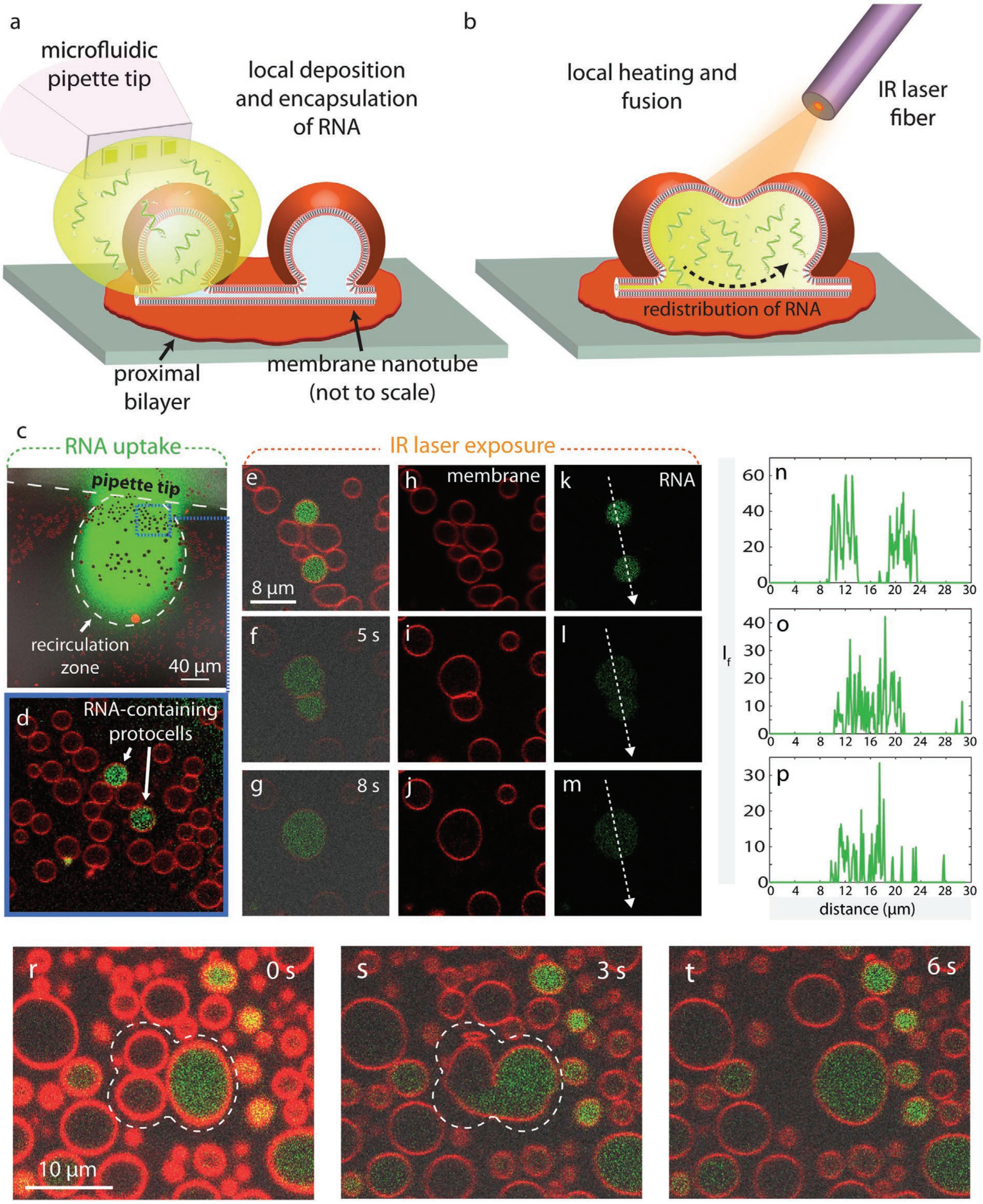

Figure 5. RNA encapsulation and redistribution. a,b) Schematic drawing showing the experimental setup. (a) An open-space microfluidic device is used for the superfusion of RNA-oligonucleotides with a designated membrane area populated with protocells. (b) IR laser is activated to induce fusion, leading to the redistribution of pre-encapsulated RNA into the fused protocell. c,d) RNA uptake. (c) Confocal image of a membrane area with the microfluidic pipette recirculating RNA above it (top view). The protocells in the recirculation zone appear as black dots. (d) Magnified view of the blue frame in (c) after termination of recirculation. Two protocells contain RNA. e–m) Laser scanning confocal microscopy images showing the fusion of RNA encapsulating protocells and redistribution of contents upon fusion. (e–g) Membrane, RNA fluorescence, and bright field channels are overlaid. (h–j) Membrane fluorescence channel only. (k–m) RNA fluorescence channel only. n–p) Plots showing the fluorescence intensity over the white dashed arrows in (k), (l), and (m), respectively. r–t) Laser scanning confocal microscopy images showing the fusion of RNA-encapsulating protocells and redistribution of contents upon fusion. Membrane, RNA fluorescence, and bright field channels are overlaid.

The result is the rapid growth of previously nucleated vesicular buds to cell-sized unilamellar compartments, some of which eventually establish physical contact with each other.

Fusion of lipid compartments that are in close proximity does not occur spontaneously, but requires external stimuli. There have been several studies focusing on the fusion of giant amphiphile vesicles as model systems of proto- or contemporary cells. The reported fusion mechanisms vary. Some examples are the fusion driven by attraction of oppositely charged vesicles,[29] fusion induced by multivalent ions between vesicles of special amphiphilic compositions, e.g., Eu^{3+}[30] or La^{3+},[31] ultraviolet light radiation-induced fusion,[32] electrofusion,[33] fusion involving amphiphilic catalysts,[34] also in combination with thermal cycles and pH changes,[35] and the fusion mediated by the hybridization of complementary SNARE proteins[36] or DNA linkers,[37] embedded in initially distinct vesicle membranes.

The vesicular membranes we utilize in this study do not contain embedded species which would facilitate fusion. The membranes and their individual monolayer leaflets possess the same composition, thus they are free of spontaneous curvature and have the same electrostatic potential. All experiments are performed at constant pH, under identical conditions. The main stimulus for fusion is the controlled increase in temperature. The temperature increase is known to lower the microviscosity of the membrane and facilitate the formation of defects, especially in the presence of multivalent ions.[38,39] Ca^{2+} binding perturbs the membrane by pulling the headgroups inward,[25,38] causing formation of defects. With localized heating this process is facilitated,[39] resulting in fusion.[40]

3.3. Impact of Nanotubes in Growth and Fusion

Figures 3 and 4 show that the nanotubes, which physically connect distant protocells, facilitate fusion. During growth, the nanotubes can provide an additional advantage for compound delivery. They provide a transport pathway for a continuous influx of molecules through the network, by which larger molecules can potentially also be transported. The transport of molecules or particles through nanotubes occurs by diffusion,[41,42] or is tension-driven (Marangoni flow).[15,16] The transport phenomena within the nanotube networks have not been investigated here, but the earlier established evidence of nanotube-enhanced transport between lipid vesicles combined with the involvement of nanotubes in the fusion process, as elucidated in this study, points to a beneficial contribution of an existing tubular network for growth, transport, and fusion of protocells.

3.4. Impact of Temperature in the Context of Origin of Life

In this study we show that a successive increase in temperature from 20 °C to ≈40, 70, and 90 °C on a nanotube network facilitates the nucleation, growth, and fusion of surface adhered protocells. The role of temperature has been a central discussion point in the origin of life debate.[43] The competing hypotheses regarding the environment for the emergence of the RNA world, concentrate either around deep ocean hydrothermal vents, or around warm ponds.[43] A major criticism for the emergence of life in hydrothermal environment[44] has been the hot temperatures, large pH gradients, high salinity, and high concentrations of divalent cations, which may adversely affect the amphiphile compartment formation. The hot environments typically referred to in such discussion involve black smoker type hydrothermal vents where temperature can commonly exceed 300 °C. In 2000, a new type of hydrothermal vent: the Lost City hydrothermal field (LCHF) with a chemical composition similar to lavas that erupted into the primordial oceans on early Earth, was discovered.[45] The temperature range of the LCHF is 40–90 °C, surprisingly similar to the experimental conditions used in this work that promote compartment formation, growth and fusion. This temperature range also represents the conditions in warm ponds: 50–80 °C.[43] Recent evidence shows that the mixtures of single chain amphiphiles form vesicles most readily at temperatures of ≈70 °C in aqueous solutions containing mono- and divalent cations in broad pH range.[7] In the light of these observations, it appears that warm temperatures of ponds or LCHFs can allow and even favor protocell compartmentalization. Our investigation focusing on the subsequent steps, i.e., the rapid growth and fusion, is in alignment with these recent findings.

Apart from temperature, another point disfavoring the hydrothermal vent hypothesis over the warm pond hypothesis, has been the lack of dry-wet cycles, which is known to significantly facilitate polymerization, e.g., from nucleotides to RNA.[43] In our experiments, the lipid reservoirs, i.e., multilamellar vesicles (MLVs), from which the double bilayer films spread and proceed to protocell formation, are the product of a dry-wet cycle. The lipid layers form in a dry environment and upon hydration they spontaneously form MLVs. It is conceivable that this is a repeatable process. Accordingly, protocell formation, growth, and fusion events we report here can in principle occur during dry-wet cycles. Potentially, a new cycle of protocell formation–growth–division can be started by attachment and fusion of fresh lipid reservoirs, i.e., multilamellar vesicles, to protocells that have been generated, grown, separated, and resettled on the substrate. It should be possible to experimentally investigate if simulated dry–wet, day–night, heating–cooling cycles support the formation of new protocell generations.

4. Conclusion

We show that the nucleation, growth, and fusion of protocells are significantly accelerated and enhanced at temperatures ranging from 40 to 90 °C. Some of the protocells generated in this manner have been demonstrated to encapsulate RNA, and to redistribute it upon fusion with other compartments. In the context of protocell development on the early Earth, these results suggest that both Lost City-type hydrothermal vents, and warm ponds could have been a suitable environment for protocell formation, growth, and fusion events. Additionally, a supporting surface in conjunction with the physical interconnections provided by the spontaneously formed nanotubular networks pose an advantage over lipid assemblies in bulk solution. Neighboring vesicles can join and fuse more rapidly than in bulk suspensions, where protocells would only randomly encounter each other for limited periods of time. To what extent it is possible for emerging protocells to chemically communicate prior to, and during, fusion processes through interconnecting tubes remains to be elucidated. If this can be verified, new hypotheses for primordial chemical transformations within primitive membrane structures in the early Earth environment can be experimentally investigated.

5. Experimental Section

Surface Fabrication and Characterization: An ≈84 nm SiO_2 film was deposited onto Menzel Gläser (rectangular) or Wilco Well (circular) glass substrates by either E-beam, or thermal Physical Vapor Deposition, using an EvoVac (Ångstrom Engineering) or L560K (Leybold) evaporator. The thickness of the films was verified by ellipsometry (SD 2000 Philips). No precleaning was performed before deposition. The substrates were stored at room temperature prior to use.

Formation of Lipid Nanotube Network and Protocells: The lipid nanotube network on a solid supported bilayer was formed as described earlier.[3] Briefly, a stock suspension of multilamellar lipid reservoirs containing 50% soybean polar lipid extract, 49% *Escherichia coli* polar lipid extract, and 1% Rhodamine-PE or Cy5-PE was prepared by the dehydration/rehydration method.[46] An aliquot from this suspension (4 µL) was dehydrated in a desiccator for 20 min. The dry film was rehydrated with HEPES buffer (≈1 mL) containing HEPES (10×10^{-3} м) and NaCl (100×10^{-3} м), pH 7.8, for 10 min to form multilamellar reservoirs. The reservoirs were then transferred into an open-top observation chamber on a SiO_2 substrate. The chamber contained HEPES buffer (≈ 1 mL) with HEPES (10×10^{-3} м), NaCl (100×10^{-3} м), and $CaCl_2$ (4×10^{-3} м), pH = 7.8. On the SiO_2 substrate the reservoirs self-spread as a double bilayer. The distal bilayer ruptures,[9] and a nanotubular network forms on the proximal bilayer.[3] Protocells on nanotubes were either formed spontaneously overnight (RNA redistribution experiments) or within seconds or minutes using local IR-B radiation (nucleation, growth, and fusion).

Heating System: The lipid nanotube network was heated locally using IR-B laser radiation through a flat optical fiber tip. A 1470 nm semiconductor diode laser (Seminex) in combination with a 50 µm core diameter, 0.22 NA multimode optical fiber (Ocean Optics), was used. The fiber was prepared by removing the outer sheath cladding, followed by carefully cutting and polishing using a fiber cleaning kit (Ocean Optics). The fiber was positioned using a 3-axis water hydraulic micromanipulator (Narishige, Japan) and the tip was located at 50 µm from the surface, resulting in a volume of ≈1 nL being efficiently heated. Three different laser intensities were employed. The laser current was adjusted to 0.72 A (protocell nucleation), 0.97 A (growth), and 1.21 A (fusion). The temperature was determined directly by a microthermocouple in situ (cf., Section S2, Supporting Information, for details).

Encapsulation with Microfluidic Pipette: An open-volume microfluidic device/pipette (Fluicell AB, Sweden),[22] positioned using a second 3-axis water hydraulic micromanipulator (Narishige, Japan), was used to expose the matured surface-adhered protocells to Ca^{2+}-HEPES buffer containing fluorescein sodium salt (100×10^{-6} м) (Sigma-Aldrich) and FAM-conjugated RNA oligonucleotides (40×10^{-6} м) (Dharmacon, USA), at pH 7.8.

Microscopy Imaging: A confocal laser scanning microscopy system (Leica SP8, Germany), with an HCX PL APO CS 40x (NA 1.3) oil objective was used for acquisition of the confocal images. The utilized excitation/emission wavelengths for the imaging of the fluorophores, were as follows: λ_{ex}: 560 nm, λ_{em}: 583 nm for membrane fluorophore Rhodamine-PE, λ_{ex}: 655 nm, λ_{em}: 670 nm for Cy5, λ_{ex}: 488 nm, λ_{em}: 515 nm for fluorescein (SI), λ_{ex}: 494 nm, λ_{em}: 525 nm for FAM.

Image Processing/Analysis: 3D fluorescence images were reconstructed using the Leica Application Suite X Software (Leica Microsystems, Germany). Image enhancements to fluorescence images were performed with the NIH Image-J Software and Adobe Photoshop CS4 (Adobe Systems, USA). The colors assigned to the labeled lipid membranes (red and blue) and to labeled RNA (green) are resulting from the false coloring of the gray scale images of the fluorescence signals, and are assigned arbitrarily. Schematic drawings and image overlays were created with Adobe Illustrator CS4 (Adobe Systems, USA). Protocell counts, density, size distribution, total membrane area, and volume analyses were also performed in Image-J and plotted in Matlab R2018a. The analysis of protocell number and size over time during fusion was performed with Matlab. Fluorescence intensity profiles were drawn in Matlab after applying median filtering.

Supporting Information

Supporting Information is available from the Wiley Online Library or from the author.

Acknowledgements

The authors thank A. Jesorka from Chalmers University of Technology, Sweden, for technical advice on temperature measurements. This work was made possible through financial support obtained from the Research Council of Norway (Forskningsrådet), Project Grant No. 274433, UiO: Life Sciences Convergence Environment, the Swedish Research Council (Vetenskapsrådet), Project Grant No. 2015-04561, as well as the startup funding provided by the Centre for Molecular Medicine Norway (RCN 187615), and the Faculty of Mathematics and Natural Sciences at the University of Oslo. S.L. and A.C. gratefully acknowledge funding from the Research Council of Norway, Project Grant No. 263056, and R.R. the H2020 ITN "Chemical Reaction Networks – CReaNET" – Ref. 812868.

Conflict of Interest

The authors declare no conflict of interest.

Author Contributions

E.S.K. and I.G. designed the research, E.S.K., S.L., L.X., R.R., A.C., and I.G. performed the research, E.S.K., L.X., R.R., and L.V. analyzed the experimental data, and all authors contributed to the drafting of the paper. I.G. suggested the investigation of the behavior of lipid compartments in thermal gradients and supervised the project.

Keywords

lipid nanotubes, origin of life, protocells, temperature-induced fusion

Received: April 21, 2020
Revised: June 26, 2020

[1] M. M. Hanczyc, S. S. Mansy, J. W. Szostak, *Origins Life Evol. Biospheres* **2007**, *37*, 67.
[2] M. M. Hanczyc, S. M. Fujikawa, J. W. Szostak, *Science* **2003**, *302*, 618.
[3] E. S. Koksal, S. Liese, I. Kantarci, R. Olsson, A. Carlson, I. Gozen, *ACS Nano* **2019**, *13*, 6867.

[4] İ. Gözen, *ACS Nano* **2019**, *13*, 10869.
[5] B. Xu, J. Xu, T. Yomo, *Biochem. Soc. Trans.* **2019**, *47*, 1909.
[6] O. Sandre, L. Moreaux, F. Brochard-Wyart, *Proc. Natl. Acad. Sci. USA* **1999**, *96*, 10591.
[7] S. F. Jordan, H. Rammu, I. N. Zheludev, A. M. Hartley, A. Marechal, N. Lane, *Nat. Ecol. Evol.* **2019**, *3*, 1705.
[8] S. Jõemetsa, K. Spustova, K. Kustanovich, A. Ainla, S. Schindler, S. Eigler, T. Lobovkina, S. Lara-Avila, A. Jesorka, I. Gözen, *Langmuir* **2019**, *35*, 10286.
[9] I. Gozen, P. Dommersnes, I. Czolkos, A. Jesorka, T. Lobovkina, O. Orwar, *Nat. Mater.* **2010**, *9*, 908.
[10] I. Gözen, M. Shaali, A. Ainla, B. Örtmen, I. Põldsalu, K. Kustanovich, G. D. M. Jeffries, Z. Konkoli, P. Dommersnes, A. Jesorka, *Lab Chip* **2013**, *13*, 3822.
[11] C. Billerit, I. Wegrzyn, G. D. M. Jeffries, P. Dommersnes, O. Orwar, A. Jesorka, *Soft Matter* **2011**, *7*, 9751.
[12] C. Billerit, G. D. M. Jeffries, O. Orwar, A. Jesorka, *Soft Matter* **2012**, *8*, 10823.
[13] C. I. McPhee, G. Zoriniants, W. Langbein, P. Borri, *Biophys. J.* **2013**, *105*, 1414.
[14] K. I. Akashi, H. Miyata, H. Itoh, K. Kinosita Jr., *Biophys. J.* **1996**, *71*, 3242.
[15] R. Karlsson, M. Karlsson, A. Karlsson, A. S. Cans, J. Bergenholtz, B. Åkerman, A. G. Ewing, M. Voinova, O. Orwar, *Langmuir* **2002**, *18*, 4186.
[16] P. G. Dommersnes, O. Orwar, F. Brochard-Wyart, J. F. Joanny, *Europhys. Lett. (EPL)* **2005**, *70*, 271.
[17] G. Bolognesi, M. S. Friddin, A. Salehi-Reyhani, N. E. Barlow, N. J. Brooks, O. Ces, Y. Elani, *Nat. Commun.* **2018**, *9*, https://doi.org/10.1038/s41467-018-04282-w.
[18] J. Prives, M. Shinitzky, *Nature* **1977**, *268*, 761.
[19] K. A. Brakke, *Exp. Math.* **1992**, *1*, 141.
[20] K. A. Brakke, Surface Evolver Manual Version 2.70, **2013**.
[21] W. Helfrich, *Z. Naturforsch. C* **1973**, *28*, 693.
[22] A. Ainla, G. D. M. Jeffries, R. Brune, O. Orwar, A. Jesorka, *Lab Chip* **2012**, *12*, 1255.
[23] I. Wegrzyn, A. Ainla, G. D. M. Jeffries, A. Jesorka, *Sensors* **2013**, *13*, 4289.
[24] T. Bilal, I. Gözen, *Biomater. Sci.* **2017**, *5*, 1256.
[25] A. Melcrová, S. Pokorna, S. Pullanchery, M. Kohagen, P. Jurkiewicz, M. Hof, P. Jungwirth, P. S. Cremer, L. Cwiklik, *Sci. Rep.* **2016**, *6*, https://doi.org/10.1038/srep38035.
[26] K. I. Akashi, H. Miyata, H. Itoh, K. Kinosita Jr., *Biophys. J.* **1998**, *74*, 2973.
[27] T. Lobovkina, I. Gözen, Y. Erkan, J. Olofsson, S. G. Weber, O. Orwar, *Soft Matter* **2010**, *6*, 268.
[28] A. Kunze, F. Zhao, A. K. Marel, S. Svedhem, B. Kasemo, *Soft Matter* **2011**, *7*, 8582.
[29] D. P. Pantazatos, R. C. MacDonald, *J. Membr. Biol.* **1999**, *170*, 27.
[30] C. K. Haluska, K. A. Riske, V. Marchi-Artzner, J. M. Lehn, R. Lipowsky, R. Dimova, *Proc. Natl. Acad. Sci. USA* **2006**, *103*, 15841.
[31] T. Tanaka, M. Yamazaki, *Langmuir* **2004**, *20*, 5160.
[32] Y. Suzuki, K. H. Nagai, A. Zinchenko, T. Hamada, *Langmuir* **2017**, *33*, 2671.
[33] N. G. Stoicheva, S. W. Hui, *Biochim. Biophys. Acta, Biomembr.* **1994**, *1195*, 31.
[34] K. Adamala, J. W. Szostak, *Nat. Chem.* **2013**, *5*, 495.
[35] K. Kurihara, Y. Okura, M. Matsuo, T. Toyota, K. Suzuki, T. Sugawara, *Nat. Commun.* **2015**, *6*, https://doi.org/10.1038/ncomms9352.
[36] J. J. Diao, Y. Ishitsuka, H. Lee, C. Joo, Z. L. Su, S. Syed, Y. K. Shin, T. Y. Yoon, T. Ha, *Nat. Protoc.* **2012**, *7*, 921.
[37] Y. H. M. Chan, B. van Lengerich, S. G. Boxer, *Proc. Natl. Acad. Sci. USA* **2009**, *106*, 979.
[38] M. A. Wilson, A. Pohorille, *J. Am. Chem. Soc.* **1996**, *118*, 6580.
[39] P. Urban, S. R. Kirchner, C. Mühlbauer, T. Lohmüller, J. Feldmann, *Sci. Rep.* **2016**, *6*, https://doi.org/10.1038/srep22686.
[40] T. D. Ingolia, D. E. Koshland, *J. Biol. Chem.* **1978**, *253*, 3821.
[41] L. Lizana, Z. Konkoli, *Phys. Rev. E* **2005**, *72*, https://doi.org/10.1103/PhysRevE.72.026305.
[42] L. Lizana, Z. Konkoli, O. Orwar, *J. Phys. Chem. B* **2007**, *111*, 6214.
[43] B. K. D. Pearce, R. E. Pudritz, D. A. Semenov, T. K. Henning, *Proc. Natl. Acad. Sci. USA* **2017**, *114*, 11327.
[44] D. Milshteyn, B. Damer, J. Havig, D. Deamer, *Life* **2018**, *8*, 11.
[45] W. Martin, J. Baross, D. Kelley, M. J. Russell, *Nat. Rev. Microbiol.* **2008**, *6*, 805.
[46] M. Karlsson, K. Nolkrantz, M. J. Davidson, A. Stromberg, F. Ryttsen, B. Akerman, O. Orwar, *Anal. Chem.* **2000**, *72*, 5857.

Supplementary Information for:

Rapid Growth and Fusion of Protocells in Surface-adhered Membrane Networks

Elif S. Köksal, Susanne Liese, Lin Xue, Ruslan Ryskulov, Lauri Viitala, Andreas Carlson, Irep Gözen*

*To whom correspondence should be addressed. Email: irep@uio.no

This PDF file includes:

Supplementary text
- S1. Experimental setup
- S2. Characterization of IR-laser heating
- S3. Image analyses
- S4. Details of computational model
- S5. Stable pore formation in fused compartments
- S6. Encapsulation of fluorescein vs. RNA by the protocells

Figures S1 to S7
Captions for movies S1 to S7
References for SI

Other supplementary materials for this manuscript include the following:

Movies S1 to S7
Matlab Script: Detection of vesicular compartments from micrographs

S1. Experimental setup

The optical fiber for co-application of IR-B radiation and the microfluidic pipette for the superfusion of RNA-oligonucleotides were positioned above the substrate surface, using 3-axis water hydraulic micromanipulators (**Figure S1**). The tip of the fiber and the pipette are placed on opposite sides in order to target the same membrane area on the substrate. The inset in the upper left corner of **Figure S1** shows the flat polished tip of the optical fiber with a core diameter of 50 μm.

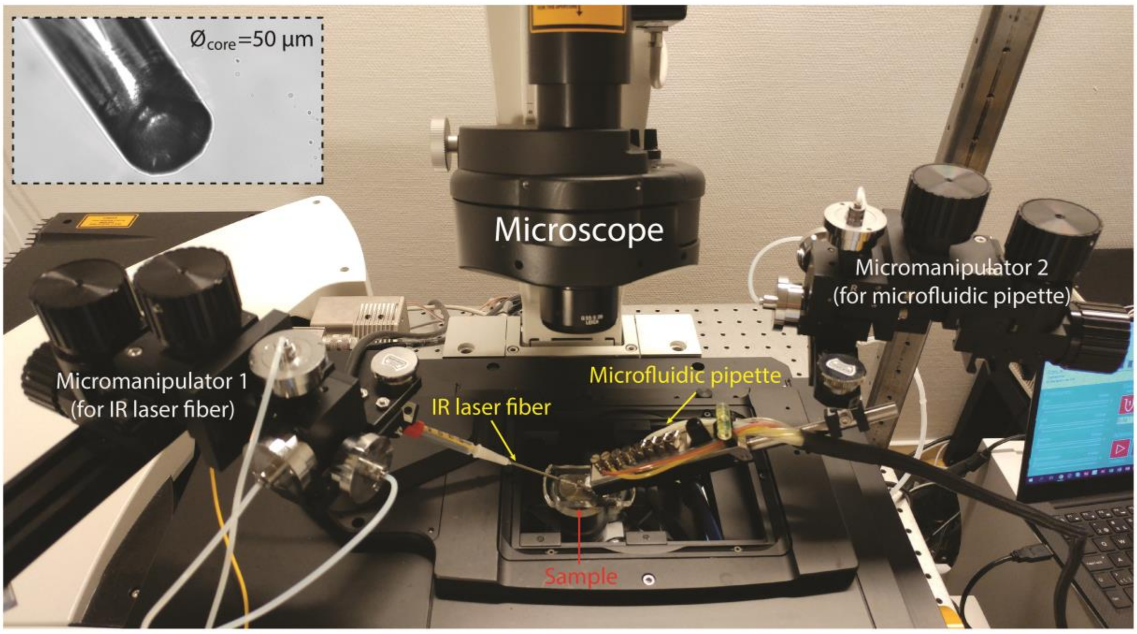

Figure S1 | Photograph of the experimental setup. Inset: flat tip of the IR laser fiber.

S2. Characterization of IR-laser heating

The local temperature changes caused by the IR laser heating were estimated from the absolute temperature measurements with a CHCO-005 E-type microtemp thermocouple (junction diameter: 25 μm, Omega Engineering, UK). Optical fiber and thermocouple were positioned above the sample using motorized micromanipulators (Scientifica, UK) (**Figure S2a**). For the measurements, the thermocouple was placed above the surface in the center of the heated region. Temperatures were recorded while the thermocouple was lifted up in z-direction in 10 μm steps. Measurements were performed for three different laser intensities, as employed in the compartment formation, growth and merging experiments. Plots of the obtained data are presented in **Figure S2b**.

Due to the unavoidable direct absorption of IR irradiation by the thermocouple itself, the measured temperatures are somewhat higher than the actual temperatures in the medium. This is particularly grave in the range between 0-40 μm in z-direction (open circles in **Figure S2b**), where the measured temperatures increase to unphysical values above the boiling point of water. Since boiling is not observed, we can conclude that the actual temperatures are below 100 °C. These data points were excluded, and only the data points shown with filled circles are fitted by means of a linear regression in order to estimate the temperature on the surface (*z*=0). According to this approximation, the lipid sample is heated up to temperatures of 39, 89 and 122 °C (as measured, see section below for discussion of these values) when the laser diode current is 0.73, 0.97 and 1.22 A, respectively. The directly measurable laser current is stated rather than the laser power, which can be extracted from the U/I/P chart in the manufacturer data sheet (www.seminex.com) of the 4PN-104 1470 nm (NA 0.22 fiber coupled) laser diode. The continuous wave power output at 1 A corresponds to approximately 100 mW.

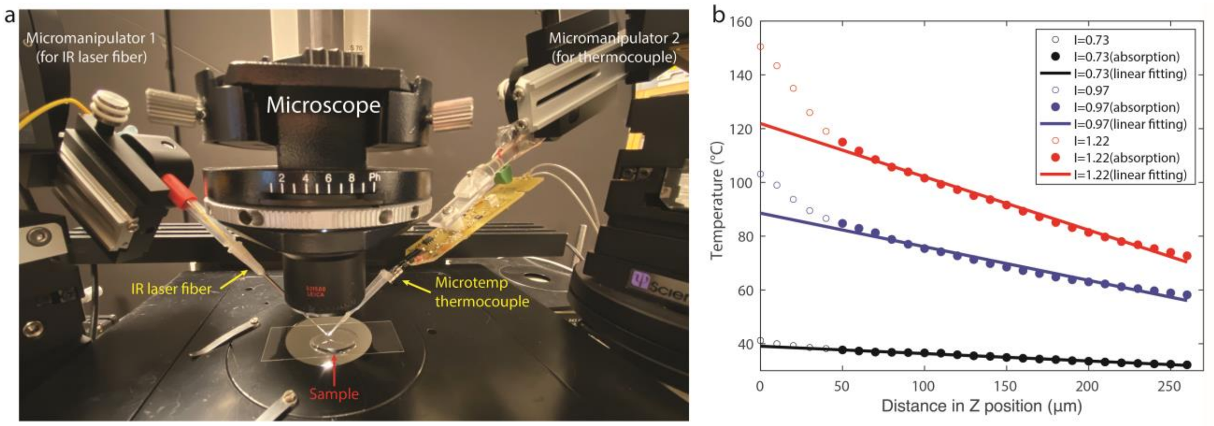

Figure S2 | Characterization of the local temperature profile caused by IR-laser heating. (a) Photograph of the experimental setup for the temperature measurement using thermocouple. **(b)** Plot of measured temperatures at three different laser intensities employed in the experiments.

We can distinguish between three different temperature ranges for each of the three different laser settings. There may be an additional component in the temperature/distance relationship for the two higher laser power settings for the height range between 200 and 250 μm distance from the surface, which corresponds to the situation where the thermocouple is outside the irradiated volume (cone of acceptance), which we have not considered in the analysis. At the lowest power setting, the direct absorption by the thermocouple metal is greatly reduced, due to the almost complete absorption of the light by the water volume in between fiber end and thermocouple. The measured values are for this setting accordingly very close to the actual temperatures near the membrane. Temperatures obtained from the measurements for the two higher power settings are biased by the self-absorption of the thermocouple, and need to be also corrected for the influence of strong local heat convection, which continuously supplies a stream of cold medium to the lipid assemblies on the surface. We estimate that the temperatures on the surface are likely not exceeding 70 and 90 °C for the two higher power settings. More accurate direct temperature determinations would be possible using ion conductivity measurements in a glass capillary,[1] or a different means of temperature control (bulk heating) can be considered.

S3. Image analyses

We performed image analysis using Matlab2018a to detect the compartments in the recorded micrographs to be able to count their number and to calculate their diameter, over time. Briefly, a suitable threshold to convert the gray scale micrographs to binary images, was adjusted every 250 frames of the time series to correct the intensity fluctuations, photo-bleaching and similar effects. Next, *imfindcircles* function was used to detect the circles using circular Hough transform. **Figure S3** shows a sample output image from the analysis shown in **Figure 3c**. A Matlab script has been provided as a separate supplementary file.

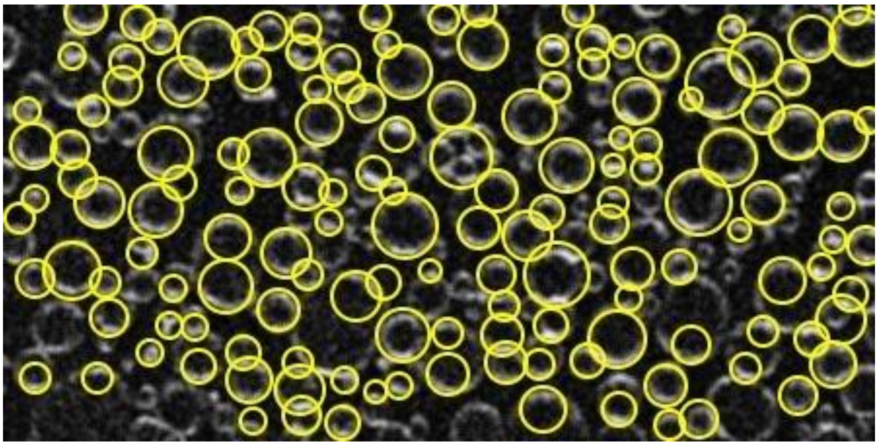

Figure S3 | Sample output image of *imfindcircles* function of Matlab, showing the identified circular compartments.

S4. Details of computational model

We perform two sets of simulations: (1) fusion initiating at the equator of the compartments and (2) fusion initiating along the connecting tube. For both simulations the initial configurations are similar (schematically depicted in **Figure S4**). In the first case, the vertices highlighted in red are connected along the contact (neck) line (red solid line in **Figure S4**), and the circumference of the contact line is constrained. In the second case, two vertices with the same initial coordinates are placed along the red dashed line in **Figure S4**, which allows us to define two faces that separate the two neighboring vesicles. In the set of simulations regarding case 1, the energy minimization leads to a separation of the vertices within the first steps, thus preventing an intersection of the two vesicles. In the second set of simulations the midline along the tube (red dashed line in **Figure S4**) is constrained. In all simulations, the outer points (shown in green in **Figure S4**) and the faces between them are constrained to a cylinder of radius 1, where we define all lengths in units of the cylinder radius. The lowest vertices and the lines connecting these vertices are constrained to a height z=0, while all other vertices, lines and faces are constrained to *z*>0. The total area is constrained to 450.

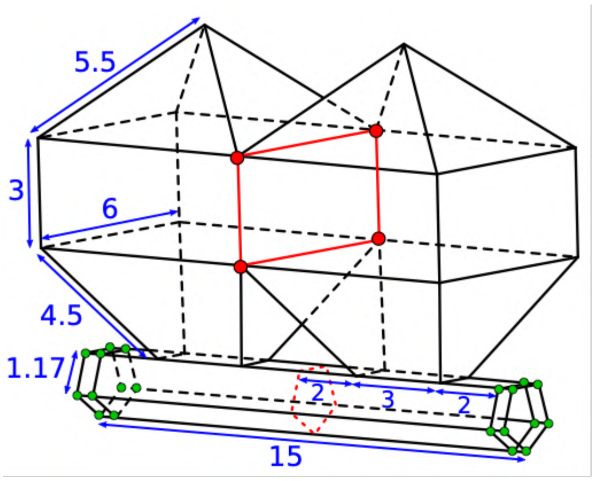

Figure S4 | Initial configuration of the simulation. All lengths are given in units of the tube radius.

We determined the bending energy by integrating the mean curvature over the entire surface, using the built-in *star_perp_sq_mean_curvature* method. The *Surface Evolver* software[2] uses finite element methods on a two-dimensional mesh in space to minimize the bending energy, which is defined as the integral of the squared mean curvature over the surface. The bending energy E_v of each vertex reads:

$$E_v = A_v \frac{3}{4} \left(\frac{\nabla A_v \boldsymbol{N}_v}{\boldsymbol{N}_v \boldsymbol{N}_v} \right)^2, \tag{1}$$

with A_v the area of the facets adjacent to the vertex and $\boldsymbol{N}_v$ the volume gradient, which is defined as:

$$\boldsymbol{N}_v = \frac{1}{6} (\boldsymbol{v}_1 \times \boldsymbol{v}_2 + \boldsymbol{v}_2 \times \boldsymbol{v}_3 + \cdots + \boldsymbol{v}_n \times \boldsymbol{v}_1), \tag{2}$$

with $\boldsymbol{v}_1, \ldots, \boldsymbol{v}_n$the neighboring vertices. A detailed description of the numerical methods can be found in the *Surface Evolver* manual.[3]

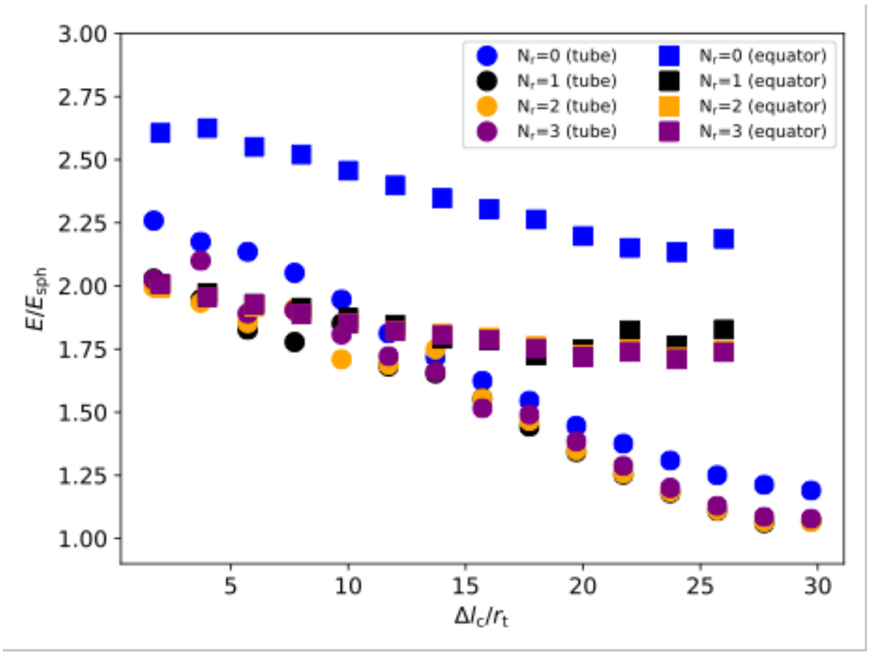

Figure S5 | The bending energy, rescaled by the energy of a spherical vesicle is shown in dependence of the length of the contact line. The number of mesh refinements N_r, corresponding to simulation step 1, 2, 3 and 4 are shown in different colors.

The equilibrated membrane shape is obtained through a series of four energy minimization steps, which read in the *Surface Evolver* letter code:

Fusion at the tube:

step 1: {g 20; u}3;{{V;g 20}30; u ;g 20}2
step 2: r;w 0.1;U;{V;g 50}10; U;g 20
step 3: r;w 0.05;U;{V;g 50}10; U;g 20
step 4: r;w 0.02;U;V;g 50;u;{V;g 50}9; U;g 20

Fusion at the equator:

step 1: g 50; u; g 100;U; g 100;U
step 2: r;w 0.1;{{u;g 50}4;{V;g 50}}2;g 20
step 3: r;w 0.05;{{u;g 50}4;{V;g 50}}2;g 20
step 4: r;w 0.02;{{u;g 50}4;{V;g 50}}2;g 20

Step 2, 3 and 4 start with a mesh refinement (‘r’). In **Figure S5** we see that only the first mesh refinement leads to a significant improvement of the energy minimization. In **Figure 4** in the main text the minimal energy found within the four simulation steps is shown.

S5. Stable pore formation in fused compartments

The mathematical model for fusion shows the formation of a stable pore when fusion initiates at the equator of two adjacent compartments. We also observe stable pores in fused compartments in our experiments (**Figure S6**, also **Figure 3** of the main manuscript). Such pores are not observed before fusion, or if the fusion occurs between the compartments initially residing on the same nanotube (**Figure 3d-k** for fused compartments initially were on the same nanotube vs. **Figure 3l-u** for compartments initially were on different nanotubes).

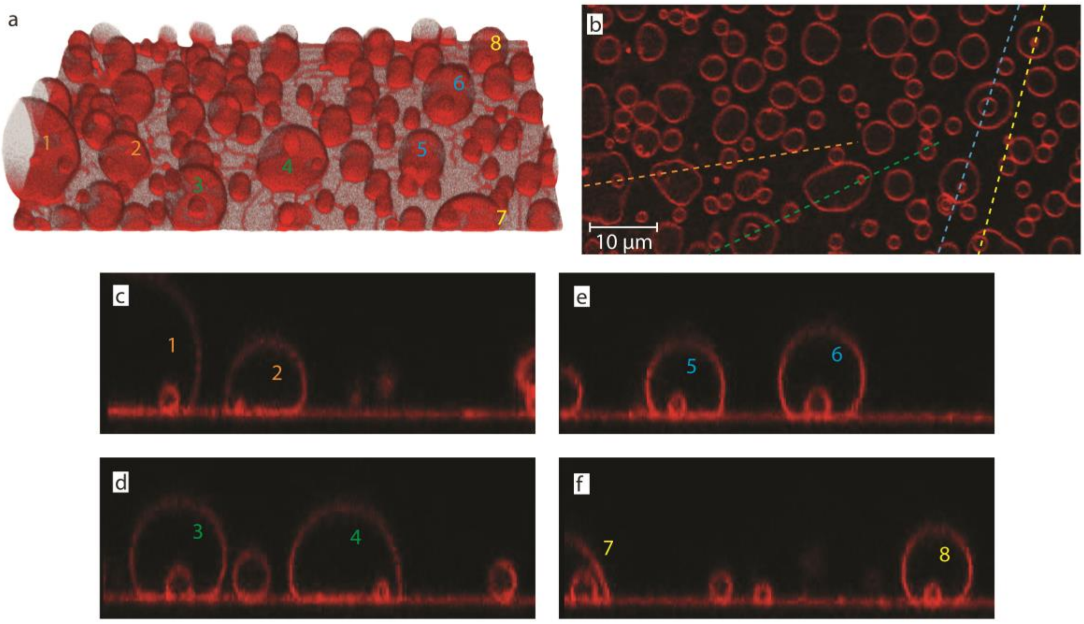

Figure S6 | Stable pores in fused compartments. (a) 3D confocal micrograph of the formed protocells **(b)** cross section of protocell sample close to the surface (x-y plane) **(c-f)** cross sections of protocell sample (x-z plane). Protocells numbered 1-8 in **(a)** have small cavities formed after fusion of adjacent protocells. Cross sectional profile of the numbered protocells, along the color-coded dashed lines in **(b)**, are shown in **(c-f)**.

S6. Encapsulation of fluorescein vs. RNA inside the protocells

As described in the manuscript, we delivered the RNA to the compartments locally using an open-space microfluidic device which resulted in the encapsulation of RNA inside some of the compartments. FAM conjugated 10 base long polyA RNA oligonucleotides were prepared in nuclease-free water. For experiments, the RNA concentration was adjusted to 40 µM with HEPES buffer. The encapsulation efficiency of free fluorescein sodium salt is compared to FAM-RNA oligonucleotides. The fluorescein encapsulation shows higher efficiency (**Figure S7**). Only a few protocells encapsulate and maintain RNA fragments. This might be due to the higher molecular weight and structure of RNA compared to the fluorescein dye.

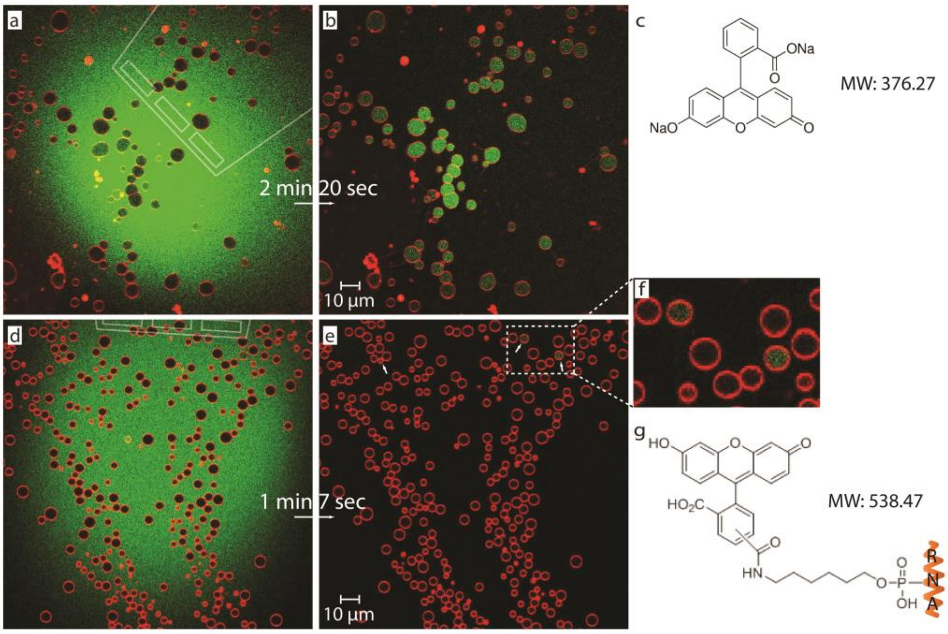

Figure S7 | Encapsulation of fluorescein dye vs. FAM conjugated RNA oligonucleotides. A microfluidic pipette is used for the superfusion of free fluorescein and FAM-conjugated RNA oligonucleotides to a membrane area populated with protocells. **(a)** Confocal micrograph of a membrane area with the microfluidic pipette re-circulating free fluorescein above it (top view). **(b)** After exposure is stopped, the initially fluorescein-free compartments are observed with fluorescein cargo. **(c)** fluorescein sodium salt molecule (MW: 376.27 g/mol). **(d)** Confocal micrograph of a membrane area with the microfluidic pipette re-circulating FAM-conjugated RNA fragments above it (top view). **(e)** After exposure, only a few protocells, shown in **(e)** (white arrows), and in **(f)**, encapsulate and maintain RNA fragments in the ambient aqueous solution. **(g)** Fluorophore-conjugated RNA molecule (MW: 538.47 g/mol).

S7. Supplementary Movies

Movie S1-3 | Rapid nucleation and growth of protocells. Movies S1-S3 show the rapid nucleation and growth of vesicular compartments from the underlying lipid nanotube network upon increase in temperature.

The region shown in Movie S1 ‘Experiment 2’ corresponds to **Figure 1c-e** and **Figure 2a**. The region shown in Movie S1 ‘Experiment 1’ corresponds to **Figure 1f-h**. ‘Experiment 1-2’ in Movie S1 is accelerated 94x and 71x, respectively.

‘Experiment 3-5’ in Movie S2 are accelerated 101x, 114x and 136x, respectively.

The region shown in Movie S3 corresponds to **Figure 2c-f**, and the movie is accelerated 5x.

Movie S4-6 | Fusion of protocells. Movie S4-S6 show the fusion of protocells on lipid nanotube networks upon exposure to higher intensity IR laser radiation.

Movie S4 and S5 correspond to **Figure 3**. In Movie S5, the outline of lipid nanotube network is overlaid to facilitate the observation of location of fusion events with respect to the nanotubes, i.e. same or different tubes. Movies are sped up 5x. Between each part (Part I-III) the recording is stopped and re-started.

Movie S6 is accelerated 85x.

Movie S7 | Encapsulation of RNA oligonucleotides and following fusion of protocells. Movie S7 shows the superfusion of FAM-conjugated RNA oligonucleotides by means of a microfluidic pipette (Part I) followed by fusion events induced by activation of the IR laser (Part II).

Movie S7 Experiment 1 and Experiment 2 correspond to **Figure 5c-m** and **Figure 5r-t**, respectively. Movies are accelerated 5x.

References

1. Zeeb, V.; Suzuki, M.; Ishiwata, S., *Journal of Neuroscience Methods* **2004,** *139* (1), 69-77. DOI 10.1016/j.jneumeth.2004.04.010.
2. Brakke, K. A., *Experimental Mathematics* **1992,** *1* (2), 141-165. DOI 10.1080/10586458.1992.10504253.
3. Brakke, K. A. *Surface Evolver Manual Version 2.70*; **2013**.

II

Nanoscale

ROYAL SOCIETY OF CHEMISTRY

PAPER

View Article Online
View Journal | View Issue

Check for updates

Cite this: *Nanoscale*, 2022, **14**, 10418

Transport among protocells *via* tunneling nanotubes†

Ingrid Jin Schanke, ‡ Lin Xue, ‡ Karolina Spustova and Irep Gözen *

Received 26th April 2022,
Accepted 11th June 2022

DOI: 10.1039/d2nr02290g

rsc.li/nanoscale

We employ model protocell networks for evaluation of molecular transport through lipid nanotubes as potential means of communication among primitive cells on the early Earth. Network formation is initiated by deposition of lipid reservoirs onto a SiO_2 surface in an aqueous environment. These reservoirs autonomously develop into surface-adhered protocells interconnected *via* lipid nanotubes while encapsulating solutes from the ambient buffer. We observe the uptake of DNA and RNA, and their diffusive transport between the lipid compartments *via* the interconnecting nanotubes. By means of an analytical model we determine key physical parameters affecting the transport, such as nanotube diameter and compartment size. We conclude that nanotube-mediated transport could have been a possible pathway of communication between primitive cells on the early Earth, circumventing the necessity for crossing the membrane barrier. We suggest this transport as a feasible means of RNA and DNA exchange under primitive prebiotic conditions, possibly facilitating early replication.

Introduction

How the first living cell emerged from prebiotic matter on the early Earth is still an unsolved question. Current studies focusing on this problem utilize synthetic model precursors of primitive cells, the 'protocells'. Protocells carry features of living cells, but are structurally and functionally much simpler.[1] A feature in common with a modern cell, which is surrounded by a plasma membrane is a biosurfactant bilayer, which establishes a boundary, an identity, and an interface suitable for chemical exchange.[2,3] A bilayer envelope satisfies one of the three conditions of the Chemoton model, the hypothetical chemical entity which features all necessary criteria of 'living'.[4] A membranous protocell is typically prepared under laboratory conditions *via* self-assembly of bulk amphiphiles in an aqueous solution.[2,3]

In order to cross the boundary between the non-living and living matter, a primitive cell needs to be able to develop, grow and eventually self-replicate, resulting in formation of genetically identical daughter cells. To undergo Darwinian evolution during this process, protocells should attain the ability to sense, and adapt to, relevant changes in the environment. Such changes can include perturbations caused by other protocells. Modern cells, for example, can communicate by secreting chemical signals into their surroundings, which is recognized by nearby cells, that are either in direct contact, or a short distance away.[5–9] The response can be manifold, for example tuning the gene expression to change density of the cell population, or induce cell division. Whether bacteria or eukaryotes, cellular communication and division pathways require the coordination of multiple sets of proteins and ligands[7] which primitive cells were initially lacking. How protocells could have attained over time the ability to expediently perform communication and division, is a pending question.

Recently, we reported spontaneous formation of protocell-nanotube networks following a set of autonomous shape transformations on solid substrates.[10,11] The resulting structure is a population of surface-adhered protocells interconnected with lipid nanotubes. The nanotubular structures within the networks resemble the tunneling nanotubes (TNTs) between mammalian cells, which enable direct communication by transporting signaling molecules and even organelles.[12,13] TNTs are also observed in bacterial cells, and likely provide an alternative route of intercellular exchange of cytoplasmic molecules and plasmids.[14–17] Whether the nanotubes in protocell networks[10] would allow the transport of molecules, *e.g. via* molecular diffusion,[18] was initially not established.

In this work, we have investigated the ability of lipid nanotubes in surface-supported networks to transport prebiologically relevant constituents between the compartments: small water-soluble molecules, RNA and DNA. The protocell networks were formed for that purpose from label-free lipid membranes, allowing the focus of observations to be solely on fluorescently-labeled cargo. Our findings confirm that the nano-

---

Centre for Molecular Medicine Norway, Faculty of Medicine, University of Oslo, 0318 Oslo, Norway. E-mail: irep@uio.no

† Electronic supplementary information (ESI) available. See DOI: **https://doi.org/10.1039/d2nr02290g**

‡ These authors contributed equally to this work.

tubes function as tunneling interconnections between protocells, and are capable of transporting molecules and genetic polymers diffusively among them. We also characterized, supported by a dynamic analytical model, key physical parameters that are influential for the transport process. We hypothesize that nanotubes could have established a feasible means of communication and replication between prebiotic protocells, as in the investigated environment identical RNA and DNA fragments are easily distributed to nearby network nodes.

Results and discussion

Formation of protocell-nanotube networks free of fluorophore

We started our experiments by preparing protocell-nanotube networks (PNNs) according to the protocol by Köksal *et al.*[10] Briefly, a suspension of multilamellar vesicles (MLVs) is brought in contact with a SiO_2 surface in an aqueous environment. Upon contact with the surface, each MLV acts as a lipid reservoir and spontaneously spreads as a double bilayer membrane, driven by the surface adhesion. Continuous spreading causes a buildup of membrane tension, and the distal (upper with respect to the surface) bilayer eventually ruptures followed by its transformation to a network of lipid nanotubes. The network resides on the proximal (lower) bilayer. In order to minimize the membrane curvature and overall surface free energy, sections of the nanotubes swell over time and form spherical unilamellar compartments. The resulting structure is a PNN consisting of several lipid compartments connected *via* lipid nanotubes. The detailed characterization of this process was reported in our earlier work.[10,11] A schematic drawing and a fluorescence micrograph of a fluorescently-labeled PNN (control) are shown in Fig. 1a and b respectively. Thereafter we prepared PNNs from label-free lipid membranes in order to exclusively visualize cargo molecules in the network without crosstalk[19] with membrane fluorescence.

We used differential interference contrast (DIC) microscopy to visualize the label-free PNNs (Fig. 1c–h), and the lipid nanotubes therein (Fig. 1d, e, g and h). The lack of fluorophore-conjugated lipids appeared to not interfere with the spontaneous formation of phospholipid protocell-nanotube networks. Overall, the findings were consistent with the PNNs formed from lipid preparation containing labeled phospholipids (Fig. 1b).

Encapsulation and transport of cargo

Following the formation of PNNs, we introduced fluorescent cargo to the ambient solution in the vicinity of the compartments by means of an open-volume microfluidic device.[20,21] A selected sample region was locally superfused with an aqueous buffer containing the cargo molecules (Fig. 2a). The supplied cargo molecules were ATTO 488 (Fig. 2a), a 10-base RNA labeled with fluorescein amidite (FAM), or a 20-base single-stranded DNA (ssDNA), also labeled with FAM. During superfusion, fluorescently-labeled cargo molecules are spontaneously internalized by the protocells. Although the lipid compartments have similar diameter, the fluorescence intensities of their internal volumes vary after superfusion (Fig. S1†). If the uptake solely depended on direct permeation of molecules across the lipid membrane, compartments of similar size would have reached similar internal concentrations after exposure for the same time period.[22] Since we observe very different intensities for different vesicles, we think that a transient pore-enhanced uptake route dominates. A similar observation was reported in an earlier study, where the concentration of encapsulated fluorescein inside containers of similar size ranged from 20% to 90% of the concentration of the external medium.[22] Finite element simulations of diffusion through membrane pores predicted the experimental findings well.[22] According to these simulations, 3–5 pores of nm size in a micrometer-sized container would account for the experimentally observed uptake.[22]

Earlier research has shown that lipid membranes open up transient pores to reduce membrane tension that arises due to factors such as mechanical stress,[23] osmotic stress[24] or optical illumination.[25] The opening of a pore enables the lipids to cover a smaller surface area, lessening the tension on the membrane while simultaneously releasing the excess internal liquid volume. Subsequent closure of the pore is driven by the edge (line) tension of the curved lipids at the edge of the pore.[25,26] Determining the position and number of pores in a vesicle can only be performed in very specific environments, *e.g.* extreme solvent viscosity to stabilize the pores.[23]

In protocell-nanotube networks, simultaneous collapse and emergence of vesicles on the same membrane region can be observed,[10] which indicates variations in local membrane tension. Additionally, during superfusion the network is exposed to a gentle hydrodynamic flow (10–100 nl s^{-1}), which may add to the mechanical stress on the membranous protocells, increasing the membrane tension and facilitating the formation of transient nanopores through which the cargo can diffuse. Our observations on surface-adhered lipid compartment systems[11,22,27] show that the transient pores can contract and close, indicated by the prolongation of fluorescence signal of the encapsulated constituents in the sealed compartments which is distinguishable from the ones which immediately leak the constituents (several minutes *vs.* seconds).[22] The latter leads to a sudden decay in fluorescence intensity measured inside the compartments.[22]

The concentration of FAM-RNA and FAM-ssDNA inside the compartments after 4 min of superfusion was observed to be lower compared to ATTO 488 (Fig. S1†). This is likely due to the higher molecular weight of the RNA and DNA, slowing down their diffusion through the pores (6.8 kDa for FAM-ssDNA, 3.4 kDa for FAM-RNA *vs.* 0.8 kDa for ATTO 488). The cargo molecules that are not encapsulated by the PNN during superfusion, are aspirated by the microfluidic pipette due to continuous recirculation.[21] Upon termination of superfusion, the ambient buffer instantly becomes free of cargo.

The encapsulated cargo could be observed within the model protocells and nanotubes of the network *via* confocal microscopy. The confocal micrograph presented in Fig. 2b

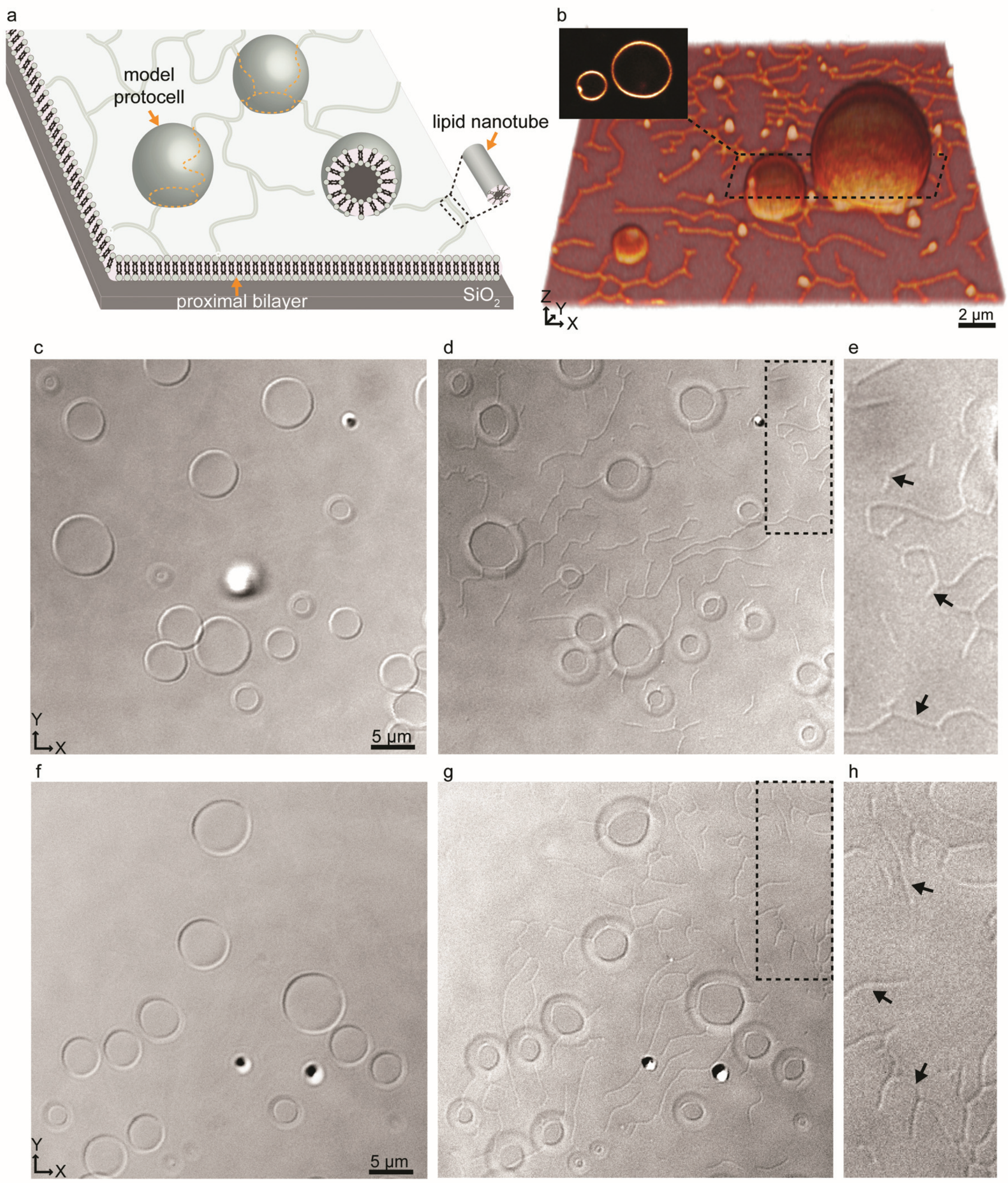

Fig. 1 Protocell-nanotube networks (PNNs). (a) Schematic drawing of a protocell-nanotube network. The network and compartments are adhered to a surface supported bilayer. (b) 3D reconstructed confocal fluorescence micrograph of a PNN formed from a fluorescently-labeled membrane (control). The inset shows a *xy* cross section of the two adjacent vesicles. (c–h) Differential interference contrast (DIC) microscopy images showing PNNs formed from unlabeled lipid membranes. DIC micrographs showing sections from the equator (c and f), and base (d and g) of the PNNs. The magnified version of the regions framed in dashed lines in (d and g) are shown in (e and h), revealing several nanotubes (black arrows).

shows encapsulated ATTO 488 inside a surface-supported PNN. It confirms that the cargo molecules can enter the nanotubes, but cannot alone affirm their ability to transport the cargo. There remains still the possibility that the nanotubes are not conducting, but contain membrane defects which could block the tubes and prevent the exchange of molecules between the compartments.

After encapsulating the cargo, we investigated the transport of the molecules within the network by means of fluorescence recovery after photobleaching (FRAP) experiments (Fig. 2c–f).

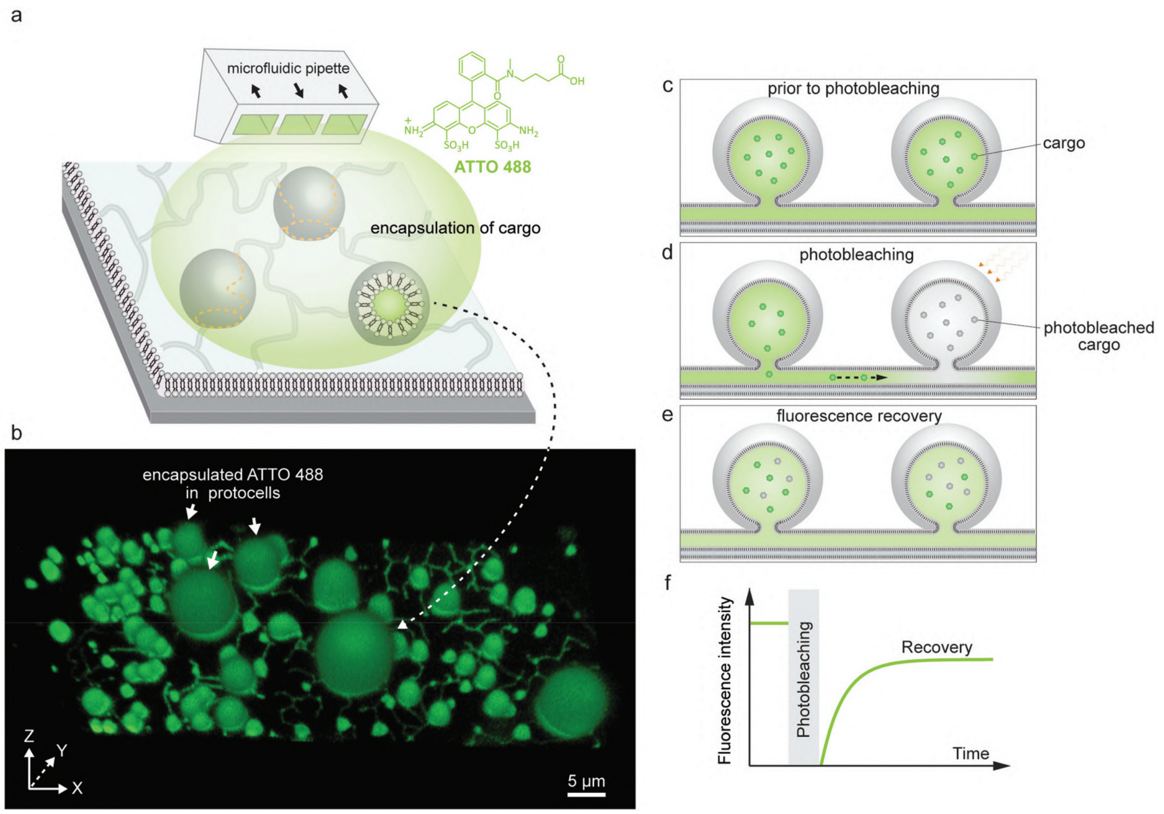

Fig. 2 Encapsulation of molecular cargo inside PNN and FRAP experiment. (a) Schematic representation of the encapsulation experiment. An open-volume microfluidic device (microfluidic pipette) creates a confined exposure zone around the protocells, delivering different cargo molecules, *e.g.* fluorescent dye ATTO 488. (b) 3D confocal micrograph of a label-free PNN upon encapsulating fluorescent dye inside the nanotubes and the protocells. (c–e) Schematic drawing of the FRAP (fluorescence recovery after photobleaching) experiment. (c) The fluorescent cargo is encapsulated inside the protocells and the connecting nanotubes, corresponding to (b). (d) Cargo in one of the protocells in (a) is photobleached using high laser intensity. (e) The fluorescence recovers due to the diffusion of fluorescent cargo from neighboring protocell through the nanotube. (f) Schematic graph depicting typical FRAP curve.

FRAP is a commonly used technique in cell biology and biomaterials science to determine dynamic processes *e.g.* membrane fluidity,[13] protein localization and mobility,[28] protein trafficking in intercellular nanotubes[29,30] and intracellular protein transport in ER or Golgi.[31,32] When an isolated lipid vesicle encapsulating a fluorescent solution suspended in a non-fluorescent aqueous environment is photobleached, its intensity does not recover as there is no access to a new source of fluorophores for replenishment (Fig. S2†).[33] If the vesicles are physically connected through the tunneling nanotubes (Fig. 2c and d), and the molecules are able to diffuse through the tubes, the fluorescence of the photobleached vesicles recovers (Fig. 2e and f).

We verified this hypothesis by encapsulating ATTO 488, FAM-RNA and FAM-ssDNA in several nodes of the protocell networks, photobleaching selected compartments in the network and subsequently measuring the recovery of the initially photobleached compartments. The results from multiple experiments are shown in Fig. 3. Each plot in graphs Fig. 3a, h and l, labeled with a capital letter, shows the fluorescence recovery of a single compartment within a network. Fig. 3a–g are associated with the experiments using ATTO 488, Fig. 3h–k RNA, and Fig. 3l–o DNA as encapsulated molecular cargo. Fig. 3b–d and e–g show confocal microscopy time series from two different experiments. For each experiment, the recovery of the compartments encircled in dashed lines was monitored and plotted in Fig. 3a (I and B). Plot E in Fig. 3h is obtained from the lipid compartment shown in Fig. 3i–k, and plot C in Fig. 3l from the compartment in Fig. 3m–o. Confocal microscopy time series corresponding to all other plots shown in Fig. 3 are presented in Fig. S3–5.†

Plots A–D in Fig. 3a show a final recovery of ~10–20% of the initial fluorescence intensity. Plots E–I show more rapid recovery up to 65% (plot G) of initial intensity. The compartment represented in plot H could only be monitored until 115 s and further data collection could not be achieved. Plots F and I show a decline after reaching 40% of the initial intensity. Decrease in fluorescence intensity can be due to inherent photobleaching caused by continuous imaging,[34] or leakage from the compartments into the ambient solution *via* transient pores or defects in the membrane.[25,35] Sott *et al.* characterized diffusive transport of fluorescein within vesicle-nanotube networks.[18] These networks were manually generated by a microneedle technique. The authors concluded that dissipation factors such as leakage and photobleaching led to a

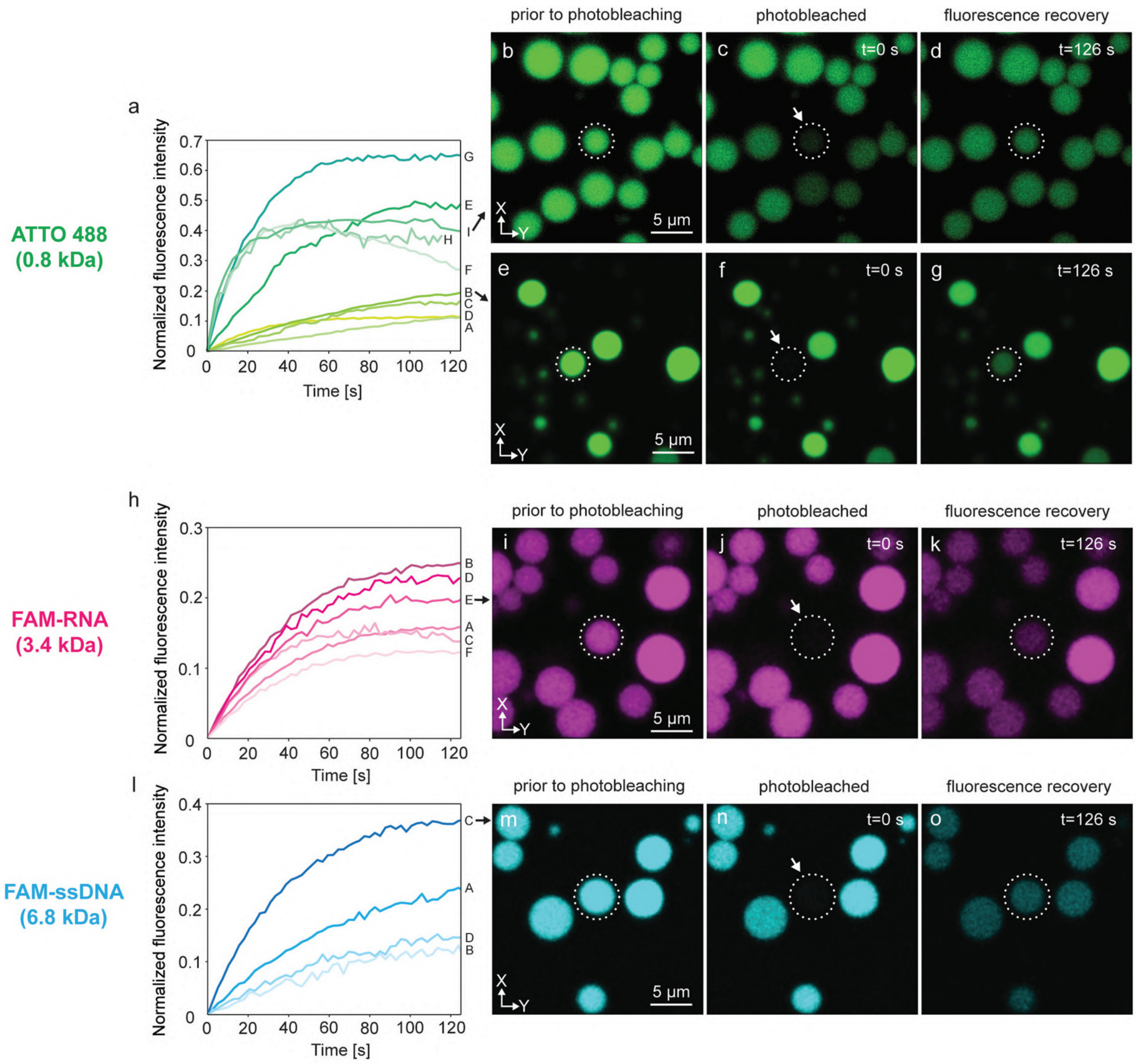

Fig. 3 FRAP of selected compartments within PNNs. Three different cargo molecules, ATTO 488 (green color), FAM-RNA (magenta color) and FAM-ssDNA (cyan color) were loaded into protocell networks. (a) Plots show 9 FRAP experiments of ATTO 488 (A–I), each plot representing one experiment. (b–d) Confocal micrographs corresponding to plot I in panel (a): (b) ATTO 488-containing model protocell prior to, (c) during, (d) after, photobleaching. (e–g) Micrographs of the experiment corresponding to plot B in panel (a). (h) FRAP curves for RNA (plots A to F). (i–k) Micrographs of the FRAP experiment corresponding to plot E in panel (h). (l) Plots showing 4 FRAP experiments for DNA (plots A to D). Micrographs of experiment C are shown in (m–o). The compartments monitored for recovery are encircled in white dashed lines.

minor reduction of fluorescent contents in the network. We provided a detailed discussion in ESI section 4† based on the experimental results depicted in Fig. S6.† It is plausible that up to a 20% fluorescence loss over time could be due to leakage through the membrane, but we also take into account content loss from photobleaching. The latter is not a physical loss, but a reduction of signal from fluorescent species that are still within the container.

Another possibility is transport of content from the recovered vesicle to adjacent compartments through other established nanotubular connections. It is challenging to determine to which exact compartments transfer of material would occur, as protocell-nanotube networks are extending out of the field of view for tens to hundreds of micrometers. RNA-containing compartments (Fig. 3h–k and Fig. S4†) recover ~12–26% of the original intensity over a time period of 100–120 s. It was more challenging to internalize DNA inside the network compared to ATTO 488 and RNA, due to its comparatively larger size. We conducted a total of four FRAP experiments with DNA (Fig. 3l–o and Fig. S5†). The amount of recovery varied between ~12% and 36%. We observed the transfer of all cargo molecules between the compartments, and established thus proof of principle.

Geometric parameters influencing transport

We employed a simple analytical model to determine the impact of certain geometrical parameters for the molecular transport within the protocell-nanotube networks (Fig. 4). Although other transport mechanisms between vesicles *via* nanotubes have been reported, *e.g.* Marangoni transport,[36] for the model we mainly focus on molecular diffusion as means of transport. Rate equations describing the equilibration of particles between two[37,38] or more[38] chambers connected with a capillary (Fig. 4a) were previously established. Volume of the compartments, diffusion coefficient of the molecules traveling between the compartments, length and radius of the connective nanoconduits were taken into account to calculate the diffusion rate[37,38] and relaxation time.[37]

The fluorescence recovery, F, over time, t, takes the form of an exponential function (Fig. 2f) and a FRAP curve can be fitted to:[39]

$$F = F_{\max}\left(1 - e^{-\frac{t}{\tau_{\text{relax}}}}\right) \tag{1}$$

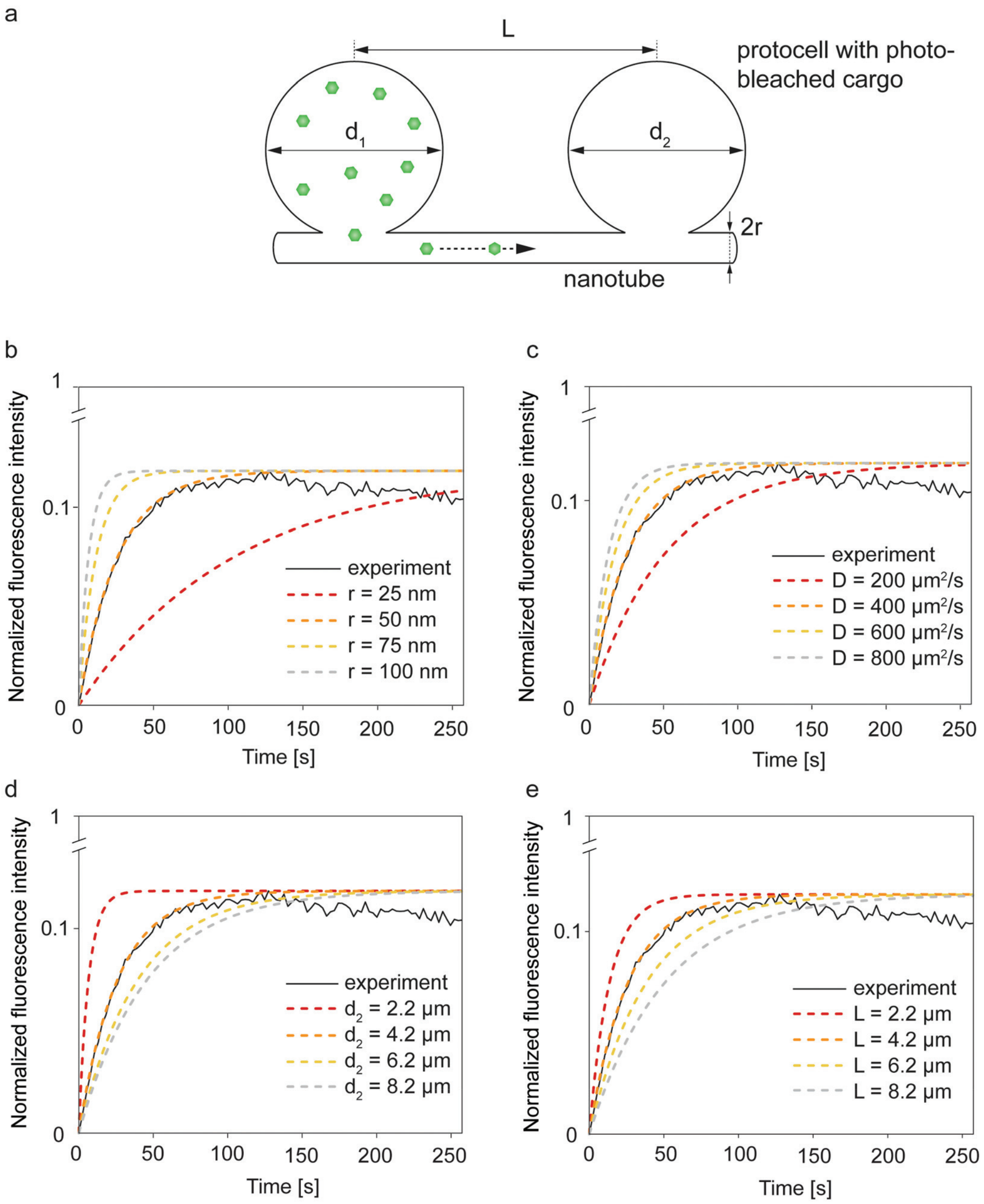

Fig. 4 Geometric parameters influencing molecular diffusion in a two-vesicle system. (a) The analytical model is based upon two vesicles with diameters d_1 and d_2, connected through nanotube with a radius of r and distance L. ATTO 488 transports to the photobleached vesicle. Plot depicted in a black continuous line in (b-e) is experiment shown in Fig. S6.† Dashed lines in (b-e) are obtained with different variables applied to eqn (3). One of the curves in each graph fits to the recovery curve of the photobleached vesicle (solid line) while changing the (b) tube radius (r), (c) diffusion coefficient of the cargo molecule (D), (d) compartment diameter (d), and (e) nanotube length (L).

where $F_{\max}$ is the maximum fluorescence recovery and τ_{relax} is the relaxation time, which is the time for the system to reach chemical equilibrium ($F_{\max}$) at constant, initial diffusion rate. In reality the diffusion rate decreases over time as the concentration gradient between two compartments decreases. The relaxation time (eqn (1)) stands for the duration of time at the end of which, the fluorescence recovery reaches $(1 - 1/e)$ of $F_{\max}$.

For a simple system with two spherical vesicles, the relaxation time, τ_{relax}, is given by:[37]

$$\tau_{\text{relax}} = \frac{V_1 V_2}{V_1 + V_2}\left(\frac{L}{\pi r^2 D}\right) \tag{2}$$

where V_1 and V_2 are the volumes of the compartments between which the diffusion takes place. The diffusion coefficient, D, is distinct for each molecule, while r and L are the radius and length of the nanotube. Because $V = \pi d^3/6$, this expression can be written using the diameters, d, of the vesicles:

$$\tau_{\text{relax}} = \frac{d_1^3 d_2^3}{d_1^3 + d_2^3}\left(\frac{L}{6r^2 D}\right) \tag{3}$$

The above-mentioned models are based on simple, closed systems (dead ends) containing straight tubular connections[37,38,40] (Fig. 4a), where the networks in our experiments typically consists of multiple protocells with a branched, complex network of nanotubes extending outwards with many inter-connections and junctions (Fig. 1). Another feature that is different in our experiments is that the receiving (photobleached) lipid compartments are not free of cargo but contain the cargo with quenched fluorophores (Fig. 2d). Despite these differences, the models appear to provide a good approximation to the experimental system we have.

We compared the fluorescence recovery time of the compartment shown in Fig. S6† to the relaxation time (eqn (3)) predicted by the model[37] (Fig. 4b–e). The two adjacent compartments in the experiment contain ATTO 488, which has a diffusion coefficient (D) of 400 $\mu\text{m}^2\ \text{s}^{-1}$.[41] We assume that the protocell compartments are spherical and connected with a straight tube of length L between the centers of their base. Each of the two compartments has a diameter of 4.2 µm and we take L = 4.2 µm since the compartments are located very close to each other (Fig. S6†). Despite their proximity, it is not likely that these two compartments are fused, based on the mathematical model characterizing the fusion within the PNNs[11] (Fig. S7†). The radius of the nanotube, r, is the unknown variable.

Recovery time based on nanotubular connections with varying nanotube radii were plotted while keeping d_1 = 4.2 µm, d_2 = 4.2 µm, D = 400 $\mu\text{m}^2\ \text{s}^{-1}$, L = 4.2 µm (*cf.* eqn (1) and (3)) (Fig. 4b). The best match of the experimental curve to the theoretical curve was achieved for the tube with a radius of 50 nm (Fig. 4b). This is within the range of tunneling nanotubes observed in cellular[12] and artificial systems.[42]

Next, we focused on diffusion coefficient of the cargo molecule. Fig. 4c shows how diffusion coefficients varying from 200–800 $\mu\text{m}^2\ \text{s}^{-1}$ would change the recovery time of the photobleached molecules, *i.e.* the time for the fluorescently-labeled molecules to travel from one compartment to the photobleached one in the two-vesicle system our model is based on (Fig. 4a and c). The recovery curve for ATTO 488 shown in ESI section S4,† follows the trend predicted for D = 400 $\mu\text{m}^2\ \text{s}^{-1}$ in Fig. 4c. This agrees with the reported diffusion coefficient of ATTO 488.[41] Since we do not have any control on the locations of vesicle nucleation sites, which later transform into protocells, we could not identify an isolated two-vesicle network in experiments involving RNA and DNA. Here we would expect a slower transport as the diffusion coefficients of the RNA and DNA are smaller than of ATTO 488. For a 20-base single-stranded DNA in aqueous solution, D was determined to be 152 $\mu\text{m}^2\ \text{s}^{-1}$ (ref. 43) and for 10-base RNA, 186 $\mu\text{m}^2\ \text{s}^{-1}$.[44] Therefore in a closed two-vesicle setting, the recovery, *i.e.*, transport, of RNA/DNA would be similar to the one shown with red dashed line in Fig. 4c.

Fig. 4d shows multiple plots corresponding to compartments with varying sizes. As anticipated, the larger the diameter of the compartments, the more time it takes to reach equilibrium. For the receiving (photobleached) vesicle this means more volume needs to be filled, while for the donating vesicle it means a lower probability for the cargo to reach the entrance to the nanotube.

Finally we investigated the length of the nanotube (Fig. 4e). With increasing nanotube length the travel time of the cargo in the nanotube increases, resulting in slower fluorescence recovery (Fig. 4e). The nanotube length, related to the distance between the protocells, is directly proportional to the relaxation time (eqn (3)). The exact length of the connecting nanotubes in the experiments is difficult to predict, as they are almost never straight due to pinning and branching.[11,45]

The recovery curve of the experiment shown in Fig. S6† (plot shown with a continuous black line in Fig. 4b–e) declines gradually over time. This can be due to inherent photobleaching caused by continuous imaging,[34] or leakage from the compartments[25,35] as discussed above.

Conclusion

Our findings confirm that the lipid nanotubes in surface-adhered protocell networks are open, and allow molecular transport between the interconnected bilayer-encapsulated compartments. The rate of the diffusive transport is highly dependent on the structure of the network and influenced by the parameters such as the radius and length of the nanotubes, size of the compartments and the diffusion coefficient of the molecule that is transported. There is a physical limit to how small the radius of the lipid nanotubes can be without the presence of curvature stabilizing proteins,[46] rendering the other parameters deciding factors for the diffusion rate in a prebiotically relevant context. We conclude that it appears feasible to increase complexity by encapsulating reactants for prebiotic reactions in PNNs, in order to gain a deeper understanding of possible chemical communication processes within primitive cell populations at the origin of life.

Materials and methods

Lipid preparation

Lipid suspensions were prepared with soybean polar extract and *E. coli* polar extract (Avanti Polar Lipids, USA) (50 : 50 wt%), using the dehydration-rehydration method.[47] Briefly, lipids were dissolved in chloroform in a 10 mL pear shaped bottom flask leading to a final concentration of 10 mg mL^{-1}. Chloroform is toxic and highly volatile and should always be handled under a fume hood with associated personal protective equipment. For the sample shown in Fig. 1b, 1 wt% of lipid-conjugated fluorophore 16:0 Rhod Liss PE (Avanti Polar Lipids, USA) was added into the lipid mixture, and for the sample shown in Fig. S2a,† 1 wt% ATTO 655 DOPE (Atto-Tech GmbH, Germany). 300 µL of the dissolved lipid mixture was placed in a rotary evaporator and the solvent was removed at 24 rpm and reduced pressure (20 kPa) for 6 hours to form a dry lipid film. The dry lipid film was rehydrated with 3 mL phosphate-buffered saline (PBS) followed by addition of 30 µL glycerol. The PBS contained 5 mM Trizma base, 30 mM K_3PO_4, 30 mM KH_2PO_4, 3 mM $MgSO_4 \cdot 7H_2O$, and 0.5 mM Na_2-EDTA (pH = 7.4, adjusted with H_3PO_4). The lipid suspension was kept at 4 °C overnight to allow swelling of the lipid cake. The following day, the suspension was sonicated for 5–10 s at room temperature, leading to formation of a giant vesicle suspension. The suspension was aliquoted and stored at −18 °C.

Surface preparation

SiO_2 surfaces were fabricated at the Norwegian Micro- and Nano-Fabrication Facility at the University of Oslo (MiNaLab). SiO_2 films were deposited onto glass cover slips (Menzel Gläser #1, 100–150 µm thickness; WillCo Wells B.V., Amsterdam, NL) by E-beam physical vapor deposition using an EvoVac instrument (Ångstrom Engineering, Canada), to a final film thickness of 84 nm.

Sample preparation

For sample preparation, two 4 µL droplets of lipid suspension were placed on a clean glass and dehydrated in desiccator for 20–25 min under low pressure. The dry lipid film was rehydrated for 10 min with 0.5–1 mL of Na-HEPES buffer containing 10 mM HEPES and 100 mM NaCl (pH = 7.8, adjusted with NaOH). The rehydrated suspension was later transferred into an observational chamber containing Ca-HEPES buffer (10 mM HEPES, 100 mM NaCl and 4 mM $CaCl_2$, pH = 7.8, adjusted with NaOH). The sample was kept at room temperature for 2–3 days for PNN formation and protocell growth. Alternatively, to speed up the protocell growth, the sample was incubated at 35 °C until the following day to promote protocell growth.[11]

Encapsulation of cargo molecules

The cargo molecules were delivered with an open-volume microfluidic pipette[20,21] (Fluicell AB, Sweden) positioned using 3-axis hydraulic micromanipulator (Narishige, Japan) to the vicinity of the protocell-nanotube structures. The protocells were superfused with solutions of Ca-HEPES buffer containing 500 µM of ATTO 488 carboxyl (Atto-Tech GmbH, Germany). DNA solution was prepared and delivered in nuclease-free water (Thermo Fisher Scientific, USA) by dissolving 200 µM of 20-base ssDNA (5′-/56-FAM/TGT ACG TCA CAA CTA CCC CC-3′, Integrated DNA Technologies, USA). 10-base RNA oligomers (5′-FAM-AAA AAA AAA A-3′, Dharmacon, USA) were dissolved in nuclease-free water to a final concentration of 100 µM. Exposing the nanotube networks rapidly to nuclease-free deionized water -a hypotonic environment- facilitated the rapid swelling and growth of membranous compartments (Movie S1†), reducing the time period of growth from hours[10] to minutes.

Microscopy imaging and analysis

Imaging has been performed using Laser scanning confocal microscope DMi8 (Leica Microsystems, Germany) equipped with a 40× oil objective (NA: 1.3). The 3D fluorescence micrographs in Fig. 1b and 2b were reconstructed using the Leica Application Suite X Software (Leica Microsystems, Germany). Image enhancement (brightness/contrast) of fluorescence micrographs in the figures was performed with the Adobe Photoshop CS4 (Adobe Systems, USA). Schematic drawings were created with Adobe Illustrator CS4 (Adobe Systems, USA).

FRAP

FRAP experiments were performed using the FRAP module in the Leica Application Suite X Software. UV diode laser (405 nm, 50 mW) with 50% intensity was used for the photobleaching. A circular region of interest (ROI) on each protocell was defined. The ROIs were monitored during pre-photobleaching (~10 s), photobleaching (~10 s) and post-photobleaching (>115 s), consecutively.

The FRAP curves in Fig. 3, 4 and S6† show the recovery period after photobleaching. The FRAP curve in Fig. S2† includes the period prior to photobleaching. The normalized fluorescence intensity ($I_{\text{normalized}}$) of the plots in Fig. 3, 4 and S2† was determined as: $= \frac{I(t) - I_0}{I_{\text{initial}} - I_0}$, where $I(t)$ is the fluorescence intensity at time t, I_0 is the fluorescence intensity right after the photobleaching/at the beginning of the recovery, and I_{initial} is the fluorescence intensity prior to the photobleaching. In Fig. S6,† the normalized fluorescence intensity of the donor ($I_{\text{normalized,donor}}$) and acceptor ($I_{\text{normalized,acceptor}}$) protocell after photobleaching was determined as: $I_{\text{normalized, donor}} = \frac{I_{\text{donor}}(t) - I_{0,\text{acceptor}}}{I_{0,\text{donor}} - I_{0,\text{acceptor}}}$ and $I_{\text{normalized, acceptor}} = \frac{I_{\text{acceptor}}(t) - I_{0,\text{acceptor}}}{I_{0,\text{donor}} - I_{0,\text{acceptor}}}$, respectively. $I_{\text{donor}}(t)$ and $I_{\text{acceptor}}(t)$ are the fluorescence intensity of donor and acceptor protocell, respectively, at time t. $I_{0,\text{ donor}}$ and $I_{0,\text{ acceptor}}$ are the fluorescence intensities when $t = 0$, *i.e.* the beginning of the fluorescence recovery, for the donor and acceptor protocell, respectively. All graphs in Fig. 3, 4, S2 and S6† were plotted using MATLAB R2020b.

Conflicts of interest

The authors declare no competing financial interest.

Acknowledgements

This work was made possible through financial support obtained from the Research Council of Norway (Norges Forskningsråd) Project Grant 274433, UiO: Life Sciences Convergence Environment, as well as the startup funding provided by the Centre for Molecular Medicine Norway (RCN 187615) at the University of Oslo.

References

1 P. Walde, Building artificial cells and protocell models: Experimental approaches with lipid vesicles, *BioEssays*, 2010, **32**(4), 296–303.
2 A. J. Dzieciol and S. Mann, Designs for life: protocell models in the laboratory, *Chem. Soc. Rev.*, 2011, **41**(1), 79–85.
3 S. F. Jordan, H. Rammu, I. N. Zheludev, A. M. Hartley, A. Maréchal and N. Lane, Promotion of protocell self-assembly from mixed amphiphiles at the origin of life, *Nat. Ecol. Evol.*, 2019, **3**(12), 1705–1714.
4 T. Gánti, *The principles of life*, Oxford University Press, 2003.
5 Y. Huang, B. Zucker, S. Zhang, S. Elias, Y. Zhu, H. Chen, T. Ding, Y. Li, Y. Sun, J. Lou, M. M. Kozlov and L. Yu, Migrasome formation is mediated by assembly of micron-scale tetraspanin macrodomains, *Nat. Cell Biol.*, 2019, **21**(8), 991–1002.
6 M. Liang, L. Ying, P. Junya, W. Danni, Z. Xiaoxin, C. Yitong, C. Lilian, Y. Xiaojun, D. Yanan and Y. Li, Discovery of the migrasome, an organelle mediates release of cytoplasmic contents during cell migration, *Cell Res.*, 2015, **25**, 24–38.
7 B. Alberts, J. H. Wilson and T. Hunt, *Molecular biology of the cell*, Garland Science, New York, 6th edn, 2015.
8 P. Albuquerque and A. Casadevall, Quorum sensing in fungi – a review, *Med. Mycol.*, 2012, **50**(4), 337–345.
9 K. Papenfort and B. L. Bassler, Quorum sensing signal-response systems in Gram-negative bacteria, *Nat. Rev. Microbiol.*, 2016, **14**(9), 576–588.
10 E. S. Köksal, S. Liese, I. Kantarci, R. Olsson, A. Carlson and I. Gözen, Nanotube-Mediated Path to Protocell Formation, *ACS Nano*, 2019, **13**, 6867–6878.
11 E. S. Köksal, S. Liese, L. Xue, R. Ryskulov, L. Viitala, A. Carlson and I. Gözen, Rapid Growth and Fusion of Protocells in Surface-Adhered Membrane Networks, *Small*, 2020, **16**(38), 2002529.
12 A. Rustom, R. Saffrich, I. Markovic, P. Walther and H.-H. Gerdes, Nanotubular Highways for Intercellular Organelle Transport, *Science*, 2004, **303**(5660), 1007–1010.
13 X. Wang and H. H. Gerdes, Transfer of mitochondria via tunneling nanotubes rescues apoptotic PC12 cells, *Cell Death Differ.*, 2015, **22**(7), 1181–1191.
14 G. P. Dubey and S. Ben-Yehuda, Intercellular Nanotubes Mediate Bacterial Communication, *Cell*, 2011, **144**(4), 590–600.
15 A. K. Baidya, S. Bhattacharya, G. P. Dubey, G. Mamou and S. Ben-Yehuda, Bacterial nanotubes: a conduit for intercellular molecular trade, *Curr. Opin. Microbiol.*, 2018, **42**, 1–6.
16 G. P. Dubey, G. B. Malli Mohan, A. Dubrovsky, T. Amen, S. Tsipshtein, A. Rouvinski, A. Rosenberg, D. Kaganovich, E. Sherman, O. Medalia and S. Ben-Yehuda, Architecture and Characteristics of Bacterial Nanotubes, *Dev. Cell*, 2016, **36**(4), 453–461.
17 J. Matko and E. A. Toth, Membrane nanotubes are ancient machinery for cell-to-cell communication and transport. Their interference with the immune system, *Biol. Futura*, 2021, **72**(1), 25–36.
18 K. Sott, T. Lobovkina, L. Lizana, M. Tokarz, B. Bauer, Z. Konkoli and O. Orwar, Controlling Enzymatic Reactions by Geometry in a Biomimetic Nanoscale Network, *Nano Lett.*, 2006, **6**(2), 209–214.
19 J. W. Lichtman and J.-A. Conchello, Fluorescence microscopy, *Nat. Methods*, 2005, **2**(12), 910–919.
20 A. Ainla, E. T. Jansson, N. Stepanyants, O. Orwar and A. Jesorka, A Microfluidic Pipette for Single-Cell Pharmacology, *Anal. Chem.*, 2010, **82**(11), 4529–4536.
21 A. Ainla, G. D. M. Jeffries, R. Brune, O. Orwar and A. Jesorka, A multifunctional pipette, *Lab Chip*, 2012, **12**(7), 1255–1261.
22 K. Spustova, E. S. Köksal, A. Ainla and I. Gözen, Subcompartmentalization and Pseudo-Division of Model Protocells, *Small*, 2021, **17**(2), e2005320.
23 O. Sandre, L. Moreaux and F. Brochard-Wyart, Dynamics of Transient Pores in Stretched Vesicles, *Proc. Natl. Acad. Sci. U. S. A.*, 1999, **96**(19), 10591–10596.
24 Y. Levin and M. A. Idiart, Pore dynamics of osmotically stressed vesicles, *Phys. A*, 2004, **331**(3), 571–578.
25 E. Karatekin, O. Sandre and F. Brochard-Wyart, Transient pores in vesicles, *Polym. Int.*, 2003, **52**(4), 486–493.
26 I. Gozen and P. Dommersnes, Pore dynamics in lipid membranes, *Eur. Phys. J.: Spec. Top.*, 2014, **223**(9), 1813–1829.
27 E. S. Köksal, I. Põldsalu, H. Friis, S. J. Mojzsis, M. Bizzarro and I. Gözen, Spontaneous Formation of Prebiotic Compartment Colonies on Hadean Earth and Pre-NoachianMars**, *ChemSystemsChem*, 2022, **4**, e20210004.
28 E. A. Reits and J. J. Neefjes, From fixed to FRAP: measuring protein mobility and activity in living cells, *Nat. Cell Biol.*, 2001, **3**(6), E145–E147.
29 S. Desir, P. Wong, T. Turbyville, D. Chen, M. Shetty, C. Clark, E. Zhai, Y. Romin, K. Manova-Todorova,

T. K. Starr, D. V. Nissley, C. J. Steer, S. Subramanian and E. Lou, Intercellular transfer of oncogenic KRAS via tunneling nanotubes introduces intracellular mutational heterogeneity in colon cancer cells, *Cancers*, 2019, **11**(7), 892.

30 N. Rainy, D. Chetrit, V. Rouger, H. Vernitsky, O. Rechavi, D. Marguet, I. Goldstein, M. Ehrlich and Y. Kloog, H-Ras, transfers from B to T cells via tunneling nanotubes, *Cell Death Dis.*, 2013, **4**(7), e726.

31 A. S. Verkman, Solute and macromolecule diffusion in cellular aqueous compartments, *Trends Biochem. Sci.*, 2002, **27**(1), 27–33.

32 J. F. Presley, K. Hirschberg, K. J. M. Zaal, J. Lippincott-Schwartz, N. B. Cole and T. A. Schroer, ER-to-Golgi transport visualized in living cells, *Nature*, 1997, **389**(6646), 81–85.

33 A. Fragasso, N. De Franceschi, P. Stömmer, E. O. van der Sluis, H. Dietz and C. Dekker, Reconstitution of Ultrawide DNA Origami Pores in Liposomes for Transmembrane Transport of Macromolecules, *ACS Nano*, 2021, **15**(8), 12768–12779.

34 M. Kang, M. Andreani and A. K. Kenworthy, Validation of normalizations, scaling, and photofading corrections for FRAP data analysis, *PLoS One*, 2015, **10**(5), e0127966.

35 A. S. Ladokhin, W. C. Wimley and S. H. White, Leakage of membrane vesicle contents: determination of mechanism using fluorescence requenching, *Biophys. J.*, 1995, **69**(5), 1964–1971.

36 J. Hurtig and O. Orwar, Injection and transport of bacteria in nanotube-vesicle networks, *Soft Matter*, 2008, **4**(7), 1515–1520.

37 L. Dagdug, A. M. Berezhkovskii, S. Y. Shvartsman and G. H. Weiss, Equilibration in two chambers connected by a capillary, *J. Chem. Phys.*, 2003, **119**(23), 12473–12478.

38 L. Lizana and Z. Konkoli, Diffusive transport in networks built of containers and tubes, *Phys. Rev. E: Stat., Nonlinear, Soft Matter Phys.*, 2005, **72**(2 Pt 2), 026305–026305.

39 C. Kappel and R. Eils, Fluorescence recovery after photobleaching with the Leica TCS SP2, *Confocal Appl. Lett.*, 2004, **18**, 1–12.

40 H. Zhang, *Artificial and Intercellular Nanotubes*, PhD, Chalmers University of Technology, 2013.

41 P. Kapusta, *Absolute Diffusion Coefficients: Comilation of Reference Data for FCS Calibration*, 2010.

42 T. Lobovkina, P. Dommersnes, J.-F. Joanny, J. Hurtig and O. Orwar, Zipper dynamics of surfactant nanotube Y junctions, *Phys. Rev. Lett.*, 2006, **97**(18), 188105–188105.

43 E. Stellwagen and N. C. Stellwagen, Determining the electrophoretic mobility and translational diffusion coefficients of DNA molecules in free solution, *Electrophoresis*, 2002, **23**(16), 2794–2803.

44 A. Werner, Predicting translational diffusion of evolutionary conserved RNA structures by the nucleotide number, *Nucleic Acids Res.*, 2011, **39**(3), e17.

45 T. Bilal and I. Gzen, Formation and dynamics of endoplasmic reticulum-like lipid nanotube networks, *Biomater. Sci.*, 2017, **5**(7), 1256–1264.

46 Y. F. Barooji, A. Rørvig-Lund, S. Semsey, S. N. S. Reihani and P. M. Bendix, Dynamics of membrane nanotubes coated with I-BAR, *Sci. Rep.*, 2016, **6**(1), 30054–30054.

47 M. Karlsson, K. Nolkrantz, M. J. Davidson, A. Strömberg, F. Ryttsén, B. Åkerman and O. Orwar, Electroinjection of Colloid Particles and Biopolymers into Single Unilamellar Liposomes and Cells for Bioanalytical Applications, *Anal. Chem.*, 2000, **72**(23), 5857–5862.

Electronic Supplementary Material (ESI) for Nanoscale.

Supporting Information for:

Transport among protocells via tunneling nanotubes

Ingrid Jin Schanke[1†], Lin Xue[1†], Karolina Spustova[1], Irep Gözen[1,2*]

[1]Centre for Molecular Medicine Norway, Faculty of Medicine, University of Oslo, 0318 Oslo, Norway
[2]Department of Chemistry, Faculty of Mathematics and Natural Sciences, University of Oslo, 0315 Oslo, Norway

†These authors contributed equally to this work.

*To whom correspondence should be addressed. Email: irep@uio.no

Table of Contents

S1. Encapsulation of cargo molecules 2
S2. FRAP of an isolated vesicle (control) 3
S3. FRAP experiments 4
S4. Fluorescence recovery in a two-compartment system 7
S5. Supporting Movie 9
References 9

S1. Encapsulation of cargo molecules

Three different fluorescent cargo molecules with varying molecular weights were introduced to the protocell-nanotube networks (PNNs) using an open-space microfluidic pipette[1, 2]: a fluorescent dye (ATTO 488) (**Fig. S1a-b**), RNA (**Fig. S1c-d**) and DNA (**Fig. S1e-f**). Panels **a**,**c** and **e**, represent the part of the experiment during which the fluorescently labeled cargo molecules are continuously exposed to a region on the PNNs. Panels **b**,**d** and **f** shows the networks after ~4 min of exposure.

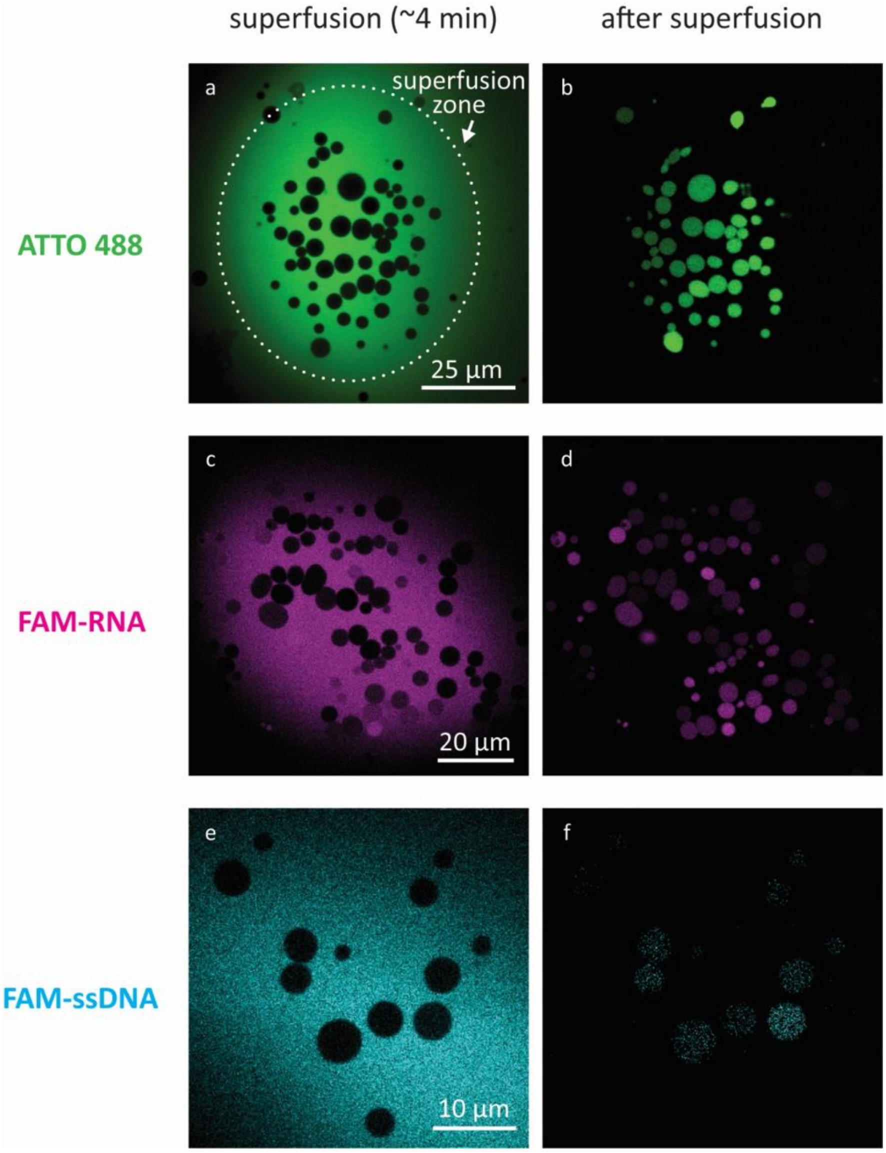

Figure S1. Encapsulation of different cargo molecules. **a, c, e**) Confocal micrographs ~4 min into the superfusion, and **b, d, f**) right after superfusion is terminated. (**a-b**) ATTO 488, (**c-d**) FAM-RNA, (**e-f**) FAM-ssDNA.

S2. FRAP of an isolated vesicle (control)

We performed a control FRAP experiment on an isolated, surface-adhered giant unilamellar vesicle (GUV) containing ATTO 488 (**Fig. S2a-b**). Upon photobleaching, no recovery was observed (**Fig. S2c-d**). This result confirms necessity of a nanotubular connection for recovery of the fluorescence intensity of a lipid compartment in PNNs.

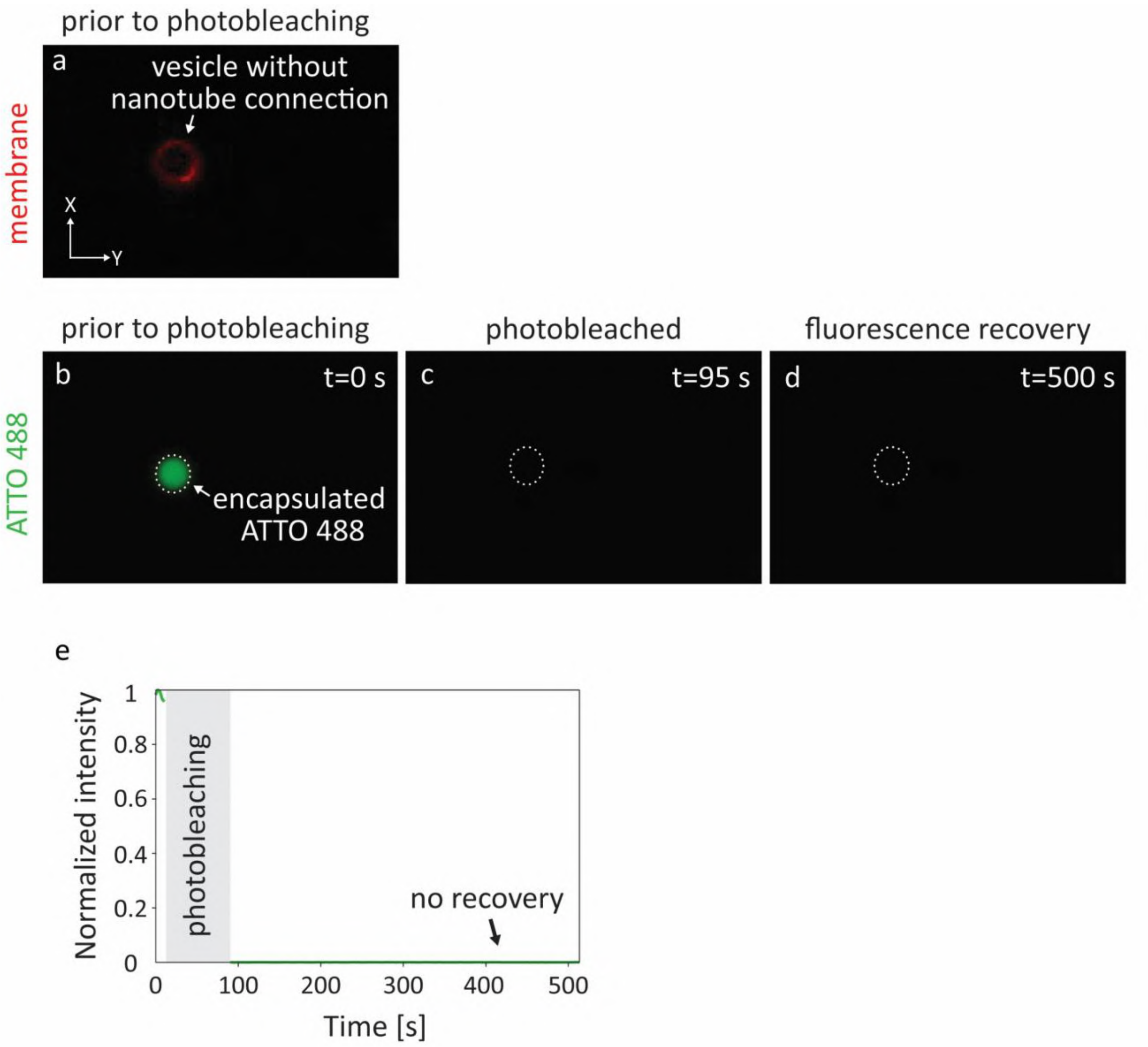

Figure S2. FRAP of an isolated GUV on a solid substrate. (**a-b**) Confocal micrograph of an isolated GUV, encapsulating ATTO 488. (**a**) shows the membrane fluorescence, and (**b**) the fluorescence of the internalized dye, ATTO 488. Photobleached GUV (**c-d**). (**e**) FRAP curve corresponding to (**b-d**). The diameter of the vesicle is 4 μm.

S3. FRAP experiments

Confocal microscopy time series corresponding to the plots shown in **Fig. 3** of the main manuscript. Several FRAP experiments were performed for each cargo molecule ATTO 488 (**Fig. S3**), RNA (**Fig. S4**) and DNA (**Fig. S5**). Each experiment is labeled with the capital letters matching the labels of the plots in **Fig. 3a,h,l**.

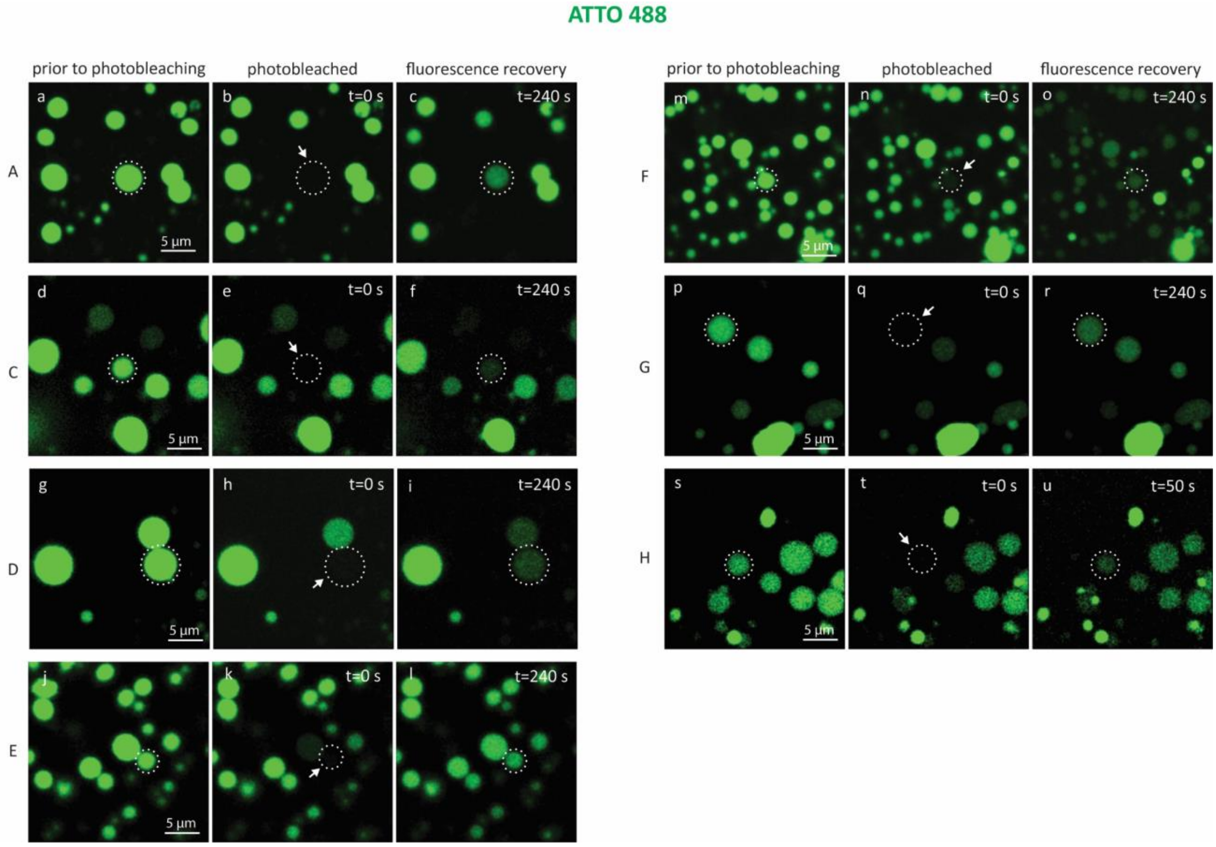

Figure S3. Confocal micrographs showing before, during and after photobleaching of compartments encapsulating **ATTO 488** in different experiments: A (**a-c**), C–H (**d-u**). Each set of micrographs show a model protocell targeted for photobleaching (encircled in dotted lines). Three time points in each experiment represent: prior to photobleaching, during photobleaching (arrows) and during fluorescence recovery.

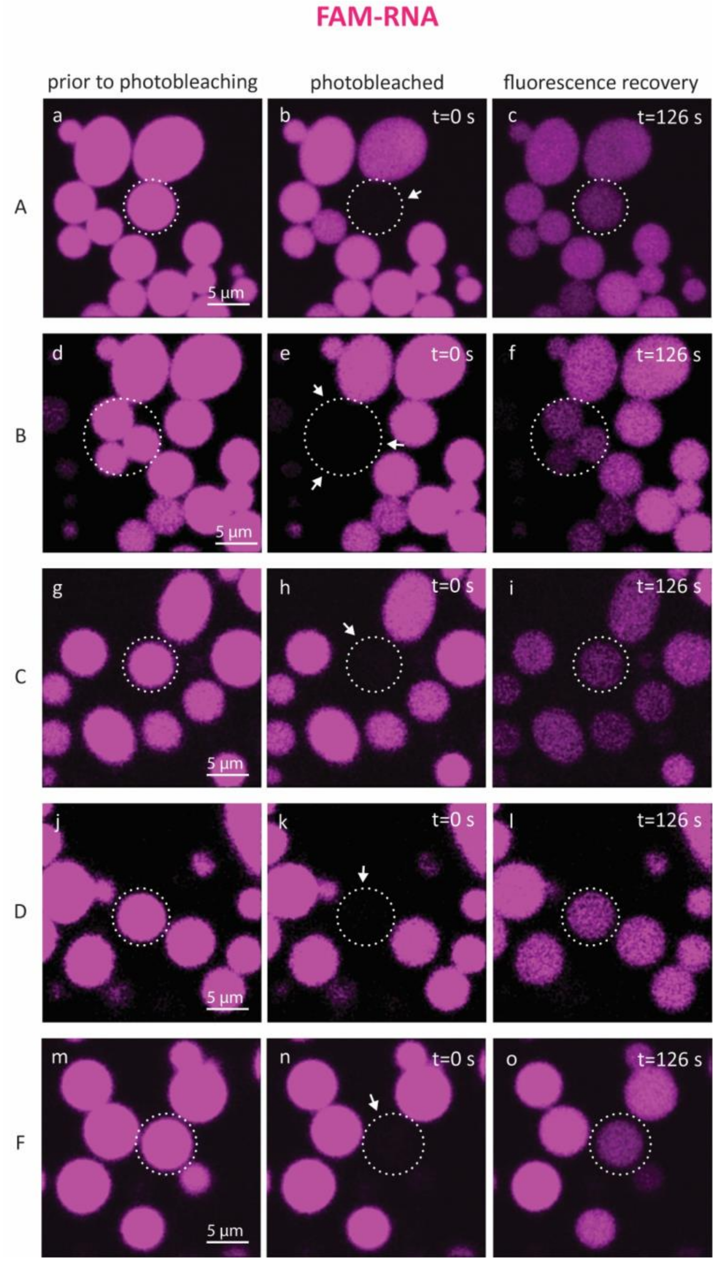

Figure S4. Confocal micrographs showing before, during and after photobleaching of compartments encapsulating **RNA** in different experiments: A-F (**a-o**). Each set of micrographs show a model protocell targeted for photobleaching (encircled in dotted lines). Three time points in each experiment represent: prior to photobleaching, during photobleaching (arrows) and during fluorescence recovery.

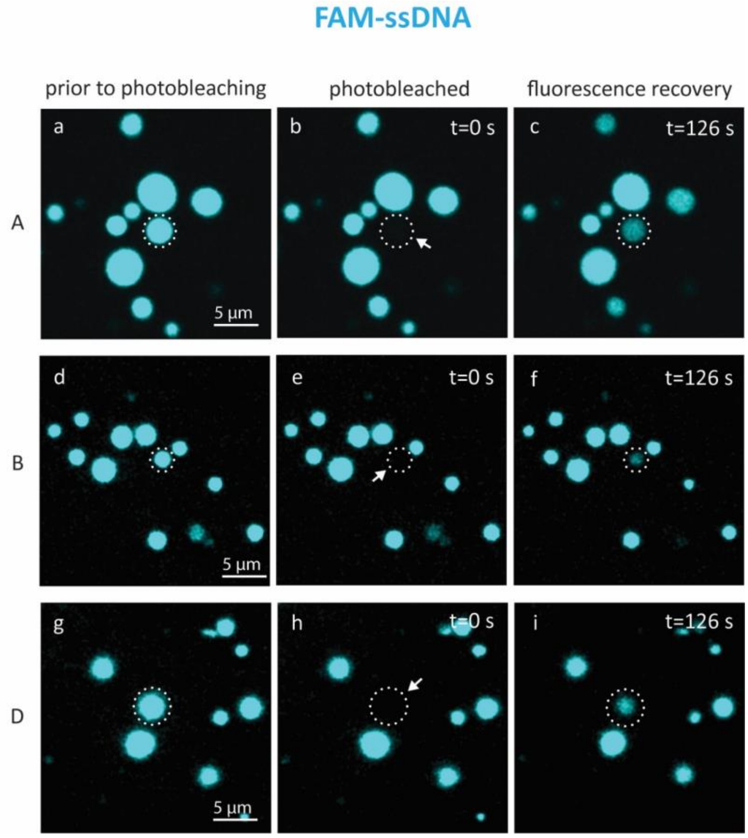

Figure S5. Confocal micrographs showing before, during and after photobleaching of compartments encapsulating **DNA** in different experiments: A-D (**a-i**). Each set of micrographs show a model protocell targeted for photobleaching (encircled in dotted lines). Three time points in each experiment represent: prior to photobleaching, during photobleaching (arrows) and during fluorescence recovery.

S4. Fluorescence recovery in a two-compartment system

A FRAP experiment followed by the transport of ATTO 488 between two adjacent protocells has been presented in **Fig. S6a-c** (same as **Fig. S3d**). **Fig. S6d** shows the fluorescence intensity of the donor (yellow plot) and acceptor (green plot) protocell, over time. The dashed line is the theoretical fit based on a two-compartment model[3] (**Fig. 4**), which overlaps with the fluorescence recovery (green plot). The high fluorescence intensity of the leftmost protocell in **Fig. S6c** maintains during several minutes, indicating that it has no open nanotubular connection to protocell 1 or 2, and is not a contributing donor compartment (**Fig. S6a**).

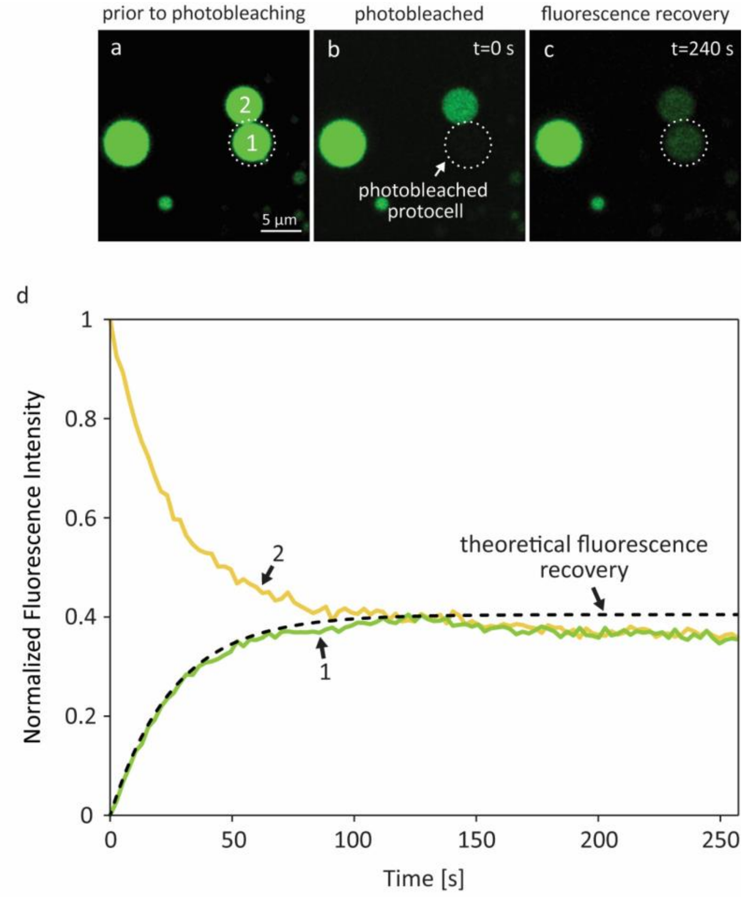

Figure S6. Fluorescence intensity of a two-compartment system after photobleaching of one of the compartments. (**a-c**) Protocell 1 (encircled in dotted line) is photobleached. (**d**) Fluorescence intensity of the donor (yellow plot) and acceptor (green plot) vesicle, over time.

After 100 s the fluorescence intensity of compartments #1 and #2 (**Fig. S6d**) reach an equilibrium at 40% of the initial concentration of the donor compartment (#2). If the experimental system depicted in **Fig. S6** was free of dissipation factors[4] such as leakage or photobleaching, both protocells would reach 50% of the initial concentration, as predicted by analytical and numerical methods that describe diffusive transport of non-interacting particles in a two-vesicle system[5]. However, the total amount of fluorescence intensity of the two protocells in **Fig. S6** reaches approximately 80% after 100 s; 20% have been lost due to other factors than inter-vesicular transport.

The characteristic time of leakage from a single lipid vesicle, τ, can be used to calculate the permeability coefficient P of a solute through the vesicular membrane: $\tau = \frac{V}{SP}$ where V and S are the internal volume and surface area of the vesicle, respectively[6, 7]. This expression can be simplified as $= \frac{R}{3P}$, where R is the vesicle radius. The fluorescence intensity $I(t)$ inside a vesicle at a given time t is given as $I(t) = I_0 + (I_\infty - I_0)\left(1 - e^{-\frac{t}{\tau}}\right)$, where I_0 is the initial fluorescence intensity of the vesicle, i.e. before leakage, and I_∞ is the intensity after an infinite period[6, 7]. $I_0 = 1$ (100% at t=0 s in **Fig. S6**). After an infinite period, the cargo completely leaks out and is diluted in the ambient buffer, thus $I_\infty = 0$. This leads to $I(t) = e^{-\frac{t}{\tau}}$ and $P = \frac{-R \ln I(t)}{3t}$.

Assuming that a loss of 20% of the total intensity from a vesicle during 100 s is entirely due to leakage ($I(t) = 0.8$), where R =2.1 µm (Fig. S6), P can be determined as $0.156 \times 10^{-6} cm/s$. The permeability coefficient depends on various factors[8], e.g. membrane composition, lipid phase, chain length, sterol type. Permeability coefficients of different lipid membranes have been reported[9-12]. P across a DMPC:DPPC (50:50) bilayer was calculated as $0.2 \times 10^{-9} cm/s$ for ATP. P of fluorescein through GUVs composed of DPPC, DOPC and cholesterol (1:1:1) was determined as $19.4 \pm 1.8 \times 10^{-6}\ cm/s$ by Li et al. [12]. For vesicles with the same phospholipid composition as used in our work, P values for fluorescein and 10-base RNA taken up are $\sim 0.5 - 1.0 \times 10^{-6}\ cm/s$ [11], slightly higher than what we determine for ATTO 488 in the experiment related to **Fig. S6**. In summary, it is plausible that the 20% fluorescence loss over time could be due to leakage through the membrane, but we also take into account content loss from photobleaching. The latter is not a physical loss, but a reduction of signal from fluorescent species that are still within the container.

Fig. S7a shows the cross-section of the protocells in **Fig. S6a**. Despite their proximity, spontaneous fusion between the compartments is not likely, as energy input is required to create pores in initially isolated bilayers. Fusion in PNNs induced by external cues was previously observed, and characterized with a mathematical model[13]. It is expected that if the two compartments fuse at their equator, they will rapidly form a larger compartment containing a stable circular pore (**Fig. S7b-d**). Maintaining a transient state over minutes (**Fig. S7c**) is not energetically favorable, therefore it is not likely that the compartments shown in **Fig. S6a/S7a**, are fused.

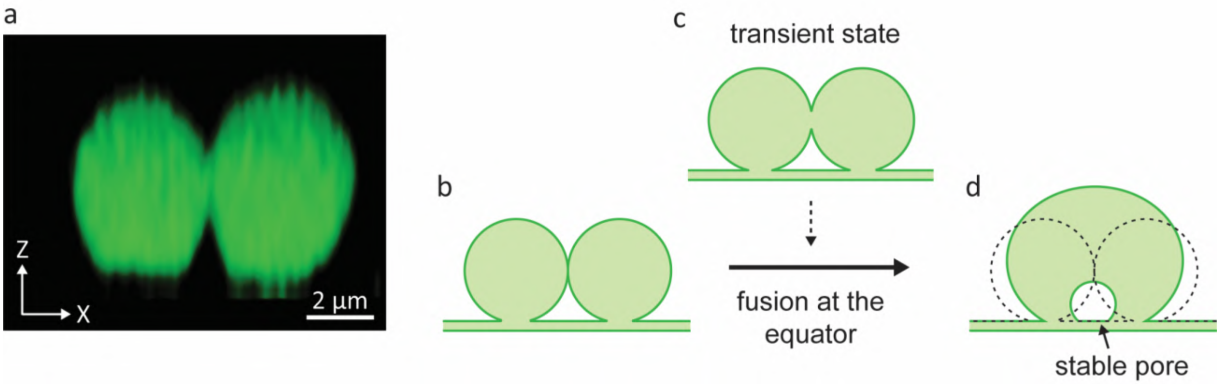

Figure S7. Possible steps of fusion of adjacent protocells. (**a**) Cross-section of the adjacent protocells in Fig. S6. (**b-d**) The possible steps of fusion between the compartments in PNNs, induced by external cues.

S5. Supporting Movie

Movie S1. Rapid formation of protocells during DNA exposure. Laser scanning confocal microscopy time series showing rapid formation and growth of protocells from the nanotube network during DNA exposure.

References

1. Ainla, A.; Jansson, E. T.; Stepanyants, N.; Orwar, O.; Jesorka, A., A Microfluidic Pipette for Single-Cell Pharmacology. *Anal. Chem* **2010,** *82* (11), 4529-4536.
2. Ainla, A.; Jeffries, G. D. M.; Brune, R.; Orwar, O.; Jesorka, A., A multifunctional pipette. *Lab Chip* **2012,** *12* (7), 1255-1261.
3. Dagdug, L.; Berezhkovskii, A. M.; Shvartsman, S. Y.; Weiss, G. H., Equilibration in two chambers connected by a capillary. *The Journal of chemical physics* **2003,** *119* (23), 12473-12478.
4. Sott, K.; Lobovkina, T.; Lizana, L.; Tokarz, M.; Bauer, B.; Konkoli, Z.; Orwar, O., Controlling Enzymatic Reactions by Geometry in a Biomimetic Nanoscale Network. *Nano Letters* **2006,** *6* (2), 209-214.
5. Lizana, L.; Konkoli, Z., Diffusive transport in networks built of containers and tubes. *Phys Rev E Stat Nonlin Soft Matter Phys* **2005,** *72* (2 Pt 2), 026305-026305.
6. Lawaczeck, R., On the permeability of water molecules across vesicular lipid bilayers. *The Journal of membrane biology* **1979,** *51* (3-4), 229-261.
7. Faure, C.; Nallet, F.; Roux, D.; Milner, S. T.; Gauffre, F.; Olea, D.; Lambert, O., Modeling Leakage Kinetics from Multilamellar Vesicles for Membrane Permeability Determination: Application to Glucose. *Biophys J* **2006,** *91* (12), 4340-4349.
8. Frallicciardi, J.; Melcr, J.; Siginou, P.; Marrink, S. J.; Poolman, B., Membrane thickness, lipid phase and sterol type are determining factors in the permeability of membranes to small solutes. *Nat Commun* **2022,** *13* (1), 1605-1605.

9. Sacerdote, M. G.; Szostak, J. W., Semipermeable Lipid Bilayers Exhibit Diastereoselectivity Favoring Ribose. *Proc Natl Acad Sci U S A* **2005,** *102* (17), 6004-6008.
10. Monnard, P.-A.; Deamer, D. W., Nutrient uptake by protocells: A liposome model system. *Orig Life Evol Biosph* **2001,** *31* (1-2), 147-155.
11. Poldsalu, I.; Koksal, E. S.; Gozen, I., Mixed fatty acid-phospholipid protocell networks. *Phys Chem Chem Phys* **2021,** *23* (47), 26948-26954.
12. Li, S.; Hu, P.; Malmstadt, N., Confocal Imaging to Quantify Passive Transport across Biomimetic Lipid Membranes. *Anal. Chem* **2010,** *82* (18), 7766-7771.
13. Köksal, E. S.; Liese, S.; Xue, L.; Ryskulov, R.; Viitala, L.; Carlson, A.; Gözen, I., Rapid Growth and Fusion of Protocells in Surface-Adhered Membrane Networks. *Small (Weinheim an der Bergstrasse, Germany)* **2020,** *16* (38), 2002529-n/a.

III